

TABLE OF CONTENTS

RÉSUMÉ	IV
ABSTRACT	VIII
DEDICATION	XI
ACKNOWLEDGMENTS	XII
TABLE OF CONTENTS	XIII
LIST OF TABLES	XVIII
LIST OF FIGURES	XXI
LIST OF SYMBOLS	XXXII
LIST OF ABBREVIATIONS	XXXIII
PREFACE	XXXIV
CHAPTER 1 INTRODUCTION	35
1.1 Structure of the thesis	40
CHAPTER 2 LITERATURE REVIEW	42
2.1 Introduction	42
2.2 The compliance of non-rigid parts	42
2.3 Measurement and 3D data acquisition methods	44
2.4 Dimensioning, tolerancing and inspection specification of non-rigid parts ...	46
2.4.1 Rigid registration	50
2.4.2 Fixtureless inspection of non-rigid parts (non-rigid registration)	51
2.4.2.1 Fixtureless inspection based on virtually deforming the scan model .	52
2.4.2.2 Fixtureless inspection based on virtually deforming the CAD model	56
2.5 Verification and validation methods based on ASME recommendations	64

2.6	State of the art summary	67
CHAPTER 3 GENERAL PLANNING OF THE THESIS		68
3.1	Statement of the problem	68
3.2	Research objectives	71
3.3	Hypotheses used in the project.....	73
3.4	The synthesis of researches and logical links between articles	74
3.4.1	Simulated scan models for validation cases.....	74
3.4.2	Automatic fixtureless CAI based on filtering corresponding sample points (Article 1).....	77
3.4.3	Validation and verification of our CAI method (Article 2)	78
3.4.4	Virtual inspection in assembly-state using permissible loads for deviated non-rigid parts (Article 3)	79
CHAPTER 4 AUTOMATIC FIXTURELESS INSPECTION OF NON-RIGID PARTS BASED ON FILTERING REGISTRATION POINTS.....		81
4.1	Abstract	81
4.2	Introduction.....	82
4.3	Literature review	85
4.4	Methodology and implementation	89
4.4.1	Description of the proposed methodology	89
4.4.2	Implementation	102
4.4.3	Validation on a case with no defects.....	103
4.5	Results.....	106
4.5.1	Introduction: validation cases	106

4.5.2	Validation cases for part A.....	107
4.5.3	Validation cases for part B.....	119
4.6	Conclusion	132
4.7	Acknowledgment	133
4.8	References.....	134
CHAPTER 5 ASSESSMENT OF THE ROBUSTNESS OF A FIXTURELESS INSPECTION METHOD FOR NON-RIGID PARTS BASED ON A VERIFICATION AND VALIDATION APPROACH.....		138
5.1	Abstract	138
5.2	Introduction.....	139
5.3	Background on the approach to fixtureless CAI for non-rigid parts.....	143
5.4	Assessing the robustness of our CAI method based on ASME V&V recommendations	148
5.4.1	ASME recommendations for verification and validation	148
5.4.2	Verification and validation methodology for CAI.....	151
5.4.3	Robustness of our CAI method.....	155
5.5	Validation results for cases with small free-state deformation	157
5.5.1	Validation cases considered	157
5.5.2	Results for part A	159
5.5.3	Results for part B	167
5.5.4	Conclusions about validation cases for part B	180
5.6	Effect of large free-state deformation	181
5.6.1	Cases considered and results obtained	181

5.6.2	Conclusions about the effect of large free-state deformation	188
5.7	Discussion about results.....	190
5.8	Conclusion	191
5.9	Acknowledgment	193
5.10	References.....	193
CHAPTER 6 FIXTURELESS INSPECTION OF NON-RIGID PARTS BASED ON VIRTUAL MOUNTING IN AN ASSEMBLY-STATE USING PERMISSIBLE LOADS		
199		
6.1	Abstract	199
6.2	Introduction.....	200
6.3	Literature review	205
6.4	Virtual Mounting Assembly-State Inspection method (VMASI)	209
6.4.1	Pre-registration and partition of the scan mesh.....	211
6.4.2	Non-rigid registration using restraining pressures optimization (RPO) ...	213
6.4.3	Inspection and evaluation.....	216
6.4.4	The proposed VMASI algorithm	219
6.5	Application of proposed VMASI method on real parts	221
6.5.1	Introduction: validation cases	221
6.5.2	Results for part A	223
6.5.2.1	Scan models of part A with defects generated by geometric alteration 225	
6.5.2.2	Scan models of part A with defects simulated by plastic deformation 231	
6.5.3	Results for part B	234

6.5.4	Discussion	246
6.6	Conclusion	247
6.7	Acknowledgments.....	248
6.8	References	248
CHAPTER 7	GENERAL DISCUSSION.....	252
7.1	Discussion on the sample points filtering method	252
7.2	Discussion on nonlinear FEA	254
7.3	Discussion on our developed V&V method	261
7.4	Discussion on our developed virtual mounting method.....	261
CHAPTER 8	CONTRIBUTIONS, PERSPECTIVES, AND CONCLUSIONS.....	263
8.1	Major contributions.....	263
8.2	Perspectives.....	265
8.3	Conclusions.....	270
BIBLIOGRAPHY	272
APPENDIX A: GENERALIZED NUMERICAL INSPECTION FIXTURE (GNIF)		277

LIST OF TABLES

Table 2-1: The classification for compliant behavior of parts concerning the induced displacement under applied force (Abenhaim, Desrochers et al. 2012).	44
Table 4-1: Estimated size of defects and errors based on curvature and von Mises criteria for Part A with small (local) defects and bending deformation.	101
Table 4-2: Estimated size of defects and errors based on curvature and von Mises criteria for part A with small (local) defects and torsion deformation.	111
Table 4-3: Estimated size of defects and errors based on curvature and von Mises criteria for Part A with a big (global) defect and bending deformation.	115
Table 4-4: Estimated size of defects and errors based on curvature and von Mises criteria for Part A with a big (global) defect and torsion deformation.	119
Table 4-5: Estimated size of defects and errors based on curvature and von Mises criteria for Part B with small (local) defects and bending deformation.	124
Table 4-6: Estimated size of defects and errors based on curvature and von Mises criteria for Part B with small (local) defects and torsion deformation.	127
Table 4-7: Estimated size of defects and errors based on curvature and von Mises criteria for Part B with a big (global) defect and bending deformation.	130
Table 4-8: Estimated size of defects and errors based on curvature and von Mises criteria for Part B with a big (global) defect and torsion deformation.	132
Table 5-1: Estimated size of defects and errors for part A with small (local) defects and bending deformation.	163
Table 5-2: Validation results with K-S tests (H_0 : the distance distribution of nominal and estimated defects are sufficiently similar) at 5% significance level for part A with small (local) defects and bending deformation.	164
Table 5-3: Estimated size of defects and errors for part A with a big (global) defect and bending deformation.	166

Table 5-4: Validation results with K-S tests (H_0 : the distance distribution of nominal and estimated defects are sufficiently similar) at 5% significance level for part A with a big (global) defect and bending deformation.	167
Table 5-5: Estimated size of defects and errors for part B with small (local) defects and bending deformation.	171
Table 5-6: Estimated size of defects and errors for part B with small (local) defects and torsion deformation.	174
Table 5-7: Validation results with K-S tests (H_0 : the distance distribution of nominal and estimated defects are sufficiently similar) at 5% significance level for part B with small (local) defects under bending and torsion deformation.	175
Table 5-8: Estimated size of defects and errors for part B with a big (global) defect and bending deformation.	177
Table 5-9: Estimated size of defects and errors for part B with a big (global) defect and torsion deformation.	179
Table 5-10: Validation results with K-S tests (H_0 : the distance distribution of nominal and estimated defects are sufficiently similar) at 5% significance level for part B with a big (global) defect and under bending and torsion deformation.	180
Table 5-11: Estimated size of defects and errors for part A with small (local) defects and large bending deformation.	184
Table 5-12: Validation results with K-S tests (H_0 : the distance distribution of nominal and estimated defects are sufficiently similar) at 5% significance level for part A with small (local) defects and large bending deformation.	185
Table 5-13: Estimated size of defects and errors for part A with a big (global) defect and large bending deformation.	187
Table 6-1: Synthesis of validation cases defects for part A.	225
Table 6-2: Assembly pressure and force results for the validation case A-1.	227

Table 6-3: Position, profile and orientation results for the validation case A-1.	227
Table 6-4: Assembly pressure and force results for the validation case A-2.....	229
Table 6-5: Position, profile and orientation results for the validation case A-2.	229
Table 6-6: Assembly pressure and force results for the validation case A-3.....	231
Table 6-7: Position, profile and orientation results for the validation case A-3.	231
Table 6-8: Assembly pressure and force results for the validation case A-4.....	232
Table 6-9: Position, profile and orientation results for the validation case A-4.	233
Table 6-10: Assembly pressure and force results for the validation case A-5.....	234
Table 6-11: Position, profile and orientation results for the validation case A-5.	234
Table 6-12: Assembly pressure and force results for the validation case of part B simulated as a small plastic defect.	239
Table 6-13: Position, profile and orientation results for the validation case of part B simulated as a small plastic defect.	239
Table 6-14: Assembly pressure and force results for the validation case of part B simulated as an intermediate plastic defect.	242
Table 6-15: Position, profile and orientation results for the validation case of part B simulated as an intermediate plastic defect.	242
Table 6-16: Assembly pressure and force results for the validation case of part B simulated as a large plastic defect.	245
Table 6-17: Position, profile and orientation results for the validation case of part B simulated as a large plastic defect.	245
Table 7-1: Estimated size of defects and errors implementing nonlinear and linear FENR.	260

LIST OF FIGURES

Figure 1-1: An ordinary aerospace panel, a) in free-state, b) constrained on supports of the inspection fixture (Abenhaim, Desrochers et al. 2015).....	37
Figure 1-2: An aerospace panel restrained under known loads by using weights (the black sandbags) on its surface (Abenhaim, Desrochers et al. 2015).	38
Figure 1-3: Structure of the thesis based on the articles.	41
Figure 2-1: Classification of the compliant behavior of parts (Abenhaim, Desrochers et al. 2012).....	44
Figure 2-2: Measuring tools, a) using CMM for measuring a rigid part (Li and Gu 2004), b) using a noncontact scanner for scanning the surface of a non-rigid part.....	46
Figure 2-3: Categorization of the quality requirements specifications for GD&T of non-rigid parts (Abenhaim, Desrochers et al. 2012).	48
Figure 2-4: The restrained conditions for non-rigid parts, a) an inspection fixture restraining a curved aerospace panel (Ascione and Polini 2010) b) A non-rigid part restrained to the design shape using datum targets (ASME Y14.5).	49
Figure 2-5: The process chain of the virtual distortion compensation method (Weckenmann and Weickmann 2006).	54
Figure 2-6: Schematic flowchart of proposed <i>virtual fixture</i> method in (Abenhaim, Desrochers et al. 2015).....	56
Figure 2-7: An overview of the non-rigid CAI method using partial measuring data (Jaramillo, Prieto et al. 2013).....	58
Figure 2-8: constructing deformed CAD model using displacement field without taking into consideration the presence of effects (Abenhaim, Tahan et al. 2011).	59
Figure 2-9: Distance preserving property of non-rigid part during an isometric deformation (Radvar-Esfahlan and Tahan 2014).....	61

Figure 2-10: Corresponding sample points (black points) generated on the CAD and scan models for a turbine blade (Radvar-Esfahlan and Tahan 2014).	62
Figure 2-11: The flowchart of the inspection process using GNIF method (Radvar-Esfahlan and Tahan 2012).....	62
Figure 2-12: verification and validation (V&V) activities and results based on ASME recommendation (Schwer, Mair et al. 2012).....	66
Figure 3-1: A complex inspection fixture set-up for a large aerospace panel.	70
Figure 3-2: simplified flowchart of a fixtureless CAI followed by a verification and validation approach.	72
Figure 3-3: A summary of CAD and simulated scan models used in this thesis.	76
Figure 4-1: An aerospace panel, a) in free-state, b) constrained on its inspection fixture [4]......	83
Figure 4-2: Surface data acquisition by a handy scanner.....	84
Figure 4-3: CAD model along with GD&T specification for part A (dimensions are in mm).	90
Figure 4-4: A non-rigid aluminum panel a) front view of the CAD model b) top view of the CAD model c) front view of the scanned part in a free-state d) top view of the scanned part in a free-state.....	91
Figure 4-5: GNIF corresponding sample points (in black) are located in the center of colored zones on CAD and scanned models.	91
Figure 4-6: a) The purple point presents a GNIF sample point to be inserted b) the sample point is inserted into the mesh by incremental Delaunay triangulation c) Testing the empty sphere criterion d) swap diagonal operator.	92
Figure 4-7: a) GNIF sample points on the CAD model represented as red spots b) displacement distribution [mm] after FENR based on using all GNIF sample points	

c) comparison between estimated and nominal size of defects [mm] when using all GNIF sample points d) estimating the area of defects [mm²]...... 93

Figure 4-8: Schematic diagram of the proposed sample point filtration method..... 95

Figure 4-9: a) distribution of the difference in maximum curvature ($K1$) [mm⁻¹] b) distribution of the difference in minimum curvature ($K2$) [mm⁻¹] c) sample points filtered using the curvature criterion (represented as blue spots) d) comparison between estimated and nominal size of defects [mm] when using sample points after filtering based on the curvature criterion e) estimating the area of defects [mm²]. 97

Figure 4-10: a) distribution of von Mises stress [Pa] after FENR when using GNIF sample points after filtering based on the curvature criterion b) sample points filtered using both curvature and von Mises stress criteria (represented as blue spots) c) comparison between estimated and nominal size of defects [mm] when using GNIF sample points after filtering based on both curvature and von Mises stress criteria d) estimating the area of defects [mm²]...... 99

Figure 4-11: Interest of using the two filters successively..... 102

Figure 4-12: a) GNIF sample points on the CAD model represented as red spots b) comparison between deformed CAD and scanned models when using all GNIF sample points [mm]...... 103

Figure 4-13: a) distribution of the difference in maximum curvature ($K1$) [mm⁻¹] b) distribution of the difference in minimum curvature ($K2$) [mm⁻¹] c) sample points filtered using the curvature criterion (represented as blue spots) d) comparison between deformed CAD and scanned models when using GNIF sample points after filtering based on the curvature criterion [mm]. 104

Figure 4-14: a) distribution of von Mises stress [Pa] after FENR when using GNIF sample points after filtering based on the curvature criterion b) sample points filtered using curvature and von Mises stress criteria (represented as blue spots) c) comparison

between deformed CAD and scanned models when using GNIF sample points after filtering based on both curvature and von Mises stress criteria [mm].	105
Figure 4-15: Synthesis of validation cases.....	107
Figure 4-16: Side view of the CAD model for part A (in green) compared with the scanned model in a free-state (in brown) with a) bending deformation b) torsion deformation.	108
Figure 4-17: Part A with small (local) defects and torsion a) GNIF sample points on the CAD model represented as red spots b) comparison between estimated and nominal size of defects [mm] based on using all GNIF sample points.....	108
Figure 4-18: Part A with small (local) defects and torsion a) distribution of the difference in maximum curvature ($K1$) [mm^{-1}] b) distribution of the difference in minimum curvature ($K2$) [mm^{-1}] c) sample points filtered using the curvature criterion (represented as blue spots) d) comparison between estimated and nominal size of defects [mm] when using GNIF sample points after filtering based on the curvature criterion.	109
Figure 4-19: Part A with small (local) defects and torsion a) distribution of von Mises stress [Pa] after FENR based on GNIF sample points after filtering using the curvature criterion b) sample points filtered using curvature and von Mises stress criteria (represented as blue spots) c) comparison between estimated and nominal size of defects [mm] when using GNIF sample points after filtering based on both curvature and von Mises stress criteria.	110
Figure 4-20: Part A with a big (global) defect and bending a) GNIF sample points on the CAD model represented as red spots b) comparison between estimated and nominal size of defects [mm] when using all GNIF sample points.	112
Figure 4-21: Part A with a big (global) defect and bending a) distribution of the difference in maximum curvature ($K1$) [mm^{-1}] b) distribution of the difference in minimum curvature ($K1$) [mm^{-1}] c) sample points filtered using the curvature criterion	

- (represented as blue spots) d) comparison between estimated and nominal size of defects [mm] when using GNIF sample points after filtering based on the curvature criterion. 113
- Figure 4-22: Part A with a big (global) defect and bending a) distribution of von Mises stress [Pa] after FENR when using GNIF sample points after filtering based on the curvature criterion b) sample points filtered using curvature and von Mises stress criteria (represented as blue spots) c) comparison between estimated and nominal size of defects [mm] when using GNIF sample points after filtering based on both curvature and von Mises stress criteria. 114
- Figure 4-23: Part A with a big (global) defect and torsion a) GNIF sample points on the CAD model represented as red spots b) comparison between estimated and nominal size of defects [mm] when using all GNIF sample points. 116
- Figure 4-24: Part A with a big (global) defect and torsion a) distribution of the difference in maximum curvature ($K1$) [mm^{-1}] b) distribution of the difference in minimum curvature ($K1$) [mm^{-1}] c) sample points filtered using the curvature criterion (represented as blue spots) d) comparison between estimated and nominal size of defects [mm] when using GNIF sample points after filtering based on the curvature criterion. 117
- Figure 4-25: Part A with a big (global) defect and torsion a) distribution of von Mises stress [Pa] after FENR based on GNIF sample points after filtering using the curvature criterion b) sample points filtered using curvature and von Mises stress criteria (represented as blue spots) c) comparison between estimated and nominal size of defects [mm] when using GNIF sample points after filtering based on both curvature and von Mises stress criteria. 118
- Figure 4-26: CAD model along with GD&T specification for part B (dimensions are in mm). 120
- Figure 4-27: GNIF corresponding sample points (in black) on the CAD and scanned models of part B. 121

- Figure 4-28: Side view of CAD model for part B (in green) compared with the scanned model (in brown) a) with bending deformation b) with torsion deformation. 121
- Figure 4-29: Part B with small (local) defects and bending a) and f) initial and filtered sample points c) and d) distribution of the difference in principle curvatures [mm^{-1}] e) distribution of von Mises stress [Pa] after the second FENR. b) and g) comparison between estimated and nominal size of defects [mm] based on initial and filtered sample points..... 122
- Figure 4-30: Part B with small (local) defects and torsion a) and f) initial and filtered sample points c) and d) distribution of the difference in principle curvatures [mm^{-1}] e) distribution of von Mises stress [Pa] after the second FENR. b) and g) comparison between estimated and nominal size of defects [mm] based on initial and filtered sample points..... 126
- Figure 4-31: Part B with a big (global) defect and bending a) and f) initial and filtered sample points c) and d) distribution of the difference in principle curvatures [mm^{-1}] e) distribution of von Mises stress [Pa] after the second FENR. b) and g) comparison between estimated and nominal size of defects [mm] based on initial and filtered sample points..... 129
- Figure 4-32: Part B with a big (global) defect and torsion a) and f) initial and filtered sample points c) and d) distribution of the difference in principle curvatures [mm^{-1}] e) distribution of von Mises stress [Pa] after the second FENR. b) and g) comparison between estimated and nominal size of defects [mm] based on initial and filtered sample points..... 131
- Figure 5-1: A regular aerospace panel, a) in free-state, b) constrained by fixing jigs on the inspection fixture [2]. 140
- Figure 5-2: 3D view of the CAD model of a non-rigid aluminum panel..... 144
- Figure 5-3: GNIF corresponding sample points (in black) are located in the center of colorful zones on the CAD and scanned models. 145

Figure 5-4: a) all GNIF sample points inserted into the CAD mesh based on classical Delaunay method (red spots) b) automatic sample point filtration based on curvature and von Mises stress criteria and criteria (blue spots).	146
Figure 5-5: Definition of maximum amplitude $Dimax$ and area of a defect Ai	147
Figure 5-6: a) the scanned part with the nominal dimensions of defects b) estimated and nominal maximum amplitude ($Dimax$) of defects [mm] c) estimated and nominal area (Ai shown as red zones) of defects [mm ²].....	147
Figure 5-7: Flowchart of our automatic fixtureless CAI method.....	148
Figure 5-8: defects are identified as red zones based on the tolerance value (0.4 mm) a) for nominal defects b) for estimated defects.	153
Figure 5-9: CDF for nominal and estimated defects for Bump #1 and Bump #2.....	154
Figure 5-10: Estimation of the distance distribution of a defect a) nominal defect, b) for an accurate inspection c) for an overestimated defect d) for a badly estimated defect.	155
Figure 5-11: a) a noise-free scan mesh b), c), d) scan meshes with synthetic noise with Gaussian distribution with zero mean value and standard deviation equal to b) 0.01mm c) 0.02mm d) 0.03mm.....	156
Figure 5-12: Synthesis of validation cases with small free-state deformation.....	158
Figure 5-13: CAD model along with GD&T specification for part A (dimensions are in mm).	160
Figure 5-14: a) nominal defect distance distribution for part A with small (local) defects, comparison between the CAD and scanned model of part A with small (local) defects and bending deformation as a distance distribution for b) noise-free scan mesh c) noisy scan mesh with $\sigma=0.01$ mm d) noisy scan mesh with $\sigma=0.02$ mm e) noisy scan mesh with $\sigma=0.03$ mm.....	161

- Figure 5-15: a) the scanned part with the nominal dimensions of big (global) defect b) nominal defect distance distribution for part A with a big (global) defect, comparison between the CAD and scanned model of part A with a big (global) defect and bending deformation as a distance distribution for c) noise-free scan mesh d) noisy scan mesh with $\sigma=0.01$ mm e) noisy scan mesh with $\sigma=0.02$ mm f) noisy scan mesh with $\sigma=0.03$ mm. 165
- Figure 5-16: CAD model along with GD&T specification for part B (dimensions are in mm). 168
- Figure 5-17: Side views of the CAD model for part B (in green) compared with scan data in a free-state (in brown) with a) bending deformation b) torsion deformation. .. 168
- Figure 5-18: a) nominal defect distance distribution for part B with small (local) defects, comparison between the CAD and scanned model with small (local) defects and bending deformation as a distance distribution for b) noise-free scan mesh c) noisy scan mesh with $\sigma=0.01$ mm d) noisy scan mesh with $\sigma=0.02$ mm e) noisy scan mesh with $\sigma=0.03$ mm. 170
- Figure 5-19: a) nominal defect distance distribution for part B with small (local) defects, comparison between the CAD and scanned model with small (local) defects and torsion deformation as a distance distribution for b) noise-free scan mesh c) noisy scan mesh with $\sigma=0.01$ mm d) noisy scan mesh with $\sigma=0.02$ mm e) noisy scan mesh with $\sigma=0.03$ mm. 173
- Figure 5-20: a) nominal defect distance distribution for part B with a big (global) defect, comparison between the CAD and scanned model with a big (global) defect and bending deformation as a distance distribution for b) noise-free scan mesh c) noisy scan mesh with $\sigma=0.01$ mm d) noisy scan mesh with $\sigma=0.02$ mm e) noisy scan mesh with $\sigma=0.03$ mm. 176
- Figure 5-21: a) nominal defect distance distribution for part B with a big (global) defect, comparison between the CAD and scanned model with a big (global) defect and torsion deformation as a distance distribution for b) noise-free scan mesh c) noisy

scan mesh with $\sigma=0.01$ mm d) noisy scan mesh with $\sigma=0.02$ mm e) noisy scan mesh with $\sigma=0.03$ mm.	178
Figure 5-22: Error intervals for part B with respect to the increase of noise amplitude.	181
Figure 5-23: 3D views of CAD model (in green) compared with scan data in a free-state (in brown) for part A with a) small bending deformation b) large bending deformation.	182
Figure 5-24: a) nominal defect distance distribution for part A with small (local) defects, comparison between the CAD and scanned model of part A with small (local) defects and large bending deformation as a distance distribution for b) noise-free scan mesh c) noisy scan mesh with $\sigma=0.01$ mm d) noisy scan mesh with $\sigma=0.02$ mm e) noisy scan mesh with $\sigma=0.03$ mm.	183
Figure 5-25: a) nominal defect distance distribution for part A with a big (global) defect, comparison between the CAD and scanned model of part A with a big (global) defect and large bending deformation as a distance distribution for b) noise-free scan mesh c) noisy scan mesh with $\sigma=0.01$ mm d) noisy scan mesh with $\sigma=0.02$ mm e) noisy scan mesh with $\sigma=0.03$ mm.	186
Figure 5-26: Absolute error (in %) in the estimation of defects for part A for small versus large deformation.	188
Figure 6-1: An ordinary aerospace panel a) in free-state, b) constrained on supports of the inspection fixture [1].	201
Figure 6-2: An aerospace panel under permissible restrained loads (the weight of black sandbags applied on the surface of part) achieves the functional shape on physical fixture [1].	202
Figure 6-3: Schematic flowchart of the proposed assembly assessing method.	211
Figure 6-4: Analysis of geometrical offset based on GD&T specification.	218

Figure 6-5: Schematic misalignment of assembly mounting hole on predicted shape of scan model with respect to the CAD model.....	219
Figure 6-6: Flowchart algorithm of proposed VMASI method.	220
Figure 6-7: Synthesis of validation cases with different types of defects.....	222
Figure 6-8: GD&T specification for part A (dimensions are in mm).	224
Figure 6-9: a) Displacement distribution [mm] of deviated scan model generated by decreasing 1 deg. of forming angle; b) The partitioned scan model and predicted assembly pressure.....	227
Figure 6-10: a) Displacement distribution [mm] of deviated scan model generated by decreasing 3 deg. of forming angle; b) The partitioned scan model and predicted assembly pressure.....	229
Figure 6-11: a) Displacement distribution [mm] of deviated scan model generated by decreasing 5 deg. of forming angle; b) The partitioned scan model and predicted assembly pressure.....	230
Figure 6-12: a) Displacement distribution [mm] of slightly deviated scan mesh simulating a plastic defect; b) The partitioned scan model and predicted assembly pressure.	232
Figure 6-13: a) displacement distribution [mm] of deviated scan mesh simulating a plastic defect; b) the partitioned scan model and predicted assembly pressure.	233
Figure 6-14: a) The manufactured part mounted on inspection fixtures where a real point cloud of scan mesh can be acquired, in our proposed method only 9 fixation features are kept as datums; b) GD&T specification for part B (dimensions are in mm). .	236
Figure 6-15: a) Displacement distribution [mm] of deviated scan mesh simulating a small plastic defect; b) The partitioned scan model and predicted assembly pressure. .	238

Figure 6-16: a) Displacement distribution [mm] of deviated scan mesh simulating an intermediate plastic defect; b) the partitioned scan model and predicted assembly pressure.	241
Figure 6-17: a) Displacement distribution [mm] of deviated scan mesh simulating a large plastic defect; b) the partitioned scan model and predicted assembly pressure....	244
Figure 7-1: 3D views of CAD model (in green) compared with scan model in a free-state (in brown) simulated based on large displacement formulation.	255
Figure 7-2: Remained sample points (as red spots) after applying filtering registration points method using a) nonlinear FENR for noise-free scan mesh b) linear FENR for noise-free scan mesh c) nonlinear FENR for noisy scan mesh with $\sigma=0.01$ mm d) linear FENR for noisy scan mesh with $\sigma=0.01$ mm.	256
Figure 7-3: Distribution of von Mises stress [Pa] when using GNIF sample points after a) nonlinear FENR for noise-free scan mesh b) linear FENR for noise-free scan mesh c) nonlinear FENR for noisy scan mesh with $\sigma=0.01$ mm d) linear FENR for noisy scan mesh with $\sigma=0.01$ mm.	257
Figure 7-4: a) nominal defect distance distribution, comparison between the deformed CAD and scan models as a distance distribution using b) nonlinear FENR for noise-free scan mesh c) linear FENR for noise-free scan mesh d) nonlinear FENR for noisy scan mesh with $\sigma=0.01$ mm e) linear FENR for noisy scan mesh with $\sigma=0.01$ mm.	259
Figure 8-1: A synthesis of contributions in the thesis.	265

LIST OF SYMBOLS

D_i^{max}	Maximum amplitude of a defect i
A_i	Area of a defect i
N_{defect}	Number of identified defects
H_0	Null hypothesis
H_A	Alternative hypothesis
Dd_a	Nominal defect
Dd_e	Estimated defect
σ	Standard deviations
μ	Mean value
\mathcal{S}^{CAD}	Set of nodes on CAD mesh
\mathcal{D}^{CAD}	Set of nodes on inspection datums of CAD mesh
\mathcal{J}^{CAD}	Set of nodes on inspecting mounting holes of CAD mesh
\mathcal{S}^{SCN}	Set of nodes on scan mesh
\mathcal{D}^{SCN}	Set of nodes on inspection datums of scan mesh
\mathcal{S}	Set of nodes on scan mesh after pre-registration
\mathcal{D}	Set of nodes on inspection datums of scan mesh after pre-registration
\mathcal{J}	Set of nodes on inspecting mounting holes of scan mesh after pre-registration
\mathcal{T}	List of partitioned zones on scan mesh after pre-registration
Δ	Distance between mounting holes on scan and CAD meshes
O	Orientation difference between mounting holes on scan and CAD meshes

LIST OF ABBREVIATIONS

CAD	Computer-Aided Design
CAI	Computer-Aided Inspection
GD&T	Geometric Dimensioning and Tolerancing
GNIF	Generalized Numerical Inspection Fixture
FEA	Finite Element Analysis
FENR	Finite Element Non-rigid Registration
K-S test	Kolmogorov–Smirnov test
VMASI	Virtual Mounting Assembly-State Inspection
RPO	Restraining Pressures Optimization
ICP	Iterative Closest Point
IDI	Iterative Displacement Inspection
RBFs	Radial Basis Functions
GMDS	Generalized Multidimensional Scaling
FMA	Fast Marching Algorithm
RNIF	Robust generalized Numerical Inspection Fixture
V&V	Verification and Validation

PREFACE

This research work is part of a collaborative research program on the metrology of non-rigid (flexible) parts. The project is defined in the framework of the Consortium de recherche et d'innovation en aérospatiale au Québec (CRIAQ), which is referred as CRIAQ MANU501. The industrial partners of this project are Bombardier Aerospace and CREAFORM companies. Three universities that are engaged in this project include École de Technologie Supérieure (ÉTS), Université du Québec à Trois-Rivières (UQTR) and Université de Sherbrooke.

This thesis is composed as a paper-based thesis and consists of eight chapters. In Chapter 1, an introduction concerning the compliant behavior of non-rigid (flexible) parts, conventional inspection methods and *Computer-Aided Inspection* (CAI) methods is presented. In Chapter 2, a comprehensive literature review regarding the different types of scanning tools, and developed fixtureless CAI methods along with their advantages and drawbacks are presented. The general planning comprising the statement of problems and objectives of this thesis are explained in Chapter 3. Chapter 4, Chapter 5 and Chapter 6 are assigned to the articles submitted to scientific journals. These articles describe the improvements and developments of original methods for automatic inspection of non-rigid parts and robustness validation of the methods. This thesis is ended with a general discussion, various perspectives, and conclusions that are presented in Chapter 7 and Chapter 8.

CHAPTER 1 INTRODUCTION

Improvements in the metal forming industry lead to manufacturing of complex parts that are commonly used in different industrial sectors among which aerospace and automobile. These complex parts may include many details, features and complex freeform shapes. The quality, efficiency, and functionality of these parts are controlled by *Geometric Dimensioning and Tolerancing* (GD&T) approaches. Manufacturing companies attempt to maintain in the competitive markets by producing high-quality parts. The quality control (QC) process, consisting of geometrical and dimensional controls, ensures the functionality of products. However, conventional inspection methods are costly, time-consuming and require manual intervention. Despite the progress in manufacturing methods for reducing the lead time of production, the quality control is still a time-consuming challenge. For example, some inspection setup for non-rigid parts in Bombardier Aerospace company demands 60 to 75 hours of operation (Radvar-Esfahlan and Tahan 2014). Therefore, the recent concern of manufacturing companies is to perform an accurate dimensional inspection in a short time. Thin walled sheet metals, which are commonly used in industrial sectors among which the aerospace and automotive, present a more serious challenge for geometrical and dimensional inspection in a quality control process. These sheet metals have a small thickness compared to the other dimensions, which gives them flexible behavior during inspection. The flexibility of these non-rigid parts is referred to as compliant behavior in tolerancing contexts. These non-rigid parts may deform during a free-state inspection process, which is the main issue in GD&T. The compliance in a free-state can take place due to the weight of the part, residual stress (release of internal stress resulting from manufacturing) remaining in the part during the manufacturing process or any geometrical deviation. Metrology standards such as ASME Y14.5 and ISO-1101-GPS require performing the inspection of parts in free-state unless otherwise specified. The exceptions to this rule, as mentioned in standards ASME Y14.5 (2009) and ISO-10579-GPS, are for non-rigid parts. In fact, free-state refers to a situation that a part is not constrained and is not submitted to

any load except its weight. A non-rigid aerospace panel in a free-state, as shown in Figure 1-1-a, is deformed due to the weight on an inspection table. Conventional inspection methods use over constrained fixtures for non-rigid parts. In some cases, the functional shape of a non-rigid part can be retrieved by using these fixtures and by restraining the part under permissible loads during the dimensional inspection process. Therefore, even though the shape variation of parts exceeds the allocated dimensioning tolerances, these non-rigid parts can still be assembled. Improvements in digital data acquisition devices such as 3D optic and laser scanners (Bi and Wang 2010) along with the computational calculation developments lead to *Computer-Aided Inspection* (CAI) methods. The 3D data acquisition tools obtain a set of points, namely point clouds, from the surface of parts during the inspection process. The scan mesh is then generated from the raw scanning data (point clouds), which is processed by mesh smoothing methods as presented by (Karbacher and Haeusler 1998). This scan mesh intends to accurately represent the geometrical shape of the part with the least required data volume (mesh size). CAI methods apply tolerancing methods along with computational meshing tools to implement an automatic and time-saving inspection. In fact, CAI methods make the comparison between the *Computer-Aided Design* (CAD) model and the scan range data in a common coordinate system to evaluate the geometrical deviations (defects) of the part. Since the CAD model is in the *Design Coordinate System* (DCS) and the scan data in the *Measurement Coordinate System* (MCS), *registration* methods developed in CAI context are required to align the CAD and scan models in a common coordinate system. Considering the flexible deformation of parts in a free-state, the comparison between CAD and scan models cannot estimate defects size on scan model. To resolve this problem, CAI methods for non-rigid parts are used to distinguish between the defects (such as geometrical deviations and distortions with respect to CAD model) and the flexible deformation (due to the compliance) of non-rigid parts. As already mentioned, conventional dimensioning and inspection methods for non-rigid parts sets up over-constrained inspection fixtures to compensate for the flexible deformation of these parts and to ensure that the measurement setup properly represents the assembly functionality

of the part (Ascione and Polini 2010). These fixtures also retrieve the functional shape of the part and align it with the reference frame during the measuring process. Figure 1-1-b illustrates an example of such an inspection fixture for the part. The same part is demonstrated in Figure 1-1-a at a free-state.

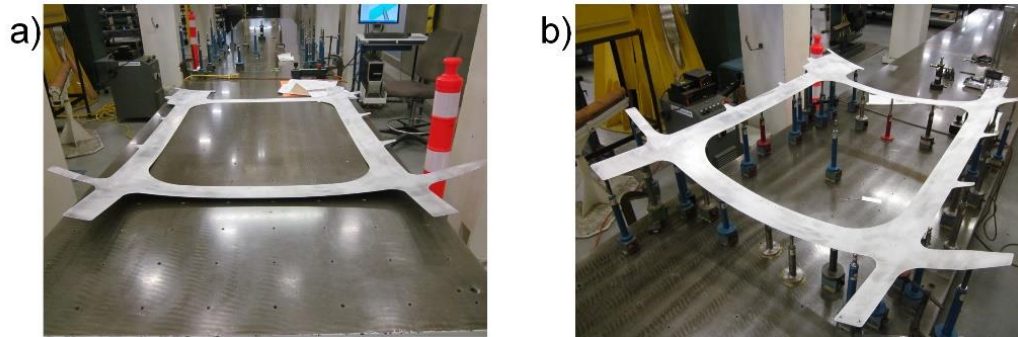


Figure 1-1: An ordinary aerospace panel, a) in free-state, b) constrained on supports of the inspection fixture (Abenhaim, Desrochers et al. 2015)

Moreover, dimensional inspection of non-rigid parts is generally accomplished in restrained conditions such as assembly loads, supports and clamps (Abenhaim, Desrochers et al. 2012). As shown in Figure 1-2, a practical inspection technique applies weights (e.g. sandbags) on the surface of a deviated non-rigid part to retrieve its functional shape constrained on a physical fixture. These weights are permissible assembly loads that are commonly presented as a note in design drawings authorizing their application during the inspection process. The limits for permissible loads are defined to prevent permanent deviations (plastic deformation) during the inspection and eventually assembly process. In drawings, a note such as “*A load of $X \text{ N/m}^2$ can be used to achieve tolerance*” is indicated next to the associated geometrical requirements specifying the permissible loads and the associated fixture. Therefore, a non-rigid part can be restrained by assembly loads that are limited to the given permissible values during the inspection. These restraining loads are usually used for large non-rigid parts such as aerospace panels for which the functional shape of parts can be retrieved by imposing constraints during assembly.

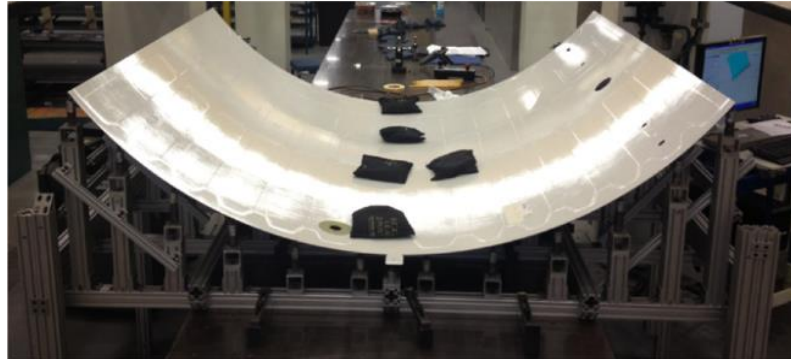


Figure 1-2: An aerospace panel restrained under known loads by using weights (the black sandbags) on its surface (Abenhaim, Desrochers et al. 2015).

Serious drawbacks of using physical inspection fixtures lead to developing fixtureless CAI methods to eliminate the need for costly and complex physical fixtures. These methods apply computational techniques to distinguish between defects and flexible deformation. This intends to virtually compensate for the flexible deformation of non-rigid parts in a free-state. The primary step for inspection of non-rigid parts is a pre-registration using rigid registration methods. Rigid registration brings the CAD and scan models closer in a common coordinate system using a transformation matrix. Among different rigid registration methods (Li and Gu 2004, Savio, De Chiffre et al. 2007), the *Iterative Closest Point* (ICP) algorithm (Besl and Mckay 1992) is widely applied in different domains. ICP algorithm provides a robust and efficient registration method for rigid parts. Applying pre-registration the CAD and scan models are aligned and brought closer without deforming the models. In fact, rigid registration does not take into consideration the flexible deformation of non-rigid parts. However, fixtureless CAI methods presented in section 2.4.2 enable the inspection by virtually compensating for the flexible deformation of scan models in a free-state. This allows the estimation of defects on the manufactured parts with respect to the nominal CAD models. In general, these fixtureless non-rigid registration methods search for correspondence between the CAD and scan models to deform the CAD or scan model towards the other one. This is performed by using FEA or gradually iterative displacements. Non-rigid registration methods based on deforming the scan mesh towards the CAD model are presented in

section 2.4.2.1, and non-rigid inspection methods based on deforming the CAD model towards the scan mesh are introduced in section 2.4.2.2. However, these non-rigid registration methods are not fully automated. An automatic fixtureless CAI for non-rigid parts that is capable of identifying and estimating both small (local) and big (global) defects is presented in Chapter 4. This method applies corresponding sample points to determine displacement boundary conditions (BCs) for a *Finite Element Non-Rigid Registration* (FENR). Distinguishing between the flexible deformation and defects, the sample points close and on defect areas are filtered out based on curvature and von Mises stress criteria. This leads to an accurate and automatic fixtureless CAI for non-rigid parts. Once a CAI method is developed, the robustness and performance of the method should be verified and validated with respect to actual measurements. To this end, a quantitative validation metric applied in a *Verification and Validation* (V&V) method is required. In Chapter 5, a new validation metric for fixtureless CAI methods is presented which analyses the robustness of CAI method with respect to scanning noise. This validation metric applies statistical hypothesis testing to validate whether the distance distribution of nominal and estimated defects are sufficiently similar.

Most of these developed fixtureless inspection methods do not take into consideration restraining loads. These loads are permitted to be used for placing deviated non-rigid parts into assembly state and are commonly mandated during inspection process especially for large parts such as aerospace panels. It should be considered that defects on non-rigid parts can generally occur during manufacturing and handling processes. In Chapter 6, a non-rigid registration method is proposed that aims to evaluate the feasibility of putting a deviated part in assembly-state. In fact, defects such as warpage, shrinkage or any type of plastic deformation on non-rigid parts result in misalignment at the assembly. However, excessive geometrical variations with respect to the assembly tolerance would be absorbed by the compliance of non-rigid parts. The developed *Virtual Mounting Assembly-State Inspection* (VMASI) method applies a new registration to virtually retrieve the functional shape of deviated parts under permissible assembly loads. The inspection is accomplished by verifying fixation features (e.g. mounting holes) on the

predicted shape of scan mesh in assembly-state with respect to the allocated assembly tolerances. The feasibility of mounting a geometrically deviated non-rigid part in assembly-state is approved when all mounting holes on the predicted shape of scan mesh are in the tolerance range.

1.1 Structure of the thesis

This thesis is composed in the form of article-based thesis wherein three articles are presented and logically connected to each other. The methodologies, results, and discussions are presented in detail inside the articles. These articles have been submitted for publication in scientific international journals with reviewing committees, which are recognized in their respective fields (advanced manufacturing for the first article, ASME V&V for the second article and Computer-Aided Design for the third article). As presented in Figure 1-3, at the time of writing this thesis, the first article is already published, the second and third articles are submitted and they are currently under review.

This thesis is enclosed in 8 chapters. A comprehensive literature review consisting of the non-rigid parts specifications, scanning tools, rigid and non-rigid registration methods for fixtureless inspection of non-rigid parts is presented in Chapter 2. In Chapter 3, the general planning of the thesis is described which consists of the statement of the problem, objectives, and hypothesis of this project. This is followed by three articles in Chapter 4, Chapter 5 and Chapter 6 respectively. A general discussion on the methodology and results of developed CAI methods and validation metric is presented in Chapter 7. Finally in Chapter 8, major contributions, perspectives for future works and conclusions of the developed methods in this thesis are presented.

CHAPTER 1	Introduction
CHAPTER 2	Literature review
CHAPTER 3	General planning of the thesis
CHAPTER 4 (Article 1)	"Automatic fixtureless inspection of non-rigid parts based on filtering registration points"
CHAPTER 5 (Article 2)	"Assessment of the robustness of a fixtureless inspection method for non-rigid parts based on a verification and validation approach"
CHAPTER 6 (Article 3)	"Fixtureless inspection of non-rigid parts based on virtual mounting in assembly-state using permissible forces"
CHAPTER 7	General discussions
CHAPTER 8	Contributions, perspectives and conclusions

Figure 1-3: Structure of the thesis based on the articles.

CHAPTER 2 LITERATURE REVIEW

2.1 Introduction

In this chapter, a comprehensive literature review concerning the compliance of non-rigid parts along with the developed inspection methods is presented. Flexible deformation and dimensional variation of non-rigid parts in a free-state, due to the compliant behavior, conventionally require inspection fixtures to recover their functional shape. These flexible deformations are due to gravity loads, residual stress, and/or assembly force. Meanwhile, dedicated fixtures such as conformation jigs should be provided in two sets for the supplier and the client for the sake of independent and repeatable inspection. To resolve these obstacles, *Computer-Aided Inspection* (CAI) methods are developed in which the fast and accurate scanning devices along with computational calculations are exploited. The fixtureless and automated CAI methods, which eliminate the need for complex fixtures are time and money savers for industrial sectors. The robustness, efficiency, and reliability of these numerical methods can also be evaluated quantitatively.

This chapter discusses background information in regards to the compliant behavior of non-rigid parts. The classification associated with the flexibility of the parts is presented in section 2.2. Then, different 3D digitization tools, which include scanners are described in section 2.3. Different inspection methods including rigid and non-rigid registration algorithms are explained in section 2.4. A review on different *Verification and Validation* (V&V) methods and their application in several disciplines of computational mechanical engineering are introduced in section 2.5. At the end of this chapter, section 2.6, a summary of the state of the art is given.

2.2 The compliance of non-rigid parts

The definition of compliant behavior (compliance) for non-rigid parts is related to material and geometrical flexibility of parts. In fact, the higher compliance value of parts implies the higher flexibility of these parts. Therefore, the flexible deformation of non-

rigid parts in a free-state is due to the compliant behavior of these parts. Considering the notation of finite element analysis, $[K]\{u\} = \{f\}$, the compliance (C) is defined in Equation 2-1.

$$C = \{u\}^t\{f\} \quad 2-1$$

Where $\{f\}$ is the force vector, $[K]$ is the global stiffness matrix and $\{u\}$ is the displacement vector. The flexibility is defined as the inverse of stiffness ($[K]^{-1}$) accordingly.

A classification for the compliance of parts is represented in (Abenhaim, Desrochers et al. 2012). The proposed force value in this classification is the permissible force, which is commonly applied during manual assembly lines and inspection techniques in the aerospace industry. The classification for compliance of parts, as depicted in Figure 2-1 and Table 2-1, categories parts in three behavior zones (zone A, B, and C). It describes that parts in zone A are considered practically as rigid parts. The induced displacement of a rigid part due to a reasonable assembly force (around 40 N) is insignificant (less than 5% of the assigned tolerance). The parts categorized in zone B are considered as non-rigid parts where the induced displacement is over 10% of the assigned tolerances. These non-rigid parts, such as thin-walled sheet metals, are commonly used in different industrial sectors such as automobile and aerospace industries. As defined in ISO-GPS standard, the flexible deformation of non-rigid parts in a free-state is beyond the dimensional and/or geometrical tolerances. This standard determines free-state as a condition that parts are not subjected to any constraining load. In fact, these parts in a free-state are submitted only to their own weight during inspection process. The parts associated with the compliant behavior in zone C enclose extremely non-rigid parts such as seals and tissues for which the part shape is extremely dependent on the part orientation and weight.

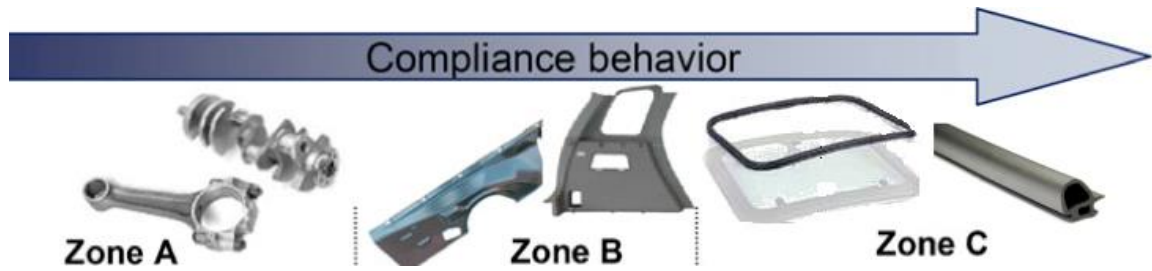


Figure 2-1: Classification of the compliant behavior of parts (Abenhaim, Desrochers et al. 2012).

Table 2-1: The classification for compliant behavior of parts concerning the induced displacement under applied force (Abenhaim, Desrochers et al. 2012).

Zones	Displacement under permissible assembly force during inspection (~40 N)	Compliant behavior of parts
A	< 5-10% of the assigned tolerance	Rigid
B	> 10% of the assigned tolerance	Non-rigid (Flexible)
C	>>10% of the assigned tolerance	Extremely Non-rigid

2.3 Measurement and 3D data acquisition methods

The traditional measuring methods apply measuring techniques that are operated by using special metrology devices such as inspection fixtures. These time-consuming techniques require skillful operators. However, developments in 3-D scanning technology allow creating a digital scan model from a physical object. Concerning the developed measuring systems (Savio, De Chiffre et al. 2007) and specifically laser scanners (Martínez, Cuesta et al. 2010), these measuring devices (scanners) can be categorized as contact and non-contact scanners.

Contact scanners (depicted in Figure 2-2-a) are based on *Coordinate Measuring Machine* (CMM) technology that can be controlled either manually or automatically by a program. These devices consist of a probe that can move along three axes, where each axis has a built-in reference standard. The advantages of these scanners are:

- They are not sensitive to colors or transparency.
- These devices have high accuracy and low cost.
- They are capable of measuring deep slots and pockets.

Unfortunately, the data collection in these type of measuring devices is slow, and the probe contact can disturb the measurement of flexible parts by causing unwanted deformation during the measuring process (Leake and Borgerson 2013).

Non-contact scanners (presented in Figure 2-2-b) use lasers and optics (using charged-coupled device (CCD) sensors) to digitally capture the geometrical shape of a part as point clouds. The non-contact scanners are fast whereas there is no physical contact between the scanners and parts. Point clouds acquired by noncontact scanners have lower accuracy compared to measured data obtained by contact scanners. However, the accuracy of acquired point clouds via noncontact scanners for common inspection applications is quite acceptable. The transparency, reflectivity and in some cases the color of surfaces also can introduce limitations for noncontact scanners, which can be resolved by applying temporary non-reflective paints. These limitations can add noise in the acquired point clouds for which the robustness of relevant inspection methods needs to be validated.

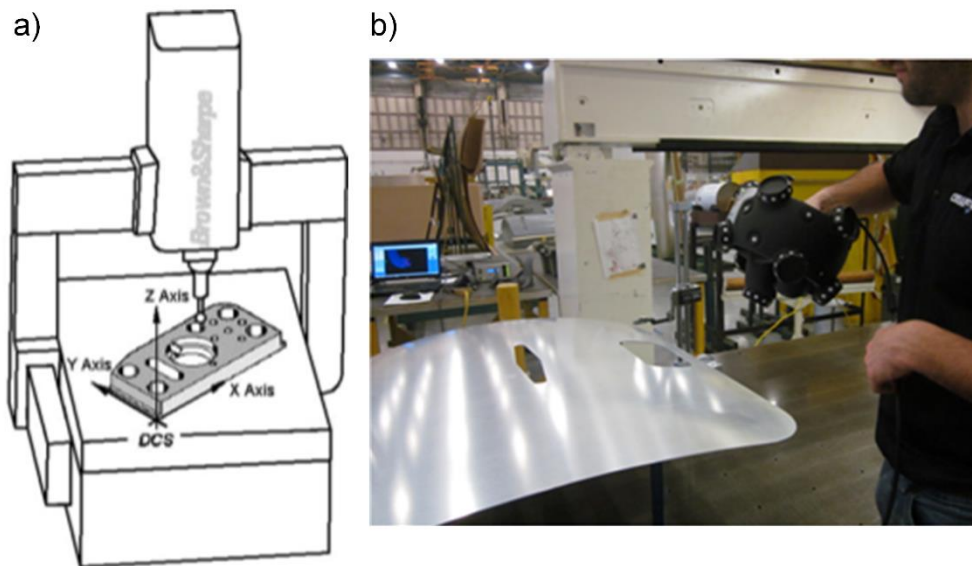


Figure 2-2: Measuring tools, a) using CMM for measuring a rigid part (Li and Gu 2004), b) using a noncontact scanner for scanning the surface of a non-rigid part.

2.4 Dimensioning, tolerancing and inspection specification of non-rigid parts

A dimension is a numerical value to define the size, location, geometrical characteristic, or surface texture of a part or features on a part. Based on ASME Y14.5, dimensions are applied to support the mating and functionality of parts. Mass-produced parts of commercial products are manufactured by applying the same production process for each part. Then, these manufactured parts are randomly assembled together. Therefore, these parts must be interchangeable to achieve a successful assembling process. However, due to the uncertainty of manufacturing processes two parts can never be the same. Therefore, slight variations in the part size are considered to prevent interference or loose assembling conditions. Tolerancing is a dimensioning technique to ensure part interchangeability by controlling the variation that exists in manufactured parts. The tolerances come off by specifying a range within which a dimension is allowed to vary. In other words,

tolerancing ensures the functionality of parts and quality of production. Tolerancing can be expressed as the following (Leake and Borgerson 2013):

- A direct tolerancing method, which includes the limit dimensioning and plus-minus tolerancing.
- General tolerancing notes, to generally address a tolerancing for all dimensions.
- The *Geometric Dimensioning and Tolerancing* (GD&T), to verify the conformity of manufactured parts with the specification defined at the design stage.

GD&T are widely applied for manufactured parts with complex shapes in different industrial disciplines. Tolerance allocation and analysis methods are used in GD&T to assign proper tolerances for assembly processes. Unlike traditional methods, non-rigid parts tolerancing methods must take into consideration compliance and permissible displacements of non-rigid parts during the assembly process. The pioneer researches on tolerance analysis of non-rigid parts are carried out by (Liu, Hu et al. 1996, Liu and Hu 1997, Camelio, Hu et al. 2002) in which tolerance analysis of non-rigid parts for advanced vehicle manufacturing is established. (Merkley 1998, Mounaud, Thiebaut et al. 2011, Chen, Jin et al. 2014) present a review of studies on *Computer-Aided Tolerancing* (CAT), tolerance analysis and allocation strategy for compliant (non-rigid) parts. In this context, the profile tolerances are assigned to free-form surfaces of parts to control surface variations. These profile tolerances can be defined with reference to datum(s) known as related profile tolerances. Related profile tolerances are applied for cases that involve the assembly of free-form surfaces with other geometric features (Li and Gu 2005). Once tolerances are allocated, the geometrical and dimensional requirements need to be verified on the part in an inspection process. Standards such as ASME-Y14.5 and ISO-GPS state that the part requirements should be evaluated in a free-state, which is represented by the symbol \textcircled{F} in drawings unless otherwise specified. However, inspection of non-rigid parts is exempted from this rule due to the compliance of these parts. Therefore, the requirements for geometric dimensioning and tolerancing of non-rigid parts based on ASME and ISO standards are classified in three categories (see Figure 2-3). Based on this

classification, the inspection requirements are respected (a) in a restrained condition, (b) in a restrictive space, and (c) using curved feature properties. The inspection requirements based on restrained conditions are also subdivided into restraining the part on a shaped fixture (Figure 2-4-a), on a hyperstatic datum reference frame, by movable datum target (Figure 2-4-b), on a basic dimension and by forces (Abenhaim, Desrochers et al. 2012).

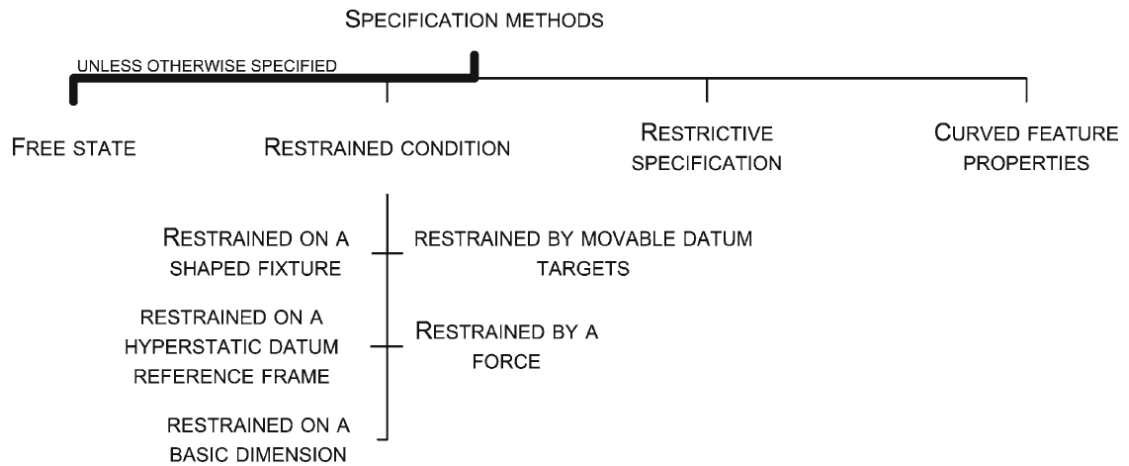


Figure 2-3: Categorization of the quality requirements specifications for GD&T of non-rigid parts (Abenhaim, Desrochers et al. 2012).

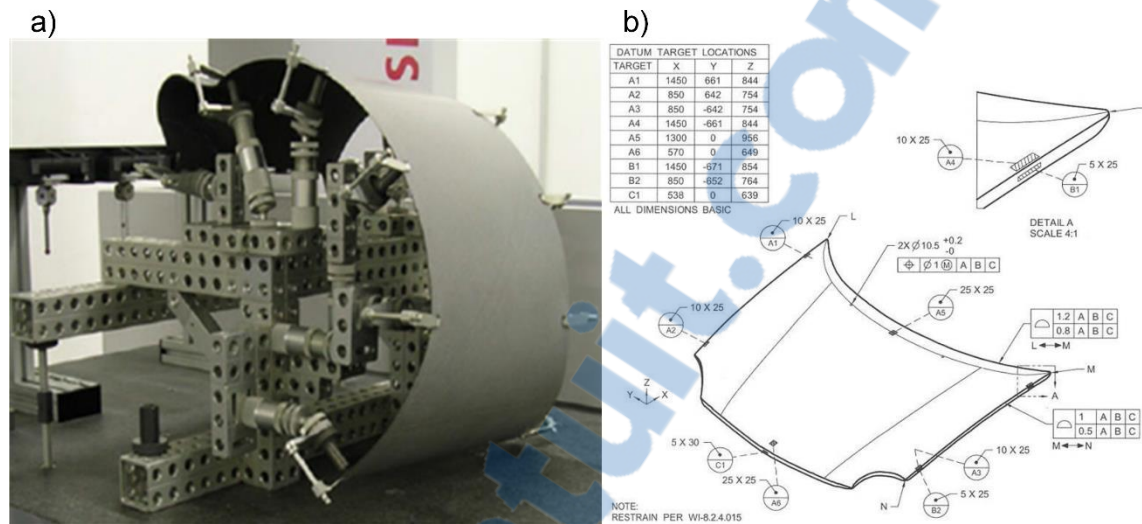


Figure 2-4: The restrained conditions for non-rigid parts, a) an inspection fixture restraining a curved aerospace panel (Ascione and Polini 2010) b) A non-rigid part restrained to the design shape using datum targets (ASME Y14.5).

The conventional inspection process applies physical fixtures that are costly and time-consuming. However, an automated reliable and efficient inspection process can diminish the production time and cost, improve the industrial competition and increase the production efficiency (Gao, Gindy et al. 2006). Computer-aided inspection (CAI) methods based on the progress in data acquisition techniques (scanners) along with computational tools are developed to improve and automate the inspection process. The inspection performed by CAI methods aim at comparing between the acquired scan model and the relevant CAD model. However, the point clouds acquired from non-contact measuring devices are presented in the *Measurement Coordinate System* (MCS) whereas the CAD model is in *Design Coordinate System* (DCS). In order to perform an inspection, the geometrical comparison between the scan and CAD models, which are in two separate and independent coordinates, has to be implemented in a common coordinate system. The process of bringing the models closer in a common coordinate system is named registration or localization (Abenhaim, Desrochers et al. 2012). CAI methods for rigid parts apply rigid registration, as presented in section 2.4.1, to align the scan model in a free-state with respect to the CAD model. Rigid registrations are performed

mathematically by finding an optimal transformation matrix between MCS and DCS. CAI for non-rigid parts is more complicated as the geometrical deviation of parts can exceed the tolerances due to the compliance of the parts in a free-state. Using physical inspection fixtures has significant drawbacks, therefore fixtureless non-rigid registration methods are developed to virtually compensate for flexible deformation of non-rigid parts. To the knowledge of the author, the first researches concerning non-rigid registration using *numerical fixtures* instead of *physical fixtures* are presented in (Blaedel, Swift et al. 2002). The virtual displacements in non-rigid registration methods can be performed via finite element analysis (FEA) or gradually iterative displacements. These fixtureless methods, presented in section 2.4.2, can be based on virtually displacing the scan model (section 2.4.2.1) or virtually displacing the CAD model (section 2.4.2.2).

2.4.1 Rigid registration

The primary step in a CAI method for non-rigid parts is a rigid registration. Rigid registration brings the CAD and scan models as close as possible in a common coordinate system without deforming the models. In fact, rigid registration uses an optimal transformation matrix to translate and rotate the models without making any changes to their shapes. Among different rigid registration methods such as those described by (Li and Gu 2004, Savio, De Chiffre et al. 2007), the *Iterative Closest Point* (ICP) algorithm (Besl and Mckay 1992) is widely applied in different domains and well-known as a robust and efficient rigid registration. For example, a rigid registration for inspection of aircraft parts is presented in (Ravishankar, Dutt et al. 2010) for which the modified ICP method is applied. Among all rigid registration methods, ICP algorithm is known as a statistically robust and efficient method. The optimal transformation (translation and rotation) matrix in ICP registration is estimated at each iteration to minimize the distance between two models. To this end, the Hausdorff distance (Henrikson 1999) between CAD mesh and acquired point clouds of scan model measures how far these two models are from each other. As illustrated in Equation 2-1, the Hausdorff distance ($d_H(X, Y)$) between two non-

empty subsets (X, Y) of a metric space can be defined as the maximum distance between every point of either set to some point of the other set.

$$d_H(X, Y) = \max\{\sup_{x \in X} \inf_{y \in Y} d(x, y), \sup_{y \in Y} \inf_{x \in X} d(x, y)\} \quad 2-1$$

The ICP has been modified and developed to improve the calculation time as well as the minimization strategy (Rusinkiewicz and Levoy 2001), and some of these improvements are presented here. The improvements on decreasing the calculation time of ICP is presented in (Masuda and Yokoya 1995) by proposing a robust method applying random sampling of the point clouds. (Greenspan and Godin 2001) proposed an improvement in searching closest points by using corresponding points of previous iterations of the ICP and searching only in their small neighborhood. (Zhu, Barhak et al. 2007) applied a mixture of techniques that accelerate the registration process and improve the efficiency of the ICP method. Many variant techniques of ICP have been investigated by (Rusinkiewicz and Levoy 2001) and (Bentley 1975). However, it should be pointed out that ICP-based algorithms are not capable of dealing with non-rigid parts where flexible deformations need to be taken into consideration.

2.4.2 Fixtureless inspection of non-rigid parts (non-rigid registration)

Applying only the rigid registration methods such as ICP method (Ravishankar, Dutt et al. 2010) is not sufficient for inspection of non-rigid parts in a free-state. Rigid registration methods do not permit any modification on the shape of CAD or scan models to compensate for the flexible deformation of non-rigid parts during the inspection process in a free-state. Meanwhile, inspection methods for non-rigid parts need to distinguish between the flexible deformation of non-rigid parts in a free-state with defects such as geometrical deviations due to faulty manufacturing. Conventional CAI methods apply restraining non-rigid parts in physical fixtures (Ascione and Polini 2010) during the inspection process. However, these sophisticated and expensive fixtures have significant drawbacks for which the setup and repeatability of the fixtures are costly. Therefore, the fixtureless inspection methods are required to eliminate these costly fixtures. Fixtureless inspection of non-rigid parts based on CAI methods is able to evaluate the geometrical

deviation of manufactured parts with respect to the assigned tolerance by taking into consideration the flexible deformation of non-rigid parts in a free-state. A categorization of fixtureless inspection methods based on literature is presented in (Abenheim, Desrochers et al. 2012). The fixtureless CAI methods are classified into four approaches as I) automated vision inspection, II) metric characteristic, III) boundary reconstruction and IV) simulated displacement. Fixtureless inspection of non-rigid parts can be performed by non-rigid registration methods classified as simulated displacement. These methods are essentially based on compensating for flexible deformation of non-rigid parts in a free-state by virtual displacement. The core idea of the fixtureless methods is to enable a comparison between the scan and CAD models by virtually compensating for the flexible deformation of the part whereas leaving the defect areas intact. The inspection methods presented in section 2.4.2.1 are based on virtually deforming the scan model towards the CAD model, while the non-rigid inspection methods presented in section 2.4.2.2 are based on virtually deforming the CAD models. Studying the displacement simulation for fixtureless inspection methods, this simulation can be performed based on FEA or gradual iterative displacement methods.

2.4.2.1 Fixtureless inspection based on virtually deforming the scan model

The fixtureless inspection methods based on virtually deforming the scan model apply boundary conditions (BCs) via *Finite Element Analysis* (FEA) to deform the scan mesh towards the corresponding CAD model. The BCs in the *virtual fixation concept* (Weckenmann and Weickmann 2006) are imposed on fixation features of the scan mesh such as inspection fixations and assembly mounting holes and edges on the part. These features can automatically be identified using feature extraction techniques (Weckenmann, Gall et al. 2004). The *virtual fixation* method consists of processing scanned data, simulation (virtual fixation) and then comparing the models. The process of this inspection method, as presented in Figure 2-5, starts with data acquisition from visible surfaces of a part using an optical surface measuring system (e.g. fringe projection measuring system). These 3D measuring devices provide some millions of point clouds

per measurement. This scan data (with huge data size) is then reduced into 30 to 50 thousand point clouds, using a curvature-based method, which allow performing finite element calculation. To reduce the size of scan mesh, the points in the flat area are removed but the points associated with curved features are kept to preserve the geometrical properties of the part. An approximation of the surface as triangulations with linear elements is then performed on the point clouds. Applying triangulation techniques such as Delaunay-based (Borouchaki, George et al. 1996) approaches on the point clouds generate a representative geometrical shape of the part as scan mesh. The data processing continues with removing the noise of the measured surface by applying mesh smoothing and filtering techniques. In the examples performed by (Weckenmann and Gabbia 2006), the local sphere assumption proposed in (Karbacher and Hausler 1998) is applied for smoothing the scanned data. In order to utilize the finite element analysis, the material properties (such as Young's modulus and Poisson's ratio and density in addition to the wall thickness of the triangulated mesh) are defined for the inspecting model. In this step, the extracted features (such as fixation holes) are used to find the correspondence (for registration process) between the CAD model and scan mesh. Then, BCs (such as imposed displacements) are applied on fixation features of scan mesh to displace these features towards the corresponding features on the CAD model via FEA. The FEA applied in this method uses updated Lagrange algorithm, which is a nonlinear large displacement FEA resolution. Then, a geometrical comparison between the deformed scan mesh (after applying FEA) and CAD model identifies defects on the scan model (inspection of part).

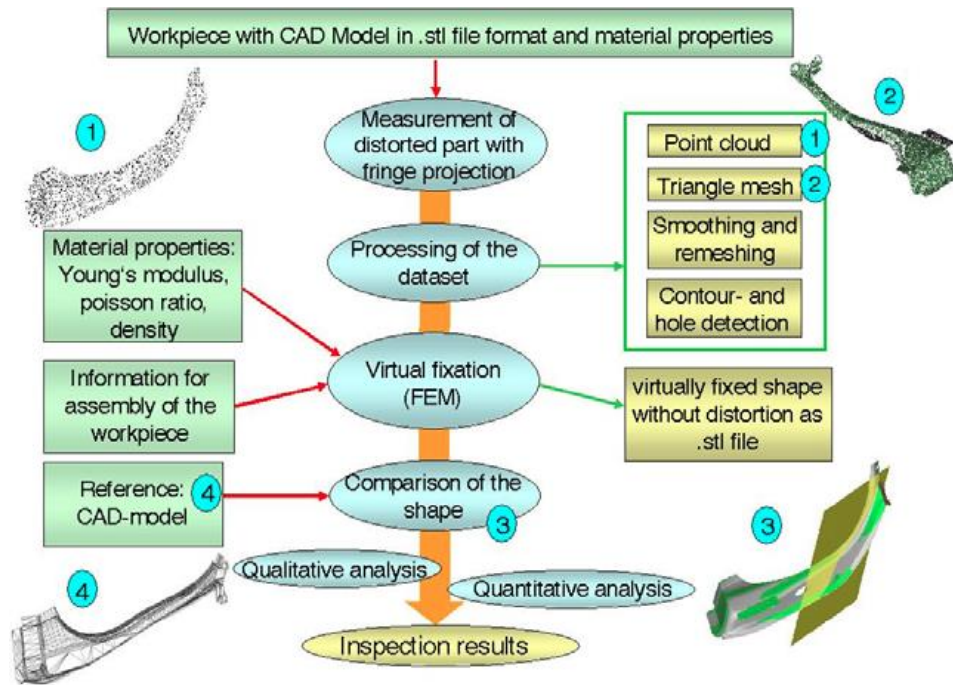


Figure 2-5: The process chain of the virtual distortion compensation method (Weckenmann and Weickmann 2006).

However, imposing BCs on all fixation features to displace them into their design location for non-rigid parts is not always possible and may result in geometrical deviations in the part. To this end, (Gentilini and Shimada 2011) proposed an alternative for applying BCs directly on fixation features. In this method, an optimization method is used to minimize the location and orientation of fixation features between the deformed scan mesh and CAD model. The specific displacement BCs that satisfies the optimization method can predict the functional shape of the part. Applying these BCs on the scan mesh via FEA, a *virtual inspection* is performed on the deformed scan mesh in its assembly-state. The geometrical comparison between the deformed scan mesh and CAD model evaluates defects on the scan model.

Considering the application of movable datum targets for restraining non-rigid parts during inspection and an industrial inspection technique (see Figure 1-2) as restraining loads, a *virtual fixture* method is presented in (Abenhaim, Desrochers et al. 2015). In this fixtureless CAI method as depicted in Figure 2-6, the scan mesh is virtually restrained by

a combination of forces located only on datum targets to minimize the weighted average of distances at specific points (constrained regions) between the deformed scan mesh and CAD model. The restraining forces, which are limited to the defined permissible assembly loads, are estimated through an optimization method that minimizes the distance at constrained regions between the scan and CAD models. Applying these optimized restraining forces on the scan mesh, the functional shape of the part in assembly-state can be retrieved. The inspection result in this method is performed on datum targets evaluating the difference between the deformed scan mesh and nominal position of datum targets.

The advantages of applying fixtureless inspection based on virtual deforming the scan model can be outlined as:

- The functional shape of scan model is used for identifying defects in fixtureless inspection. Therefore, the inspection of parts is accomplished in their functional state.
- Defects on scan model in a free-state can be affected by flexible deformation of non-rigid part. Performing the inspection of scan model in the functional state, avoid the size and area of defects to be affected by flexible deformation of part.

The drawbacks of using fixtureless inspection based on virtual deforming the scan model are as follows:

- For each acquired point clouds of scan models, a proper FE-mesh has to be generated by processing the scan mesh. The mesh processing applies mesh decimation and modification tools.
- The scanning process should be implemented accurately all over the part to enable generating a FE-mesh that perfectly represents the geometry of scanned part.

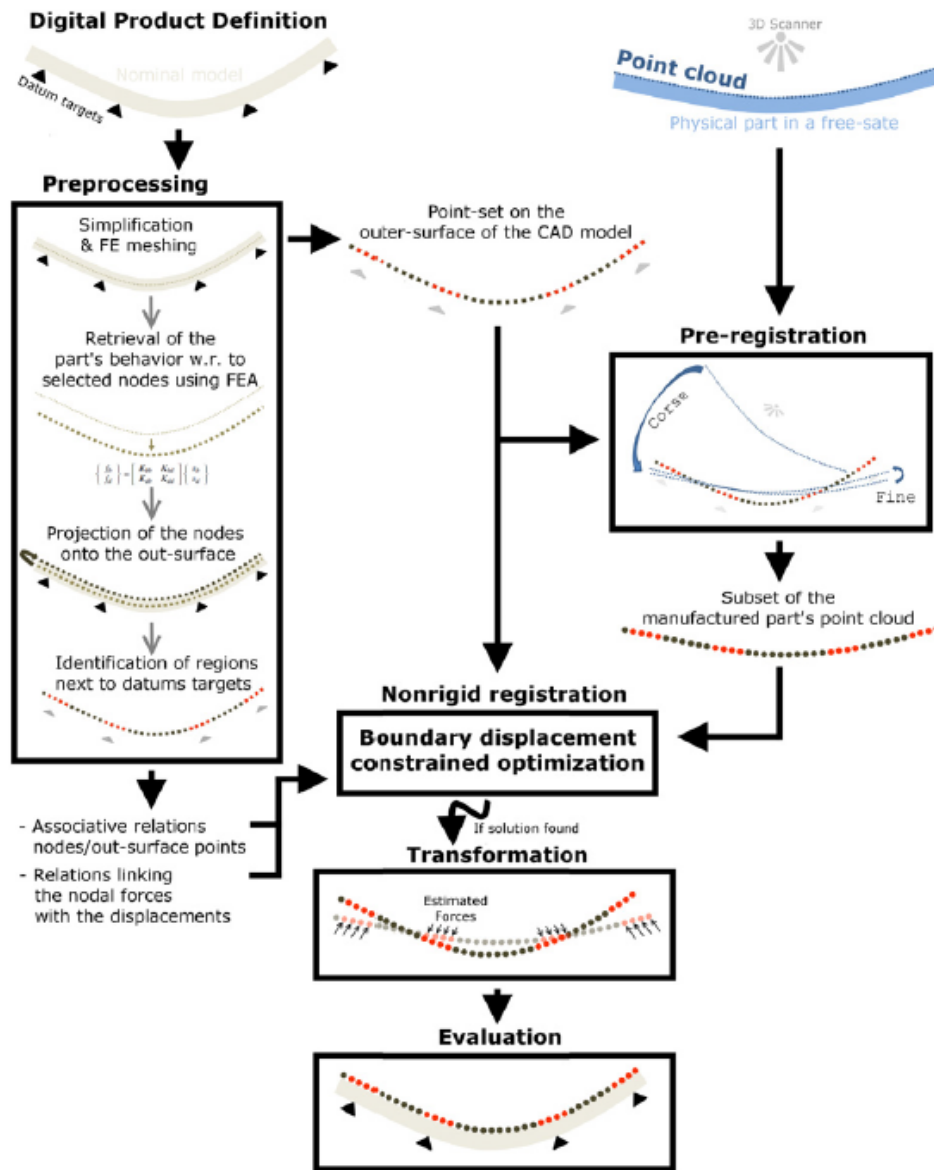


Figure 2-6: Schematic flowchart of proposed *virtual fixture* method in (Abenhaim, Desrochers et al. 2015).

2.4.2.2 Fixtureless inspection based on virtually deforming the CAD model

The second group of fixtureless CAI methods, based on simulated displacement approaches, intend to deform the CAD model towards the scan model to compensate for the flexible deformation. Therefore, the drawback of generating FE mesh for each

measured scan part is eliminated. To this end, the high-quality mesh of CAD model is used to be deformed towards the scan mesh. Tackling with the drawbacks of the *virtual fixation concept* (Weckenmann and Weickmann 2006), BCs in *virtual reverse deformation* (Weckenmann, Weickmann et al. 2007) are imposed on the fixation features of the CAD model. Applying feature extraction techniques, these required BCs are determined to displace the CAD features towards their corresponding features on the scan model. The simulation is conducted by generating FE-mesh from the CAD model, which is accomplished once for all the inspections pertaining to the same CAD model. Applying BCs on CAD mesh along with mechanical properties and thickness of the part, fixation features of CAD model is displaced towards their corresponding features on scan mesh via FEA. The geometrical comparison between the measured shape in a free-state (scan model) and the virtually deformed CAD model evaluate defects on the scanned part.

During the scanning process, some part of scan model might be missed. Missing data associated with fixation features is crucial for *virtual reverse deformation* method because the BCs concerning these features cannot be determined. A fixtureless inspection method presented in (Jaramillo, Prieto et al. 2013) estimates approximately the location of missing fixation features using an interpolating technique. As shown in Figure 2-7, the non-rigid registration in this method applies iterative transformation through which the deformed CAD model iteratively matches the partially acquired scan model. The inspection result is provided by a geometrical comparison between the deformed CAD model and partially scan mesh.

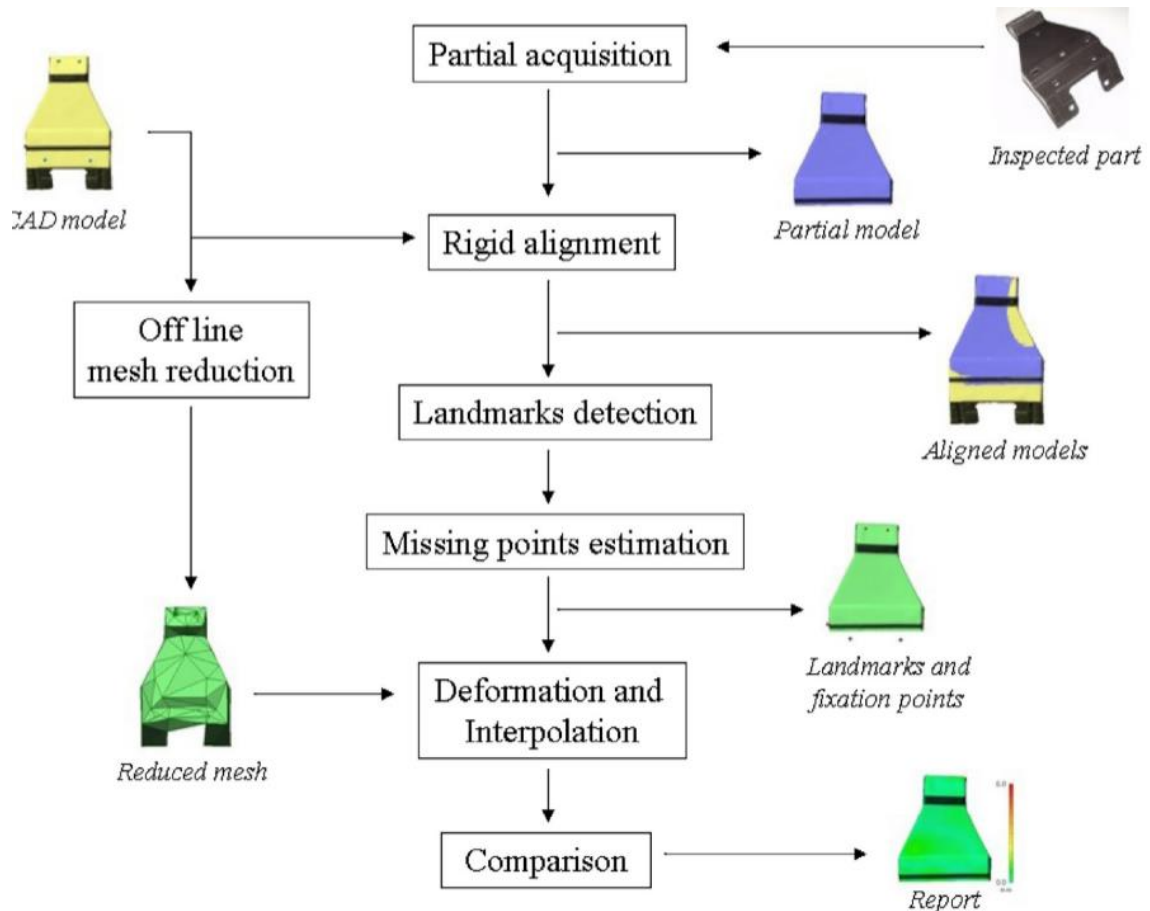


Figure 2-7: An overview of the non-rigid CAI method using partial measuring data (Jaramillo, Prieto et al. 2013).

However, determining the correspondence between the CAD model and range data for fixation features needs human intervention, which is an obstacle towards automatic CAI. For this reason, the *Iterative Displacement Inspection (IDI)* algorithm (Abenhaim, Tahan et al. 2011, Aidibe, Tahan et al. 2012) is developed based on iterative transformation of CAD model towards scan mesh without using FEA. IDI proposes an algorithm that combines the rigid with non-rigid registration methods along with an identification method to distinguish defects from flexible deformation on the point clouds of scan model. This method is developed for inspection of profile deviations, which feature dent shapes (e.g. bumps) on deformable skinned parts. The IDI method applies rigid registration, using the ICP algorithm, to minimize the Euclidian distance between the

CAD mesh and scanned point clouds without deforming the shape of models. Then, IDI applies a non-rigid registration algorithm based on iteratively finding an affine transformation matrix (Allen, Curless et al. 2003) to deform the CAD mesh towards scan model. This step is shown in Figure 2-8 wherein a defined displacement field is introduced on CAD mesh (presented by S) to displace them towards deformed CAD mesh (represented by S'), which is closer to the scan model (point clouds of P). This transformation must maintain the quality of the modified CAD mesh, by minimizing the distance between the modified CAD mesh and the original CAD mesh and keep the smoothness of the modified mesh with respect to the original CAD mesh. The displacement field is iteratively determined and applied on the CAD model to minimize the shape difference between the deformed CAD model and scan point clouds. However, the displacement fields must only consider the flexible deformation of a part excluding the effect of defects. Therefore, IDI uses an identification method on the scan part to identify the outlier point clouds that physically represents defects. This identification method is inspired from (Merkley 1998), where the nodes located out of range with reference to the neighboring nodes are identified as defects. These nodes, shown as profile deviation in Figure 2-8, are excluded from the calculation of displacement field during the iterative non-rigid registration. A smooth and iterative displacement of CAD model towards scan mesh is then performed. The inspection is implemented as a geometrical comparison between the deformed CAD mesh and scan model to evaluate the defects. Nonetheless, the identification approach in IDI limits the method to evaluate only the localized defects on the scan models.

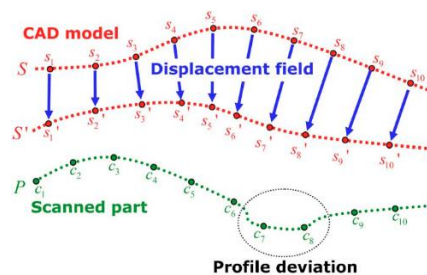


Figure 2-8: constructing deformed CAD model using displacement field without taking into consideration the presence of effects (Abenheim, Tahan et al. 2011).

The identification method in the IDI algorithm is improved in (Aidibe, Tahan et al. 2012) by applying the maximum-normed residual test that automatically identifies defects on scan models. In this approach, the nodes associated with defects are considered as statistical outliers with respect to the neighboring nodes. The drawbacks of identification algorithm in IDI method and its improved version are as follows:

- The algorithm is limited to localized defects which make it inefficient for inspection of parts with big (global) defects.
- The sharp changes in thickness is a serious challenge, because the flexibility parameters in the algorithm, which are calculated based on the thickness of the part, result in false behavior of the part in the thickness-changing zones.

A fixtureless inspection of non-rigid parts based on using the *Coherent Point Drift* (CPD) algorithm is presented in (Aidibe and Tahan 2015). CPD is a probabilistic method considered as one of the most powerful non-rigid registration techniques and efficient for extremely flexible parts. The surface of these extremely flexible parts can be stretched during a deformation, which is not the case for non-rigid parts such as thin sheet metals. These non-rigid parts retain the geodesic distance on the surfaces of the part, which requires optimizing the CPD parameters to respect the stretch and Euclidian distance criteria during non-rigid registration. The presented inspection method also applies the Thompson tactical test to distinguish between flexible deformations and defects. To this end, defects are recognized as statistical outliers of scan point clouds that exceed the assigned tolerances.

Concerning the shortcomings of the abovementioned methods, the *Generalized Numerical Inspection Fixture* (GNIF) (Radvar-Esfahlan and Tahan 2012), see Appendix A, claims to inspect both small (local) and big (global) defects and decrease the need for human intervention. This method assumes that non-rigid parts do not stretch during flexible deformation in a free-state. Therefore, the geometry of CAD and scan models are intrinsically the same based on Gauss's Theorema Egregium. This phenomenon is derived from the fact that the Gaussian curvature of a surface does not

change when the surface is bent without stretching. In fact, the flexible deformation of non-rigid parts is an isometric deformation for which the shortest inter-point (geodesic distance) between any two points remains unchanged. Based on this distance preserving property of non-rigid parts, the GNIF method compensates for the flexible deformation during an inspection. This property is depicted in Figure 2-9, where the geodesic distances on the CAD model (between x_1 and x_2) remains the same as the geodesic distance on the scan model in a free-state (between y'_1 and y'_2) (Radvar-Esfahlan and Tahan 2014).

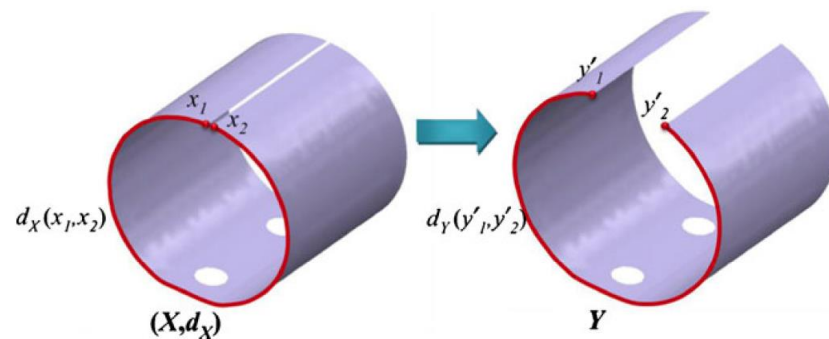


Figure 2-9: Distance preserving property of non-rigid part during an isometric deformation (Radvar-Esfahlan and Tahan 2014).

The GNIF method generates sets of corresponding sample points on the CAD and scan meshes, as shown in Figure 2-10 with black points for a turbine blade. This is done by considering the CAD and scan models as geodesic distance metric spaces. Discrete geodesic distances between each pair of nodes on CAD mesh, as well as scan mesh, are approximated by using *Fast Marching Algorithm* (FMA) (Kimmel and Sethian 1998). Applying *Generalized Multi-Dimensional Scaling* (GMDS) (Bronstein, Bronstein et al. 2006), the proper pairs of geodesic distances on the CAD and scan models are determined for which the maximum difference between the pairwise distances is minimized.

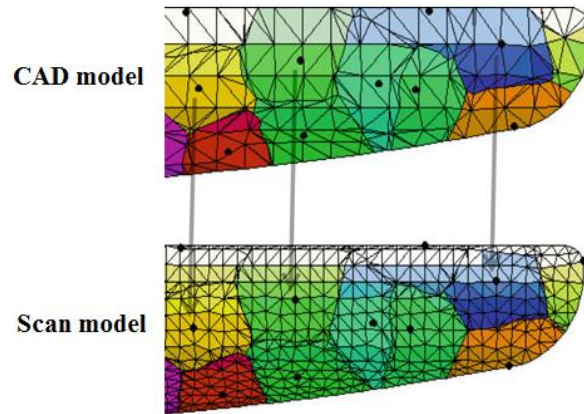


Figure 2-10: Corresponding sample points (black points) generated on the CAD and scan models for a turbine blade (Radvar-Esfahlan and Tahan 2014).

The generated corresponding sample points are used as BCs in *Finite Element Non-rigid Registration* (FENR) to compensate for the flexible deformation. In fact, FENR displaces the sample points on the CAD model toward their corresponding point on the scan model that deforms the CAD mesh towards scan mesh. As presented in Figure 2-11, the geometrical comparison between the deformed CAD model (after FENR) and the scan model lead to evaluating geometric deviations (defects) on the scan model.

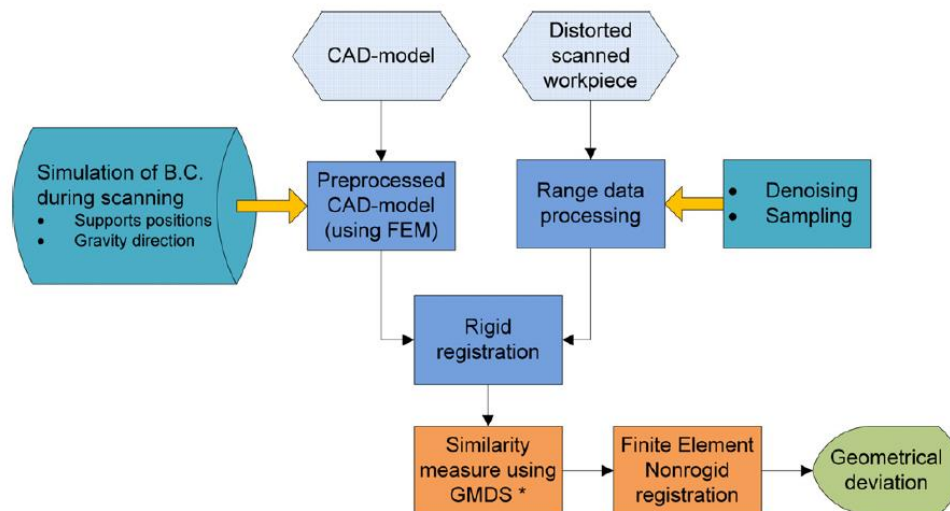


Figure 2-11: The flowchart of the inspection process using GNIF method (Radvar-Esfahlan and Tahan 2012)

The corresponding sample points generated by GNIF are evenly distributed over the CAD and scan models. Therefore, some sample points can be located on and/or around defects. Using these sample points via FENR result in an inaccurate inspection. For this reason, the inspection approach presented by (Radvar-Esfahlan and Tahan 2012) applies sample points on bounding edges and/or assembly features as BCs in FENR. However, this needs to assume that these features are perfectly scanned which is not always the case. Therefore, another approach presented by (Sabri, Tahan et al. 2016) applies specified pre-selected sample points as BCs in FENR. Therefore, specific areas on the CAD and scan models are manually selected wherein the barycenters of sample points are calculated as specified pre-selected sample points.

The advantages of applying fixtureless inspections based on virtually deforming the CAD model is outlined as:

- There is no more need to process each scan mesh of parts, instead, one high-quality FE-mesh is created from the CAD model.
- The mesh generated from the CAD model is more accurate, optimized, smoothened and noiseless, which takes less time to be automatically generated.
- Since only the critical areas such as fixation points or tolerance features are necessary for simulation process, the measurement data can only be implemented accurately for these features that result in reducing the size of measuring data.
- Missing data, except for fixation information, during scanning the part does not affect the simulation process.

The shortcomings of using fixtureless inspections based on virtually deforming the CAD model are as follows:

- The identified defects on the scan model in a free-state can be affected by flexible deformation of non-rigid parts. This can bring about errors into quantifying the size and area of defects.

- Due to flexible deformation of non-rigid parts in a free-state, the scan models does not represent the functionality of these parts. The inspection does not eventually accomplish on the functional shape of the part. Therefore, the performance of a part in its functional state cannot be verified.

2.5 Verification and validation methods based on ASME recommendations

All CAI methods, which are based on scan data and computational calculations, are required to be verified and validated. Uncertainty in computational simulations and measuring errors due to the inaccuracy of data acquisition devices are inevitable in fixtureless non-rigid inspection methods. Inaccuracy of scanners is due to the technical limits of devices, optical effects (such as light fraction and reflectivity of parts surface) or inaccessible features of parts. These noisy data can affect the performance of CAI methods. Applying *Verification And Validation (V&V)* approaches on computational simulation models allows assessing accuracy, reliability, and robustness of simulations (Schwer, Mair et al. 2012). In fact, verification assesses the accuracy of a solution in a computational model whereas validation evaluates the consistency of computational simulation results comparing with the actual results. As presented in Figure 2-12, due to various sources of uncertainty in computer codes and simulations, all computational methods, among which are CAI methods, need to be thoroughly verified and validated. Investigations on the application and theory of verification and validation in computational engineering are presented by (Oberkampf, Trucano et al. 2004, Oberkampf and Barone 2006, Sornette, Davis et al. 2007). Unlike the qualitative traditional validation activities, newly developed rigorous and systematic V&V approaches are applied in different disciplines. These approaches are published for V&V guides in computational solid mechanics (Hills and Trucano 1999), fluid dynamics (Committee 1998), heat transfer (Committee 2009) and material engineering (Cowles, Backman et al. 2012). The predictive capability of the computational model in these guides is demonstrated by comparing the features of interest (validation metrics) with respect to the real model in

its intended use. The validation metrics, which are the quantitative measure of agreement between a predictive model and physical observation (measurements), are categorized as hypothesis testing-based and distance-based (Oberkampf and Trucano 2008, Liu, Chen et al. 2011). Unlike distance-based metric, the hypothesis testing-based metrics provide an evaluation concerning the general trend of data. The hypothesis testing-based validation metrics compare the probability distributions of the prediction results and observations. The comparison, which is based on statistical distributions such as cumulative distribution functions (CDFs), is accomplished through a test of significance enclosed in the hypothesis testing theory. Several research work, in various engineering fields such as structural dynamics (Paez and Urbina 2002), steady and transient heat conduction and shocks (Hills and Leslie 2003), thermal decomposition of polyurethane foam (Rutherford and Dowding 2003, Dowding, Leslie et al. 2004) and sheet metal forming processes (Chen, Baghdasaryan et al. 2004) used hypothesis testing-based validation metrics for their numerical calculations.

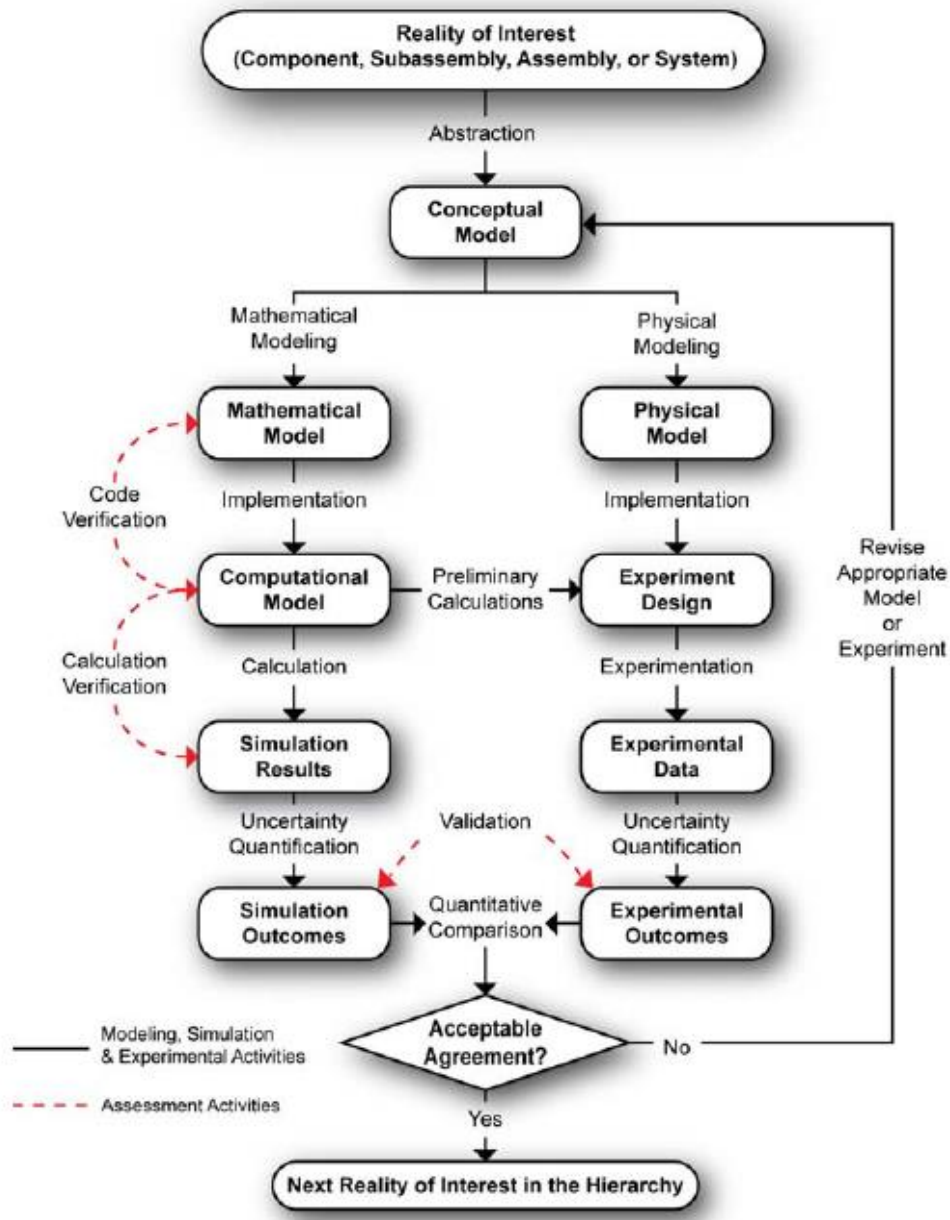


Figure 2-12: verification and validation (V&V) activities and results based on ASME recommendation (Schwer, Mair et al. 2012).

Applying a validation metric, the robustness of a computational model can be evaluated by validating the result of a numerical approach with respect to input noise. In fact, a robust computational model should provide satisfying results despite the presence of input noise. In other words, the output of a robust computational approach remains

acceptable for input data including noise with reference to the output for a noise-free input data. In CAI methods, the input noise is principally originate from measurement noise that is inherent to measuring data acquisition devices. Therefore, the robustness of CAI methods is required to be studied with respect to scanning device noise (Boehnen and Flynn 2005, Sun, Rosin et al. 2008).

2.6 State of the art summary

In this chapter the specification of non-rigid parts used in different industrial sectors such as aerospace and automobile industries is overviewed, taking into consideration the challenges of the industries for inspection of these parts. To this end, different rigid and non-rigid registration methods are introduced that use measuring data acquired by scanners. Among these methods, *Computer-Aided Inspection* (CAI) methods are presented, which tend to achieve automatic inspections. Fixtureless CAI methods push it a step further by performing inspection in a free-state, which speeds up the process and lowers the costs. Then, the robustness of these methods with respect to scanning noise also needs to be verified and validated. Meanwhile, the compliance of flexible parts can compensate for some types of geometrical deviations (defects) in assembly-state. In some cases, the functional shape of flexible parts including defects can be retrieved under permissible assembly loads. This is a practical technic that is generally used in aerospace industries to retrieve the functional shape of a deviated non-rigid manufactured part on sophisticated inspection fixtures. It concludes that the automatic inspection of non-rigid parts still remains a challenging, time-consuming and costly process for industrial sectors.

CHAPTER 3 GENERAL PLANNING OF THE THESIS

3.1 Statement of the problem

This research is focused on the automatic and fixtureless inspection of non-rigid (flexible) parts. Non-rigid parts such as thin sheet metals are commonly used in the aerospace and automobile industries as covering the body of cars and airplanes by large panels. Due to the compliance of flexible parts, these parts are deformed in a free-state in which the part is submitted only to its own weight. The flexible deformation cause geometrical deviations that exceed dedicated tolerances for the assembly process. However, the functional shape of these parts can be retrieved on inspection fixtures (see Figure 3-1) and these parts can be assembled under permissible loads in the assembly-state. Setting up fixtures that should be adjusted for each part is costly and takes significant inspection time. For example, some inspection setup processes for the type of non-rigid parts considered in our industrial partner (Bombardier Aerospace) demand 60 to 75 hours of operation. Considering the repeatability of inspection in manufacturing and customers' facilities, the cost of these fixtures doubles. In order to speed up the geometric inspection of non-rigid parts, to decrease the cost of inspection and to maintain the inspection precision during quality control process, *Computer-Aided Inspection (CAI)* methods are developed. These methods use benefits of applying 3D scanners along with computational calculations to perform a virtual inspection of scan models by geometrically comparing them with the CAD model. Dimensioning and tolerancing standards such as ASME and ISO require performing the inspection in a free-state unless otherwise specified, whereas the exemption refers to inspection of non-rigid parts. However, the measured scan model is acquired in *Measurement Coordinate System (MCS)* which is independent of the CAD model in *Design Coordinate System (DCS)*. Using an inspection fixture instantly unifies the two coordinate systems and also compensate for the flexible deformation of parts. However, serious drawbacks of using fixtures during inspection process lead to fixtureless CAI methods in which the surface of parts is acquired in a free-state. The main challenge of fixtureless CAI methods is the geometrical comparison between the CAD

and scan models in a common coordinate system considering the geometrical variation of parts in a free-state. In order to accommodate CAI methods with industrial requirements, fixtureless CAI methods need to be performed in an automated inspection process and to provide more accurate inspection results.

Like all computational models, fixtureless CAI methods based on virtual displacement approaches need to be verified and validated with respect to actual inspection results. To this end, a quantitative validation metric is required to verify estimated inspection results regarding nominal defects on the parts. In fact, the robustness of CAI methods is assessed with respect to scanning noise to ensure the accuracy of inspection results despite the presence of input noise.

Practical inspection techniques (by using inspection fixtures) show that the functional shape of geometrically deviated non-rigid parts can be retrieved under permissible assembly loads. In fact, the compliance of non-rigid parts allow retrieving the functional geometry of a deviated part (including defects) in assembly-state. These practical techniques apply permissible loads on the surface of deviated parts to put the part into its assembly-state on an inspection fixture (see Figure 1-2). However, evaluating the required assembly loads by trial-and-error on the costly fixtures lead to a time-consuming and low efficiency inspection method. Therefore, industrial companies demand for automated fixtureless CAI methods which eliminate the drawbacks of conventional inspection techniques.

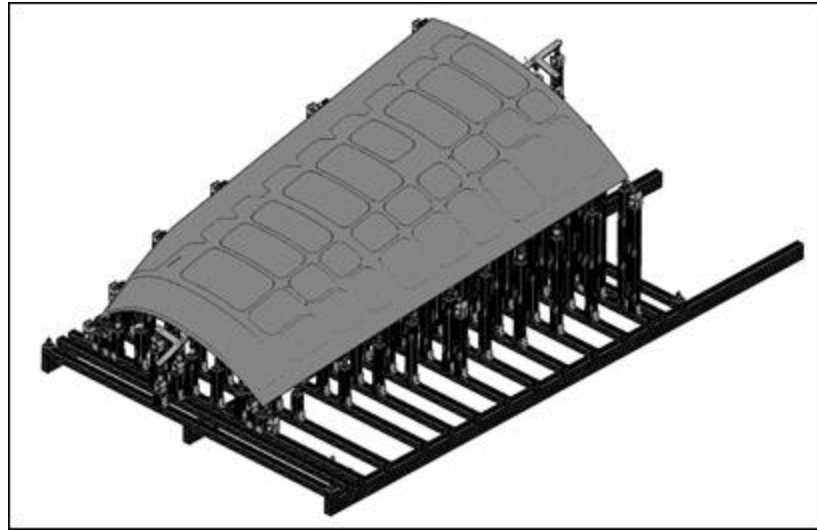


Figure 3-1: A complex inspection fixture set-up for a large aerospace panel.

Therefore, manufacturing companies are very interested in fixtureless inspection methods for non-rigid parts in a free-state for which the required assembly loads can be estimated automatically. These fixtureless methods take into consideration that:

- The method should eliminate the need for inspection fixtures.
- The method ensures performing an automatic inspection under estimated permissible assembly loads (force measuring tools and manual distribution of loads are eliminated).
- The method should be able to simulate the functional shape of the scan model in assembly-state.
- The inspection method should avoid setting up parameters that would be different from one part to the other one.
- The fixtureless inspection method should be performed automatically to avoid human intervention during the inspection process.
- The inspection results are required to be obtained within an acceptable calculation time.

- The inspection results should be accurate for further decisions on the part.
- The fixtureless CAI method should be robust with respect to different sources of input noise.

To this end, the following technical criteria are crucial for fixtureless CAI methods:

- The scan mesh which is the representative of a manufactured part in a free-state may include flexible deformation and geometrical deviation with reference to the CAD model, which does not permit a direct comparison between the models.
- A discrete surface representation of manufactured part (scan mesh) is generated and applied as an input to the CAI method.
- The inputs may include inspection noise inherent to scanning devices.
- We are specifically targeting parts that are classified in zone B as described in section 2.2. The geometrical characteristics and mechanical behavior of these parts classify them in zone B.
- The functional shape of non-rigid part is estimated in assembly-state.
- The required assembly loads, limited to the permissible loads, are estimated to retrieve the functional shape of deviated non-rigid part in assembly-state.

Concerning the serious need of industrial sectors using non-rigid parts for automatic fixtureless CAI methods, which is able to satisfy the above-mentioned problematics, the research objectives of this project are presented in section 3.2

3.2 Research objectives

The main objective of this study is to develop an automatic fixtureless CAI for non-rigid manufactured parts in a free-state and then evaluate the robustness of the developed CAI method. The main objective is fulfilled by developing two different CAI methods based on virtual displacement approaches to enable evaluating geometrical deviations (defects). The first developed fixtureless method aims at distinguishing between the flexible

deformation and possible defects of parts, then compensate for the flexible deformation by virtually displacing the CAD model towards the scan model. As depicted in Figure 3-2, all CAI methods are required to be validated to assess the robustness of developed methods with respect to noise. Therefore, developing a quantitative validation metric for validation of fixtureless CAI methods especially for non-rigid parts is taken into consideration.

The second developed method intends to virtually deform a deviated scan mesh (presenting defects) into assembly-state under permissible assembly loads. Inspired by a practical inspection technique in aerospace industries, estimating the required permissible assembly loads through a fixtureless CAI to achieve the tolerances in assembly-state is an interesting target of this project. Indeed, the possibility of assembling a deviated non-rigid part in assembly state is investigated.

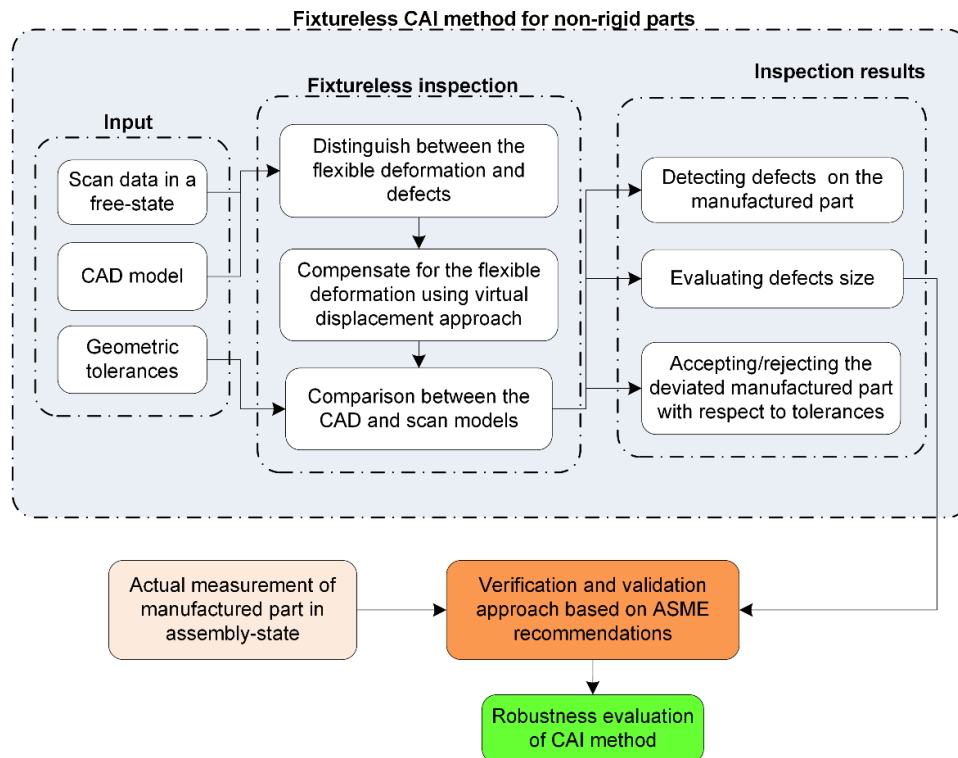


Figure 3-2: simplified flowchart of a fixtureless CAI followed by a verification and validation approach.

Therefore, the objectives of this thesis can be outlined as following:

- Distinguishing between the flexible deformation and possible defects on a non-rigid part.
- Implementing a non-rigid registration to compensate only for the flexible deformation of non-rigid parts.
- Performing a virtual inspection for estimating the size and location of defects on the non-rigid parts.
- Developing a new algorithm to predict a distribution of assembly loads on the surface of a deviated non-rigid part through which the part is put in assembly-state.
- Establishing an optimization process, for a deviated non-rigid part that can be put in assembly-state, to find the best distribution of assembly loads which minimizes the distance and orientation differences between assembly features (such as mounting holes) on the scan and CAD models.
- Developing a quantitative validation metric for the *Verification and Validation* (V&V) of CAI methods based on ASME recommendations.
- Verifying the performance of our developed methods on actual aerospace parts.

3.3 Hypotheses used in the project

This section presents the general hypotheses that are commonly considered in this research. These hypotheses are as follows:

- The parts intended to be inspected are non-rigid parts (thin-walled sheet metals) used in different industrial sectors among which aerospace and automobile industries.
- The nominal geometry of the parts is available as CAD model in the *Design Coordinate System* (DCS).

- The flexible deformation and geometrical deviation of these parts during a free-state measuring (scanning) process might exceed the dedicated tolerances. However, the developed methods in this study can also inspect non-rigid parts with no defects and lead to accept these parts since their geometrical deviation is in tolerance range.
- The acquired point clouds from a free-state scanning process presenting the surface of manufactured part in *Measurement Coordinate System* (MCS) is available.
- The CAI methods are developed for identifying and estimating defects in the surface profile and location of the parts as defined by ASME Y14.5 (2009).
- At the beginning of this project, all simulations used for non-rigid registrations were based on linear FEA assumption (small displacement formulation, linear elastic behavior, etc.). However, during the course of this research, we adapted the application of nonlinear FEA to use large displacement formulation in FENR.

3.4 The synthesis of researches and logical links between articles

A synthesis of the proposed researches is briefly presented in the remaining sections of this chapter to highlight the integration and logical links between the articles.

3.4.1 Simulated scan models for validation cases

In this research, we used different validation cases to evaluate the accuracy and limits of our developed methods. These validation cases, as shown in Figure 3-3, are non-rigid aluminum parts used typically in aerospace industries. However, all the scan models of these validation cases are simulated by deforming CAD models via FEA and by adding geometrical deviations (defects). Different geometrical deviations such as bump defects (Figure 3-3-b, c, e, f, h and i), geometric alteration (Figure 3-3-j) and plastic deformation

(Figure 3-3-k and l) are used in this thesis. The CAD models of validation cases are also presented in Figure 3-3-a, d, g, j, k and l with green color.

We can accurately evaluate the size of generated defects on simulated scanned models, whereas measuring defects on real parts includes measuring uncertainties. Therefore, using simulated scanned models instead of real scanned data allow assessing the accuracy and robustness of our developed CAI methods with respect to nominal simulated defects.

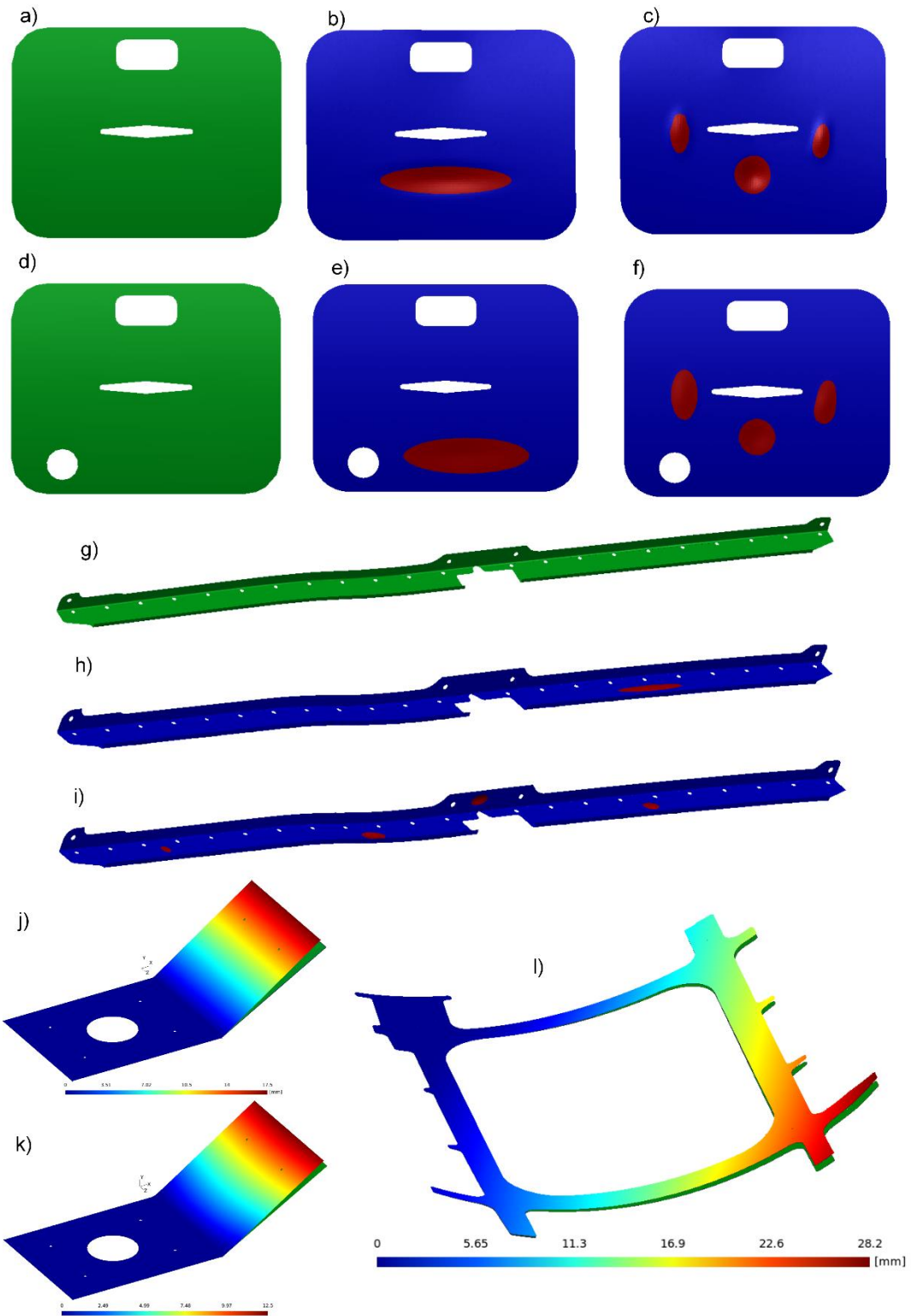


Figure 3-3: A summary of CAD and simulated scan models used in this thesis.

3.4.2 Automatic fixtureless CAI based on filtering corresponding sample points (Article 1)

Inspection of non-rigid parts is a time-consuming and costly challenge for industrial sectors. Applying inspection fixtures is sophisticated and requires human intervention. Industrial sectors demand developing fixtureless CAI methods, which perform the inspection in a free-state. Based on isometric deformation of non-rigid parts in a free-state, the *Generalized Numerical Inspection Fixture* (GNIF) method generate sample points that make links between the CAD and scan models. Using these sample points as boundary conditions (BCs) in a *FE Non-rigid Registration* (FENR) intend to deform the CAD model towards the scan model. This allows evaluating defects through a geometrical comparison between the scan model and deformed CAD model (after FENR). Corresponding sample points are evenly distributed over the CAD and scan models, and some of which are on defect areas. However, using sample points on defect areas via FENR results in an inaccurate evaluation of defects.

Chapter 4 of this thesis is devoted to developing an automated fixtureless CAI method based on filtering corresponding sample points, which are in defect areas, using curvature and von Mises stress criteria. Once the proposed sample points filtration method is applied, the accurate evaluation of defects on the scan model is achieved. The performance of this method is validated on two non-rigid parts that are commonly used in the aerospace industry. The link of this article to the subject of the thesis is that the developed fixtureless CAI allow an automatic and precise inspection compared to those that presented in literature review (section 2.4.2). In fact, the presented method is able to identify and inspect both small (local) and big (global) defects.

This article is published in *the international journal of advanced manufacturing technology, Springer-Verlag London Limited*.

S. Sattarpanah Karganroudi, J.-C. Cuillière, V. Francois, and S.-A. Tahan, "Automatic fixtureless inspection of non-rigid parts based on filtering registration points," The International Journal of Advanced Manufacturing Technology, pp. 1-26, 2016.

3.4.3 Validation and verification of our CAI method (Article 2)

Computational methods applied in different disciplines need to be verified and validated. To this end, the computational programming are verified to ensure the correctness of results with respect to computational coding. Moreover, the computational results are validated with reference to the actual ones. Unlike traditional qualitative validation methods, the developed *Verification and Validation* (V&V) methods set up a validation metric to compare quantitatively the computational and actual results. The ASME guide for V&V of computational solid mechanics (Hills and Trucano 1999) concludes that the predictive capability of a computational model is assessed by comparing its features of interest (validation metrics) with respect to the real model in its intended use. The robustness of numerical methods *versus* input noise is then evaluated using validation metrics. Uncertainties, numerical errors and scanning noise in CAI methods justify applying V&V approaches for assessing the robustness of CAI methods.

Chapter 5 of this thesis presents a new validation metric based on ASME recommendations to perform a quantitative and detailed validation for our fixtureless CAI method. This validation metric applies statistical tools to perform a detailed comparison between the estimated inspection results and nominal defects. The comparison is based on statistical distributions of cumulative distribution functions (CDFs) at a specific significance level. Along with the size (area and maximum amplitude) of defects, the newly developed validation metric assess the distribution of distances associated with the estimated defects with respect to the nominal ones. The link of this article to the subject of the thesis is that the presented validation metric is applied to assess the robustness of our developed fixtureless CAI for non-rigid parts.

This article is submitted in *the Journal of Verification, Validation and Uncertainty Quantification*, and it is under the process of review.

S. Sattarpanah Karganroudi, J.-C. Cuillière, V. Francois, and S.-A. Tahan, "Assessment of the robustness of a fixtureless inspection method for non-rigid parts based on a

verification and validation approach," *Journal of Verification, Validation and Uncertainty Quantification*.

3.4.4 Virtual inspection in assembly-state using permissible loads for deviated non-rigid parts (Article 3)

Industrial inspection techniques prove that some deviated non-rigid parts can be practically assembled under permissible assembly loads. In fact, the geometrical deviation of these parts (including defects) can be absorbed by the compliance of non-rigid parts. The inspection techniques introduce weights on the surface of parts which are constrained on physical fixtures. However, setting up sophisticated physical fixtures along with estimating proper weights by trial-and-error is time-consuming and costly. This manual and empirical process of applying weights to retrieve the functional shape of a deviated part is not efficient for large and complicated parts.

Inspired by the inspection technique, a fixtureless CAI is presented in Chapter 6 that aim at eliminating physical complex fixtures and performing a virtual inspection for deviated parts. The scan model of a geometrically deviated non-rigid part is acquired in a free-state. The proposed *Virtual Mounting Assembly-State Inspection* (VMASI) method then estimates the possibility of mounting the scan model on a virtual fixture in assembly-state under restraining loads. For those parts that can be put in a virtual fixture (assembly-state), their functional shapes are predicted by introducing the required assembly loads as boundary condition via FEA. The optimal distribution of required assembly loads is assessed using our developed *Restraining Pressures Optimization* (RPO) approach. RPO considers the required loads as a set of pressure introduced on the surface of scan mesh. The required pressures intend to deform the scan mesh through a linear FE-based transformation wherein the distance and orientation difference are minimized between tooling holes (e.g. mounting holes) on the predicted shape of scan model and on the CAD model. The final inspection is performed by evaluating the position of mounting holes on the functional shape of scan model with respect to the holes of the CAD model. The part is acceptable for pursuing forward for assembly stage if the holes on the predicted shape

of scan model in assembly-state remain in the range of dedicated tolerance with respect to the CAD model. The link of this article to the subject of the thesis is that VMASI method allows a fixtureless inspection for deviated parts diminishing the inspection cost.

This article is submitted in *Computer-Aided Design*, and it is under the process of review.

S. Sattarpanah Karganroudi, J.-C. Cuillière, V. Francois, and S.-A. Tahan, "Fixtureless inspection of non-rigid parts based on virtual mounting in an assembly-state using permissible loads," Computer-Aided Design.

CHAPTER 4 AUTOMATIC FIXTURELESS INSPECTION OF NON-RIGID PARTS BASED ON FILTERING REGISTRATION POINTS

Sasan Sattarpanah Karganroudi¹, Jean-Christophe Cuillière¹, Vincent Francois¹,
Souheil-Antoine Tahan²

¹Équipe de Recherche en Intégration Cao-CALcul (ÉRICCA), Université du Québec à Trois-
Rivières, Trois-Rivières, Québec, Canada

²Laboratoire d'ingénierie des produits, procédés et systèmes (LIPPS), École de Technologie
Supérieure, Montréal, Québec, Canada

4.1 Abstract

Computer-aided inspection (CAI) of non-rigid parts significantly contributes to improving performance of products, reducing assembly time and decreasing production costs. CAI methods use scanners to measure point clouds on parts and compare them with the nominal *Computer-Aided Design* (CAD) model. Due to the compliance of non-rigid parts and for inspection in supplier and client facilities, two sets of sophisticated and expensive dedicated fixtures are usually required to compensate for the deformation of these parts during inspection. CAI methods for fixtureless inspection of non-rigid parts aim at scanning these parts in a free-state for which, one of the main challenges is to distinguish between possible geometric deviation (defects) and flexible deformation associated with free-state. In this work the *Generalized Numerical Inspection Fixture* (GNIF) method is applied to generate a prior set of corresponding sample points between CAD and scanned models. These points are used to deform the CAD model to the scanned model via finite element non-rigid registration. Then defects are identified by comparing the deformed CAD model with the scanned model. The fact that some sample points can be located close to defects, results in an inaccurate estimation of these defects. In this paper a method is introduced to automatically filter out sample points that are close to defects. This method is based on curvature and von Mises stress. Once filtered, remaining sample points are used in a new registration, which allows identifying and quantifying defects more accurately. The proposed method is validated on aerospace parts.

Keywords: Geometric inspection, non-rigid parts, GNIF, fixtureless inspection, principal curvatures, von Mises stress.

4.2 Introduction

In many industrial sectors, an increasing need for product quality requires respecting smaller and smaller tolerances, which can be obtained by setting up accurate *Geometric Dimensioning and Tolerancing* (GD&T). Although developments at automating production processes enable manufacturing companies towards mass production with shorter delays, quality control is often time-consuming and usually requires significant human intervention. Geometric dimensioning and tolerancing standards such as ASME Y14.5 and ISO-GPS affirm that inspection of manufactured parts must be carried out in a free-state condition unless otherwise specified. Exemptions to this rule are given in ISO-10579 and ASME Y14.5 (2009) for non-rigid parts. Indeed, in several industrial sectors, such as the aerospace and automotive industries, many manufactured parts are designed and used with a very small thickness with respect to the other dimensions. The problem with these non-rigid (flexible) parts is that they are likely to deform, in a free-state, in such a way that the order of magnitude of part deformation may be equal if compared to the part defects itself. For these parts, free-state deformation mainly occurs due to gravity effects (the own weight of the part) or to residual stresses. In [1] the compliance of a part is defined as the ratio between an applied force and the induced deformation in the part. Based on this definition, manufactured parts are classified in three categories as rigid, non-rigid and extremely non-rigid parts. In this classification, a part is considered as a non-rigid part if the deformation induced by a reasonable force (around 40 N) is over 10% of the assigned tolerance. In Figure 4-1-a, a non-rigid aerospace panel in a free-state deformation due to its compliance is well illustrated.

Consequently, in common inspection methods, as described in [2], dedicated holding fixtures are designed and used to compensate for the flexible deformation of non-rigid parts during inspection. However, these dedicated fixtures are very sophisticated and very expensive to set up in most cases. Thus, in general, geometric inspection of non-rigid

manufactured parts is a significant problem since it is expensive and since it takes a large part of production lead-time. For example, some inspection setup for non-rigid parts in aerospace industry requires 60 to 75 hours of operation for setting up one fixture [3]. Meanwhile, a second identical set of fixtures is often required for repeating the inspection at the customer's facility. In Figure 4-1-b, the part introduced in Figure 4-1-a in a free-state is shown as constrained on such a fixture set.

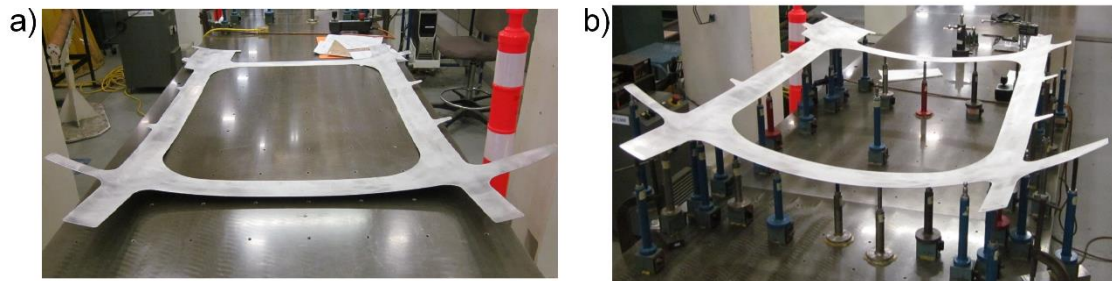


Figure 4-1: An aerospace panel, a) in free-state, b) constrained on its inspection fixture [4].

Beholden to the improvements in computer graphics and optic scanners, manual and tactile methods of measurement and inspection have progressively been replaced by *Computer-Aided Inspection* (CAI) methods. CAI methods are noteworthy due to the ability of automating all the inspection process which speeds up and increases the accuracy of inspection by eliminating human intervention and its inseparable error. To evaluate the surface profile of a part, a point cloud measured on part surfaces is compared with the *Computer-Aided Design* (CAD) model. These measurements are performed with two types of geometry acquisition tools: contact and non-contact devices. A review on measuring methods in free-state is presented in [5] and a specific focus is put on using laser scanners in [6]. For non-rigid parts, since Coordinate Measuring Machines (CMM) technology acquires points on the part by means of a probe, which can disturb its geometry due to contact with the probe, using non-contact measurements, such as laser scanners is more appropriate to acquire point cloud of surfaces in a free-state as shown in Figure 4-2.

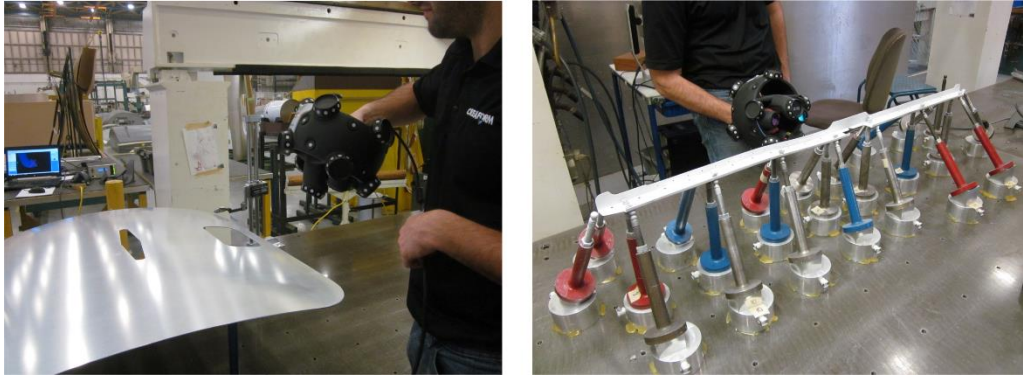


Figure 4-2: Surface data acquisition by a handy scanner.

In CAI, as mentioned above, a point cloud measured on the part surface is compared with the CAD model of this part. The objective is assessing the deviation of these points from the CAD model and comparing it with the tolerances as specified. One of the problems in CAI is that the CAD model is defined in a coordinate system that is not necessarily the same as the coordinate system associated with measured points. Of course, comparison between CAD and scanned models has to be performed in the same coordinate system and in the same state of elastic deformation. As introduced before, measuring non-rigid manufactured parts in a dedicated inspection fixture can solve these problems but, since inspection fixtures such as conformation jigs are costly and time consuming, setting up fixtureless inspections based on CAI methods is foreseen. In these fixtureless inspection methods the non-rigid part is measured in a free-state, and an optimal transformation between the CAD model and the acquired point cloud is computed. For rigid parts, this transformation can be represented by a rigid transformation matrix. For non-rigid parts, finding this transformation is much more difficult since it combines location and orientation along with elastic deformation. This process of finding the best transformation before comparing scan and CAD data is referred to as *registration*. Registration methods have been widely studied for rigid parts and several methods have been proposed [5, 7]. Among these methods, the *Iterative Closest Point (ICP)* algorithm [8] has been very popular and a source of many adaptations and enhancements for application in various domains (inspection, shape recognition, 3D modeling, robotics, etc.), which makes it an efficient and robust rigid registration method. As introduced above, non-rigid registration

(registration for non-rigid parts) is much more complex since it combines searching for a rigid transformation matrix along with a displacement field. As presented in the next section, a few non-rigid registration methods have been proposed in the literature [3, 9-23]. Basically, these methods try to find the best correspondence between CAD and scan data either by deforming CAD geometry to scan geometry or by deforming scan geometry to CAD geometry.

In general, the main problem is that, the non-rigid registration process is influenced by defects themselves, which are of course not known a priori. Consequently, strategies need to be applied towards reducing, as much as possible, the influence of defects on the non-rigid registration process and, by the way, towards improving the accuracy and efficiency of CAI for non-rigid parts. This paper is focused on this specific objective.

The paper is organized as follows. Section 4.3 presents a literature review of fixtureless CAI methods for non-rigid parts. It is followed, in section 4.4, by a description of the proposed approach towards reducing the influence of defects on the non-rigid registration process in the context of CAI methods for non-rigid parts. This approach is principally based on filtering sample points used in non-rigid registration. Validation of the approach is then presented on two non-rigid aerospace parts in section 4.5. The paper ends with a conclusion and ideas for future works on this issue in section 4.6.

4.3 Literature review

Fixtureless inspection methods of non-rigid parts has been developed relying on numerical approaches to compare the shape of measured parts (represented by scanned point clouds) in a free-state with their nominal CAD model. In order to be able to compensate for flexible deformation of non-rigid parts in a free-state and evaluate the geometrical variation of manufactured parts, either the CAD model is deformed to take on the shape of the scanned model or vice versa. For example, in [9-12] a numerical fixture was proposed to virtually constrain the scanned flexible part into its functional shape. On the contrary, methods proposed in [3, 13-23] are based on numerically

deforming the CAD nominal geometry according to the flexible deformation of the measured non-rigid part in a free-state.

The proposed method in [9] begins with acquiring the scanned model of a non-rigid part that is constrained in a reference state. This state does not need to represent the functional state of the part. This scan data in the reference state is used with a first FEA simulation to generate the shape of the part in a completely free-state (free from any external forces). From this intermediate result, a virtual functional state of the part is obtained through a second FEA simulation. This virtual functional state is finally compared with the CAD specification for metrology.

In [10, 11], the *virtual fixation* concept is introduced. It consists in generating a FE model from scanned point cloud in free-state and in identifying, on the scanned part, features such as mounting holes to identify fixation points on the scanned model. Then, this information about the location of nominal fixation points is used to apply displacement boundary conditions to the scanned model, which replicates deforming it to its virtually simulated inspection fixture. However, generating a FE mesh from scanned part requires a time consuming processing on point cloud, which cannot be automated since each measured part needs an individual mesh.

Concerning the automatic FE mesh generating from the CAD model of the part instead of its scanned model, the *virtual reverse deformation* method is introduced in [13] wherein the CAD mesh is deformed to conform to the scanned model of the non-rigid part in a free-state. In this approach, it is done by imposing boundary conditions on the nominal fixation points in the CAD model and displacing these points to the corresponding fixation points in the scanned model, which have been previously identified using feature extraction.

The method proposed in [15] is similar to the virtual reverse deformation method but, in this approach, *Radial Basis Functions* (RBFs) are used to minimize the FE mesh density. This allows accurately predicting the behavior of the part at a lower computational cost. Meanwhile, in [16, 17] fixtureless inspection is performed by using only partial views of

regions that need to be inspected. This is done by applying an interpolation technique, based on RBFs, to estimate an approximate location of the missing fixation points.

In [18] the *Generalized Numerical Inspection Fixture* (GNIF), see Appendix A, is presented. This registration method is based on the assumption that, for non-rigid parts, the deformation is isometric, which means that the inter-point shortest path (geodesic distance) between any two points on a part remains unchanged during the isometric deformation. In the GNIF method, CAD and scanned models are considered as geodesic distance metric spaces, and the similarity between them is estimated by finding the associated minimum distortion between the metrics. In this approach, discrete geodesic distances for both CAD and scanned models are calculated, from their meshes, using the *fast marching method* [24]. In the GNIF method, *Generalized Multidimensional Scaling* (GMDS) [25] minimizes the distortion between the metrics associated with CAD and scanned models. The GNIF method automatically finds corresponding sample points on the faces of CAD and scanned models. The corresponding sample points associated with assembly features are then used for computing the non-rigid registration. Indeed, these corresponding sample points between the two models are used as displacement boundary conditions in a FEA simulation that is applied to deform the CAD model towards the shape of scan data. This process is referred to as *Finite Element Non-rigid Registration* (FENR). If no information is available about the assembly process, then the sample points on boundaries of model (assuming boundaries are perfect with no defects on them) or assured sample points with negligible deformations such as rigid attachment are used in FENR. GNIF is improved in [3] as a more general and robust approach referred to as *Robust generalized Numerical Inspection Fixture* (RNIF). RNIF is based on filtering out sample points causing incoherent geodesic distances. This enhancement enables handling parts with missing range data on surfaces. Meanwhile, the robust GNIF method proposes using *distance-preserving NonLinear Dimensionality Reduction methods* (NLDR) to enhance the inspection process for parts with large deformations. Then in [26] a review and systematic comparison between NLDR methods are presented in order to evaluate their performance for applications in the metrology of flexible parts.

In [19-22] the *Iterative Displacement Inspection* (IDI) algorithm is presented along with associated identification methods. By contrast with the methods presented previously, IDI identification concepts are not based on FEA. IDI iteratively deforms the mesh of the CAD model until it matches the shape of scan data. In the IDI algorithm, a specific identification process allows distinguishing flexible deformation from eventual defects on the scanned model surface. Thus, the CAD mesh is smoothly deformed to the scanned shape, except for defects. An improvement of the identification method is proposed in [20] on which the location of points in a measured point cloud is studied statistically to detect defects as outliers with respect to the mean location of neighbor points in the point cloud. This enhancement consists in automatically setting an identification threshold by applying the maximum-normed residual test which is a statistical test to detect outliers in a point cloud.

In [23] another defect identification approach is presented. This approach is based on curvature estimation and *Thomson statistical test* to identify defects on manufactured parts. This method starts with estimating difference in principal curvatures between the measured point cloud and the nominal CAD model. Then, applying a statistical method (*Thomson* technique) the suspected outliers of estimated curvature values can be identified and detected as defects. The accuracy of inspections based on IDI method strictly depends on its defect identification algorithm, which can only identify localized defects. On the one hand, IDI method cannot evaluate defects distributed in a global manner over a non-rigid part. Meanwhile, the presented identification approach in [23] is not able to identify defects on complex geometry of non-rigid parts by applying solely a threshold for estimated curvature difference. On the other hand, in the above mentioned non-rigid registration methods using FEA for registration, the foreknown assembly information of non-rigid parts are required to specify the location of imposed boundary conditions in FENR.

In the approach presented along the following sections, the location and parameters of boundary conditions used in the non-rigid registration is automatic. Indeed, an initial set of corresponding points between CAD and scanned geometry is automatically filtered to

improve FENR, which brings about a better accuracy in the detection of defects on non-rigid parts.

4.4 Methodology and implementation

4.4.1 Description of the proposed methodology

In this paper, the *Generalized Numerical Inspection Fixture* (GNIF) [18] method is first applied as non-rigid registration method to find an initial set of corresponding points between nominal CAD and scan data in a free-state. Indeed, based on the isometric deformation assumption, GNIF generates two lists (one on the CAD model and another one on the scanned model) of estimated corresponding sample points. Then, these two lists of corresponding sample points are used to deform the CAD model to the scan data via FENR. Since these corresponding sample points are evenly distributed over both models, some of these points can be located close to defects. This results in an inaccurate estimation of the size of these defects. We have shown in a previous preliminary work [27] that filtering sample points that are close to defects in the FENR reduces this inaccuracy. The problem is that these defects are not known a priori. The proposed approach features two stages in filtering these sample points: curvature comparisons and von Mises stress calculations.

The approach proposed in this paper is described using a typical non-rigid aluminum panel used in the aerospace industry (as illustrated in Figure 4-3, dimensions are 1100 mm by 860 mm with 1 mm thickness). The CAD model is shown in Figure 4-4-a, and the associated simulated scanned model for inspection in a free-state in Figure 4-4-c. This scan data includes three bump defects. The nominal size of these defects is known a priori so that the size of defects as identified can be compared with the nominal size. The *maximum amplitude* of a given defect is defined as the distance between the deformed CAD (after non-rigid registration) and scan data at the tip (or valley) of this defect. The *area of a given defect* is defined as the area that exceeds the tolerance value, as specified on the drawing. For all validation cases presented, we considered 0.4 mm as a

representative specified tolerance value. Top views of models as shown in Figure 4-4-b and d, clearly show free-state deformation of scan data.

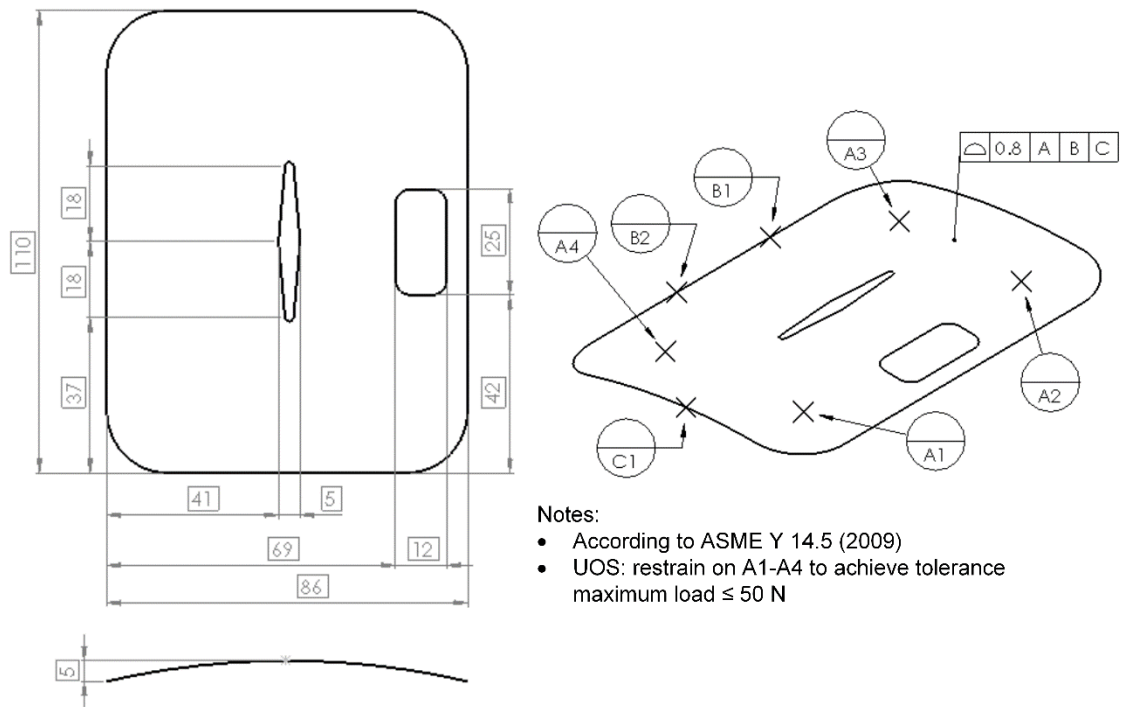


Figure 4-3: CAD model along with GD&T specification for part A (dimensions are in mm).

A pre-registration, based on the ICP algorithm [8], is followed by generating GNIF sample points on both models as shown in Figure 4-5. These corresponding sample points are then used to impose displacement boundary conditions to deform the CAD model to the scanned model through *Finite Element Non-rigid Registration* (FENR).

Since GNIF CAD sample points are not exactly located on nodes of the CAD triangulation, local modifications are performed on this triangulation before applying FENR. As shown in Figure 4-6, this is performed using a classical Delaunay point insertion method [28].

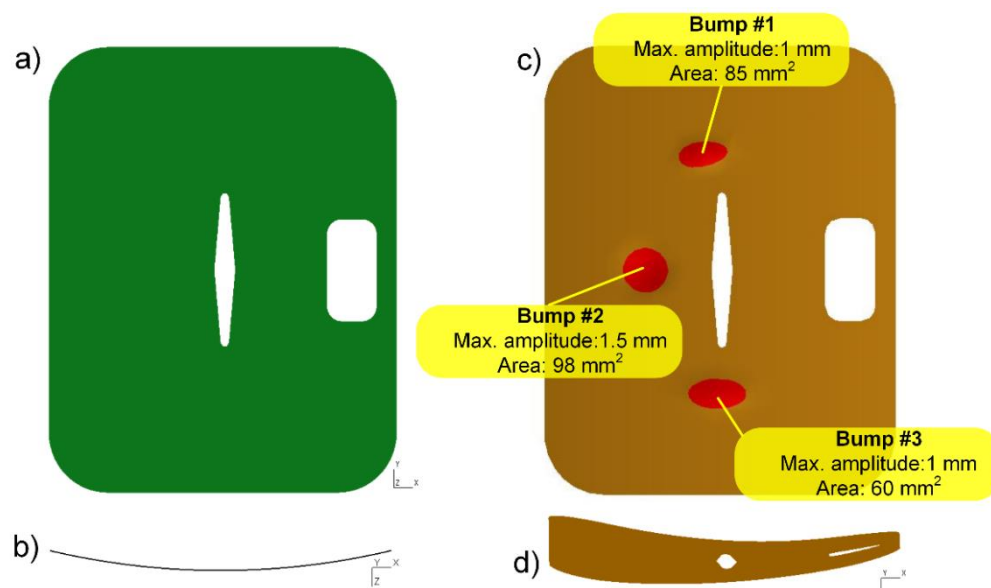


Figure 4-4: A non-rigid aluminum panel a) front view of the CAD model b) top view of the CAD model c) front view of the scanned part in a free-state d) top view of the scanned part in a free-state.

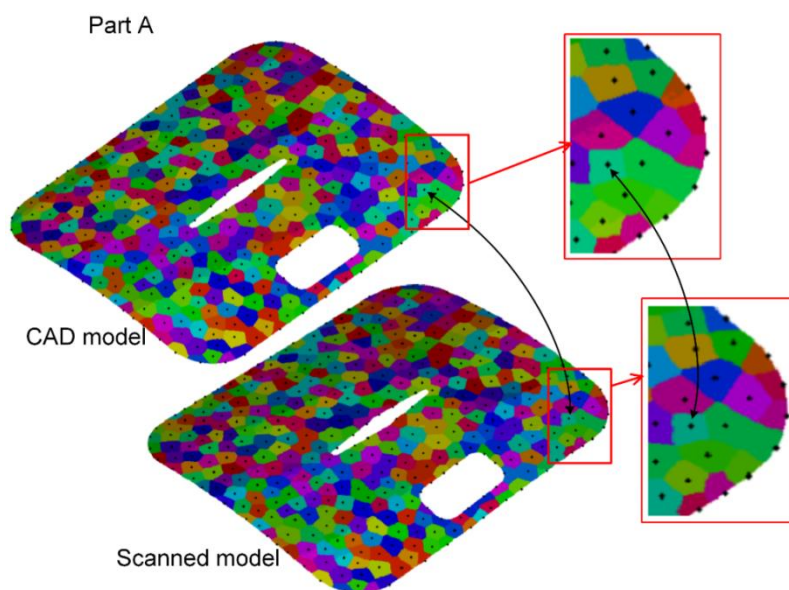


Figure 4-5: GNIF corresponding sample points (in black) are located in the center of colored zones on CAD and scanned models.



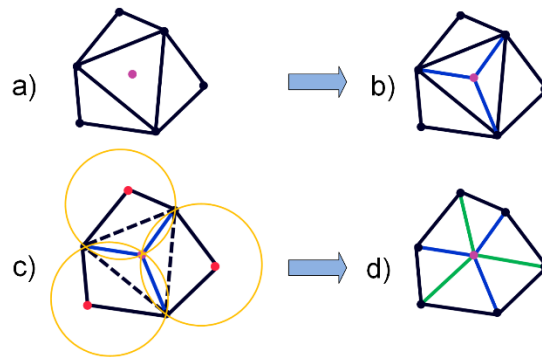


Figure 4-6: a) The purple point presents a GNIF sample point to be inserted b) the sample point is inserted into the mesh by incremental Delaunay triangulation c) Testing the empty sphere criterion d) swap diagonal operator.

For the sample part introduced in Figure 4-4, red spots in Figure 4-7-a represent GNIF sample points after insertion into the CAD mesh. As introduced above, FENR is based on imposing displacement boundary conditions on these sample points to deform the CAD mesh to the shape of scan data. The displacement distribution associated with FENR is shown in Figure 4-7-b. As shown in Figure 4-7-a, some of the corresponding sample points on the CAD mesh are located close to defects and/or on defects. These sample points tend to bring the deformed CAD model to the shape of defects in the scanned model, which is a source of error in assessing size and location of these defects. This is well illustrated in Figure 4-7-c, where the distribution of distance between deformed CAD and scan data is illustrated, and also in Figure 4-7-d, where the estimation of defects' area is depicted. Indeed, the size of the 3 defects is under-estimated, due to the fact that some of the sample points used in FENR are close to these defects.

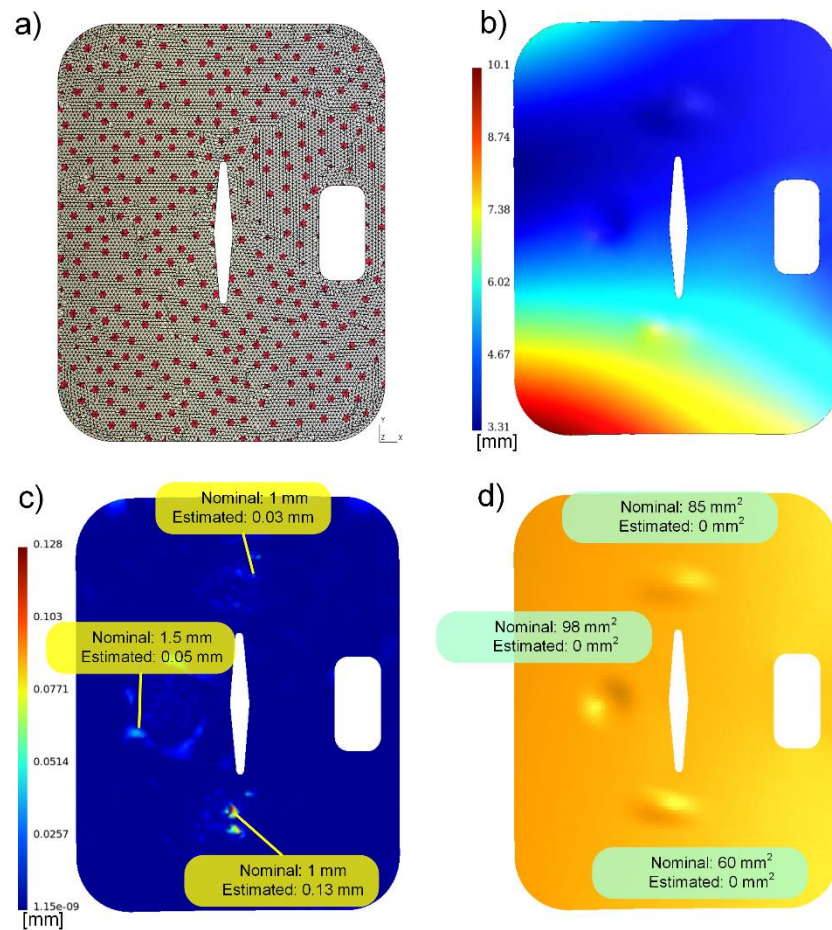


Figure 4-7: a) GNIF sample points on the CAD model represented as red spots b) displacement distribution [mm] after FENR based on using all GNIF sample points c) comparison between estimated and nominal size of defects [mm] when using all GNIF sample points d) estimating the area of defects [mm²].

This result shows that, to avoid deforming the CAD model around defects, the sample points that are located close to these defects should be filtered out. The problem is that these defects are not known a priori. Therefore, as shown in Figure 4-8, these sample points are filtered after applying a first FENR through the following two steps:

- GNIF sample points filtering based on a local curvature criterion.
- GNIF sample points filtering based on a von Mises stress criterion.

The first filtering step is based on locally comparing principal curvatures of the CAD model before deformation with principle curvatures of the CAD model after FENR (after deformation). This is done at the location of all sample points and it allows a first rough assessment of defects. Indeed, the obtained deformed CAD model using all sample points is almost similar to the shape of scanned model including the defects. Since the flexible deformation of a non-rigid part has a smoother curvature comparing to a defect such as a bump, studying the difference of each principal curvatures between the CAD before and after deformation allows roughly assessing defects. Discrete principal curvatures $K_1(p)$ and $K_2(p)$ are calculated and compared between the two triangulations (CAD and deformed CAD) using:

$$K_1(p) = K_H(p) + \sqrt{K_H^2(p) - K_G(p)} \quad 4-1$$

$$K_2(p) = K_H(p) - \sqrt{K_H^2(p) - K_G(p)} \quad 4-2$$

Where K_H is the mean curvature and K_G is the Gaussian curvature, which are calculated as discrete curvatures using the Gauss-Bonnet scheme [29].

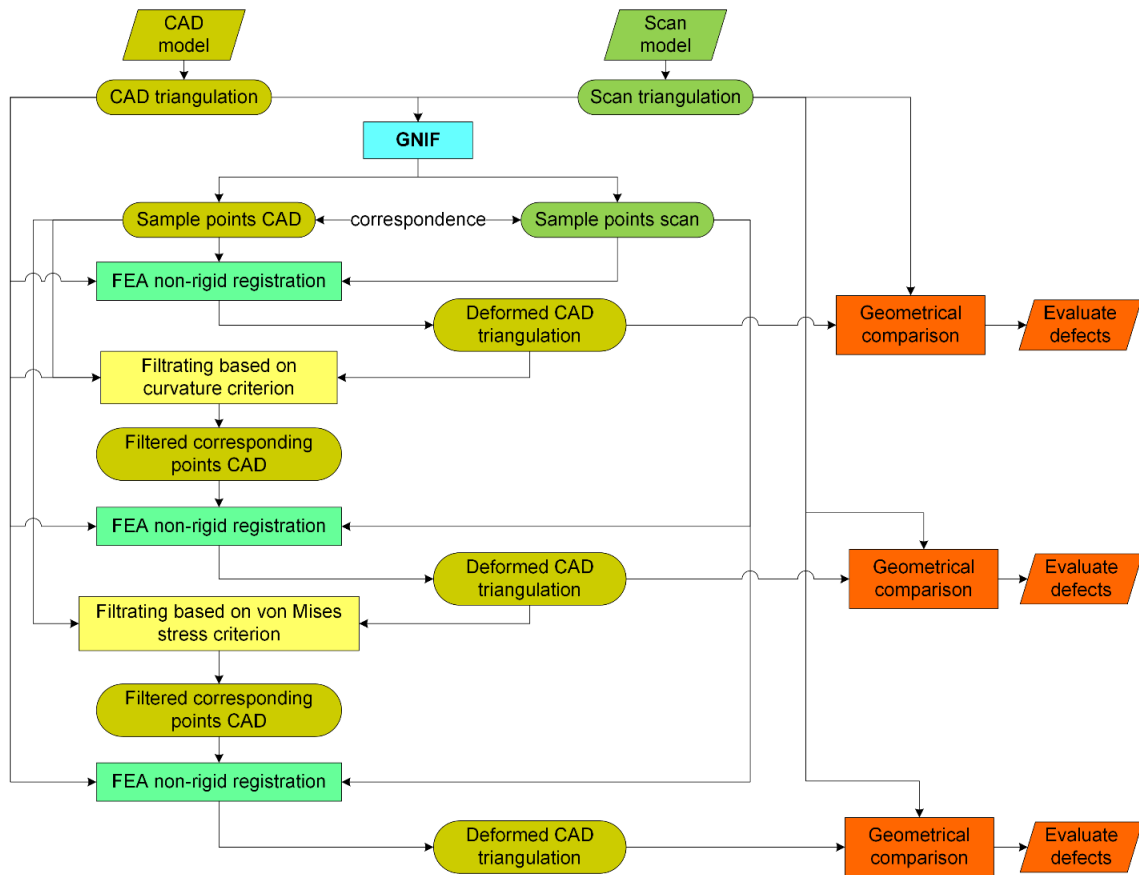


Figure 4-8: Schematic diagram of the proposed sample point filtration method.

Note that, since the criterion is based on the difference between curvature distributions and not on the curvature distribution itself, high curvature zones do not cause problems in the process. In section 4.5.3, the part used (referred to as part B) for validation results features such high curvature zones and results obtained support this statement. Distributions of the difference in discrete principal curvatures between CAD and deformed CAD triangulations, are shown in Figure 4-9-a and Figure 4-9-b. It clearly shows that areas exceeding a threshold values on these differences represent a rough estimate of defects. The maximum and minimum threshold values of the difference in principal curvatures used are -0.05 and $+0.05 \text{ mm}^{-1}$. Note that the color scale used in Figure 4-9-a and Figure 4-9-b is limited to these maximum and minimum threshold values. This allows identifying defect zones (defect tip and contour) in blue and red for maximum curvature (K_1) in Figure 4-9-a, and minimum curvature (K_2) in Figure 4-9-b.

Threshold values used are determined based on the mean value of curvature differences, which enables detecting defects as outliers. Based on these threshold, sample points can be filtered inside a radius (3 times the average mesh size ≈ 3 mm here) around sample points that have been identified as close to the defects, as shown in Figure 4-9-c. In Figure 4-9-c and other similar figures along the paper, filtered sample points are represented as blue spots while red spots represent sample points that remain after filtering and that will be used in the next step. It appears in Figure 4-9-c that a few sample points that are not located around defects are also filtered based on this curvature criterion. This is due to local effects introduced by bad mesh quality and noise in the calculation of discrete principal curvatures. However, since a large number of sample points is used (400 points here), FENR is not significantly affected by these over-filtered sample points. Then, a second FENR is applied, using sample points remaining, which leads to a new distribution of distances between deformed CAD and scan data (see Figure 4-9-d). If compared to the results shown in Figure 4-7-c and d, results presented in Figure 4-9-d and e clearly show that the maximum amplitude and area of defects are better estimated from this new registration.

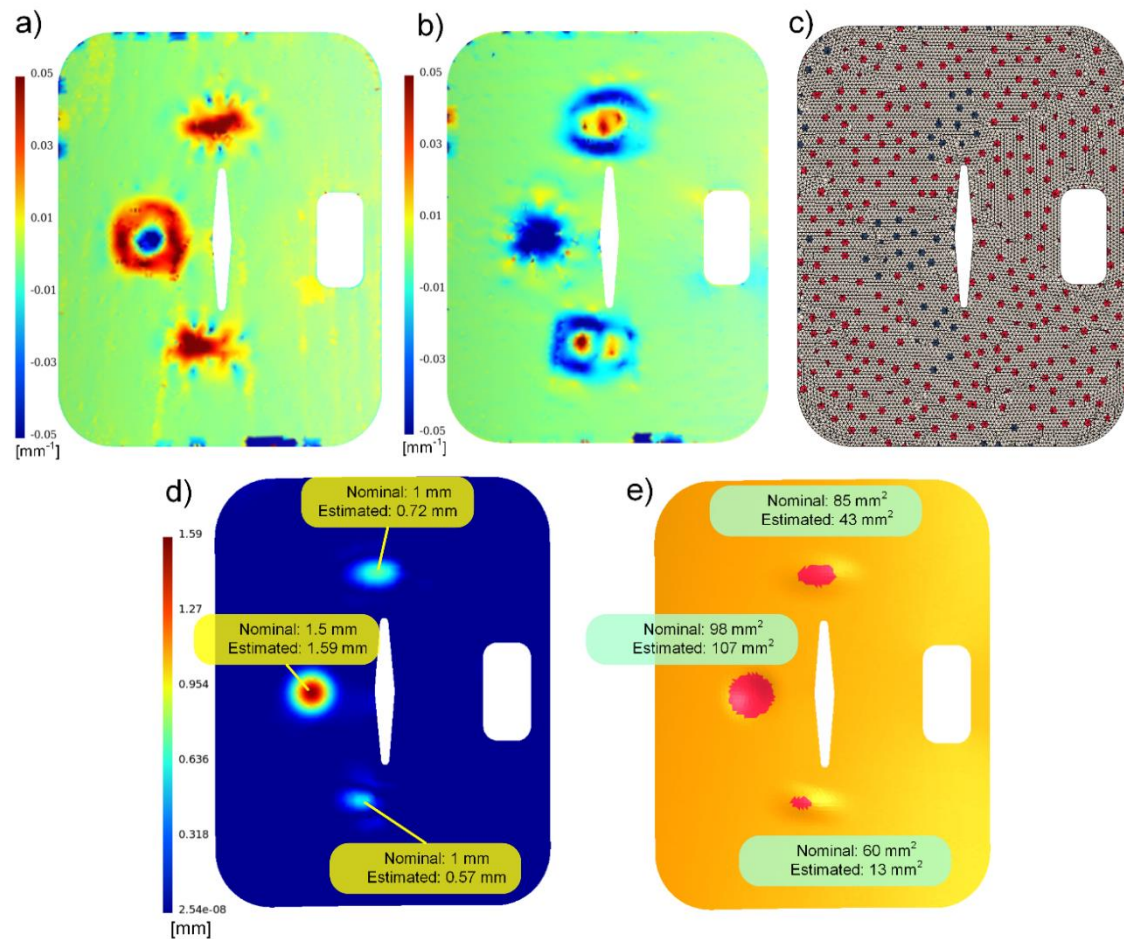


Figure 4-9: a) distribution of the difference in maximum curvature (K_1) [mm^{-1}] b) distribution of the difference in minimum curvature (K_2) [mm^{-1}] c) sample points filtered using the curvature criterion (represented as blue spots) d) comparison between estimated and nominal size of defects [mm] when using sample points after filtering based on the curvature criterion e) estimating the area of defects [mm^2].

As introduced above, a second filter is applied on the remaining sample points. This second filtering step is based on analyzing von Mises stress results (see Figure 4-10-a) associated with the second FENR. Two conclusions can be made when thoroughly analyzing this von Mises stress distribution:

- von Mises stress is quite high everywhere (the minimum value equals 23.7 MPa), which may seem surprising: this phenomenon is due to the inherent error caused

by calculating geodesic distances with the *Fast Marching Algorithm* (FMA) [24]. Indeed, it is common knowledge that fast marching introduces a bias in the calculation of geodesic distances. We quantified this bias using a shape with similar dimensions for which exact geodesic distances were known and we found that this bias can reach around 1 mm for some sample points. A 1 mm in-plane distance error causes a very high in-plane strain when applying FENR at this location and consequently a very high in-plane stress. This amplitude in geodesic distance error explains the amplitude background von Mises stress noise in Figure 4-10-a.

- Despite this background von Mises stress noise, remaining sample points that are close to defects feature even higher von Mises stress. This allows filtering a second set of sample points based on this von Mises stress distribution (the first set being filtered based on the curvature criterion).

This second filtering step is based on applying a threshold on the von Mises stress distribution as illustrated in Figure 4-10-a (the threshold is 1000 MPa in this case). This von Mises stress threshold value is also defined based on the mean value of von Mises stress over the part. Based on this second criterion, new sample points are filtered inside a radius (again 3 times the average mesh size) around sample points that have been identified as close to defects. Blue spots in Figure 4-10-b illustrate sample points that have been filtered once applied these two consecutive filters. Figure 4-10-b can be compared with Figure 4-9-c to evaluate how many new sample points have been filtered and where. Finally, a third FENR is applied, using sample points remaining after applying the two filters, which leads to a third distribution of distances between deformed CAD and scan data along with defects estimation (see Figure 4-10-c and d). If compared to results shown in Figure 4-7-c and d as well as Figure 4-9-d and e, results presented in Figure 4-10-c and d shows that the size of defects is even better estimated after this last registration.

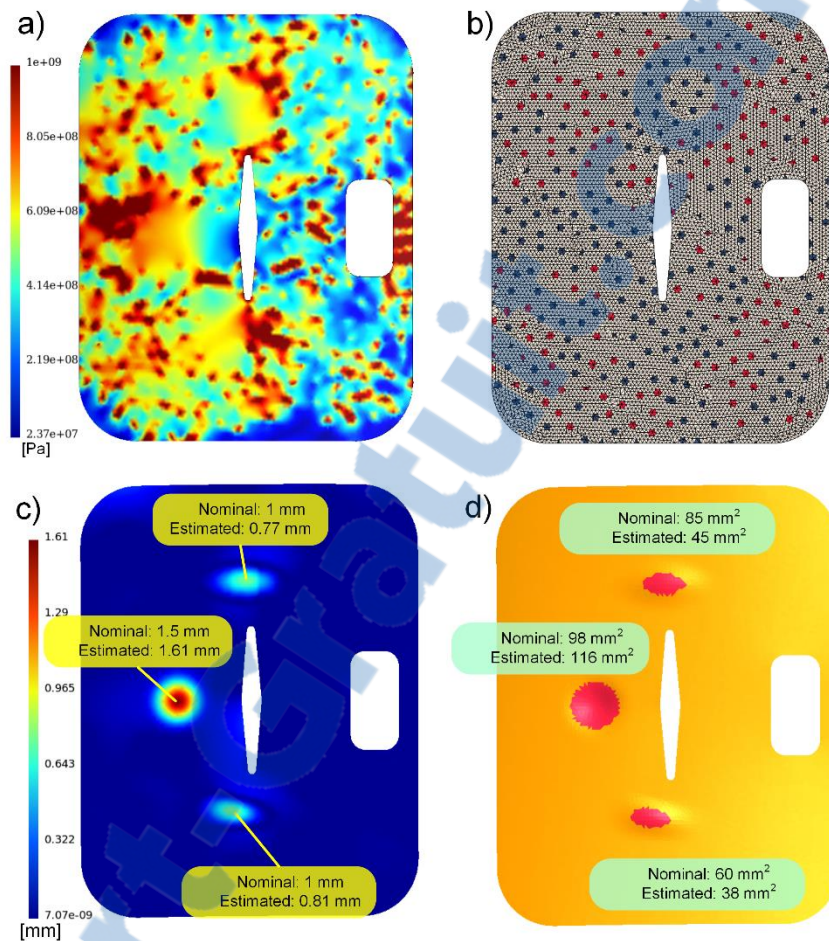


Figure 4-10: a) distribution of von Mises stress [Pa] after FENR when using GNIF sample points after filtering based on the curvature criterion b) sample points filtered using both curvature and von Mises stress criteria (represented as blue spots) c) comparison between estimated and nominal size of defects [mm] when using GNIF sample points after filtering based on both curvature and von Mises stress criteria d) estimating the area of defects [mm²].

The estimated size of defects and the associated error with respect to the nominal size of defects are summarized in Table 4-1 for this part. A comparison is presented between errors on the maximum amplitude and area of defects before and after applying the two filters. The average error on the maximum amplitude of defects for the three bumps is 94% before filtering, 26% after applying the first filter and 16% after applying both filters

while the average error on area estimation is 100%, 46% and 34% respectively. Thus, the outcome of filtering is a global improvement in the results about estimating the size of defects. Although the error for bump #2 (as identified in Figure 4-4-c) after filtering based on both criteria is slightly higher than the error based on applying the curvature criterion only, the average error for the three defects is globally decreased by applying both criteria.

As illustrated in Figure 4-11 results obtained on different types of defects show that in some cases, the second filter does not eliminate many sample points, which makes that estimated errors before and after applying this second filter may not be very different. It also appears that, in some cases, this second filter slightly degrades the estimation. This degradation is related to the fact that some sample points may be filtered, based on von Mises stress, due to GNIF local inaccuracies and not due to the presence of defects. However, this second filter globally improves the estimation since, for bigger defects (see the second case in Figure 4-11) the flat shape on top of this type of defects makes that there is no difference in principal curvatures and that some sample points are not filtered based on the curvature criterion. As shown in the figure, these remaining sample points are filtered based on von Mises stress criterion since bringing these sample points to the shape of defect through FENR induces a local stress increase. Thus, applying these two filters successively represents the best compromise for successfully handling different types of defects.

Table 4-1: Estimated size of defects and errors based on curvature and von Mises criteria for Part A with small (local) defects and bending deformation.

	Maximum amplitude of defects			Area of defects		
	Nominal [mm]	Estimated [mm]	Error [%]	Nominal [mm ²]	Estimated [mm ²]	Error [%]
Using all sample points	1	0.03	97	85	0	100
	1.5	0.05	97	98	0	100
	1	0.13	87	60	0	100
Filtering sample points with the curvature criterion only	1	0.72	28	85	43	49
	1.5	1.59	6	98	107	9
	1	0.57	43	60	13	78
Filtering sample points with the curvature and von Mises stress criteria successively	1	0.77	23	85	45	47
	1.5	1.61	7	98	116	18
	1	0.81	19	60	38	37

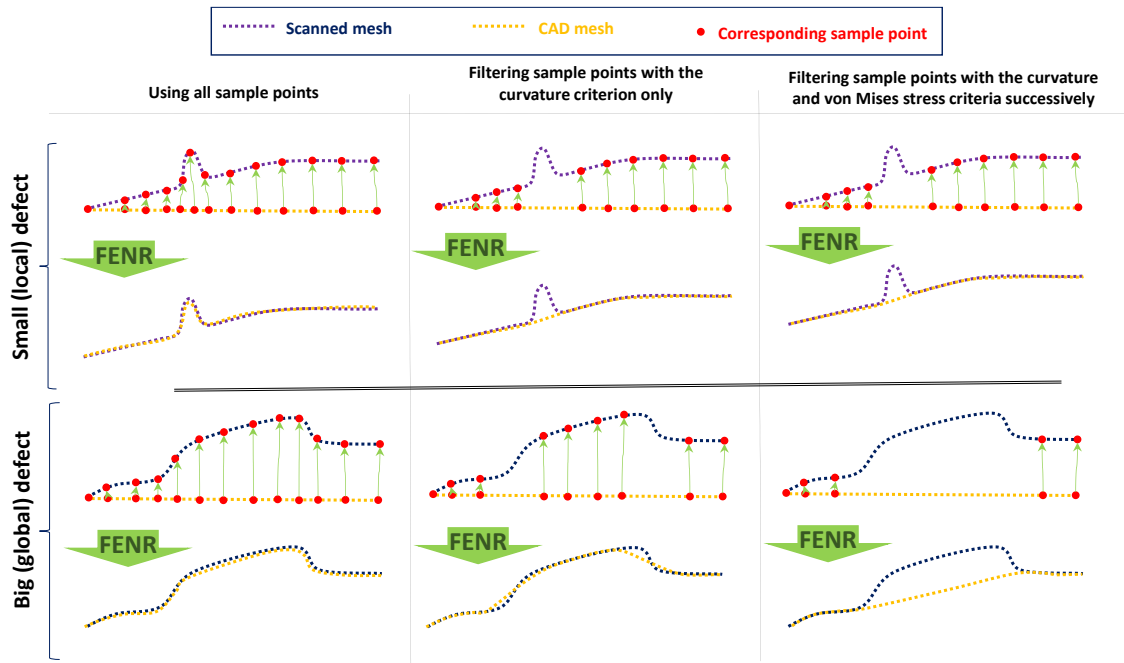


Figure 4-11: Interest of using the two filters successively.

4.4.2 Implementation

The implementation of this methodology uses several tools. GNIF calculations for generating sets of corresponding sample points are carried out using a MATLABTM code. This code takes approximately 8 minutes for generating 400 corresponding sample points on a computer with Intel^(R) CoreTM i7 at 3.60 GHz with 32 GB RAM. Mesh generation, mesh transformations, discrete curvature calculations, FENR and distance calculations between deformed CAD and scan models is done using our research platform [30]. This platform is based on C⁺⁺ code, on Open CASCADETM libraries and on Code_AsterTM as FEA solver. We also use GmshTM [31] for visualizing 3D models and distributions (discrete curvature, stress, distance). In general, filtering sample points with the two criteria approximately takes 2 minutes (for a CAD mesh with 10 000 nodes) on a computer with specifications as mentioned above. It should finally be underlined that, since this methodology is based on fast marching, FEA and discrete curvature

calculations, final results are quite sensitive to mesh size and mesh quality, both for CAD and scan data.

4.4.3 Validation on a case with no defects

In this section, our methodology is applied to a case that does not feature any defect. Thus, the only difference between CAD and scan models is due to free-state deformation. This validation aims at verifying that the proposed method has no bias and that no defects are detected. The same model as presented in section 4.4.1 is used here. GNIF sample points are shown in Figure 4-12-a and the result of the first FENR (without filtering applied) in Figure 4-12-b. The distribution of difference in discrete principal curvatures is in Figure 4-13-a and b. Sample points that are filtered based on curvature are shown by blue spots in Figure 4-13-c and the resulting second FENR in Figure 4-13-d.

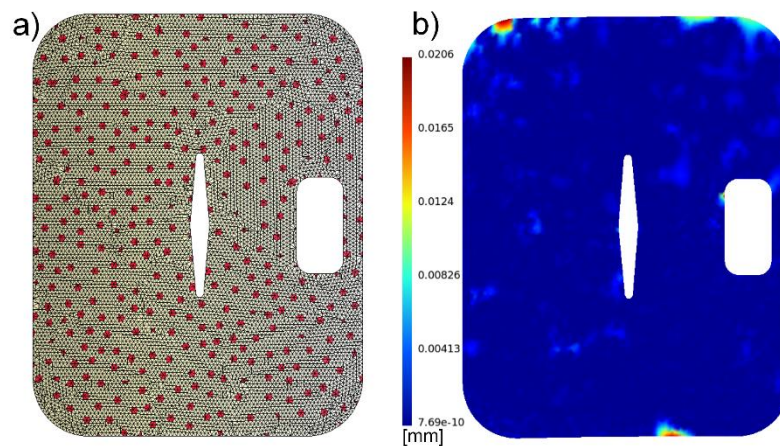


Figure 4-12: a) GNIF sample points on the CAD model represented as red spots b) comparison between deformed CAD and scanned models when using all GNIF sample points [mm].

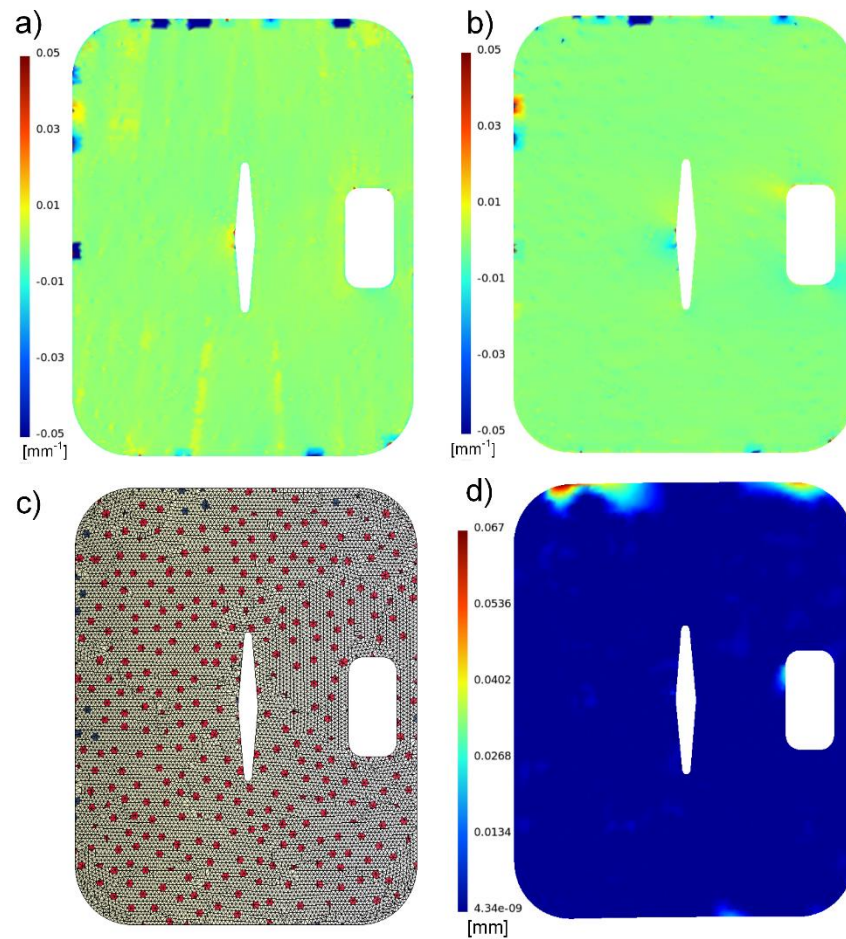


Figure 4-13: a) distribution of the difference in maximum curvature (K_1) [mm^{-1}] b) distribution of the difference in minimum curvature (K_2) [mm^{-1}] c) sample points filtered using the curvature criterion (represented as blue spots) d) comparison between deformed CAD and scanned models when using GNIF sample points after filtering based on the curvature criterion [mm].

In Figure 4-14-a, the distribution of von Mises stress after this second FENR is depicted. As introduced in section 4.4.1, although there are no defects in this case, the mean von Mises stress is quite high (around 500 MPa). This quantifies the in-plane background von Mises stress noise introduced in section 4.4.1, which is due to in-plane distance errors in the calculation of geodesic distances.

Sample points that are filtered based on both curvature and von Mises stress are shown in Figure 4-14-b and the resulting third FENR in Figure 4-14-c. A closer look at Figure 4-12-b, Figure 4-13-d and Figure 4-14-c shows that, when no defects are applied, FENR achieves very good results in general, except in the upper left zone where the maximum distance is around 0.2 mm. However, this distance remains under the tolerance (0.4 mm) which makes that, at the end, no defects are identified. It also shows that, as expected here because no defects are applied, the more sample points are filtered, the worse FENR gets. Thus, if the process tends to filter too many sample points, it may result in identifying defects that are not nominal defects. On the contrary, if the process tends to filter less sample points than required around defect zones, it may result in missing nominal defects or underestimating the size of defects.

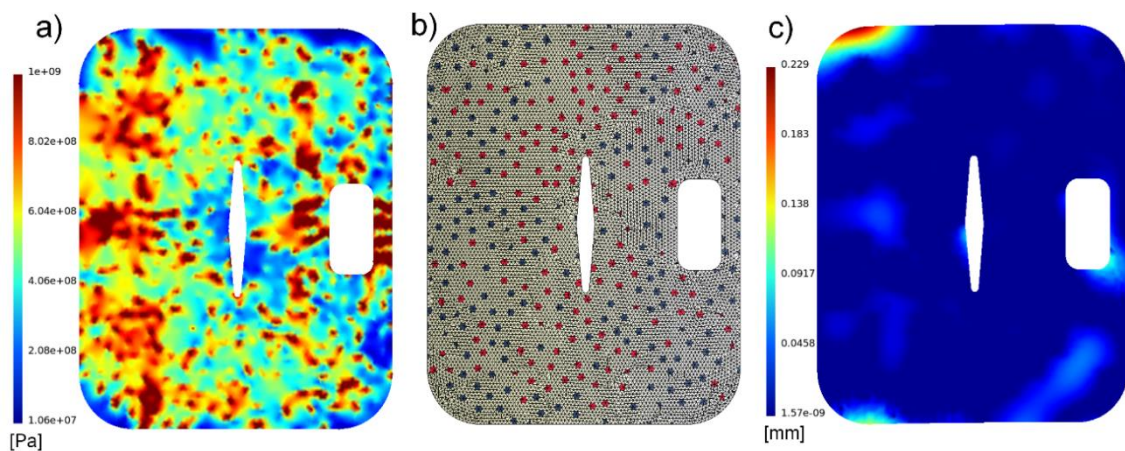


Figure 4-14: a) distribution of von Mises stress [Pa] after FENR when using GNIF sample points after filtering based on the curvature criterion b) sample points filtered using curvature and von Mises stress criteria (represented as blue spots) c) comparison between deformed CAD and scanned models when using GNIF sample points after filtering based on both curvature and von Mises stress criteria [mm].

4.5 Results

4.5.1 Introduction: validation cases

In this section, performance of the proposed approach is validated on two aluminum parts (referred to as part A and part B) with different types and sizes of defects and different types of free-state deformation. Part A is the part used in the previous section and part B is also typical of non-rigid parts used in the aerospace industry. Several validation cases have been considered for these parts, which are summarized in Figure 4-15. Two types of free-state deformation are applied (referred to as bending and torsion) and both small (local) and big (global) defects are simulated for each part, as shown in Figure 4-15.

Thus, four case studies are performed on each part and, for each case, comparisons are made between estimated and nominal size of defects:

- Using all sample points (without filtering).
- After filtering sample points based on the discrete curvature criterion only.
- After filtering sample points with curvature and von Mises criteria successively.

In all cases, initial GNIF sample points in the CAD model are illustrated as red spots (●) while filtered sample points, based on either curvature or von Mises stress criteria, are illustrated as blue spots (●). Meanwhile, color scales for the distribution of curvature differences are based on the maximum and minimum threshold values, while color scales for von Mises stress distributions is based on the von Mises stress threshold and on the minimum von Mises stress value.

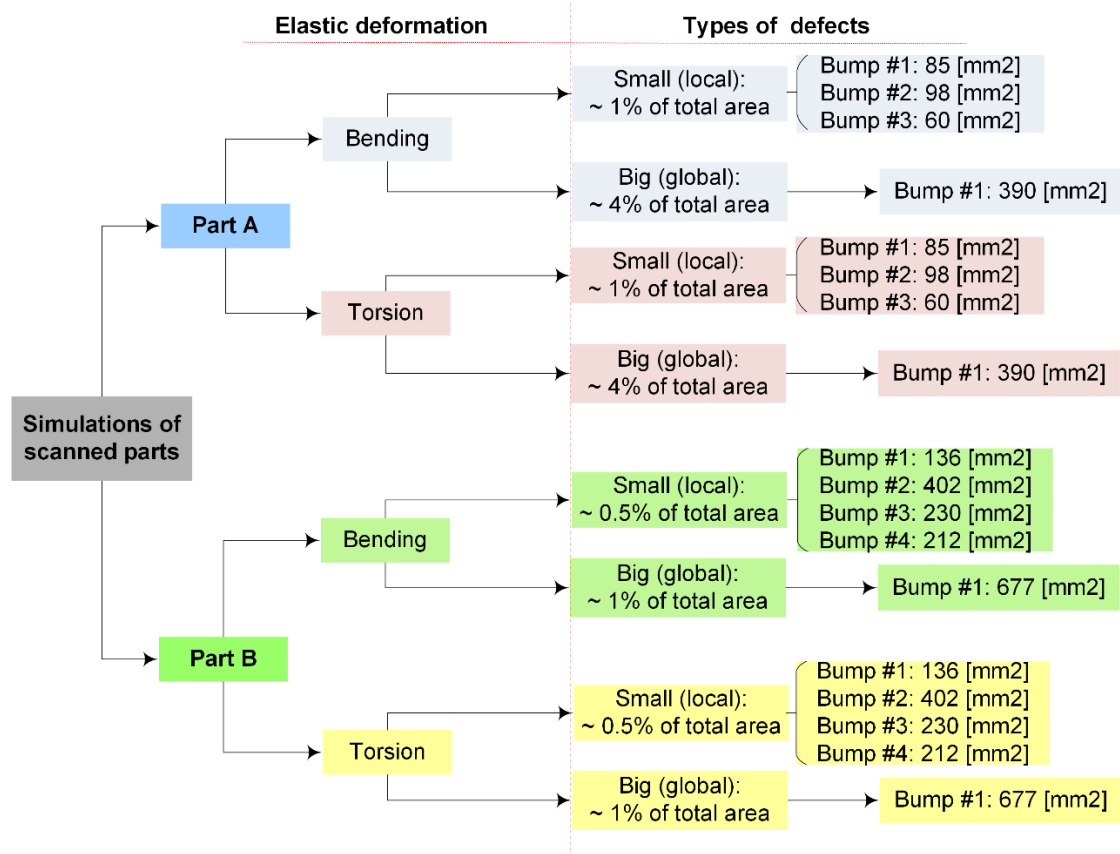


Figure 4-15: Synthesis of validation cases.

4.5.2 Validation cases for part A

Part A is presented in Figure 4-4-a and Figure 4-4-b. In its nominal state (without deformation and defects), it features a single and almost constant 0.005 mm^{-1} curvature over the whole panel. The flexible deformation of scanned model in free-state for this part is simulated by bending and torsion as introduced in Figure 4-15 and as shown in Figure 4-16. Note that top view of part A under bending deformation is also shown in Figure 4-4-d. As introduced in the previous section, thresholds used for the curvature criterion are -0.05 and $+0.05 \text{ mm}^{-1}$ and the threshold used for the von Mises stress criterion is 1000 MPa.

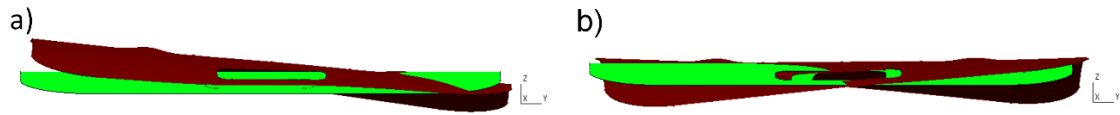


Figure 4-16: Side view of the CAD model for part A (in green) compared with the scanned model in a free-state (in brown) with a) bending deformation b) torsion deformation.

The first validation case associated with part A has been presented in section 4.4. Results show that, in this case, the average inspection error (for amplitude and area of defects) significantly decreases when using the two filters.

In the second validation case associated with part A, the scanned model in a free-state is simulated by applying torsion and three small (local) bumps are also imposed as defects. Initial GNIF sample points and associated estimation of defects are shown in Figure 4-17.

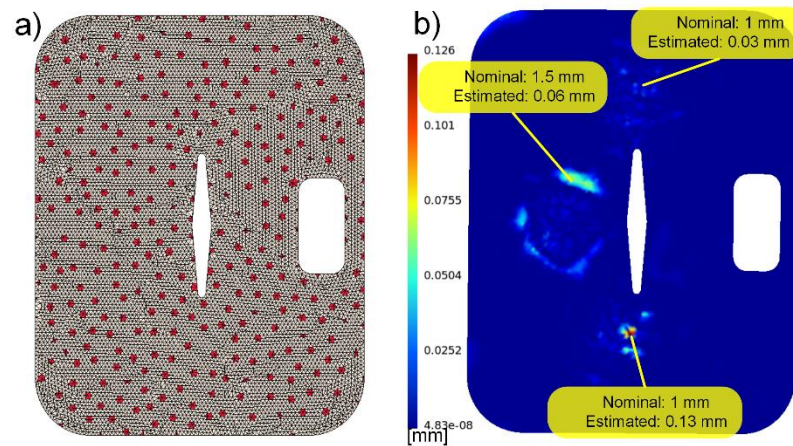


Figure 4-17: Part A with small (local) defects and torsion a) GNIF sample points on the CAD model represented as red spots b) comparison between estimated and nominal size of defects [mm] based on using all GNIF sample points.

Distributions of the difference in discrete principal curvatures between the CAD model and the deformed CAD model (using all GNIF sample points) are shown in Figure 4-18-a and b. As explained in the previous section and as shown in Figure 4-18-c, after applying

the curvature criterion, some sample points located around defects are removed and Figure 4-18-d illustrates the effect on the results after FENR.

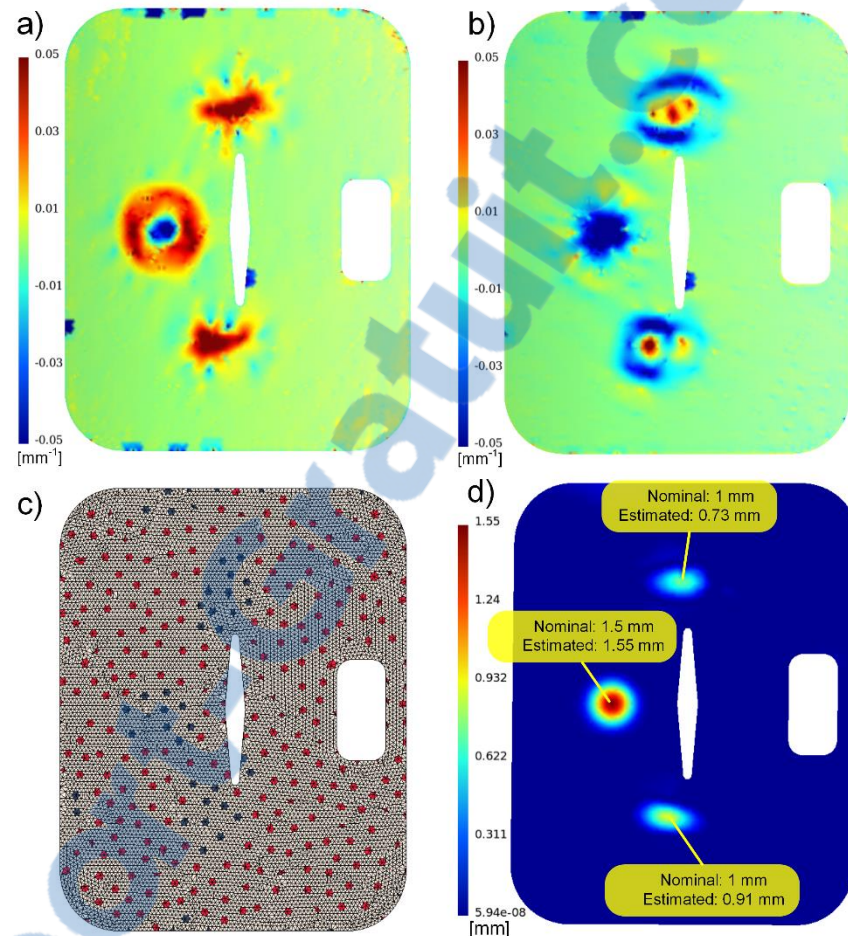


Figure 4-18: Part A with small (local) defects and torsion a) distribution of the difference in maximum curvature (K_1) [mm^{-1}] b) distribution of the difference in minimum curvature (K_2) [mm^{-1}] c) sample points filtered using the curvature criterion (represented as blue spots) d) comparison between estimated and nominal size of defects [mm] when using GNIF sample points after filtering based on the curvature criterion.

In Figure 4-19-a the von Mises stress distribution associated with this FENR is illustrated and, as shown in Figure 4-19-b, after applying the von Mises stress criterion, some more sample points are removed around defects. Figure 4-19-c, shows the result obtained after

the last FENR. A summary of quantitative results, for this second validation case on part A, is provided in Table 4-2. These results show that the estimation of the maximum amplitude of defects is slightly degraded for one defect (bump#3 as illustrated in Figure 4-4-c) after filtering sample points based on both curvature and von Mises criteria. However, the average estimation error for maximum amplitude, using all sample points, filtering sample points with the curvature criterion only and filtering sample points with the curvature and von Mises stress criteria successively, for the three bumps, is 93%, 13% and 10% respectively; while the average area estimation error, for the three bumps, is 100%, 27% and 20% respectively. Here again, the average estimation error for the three defects is decreased by applying both criteria if compared to applying the curvature criterion only.

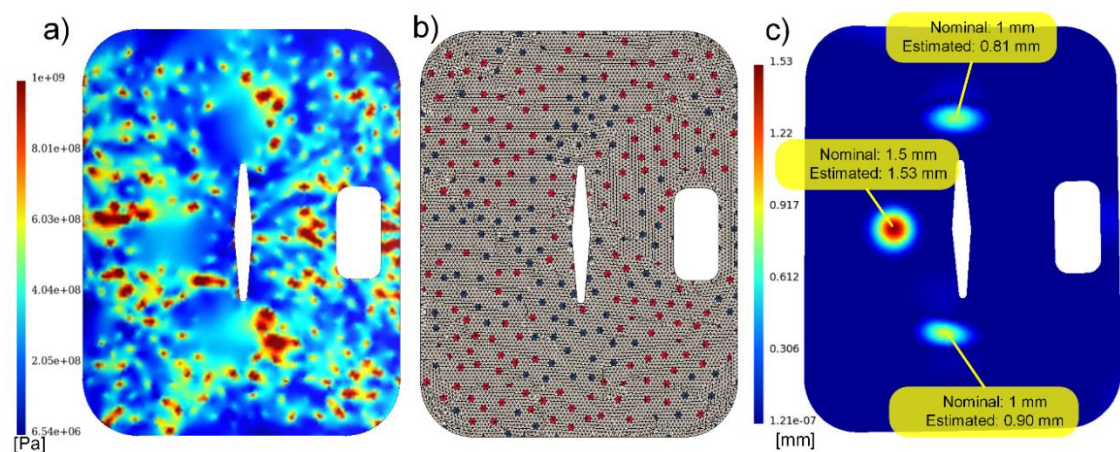


Figure 4-19: Part A with small (local) defects and torsion a) distribution of von Mises stress [Pa] after FENR based on GNIF sample points after filtering using the curvature criterion b) sample points filtered using curvature and von Mises stress criteria (represented as blue spots) c) comparison between estimated and nominal size of defects [mm] when using GNIF sample points after filtering based on both curvature and von Mises stress criteria.

Table 4-2: Estimated size of defects and errors based on curvature and von Mises criteria for part A with small (local) defects and torsion deformation.

	Maximum amplitude of defects			Area of defects		
	Nominal [mm]	Estimated [mm]	Error [%]	Nominal [mm ²]	Estimated [mm ²]	Error [%]
Using all sample points	1	0.03	97	85	0	100
	1.5	0.06	96	98	0	100
	1	0.13	87	60	0	100
Filtering sample points with the curvature criterion only	1	0.73	27	85	38	55
	1.5	1.55	3	98	101	3
	1	0.91	9	60	46	23
Filtering sample points with the curvature and von Mises stress criteria successively	1	0.81	19	85	54	36
	1.5	1.53	2	98	99	1
	1	0.9	10	60	47	22

In the following paragraph, as presented in Figure 4-15, two other validation cases are applied on part A. These cases aim at evaluating ability of our method in identifying big (global) defects. In the third validation case for part A, the scanned model in a free-state is simulated by applying bending. Initial GNIF sample points and the associated estimation of the size of defects are shown in Figure 4-20. Distributions of the difference in discrete principal curvatures between the CAD model and the deformed CAD model (using all GNIF sample points) are shown in Figure 4-21-a and Figure 4-21-b. Figure 4-21-c shows sample points that are filtered after applying the curvature criterion and Figure 4-21-d illustrates the effect on the results after FENR. In Figure 4-22-a the von Mises stress distribution associated with this FENR is illustrated, and as shown in

Figure 4-22-b after applying the von Mises stress criterion, some more sample points are removed around defects. Figure 4-22-c, shows the result obtained after the last FENR. A summary of quantitative results, for this third validation case on part A, is provided in Table 4-3. In this validation test, the error in estimating the size of this bigger defect is decreased after filtering sample points based on both curvature and von Mises criteria if compared to applying the curvature criterion only.

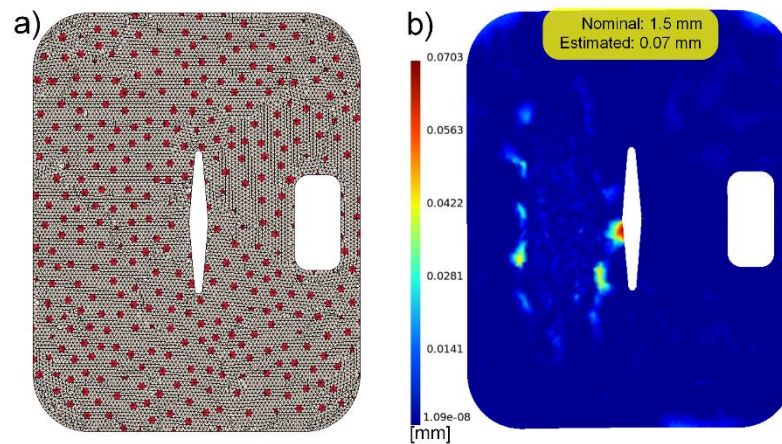


Figure 4-20: Part A with a big (global) defect and bending a) GNIF sample points on the CAD model represented as red spots b) comparison between estimated and nominal size of defects [mm] when using all GNIF sample points.

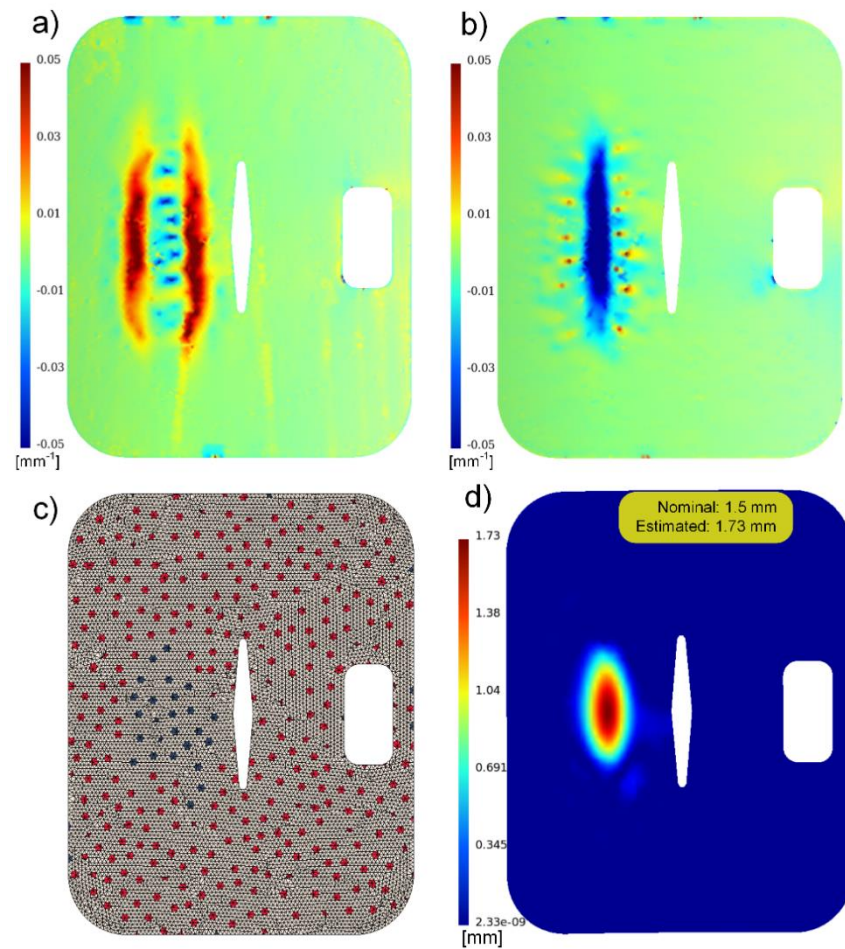


Figure 4-21: Part A with a big (global) defect and bending a) distribution of the difference in maximum curvature (K_1) [mm^{-1}] b) distribution of the difference in minimum curvature (K_1) [mm^{-1}] c) sample points filtered using the curvature criterion (represented as blue spots) d) comparison between estimated and nominal size of defects [mm] when using GNIF sample points after filtering based on the curvature criterion.

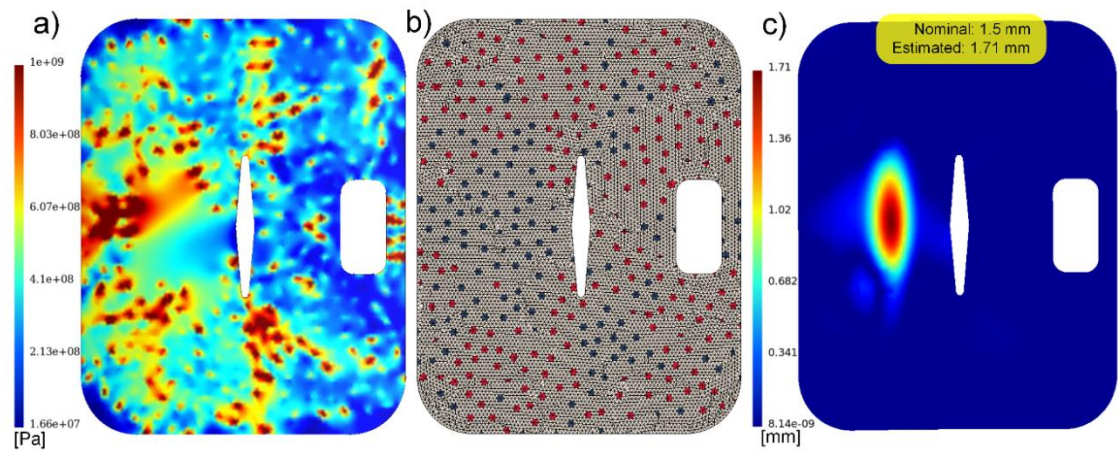


Figure 4-22: Part A with a big (global) defect and bending a) distribution of von Mises stress [Pa] after FENR when using GNIF sample points after filtering based on the curvature criterion b) sample points filtered using curvature and von Mises stress criteria (represented as blue spots) c) comparison between estimated and nominal size of defects [mm] when using GNIF sample points after filtering based on both curvature and von Mises stress criteria.

Table 4-3: Estimated size of defects and errors based on curvature and von Mises criteria for Part A with a big (global) defect and bending deformation.

	Maximum amplitude of defects			Area of defects		
	Nominal [mm]	Estimated [mm]	Error [%]	Nominal [mm ²]	Estimated [mm ²]	Error [%]
Using all sample points	1.5	0.07	95	390	0	100
Filtering sample points with the curvature criterion only	1.5	1.73	15	390	283	27
Filtering sample points with the curvature and von Mises stress criteria successively	1.5	1.71	14	390	352	10

In the last validation case associated with part A, the scanned model in a free-state is simulated by applying torsion and a big (global) defect is applied. Initial GNIF sample points and the associated estimation of the size of defects are shown in Figure 4-23. Distributions of the difference in discrete principal curvatures between the CAD model and the deformed CAD model (using all GNIF sample points) are shown in Figure 4-24-a, b. Figure 4-24-c shows sample points that are filtered after applying the curvature criterion and Figure 4-24-d illustrates the effect on the results after FENR. In Figure 4-25-a the von Mises stress distribution associated with this FENR is illustrated and, as shown in Figure 4-25-b after applying the von Mises stress criterion, some more sample points are removed around defects. Figure 4-25-c, shows the result obtained after the last FENR. A summary of quantitative results, for this last validation case on part A, is provided in Table 4-4. In this validation test, the error in estimating the maximum amplitude of this

defect is degraded after filtering sample points based on both curvature and von Mises criteria if compared to applying the curvature criterion only. Although in this case, it appears that filtering based on the von Mises criterion does not improve accuracy in the maximum amplitude estimation of defects, but the area of defect is estimated more accurately.

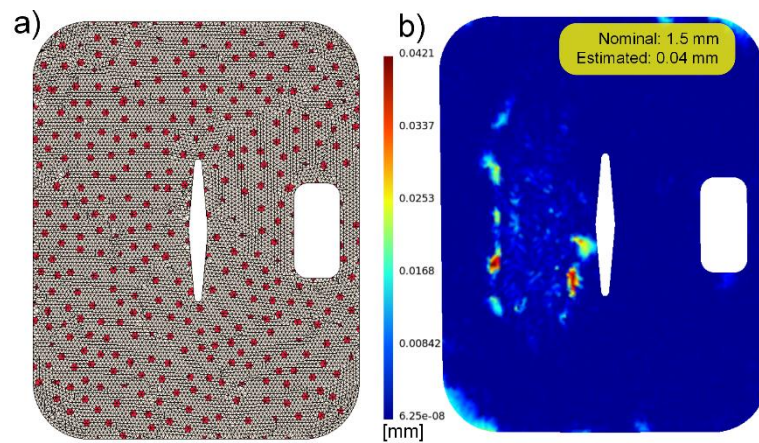


Figure 4-23: Part A with a big (global) defect and torsion a) GNIF sample points on the CAD model represented as red spots b) comparison between estimated and nominal size of defects [mm] when using all GNIF sample points.

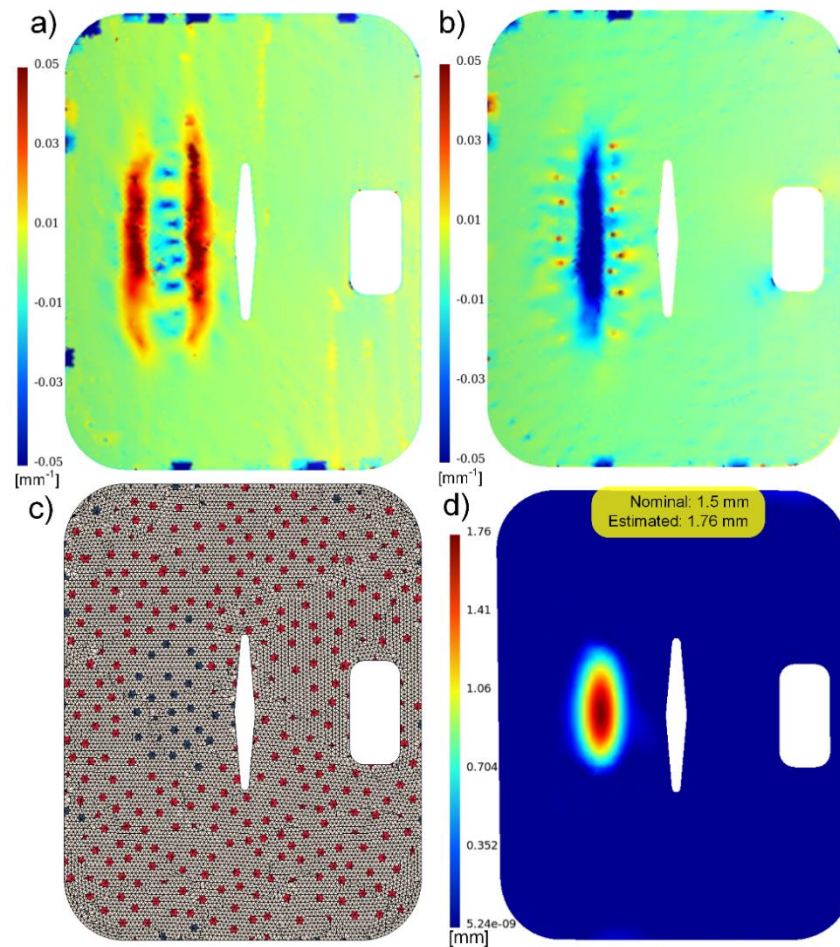


Figure 4-24: Part A with a big (global) defect and torsion a) distribution of the difference in maximum curvature (K_1) [mm^{-1}] b) distribution of the difference in minimum curvature (K_1) [mm^{-1}] c) sample points filtered using the curvature criterion (represented as blue spots) d) comparison between estimated and nominal size of defects [mm] when using GNIF sample points after filtering based on the curvature criterion.

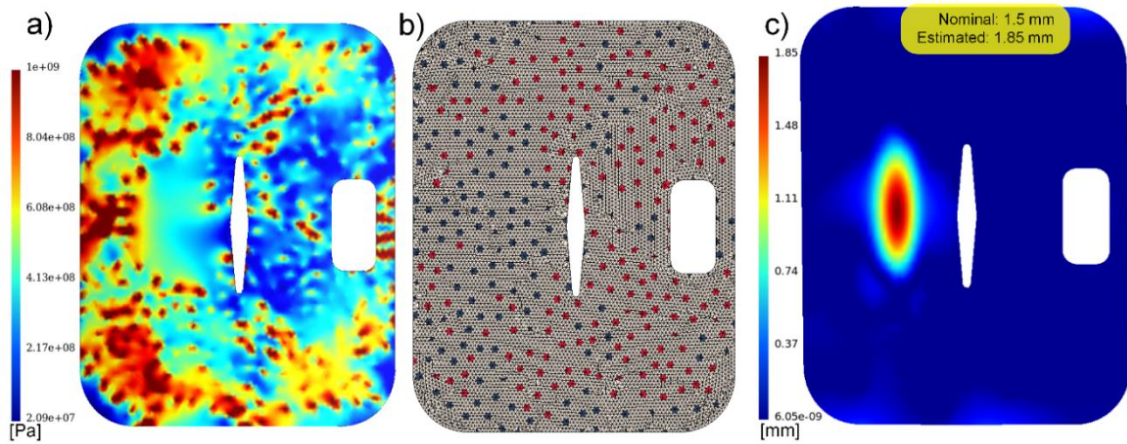


Figure 4-25: Part A with a big (global) defect and torsion a) distribution of von Mises stress [Pa] after FENR based on GNIF sample points after filtering using the curvature criterion b) sample points filtered using curvature and von Mises stress criteria (represented as blue spots) c) comparison between estimated and nominal size of defects [mm] when using GNIF sample points after filtering based on both curvature and von Mises stress criteria.

Table 4-4: Estimated size of defects and errors based on curvature and von Mises criteria for Part A with a big (global) defect and torsion deformation.

	Maximum amplitude of defects			Area of defects		
	Nominal [mm]	Estimated [mm]	Error [%]	Nominal [mm ²]	Estimated [mm ²]	Error [%]
Using all sample points	1.5	0.04	97	390	0	100
Filtering sample points with the curvature criterion only	1.5	1.76	17	390	300	23
Filtering sample points with the curvature and von Mises stress criteria successively	1.5	1.85	23	390	398	2

4.5.3 Validation cases for part B

Next validation cases are intended to illustrate applying our method on a different type of non-rigid part (see Figure 4-26). It is a long formed aluminum non-rigid part used in the aerospace industry with more complex features, smaller details and higher curvatures (channel section is 40 mm by 20 mm with 1 mm thickness and channel length is 1150 mm). As introduced in section 4.5.1, two types of defects are applied on this part as well as two types of free-state deformation. Defects are assessed on part B using the same methodology as for part A except for threshold associated with curvature and von Mises stress criteria which are determined based on new mean values for this part. Negative and positive local curvature difference threshold values for part B are -0.01 and $+0.01$ mm^{-1} and the von Mises stress threshold is 400 MPa.

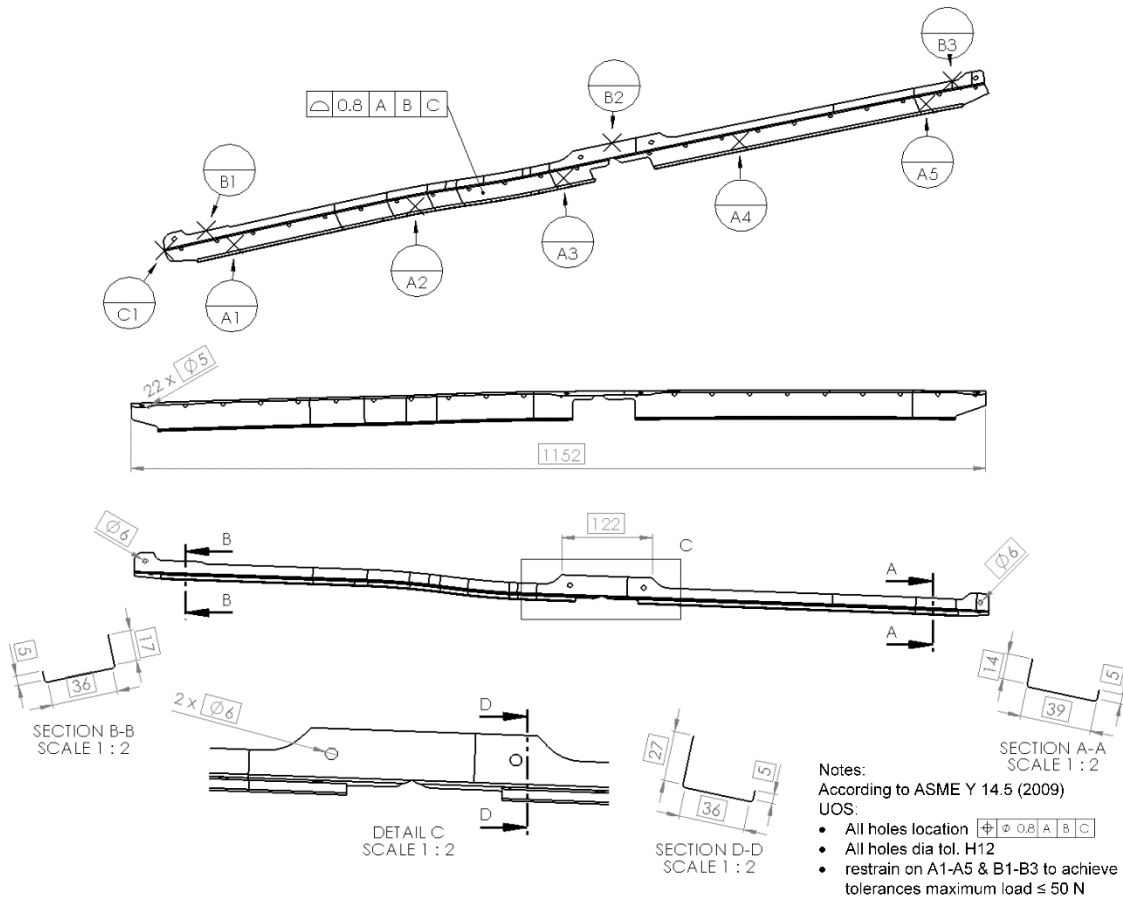


Figure 4-26: CAD model along with GD&T specification for part B (dimensions are in mm).

The initial corresponding sample points between CAD and scanned models are shown in Figure 4-27.

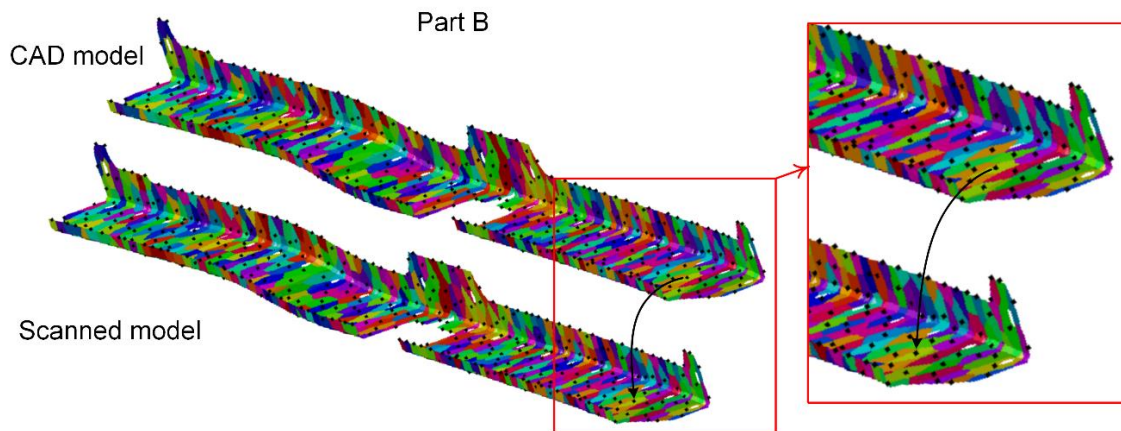


Figure 4-27: GNIF corresponding sample points (in black) on the CAD and scanned models of part B.

The free-state deformation of scanned model for part B is also simulated with bending and torsion as presented in Figure 4-28 and two types of defects are applied as for part A: small (local) and big (global) defects.

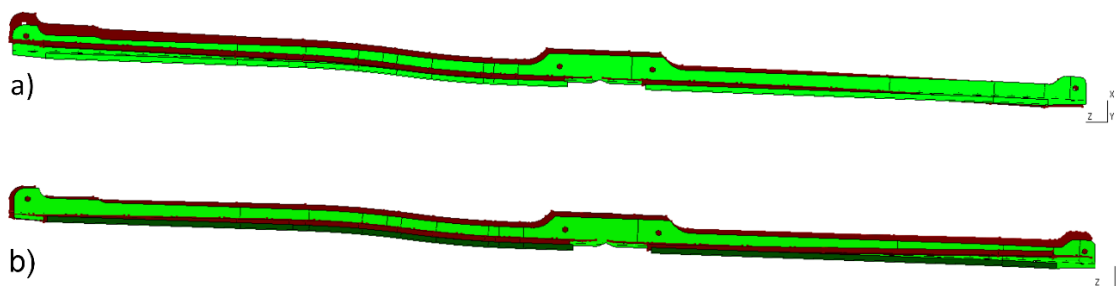


Figure 4-28: Side view of CAD model for part B (in green) compared with the scanned model (in brown) a) with bending deformation b) with torsion deformation.

In the first validation case for part B, free-state deformation is bending and four small (local) bumps are imposed. Initial GNIF sample points and the associated estimation of the size of defects are presented in Figure 4-29-a and b. Distributions of the difference in discrete principal curvatures (using all GNIF sample points) are shown in Figure 4-29-c and d. The von Mises stress distribution associated with the second FENR is presented in Figure 4-29-e. Sample points removed after applying the two filters are illustrated in Figure 4-29-f and Figure 4-29-g, shows results obtained after the last FENR.



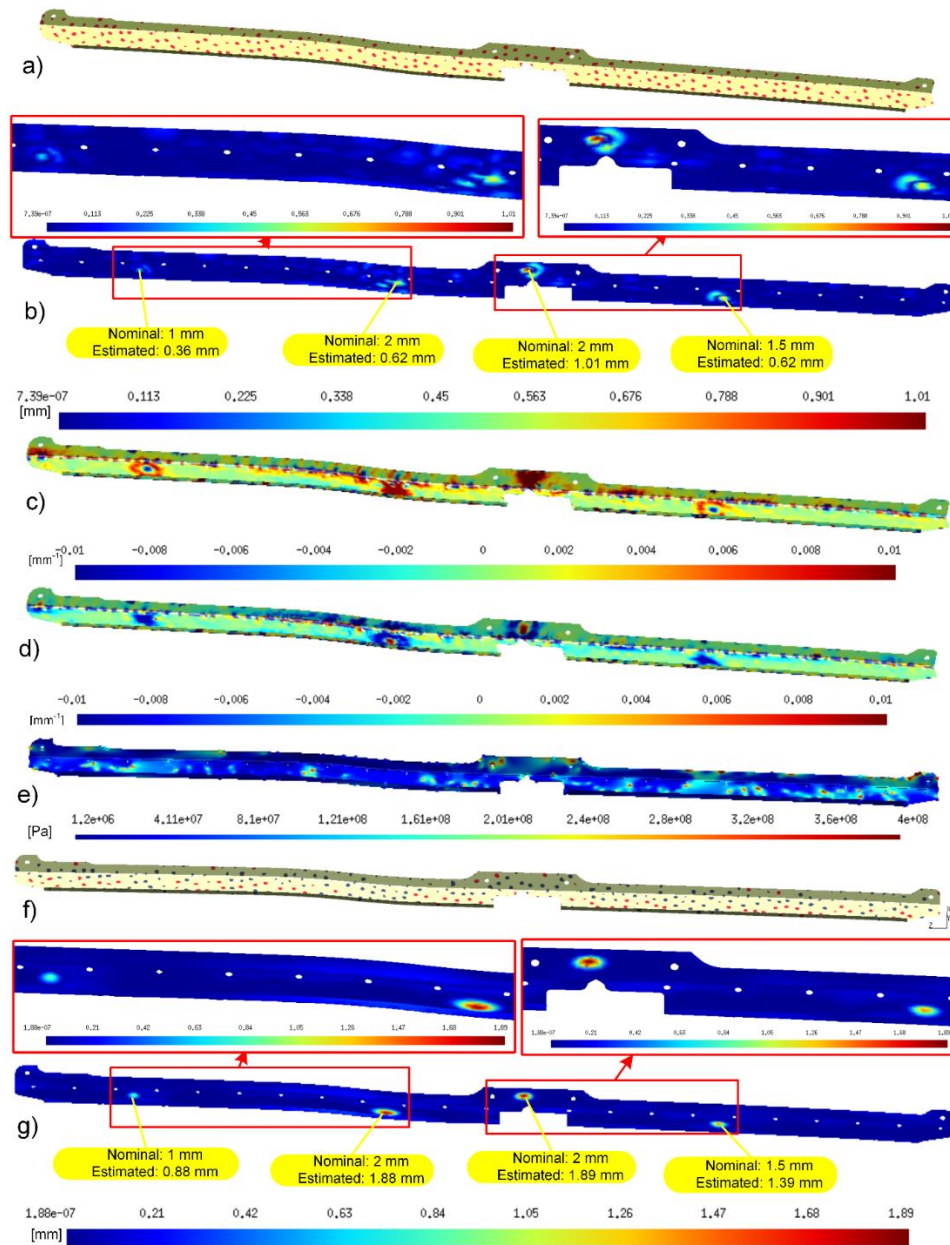


Figure 4-29: Part B with small (local) defects and bending a) and f) initial and filtered sample points c) and d) distribution of the difference in principle curvatures $[\text{mm}^{-1}]$ e) distribution of von Mises stress [Pa] after the second FENR. b) and g) comparison between estimated and nominal size of defects [mm] based on initial and filtered sample points.

A summary of quantitative results, for this first validation case on part B, is provided in Table 4-5. In this case, the error in estimating the maximum amplitude of these defects is slightly degraded for two bumps (among four) after filtering sample points based on both curvature and von Mises criteria if compared to applying the curvature criterion only. However, the average estimation error for maximum amplitude, using all sample points, filtering sample points with the curvature criterion only and filtering sample points with the curvature and von Mises stress criteria successively, for the four bumps, is 60%, 8% and 8% respectively; while the average area estimation error, for the four bumps, is 83%, 9% and 7% respectively. Therefore, the average error is globally decreased by applying both criteria.

Table 4-5: Estimated size of defects and errors based on curvature and von Mises criteria for Part B with small (local) defects and bending deformation.

	Maximum amplitude of defects			Area of defects		
	Nominal [mm]	Estimated [mm]	Error [%]	Nominal [mm ²]	Estimated [mm ²]	Error [%]
Using all sample points	1	0.36	64	136	0	100
	2	0.62	69	402	50	88
	2	1.01	50	230	70	70
	1.5	0.62	59	212	56	74
Filtering sample points with the curvature criterion only	1	0.89	11	136	118	13
	2	1.88	6	402	378	6
	2	1.92	4	230	239	4
	1.5	1.35	10	212	184	13
Filtering sample points with the curvature and von Mises stress criteria successively	1	0.88	12	136	118	13
	2	1.88	6	402	378	6
	2	1.89	6	230	228	1
	1.5	1.39	7	212	199	6

In the second validation case associated with part B, the scanned model in a free-state is simulated by applying torsion, while four small (local) bumps are imposed as defects. Initial GNIF sample points and the associated estimation of the size of defects are shown in Figure 4-30-a and b. Distributions of the difference in discrete principal curvatures between CAD and deformed CAD models (using all GNIF sample points) are shown in Figure 4-30-c and d. The von Mises stress distribution associated with the second FENR

is presented in Figure 4-30-e. Sample points removed after applying the two filters are illustrated in Figure 4-30-f and Figure 4-30-g, shows results obtained after the last FENR. A summary of quantitative results, for this second validation case on part B, is provided in Table 4-6. In this case, the error in estimating the maximum amplitude of these defects is slightly degraded for one of the four bumps after filtering sample points based on both curvature and von Mises criteria if compared to applying the curvature criterion only.

However, the average estimation error for maximum amplitude, using all sample points, filtering sample points with the curvature criterion only and filtering sample points with the curvature and von Mises stress criteria successively, for the four bumps, is 57%, 17% and 15% respectively; while the average area estimation error, for the four bumps, is 78%, 18% and 16% respectively. Thus, like in previous cases, the average error is globally decreased by applying both criteria.

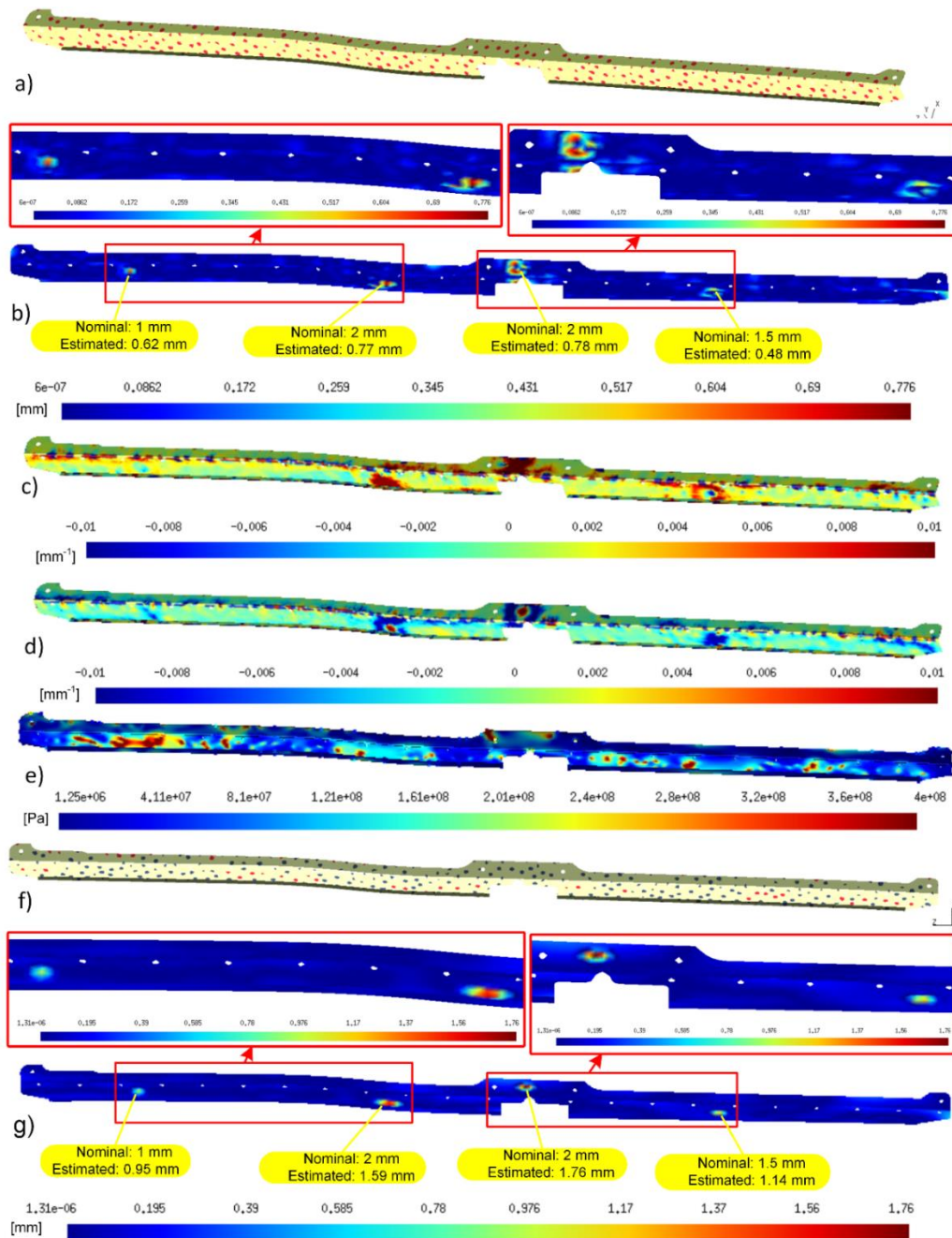


Figure 4-30: Part B with small (local) defects and torsion a) and f) initial and filtered sample points c) and d) distribution of the difference in principle curvatures [mm^{-1}] e) distribution of von Mises stress [Pa] after the second FENR. b) and g) comparison between estimated and nominal size of defects [mm] based on initial and filtered sample points.

Table 4-6: Estimated size of defects and errors based on curvature and von Mises criteria for Part B with small (local) defects and torsion deformation.

	Maximum amplitude of defects			Area of defects		
	Nominal [mm]	Estimated [mm]	Error [%]	Nominal [mm ²]	Estimated [mm ²]	Error [%]
Using all sample points	1	0.62	38	136	24	82
	2	0.77	62	402	75	81
	2	0.78	61	230	106	54
	1.5	0.48	68	212	16	92
Filtering sample points with the curvature criterion only	1	0.88	12	136	90	34
	2	1.54	23	402	388	3
	2	1.85	8	230	201	13
	1.5	1.11	26	212	164	23
Filtering sample points with the curvature and von Mises stress criteria successively	1	0.95	5	136	100	26
	2	1.59	21	402	408	1
	2	1.76	12	230	201	13
	1.5	1.14	24	212	164	23

In the rest of this section, two other validation cases are applied on part B. As presented in Figure 4-15, these cases evaluate the ability of our proposed method in identifying and

evaluating big (global) defects. The same two types of free-state deformation are applied. In the third validation case associated with part B, the scanned model in a free-state is simulated by applying bending and initial GNIF sample points and the associated estimation of the size of defects are shown in Figure 4-31-a and b. Distributions of the difference in discrete principal curvatures between the CAD model and the deformed CAD model (using all GNIF sample points) are shown in Figure 4-31-c and d. The von Mises stress distribution associated with the second FENR is presented in Figure 4-31-e. Sample points removed after applying the two filters are illustrated in Figure 4-31-f and Figure 4-31-g, shows results obtained after the last FENR. A summary of quantitative results, for this third validation case on part B, is provided in Table 4-7. In this case, the error in estimating the size of this bigger defect is clearly improved after filtering sample points based on both curvature and von Mises criteria if compared to applying the curvature criterion only.

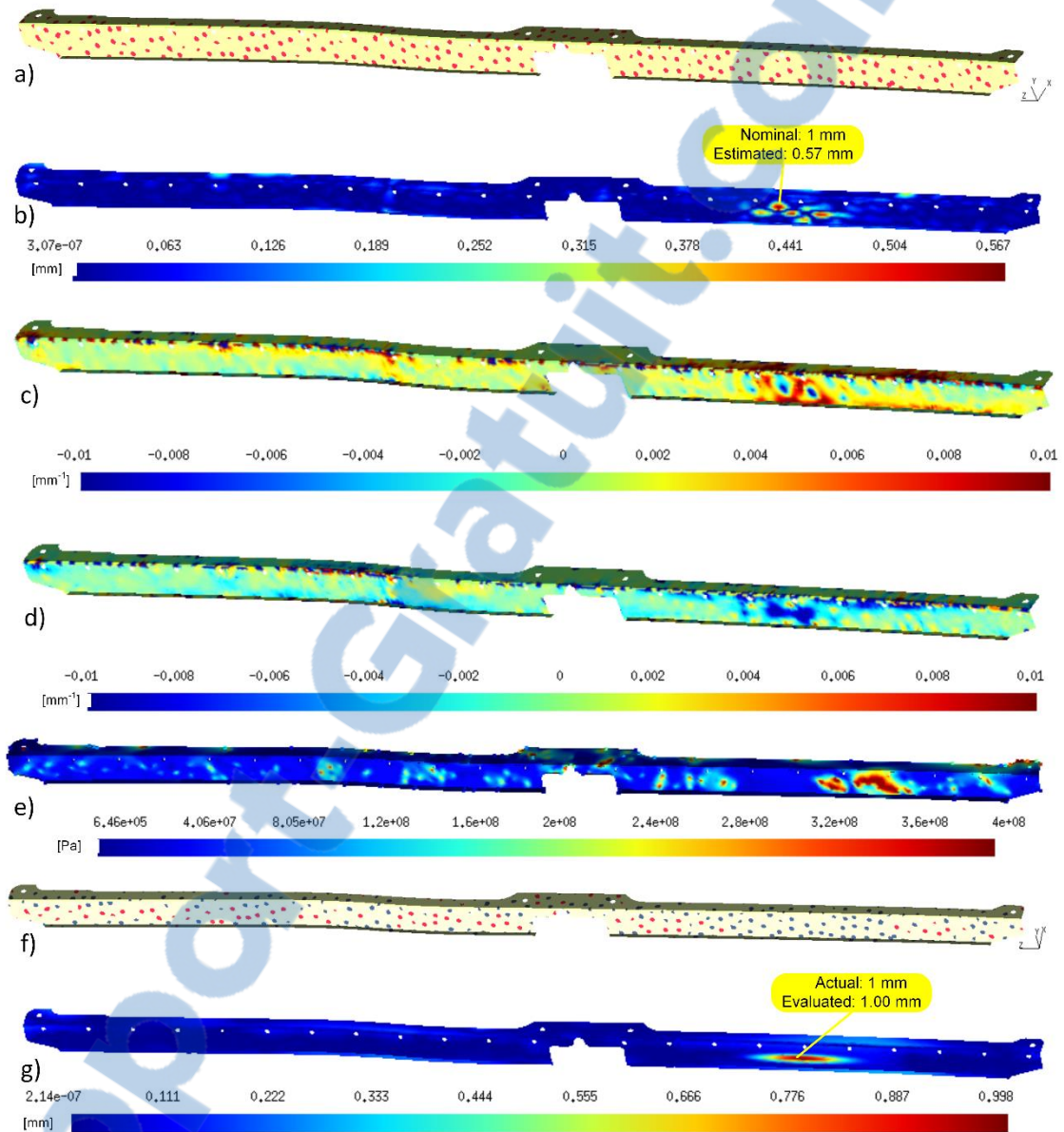


Figure 4-31: Part B with a big (global) defect and bending a) and f) initial and filtered sample points c) and d) distribution of the difference in principle curvatures $[\text{mm}^{-1}]$ e) distribution of von Mises stress [Pa] after the second FENR. b) and g) comparison between estimated and nominal size of defects [mm] based on initial and filtered sample points.

Table 4-7: Estimated size of defects and errors based on curvature and von Mises criteria for Part B with a big (global) defect and bending deformation.

	Maximum amplitude of defects			Area of defects		
	Nominal [mm]	Estimated [mm]	Error [%]	Nominal [mm ²]	Estimated [mm ²]	Error [%]
Using all sample points	1	0.57	43	677	64	91
Filtering sample points with the curvature criterion only	1	0.9	10	677	539	20
Filtering sample points with the curvature and von Mises stress criteria successively	1	1	0	677	737	9

In the last validation case associated with part B, the scanned model in a free-state is simulated by applying torsion and a big (global) defect is applied. Initial GNIF sample points and the associated estimation of the size of defects are shown in Figure 4-32-a and b. Distributions of the difference in discrete principal curvatures between the CAD model and the deformed CAD model (using all GNIF sample points) are shown in Figure 4-32-c and d. The von Mises stress distribution associated with the second FENR is presented in Figure 4-32-e. Sample points removed after applying the two filters are illustrated in Figure 4-32-f and g, shows results obtained after the last FENR. A summary of quantitative results, for this last validation case on part B, is provided in Table 4-8. For reasons explained in section 4.4.1, this validation case on part B presents a slight degradation in the accuracy of defect assessment after filtering sample points based on von Mises criterion if compared to results obtained after filtering sample points based on the curvature criterion only.

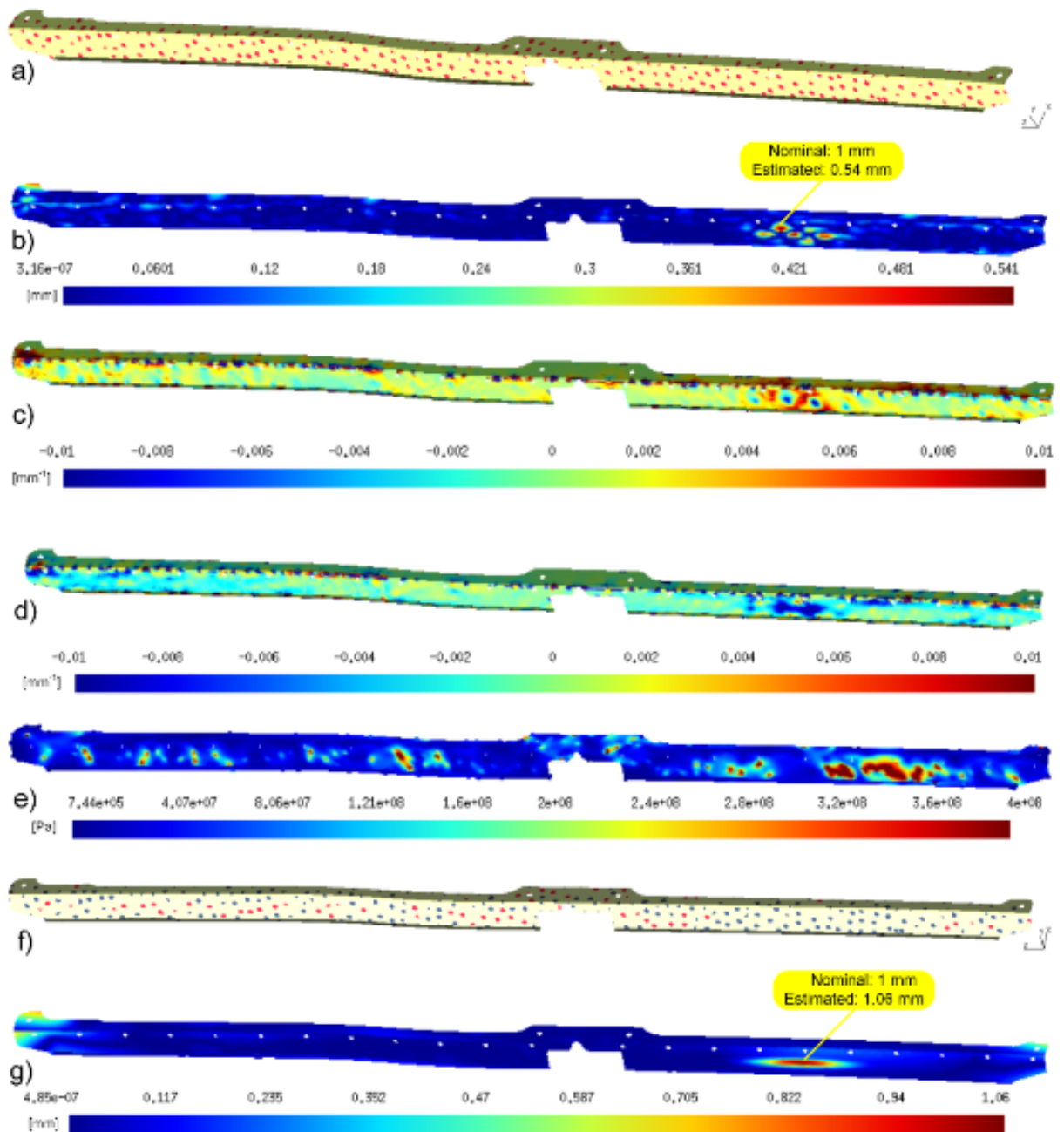


Figure 4-32: Part B with a big (global) defect and torsion a) and f) initial and filtered sample points c) and d) distribution of the difference in principle curvatures [mm^{-1}] e) distribution of von Mises stress [Pa] after the second FENR. b) and g) comparison between estimated and nominal size of defects [mm] based on initial and filtered sample points.

Table 4-8: Estimated size of defects and errors based on curvature and von Mises criteria for Part B with a big (global) defect and torsion deformation.

	Maximum amplitude of defects			Area of defects		
	Nominal [mm]	Estimated [mm]	Error [%]	Nominal [mm ²]	Estimated [mm ²]	Error [%]
Using all sample points	1	0.54	46	677	58	91
Filtering sample points with the curvature criterion only	1	0.96	4	677	541	20
Filtering sample points with the curvature and von Mises stress criteria successively	1	1.06	6	677	848	25

4.6 Conclusion

This paper proposes a method aimed at improving fixtureless inspection of non-rigid parts. GNIF-based *FEA Non-rigid Registration* (FENR) is used for the generation of corresponding sample points. Accuracy of FENR, and consequently of fixtureless inspection, is improved by automatically filtering GNIF sample points. Filtering is based on curvature and von Mises stress criteria and it allows removing sample points around defects for FENR. This filtering makes that defects are identified and quantified more accurately. Validation cases on two aerospace parts show that the method proposed brings about significant improvements towards automating fixtureless inspection of non-rigid parts in a free-state. Validation results presented in section 4.5 infer that, in general, filtering GNIF sample points based on both curvature and von Mises criteria improves the estimation of defects size. More specifically, improvements are always obtained when using the curvature criterion alone. When the curvature criterion is combined with the

von Mises criterion, some results show improvement while others show slight degradations for some of the defects. However, it appears that the average error is globally decreased by applying both criteria for all cases presented.

Even if the results obtained with this approach are promising, several improvements can be foreseen towards achieving higher accuracy in the estimation of defects. First, as introduced in section 4.4, it appears that the whole process is very sensitive to mesh size and mesh quality. Indeed, GNIF, discrete curvature and von Mises stress are sensitive to mesh size and quality. Therefore, future work will first focus on studying the effect of adaptive mesh generation on the estimation of defects with the approach as proposed in this paper. Indeed, using finer meshes in sensitive zones (such as zones with high curvature for example) is likely to improve accuracy in the quantification of defects. Also, at this point, threshold values used in filtering sample points based on both curvature and von Mises stress criteria still require limited user input. As setting up these threshold values is essentially based on geometric features (dimensions, thickness, curvature, etc.), a natural extension of the approach is setting up these values fully automatically. Meanwhile, measured data acquired from actual scanning devices always include some noise. In future works the proposed method will be validated by taking into account the effect of this noise on the results. Improving the accuracy of the process could also be achieved by improving the accuracy of GNIF itself. Indeed, computation of initial GNIF sample points mainly relies on combining multidimensional scaling with fast marching based geodesic distances computation. Since improving accuracy in the computation of these geodesic distances has a direct effect on the accuracy of GNIF registration, it also has a direct effect on the accuracy of defect identification and quantification.

4.7 Acknowledgment

The authors would like to thank the National Sciences and Engineering Research Council of Canada (NSERC), industrial partners, Consortium for Aerospace Research and Innovation in Québec (CRIAQ) and UQTR foundation for their support and financial

contribution. In this paper we use GmshTM [31] for visualizing meshes, stress, curvature and error distributions.

4.8 References

- [1] G. N. Abenhaim, A. Desrochers, and A. Tahan, "Nonrigid parts' specification and inspection methods: notions, challenges, and recent advancements," *International Journal of Advanced Manufacturing Technology*, vol. 63, pp. 741-752, Nov 2012.
- [2] R. Ascione and W. Polini, "Measurement of nonrigid freeform surfaces by coordinate measuring machine," *The International Journal of Advanced Manufacturing Technology*, vol. 51, pp. 1055-1067, 2010.
- [3] H. Radvar-Esfahlan and S.-A. Tahan, "Robust generalized numerical inspection fixture for the metrology of compliant mechanical parts," *The International Journal of Advanced Manufacturing Technology*, vol. 70, pp. 1101-1112, 2014.
- [4] G. N. Abenhaim, S. A. Tahan, A. Desrochers, and J.-F. Lalonde, "Aerospace Panels Fixtureless Inspection Methods with Restraining Force Requirements; A Technology Review," *SAE Technical Paper* 2013.
- [5] E. Savio, L. De Chiffre, and R. Schmitt, "Metrology of freeform shaped parts," *Cirp Annals-Manufacturing Technology*, vol. 56, pp. 810-830, 2007.
- [6] S. Martínez, E. Cuesta, J. Barreiro, and B. Álvarez, "Analysis of laser scanning and strategies for dimensional and geometrical control," *The International Journal of Advanced Manufacturing Technology*, vol. 46, pp. 621-629, 2010.
- [7] Y. D. Li and P. H. Gu, "Free-form surface inspection techniques state of the art review," *Computer-Aided Design*, vol. 36, pp. 1395-1417, Nov 2004.
- [8] P. J. Besl and N. D. McKay, "A Method for Registration of 3-D Shapes," *Ieee Transactions on Pattern Analysis and Machine Intelligence*, vol. 14, pp. 239-256, Feb 1992.

- [9] K. Blaedel, D. Swift, A. Claudet, E. Kasper, and S. Patterson, "Metrology of non-rigid objects," Lawrence Livermore National Lab., CA (US)2002.
- [10] A. Weckenmann and A. Gabbia, "Testing formed sheet metal parts using fringe projection and evaluation by virtual distortion compensation," *Fringe 2005*, pp. 539-546, 2006.
- [11] A. Weckenmann and J. Weickmann, "Optical Inspection of Formed Sheet Metal Parts Applying Fringe Projection Systems and Virtual Fixation," *Metrology and Measurement Systems*, vol. 13, pp. 321-330, 2006.
- [12] I. Gentilini and K. Shimada, "Predicting and evaluating the post-assembly shape of thin-walled components via 3D laser digitization and FEA simulation of the assembly process," *Computer-aided design*, vol. 43, pp. 316-328, 2011.
- [13] A. Weckenmann, J. Weickmann, and N. Petrovic, "Shortening of inspection processes by virtual reverse deformation," in 4th international conference and exhibition on design and production of machines and dies/molds, Cesme, Turkey, 2007.
- [14] S. Lemeš, "Validation of numerical simulations by digital scanning of 3D sheet metal objects," PhD thesis Submitted to Faculty of Mechanical Engineering, University of Ljubljana, 2010.
- [15] A. E. Jaramillo, P. Boulanger, and F. Prieto, "On-line 3-D inspection of deformable parts using FEM trained radial basis functions," in *Computer Vision Workshops (ICCV Workshops)*, 2009 IEEE 12th International Conference on, 2009, pp. 1733-1739.
- [16] A. Jaramillo, F. Prieto, and P. Boulanger, "Fast dimensional inspection of deformable parts from partial views," *Computers in Industry*, vol. 64, pp. 1076-1081, 2013.
- [17] A. Jaramillo, F. Prieto, and P. Boulanger, "Fixtureless inspection of deformable parts using partial captures," *International Journal of Precision Engineering and Manufacturing*, vol. 14, pp. 77-83, 2013.

- [18] H. Radvar-Esfahlan and S.-A. Tahan, "Nonrigid geometric metrology using generalized numerical inspection fixtures," *Precision Engineering*, vol. 36, pp. 1-9, 2012.
- [19] G. N. Abenhaim, A. S. Tahan, A. Desrochers, and R. Maranzana, "A Novel Approach for the Inspection of Flexible Parts Without the Use of Special Fixtures," *Journal of Manufacturing Science and Engineering-Transactions of the Asme*, vol. 133, Feb 2011.
- [20] A. Aidibe, A. S. Tahan, and G. N. Abenhaim, "Dimensioning control of non-rigid parts using the iterative displacement inspection with the maximum normed residual test," in *International conference on theoretical and applied mechanics*. Corfu Island, Greece, 2011.
- [21] A. Aidibe, S. A. Tahan, and J.-F. Lalonde, "A Robust Iterative Displacement Inspection Algorithm for Quality Control of Aerospace Non-Rigid Parts without Conformation Jig," *SAE Technical Paper*2013.
- [22] A. Aidibe, A. S. Tahan, and G. N. Abenhaim, "Distinguishing profile deviations from a part's deformation using the maximum normed residual test," *WSEAS Transactions on Applied & Theoretical Mechanics*, vol. 7, 2012.
- [23] A. Aidibe and S. A. Tahan, "An inspection approach for nonrigid mechanical parts," *Advanced Materials Research*, vol. 816, pp. 806-811, 2013.
- [24] R. Kimmel and J. A. Sethian, "Computing geodesic paths on manifolds," *Proceedings of the National Academy of Sciences*, vol. 95, pp. 8431-8435, 1998.
- [25] A. M. Bronstein, M. M. Bronstein, and R. Kimmel, "Generalized multidimensional scaling: A framework for isometry-invariant partial matching," *Proceedings of the National Academy of Sciences of the United States of America*, vol. 103, pp. 1168-1172, 2006.
- [26] H. Radvar-Esfahlan and S. A. Tahan, "Performance study of dimensionality reduction methods for metrology of nonrigid mechanical parts," *International Journal of Metrology and Quality Engineering*, vol. 4, pp. 193-200, 2013.

- [27] S. S. Karganroudi, J.-C. Cuillière, V. François, and S.-A. Tahan, "An improvement of fixtureless inspection for non-rigid parts based on filtering sample points" in Proceedings of the 25th Canadian Congress of Applied Mechanics (CANCAM 2015), London, Ontario, Canada, 2015.
- [28] H. Borouchaki, P. L. George, and S. H. Lo, "Optimal delaunay point insertion," International Journal for Numerical Methods in Engineering, vol. 39, pp. 3407-3437, 1996.
- [29] T. Surazhsky, E. Magid, O. Soldea, G. Elber, and E. Rivlin, "A comparison of gaussian and mean curvatures estimation methods on triangular meshes," in Robotics and Automation, 2003. Proceedings. ICRA'03. IEEE International Conference on, 2003, pp. 1021-1026.
- [30] J. C. Cuillière and V. Francois, "Integration of CAD, FEA and Topology Optimization through a Unified Topological Model," Computer-Aided Design and Applications, vol. 11, pp. 1-15, // 2014.
- [31] C. Geuzaine and J.-F. Remacle, "Gmsh: a three-dimensional finite element mesh generator with built-in pre- and post-processing facilities," International Journal for Numerical Methods in Engineering, vol. 79, pp. 1309-1331, 2009.

CHAPTER 5 ASSESSMENT OF THE ROBUSTNESS OF A FIXTURELESS INSPECTION METHOD FOR NON-RIGID PARTS BASED ON A VERIFICATION AND VALIDATION APPROACH

Sasan Sattarpanah Karganroudi¹, Jean-Christophe Cuillière¹, Vincent Francois¹,
Souheil-Antoine Tahan²

¹Équipe de Recherche en Intégration Cao-CALcul (ÉRICCA), Université du Québec à Trois-
Rivières, Trois-Rivières, Québec, Canada

²Laboratoire d'ingénierie des produits, procédés et systèmes (LIPPS), École de Technologie
Supérieure, Montréal, Québec, Canada

5.1 Abstract

The increasing practical use of *Computer-Aided Inspection* (CAI) methods requires assessment of their robustness in different contexts. This can be done by quantitatively comparing estimated CAI results with actual measurements. The objective is comparing the magnitude and dimensions of defects as estimated by CAI with those of the nominal defects. This assessment is referred to as setting up a validation metric. In this work, a new validation metric is proposed in the case of a fixtureless inspection method for non-rigid parts. It is based on using a nonparametric statistical hypothesis test, namely the *Kolmogorov–Smirnov* (K-S) test. This metric is applied to an automatic fixtureless CAI method for non-rigid parts developed by our team. This fixtureless CAI method is based on calculating and filtering sample points that are used in a *Finite Element Non-rigid Registration* (FENR). Robustness of our CAI method is validated for the assessment of maximum amplitude, area and distance distribution of defects. Typical parts from the aerospace industry are used for this validation and various levels of synthetic measurement noise are added to the scanned point cloud of these parts to assess the effect of noise on inspection results.

Keywords: Fixtureless inspection, verification and validation, V&V, non-rigid parts, GNIF, principal curvatures, von Mises stress, hypothesis testing, metrology, inspection.

5.2 Introduction

High-quality standards that are applied in many industrial sectors, among which aerospace and automotive industries, require setting up robust, rapid and accurate quality control processes. *Geometric Dimensioning and Tolerancing* (GD&T) and automated inspection are two key aspects of this issue. Automating inspection can be performed using non-contact scanning devices but automated inspection still faces many challenges. Automating the inspection of non-rigid parts is part of these challenges. It remains a serious problem since these parts may deform during the inspection. These parts may deform under their own weight and also from residual stress that is eventually induced by manufacturing and handling processes. Compliance is a measure of flexibility for non-rigid parts and it is defined as the ratio between an applied force and the part deformation induced by this force [1]. Referring to this definition, a manufactured part is considered as non-rigid if the deformation induced by a reasonable force (around 40 N) is 10% higher than specified tolerances. Based on standards in metrology such as ASME Y14.5 and ISO-GPS, the inspection of parts is performed in a free-state, except for non-rigid parts, as it is mentioned in ISO-10579 and ASME Y14.5 (2009). Free-state refers to a situation in which a manufactured part is not submitted to any other load than its own weight. As it is illustrated in Figure 5-1-a, a non-rigid aerospace panel in a free-state deforms due to its compliance under its own weight. Based on conventional dimensioning and inspection methods for non-rigid parts, very sophisticated and expensive inspection fixtures need to be designed and used to compensate for flexible deformation of these parts during inspection. Setting up and operating these inspection fixtures is time consuming and expensive. Figure 5-1-b illustrates an example of such an inspection fixture for the part shown in a free-state in Figure 5-1-a.

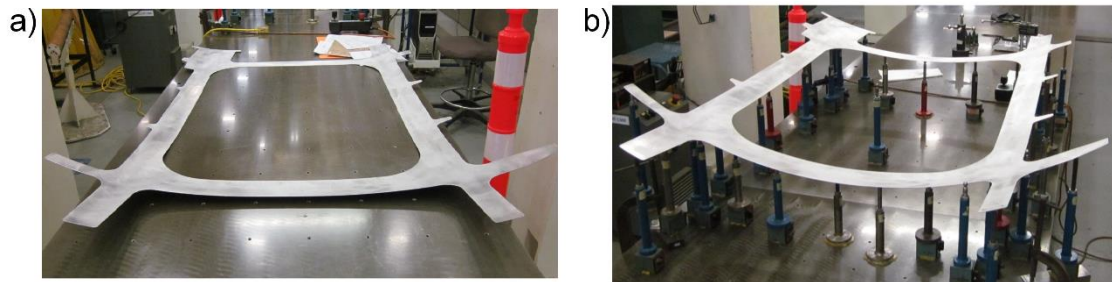


Figure 5-1: A regular aerospace panel, a) in free-state, b) constrained by fixing jigs on the inspection fixture [2].

Recent improvements in data acquisition devices, such as three-dimensional (3D) scanners, and in computational calculations, allow an ongoing progress towards *Computer-Aided Inspection (CAI)* methods. These methods facilitate inspection by using a comparison between the scanned model of a manufactured part and its *Computer-Aided Design (CAD)* model. 3D optic and laser scanners allow obtaining triangulation of the surfaces of non-rigid manufactured parts without contact, e.g. without eventual deformation caused by contact with a probe. The raw output provided by these scanners is a 3D point cloud, from which a triangulated mesh can easily be obtained. Beholden to progress about CAD and CAI methods, fixtureless non-rigid inspection methods [3-12] are developed. These methods consist in virtually compensating for the compliance of non-rigid parts. The first step of all these fixtureless CAI methods for non-rigid parts, referred to as rigid registration, is searching for a rigid transformation matrix between CAD and scanned data. Then the effective core of these methods, referred to as non-rigid registration, consists in trying to find the best correspondence between CAD and scanned data, either by deforming scanned geometry to CAD geometry or by deforming CAD geometry to scanned geometry. The core idea behind these methods is trying to distinguish between flexible deformation of scanned model that is inherent to free-state and geometrical deviations associated with defects on the scanned model. These non-rigid registration methods thus virtually compensate for the flexible deformation of non-rigid parts in a free-state and allow the estimation of geometrical deviation on the manufactured parts with respect to their nominal CAD model.

In order to apply non-rigid registration methods based on deforming the scanned model towards the CAD model, as presented in [3-5], a time-consuming process of generating a FE mesh from the acquired point cloud (scanned model in free-state) is required. Then, the scanned mesh is deformed by applying a set of displacement boundary conditions (BCs) in a *Finite Element Analysis* (FEA). In the *virtual fixation concept* [3], these BCs are imposed on fixation features of the scanned mesh to displace them towards the corresponding features on the CAD model. Features such as mounting holes are identified as fixation features on the scanned model using feature extraction techniques [13]. BCs used in [4] are defined as specific displacement boundary conditions, applied on the scanned mesh, that minimize the location and orientation of fixation features between the predicted post-assembly shape (deformed scanned model) and CAD model. This aims at predicting assembly constraints that would be applied on the scanned model. These constraints are then used to perform a *virtual inspection* on the deformed scanned model in its assembly state. Inspiring an industrial inspection method in [5], the scanned model is virtually restrained by a combination of forces located on datum targets with the objective of minimizing the Euclidian distance between the shapes of deformed scanned and CAD model. However, automating the inspection process of these virtual inspection methods faces several obstacles such as generating FE meshes for each measured part and locating appropriate BCs for each scanned model. Therefore, non-rigid inspection methods based on applying FEA on CAD models instead of scanned models have been introduced in [6-12]. Indeed, these non-rigid inspection methods generally use meshes with better quality since these meshes are generated from CAD models. In this context, displacement BCs used in [6] are imposed on the fixation features of the CAD model to displace these features towards their corresponding features in the scanned model. In [7], a fixtureless inspection method is developed based on partial views of regions that need to be inspected. In this method, location of missing fixation features is approximated from an interpolating technique. The *Iterative Displacement Inspection* (IDI) algorithm [8, 9] is also an inspection process, which instead of using the information of fixation features, applies identification methods. Without using FEA, the smooth and iterative displacement

of CAD model towards the shape of scanned model is achieved through a specific identification algorithm, which allows distinguishing between defects and flexible deformation. The major drawback of IDI is that this identification algorithm is limited to localized defects, which makes it less general than other approaches. Assuming that the deformation of a non-rigid part in free-state is isometric (preserves geodesic distances), which means that there is no stretch in the deformation, the *Generalized Numerical Inspection Fixture* (GNIF) [10], see Appendix A, is presented as a registration method that claims ability to detect both small (local) and big (global) defects. This method starts with generating sets of corresponding sample points between CAD and scanned models. These corresponding sample points, along with bounding edges, assembly features [10] and/or specified pre-selected sample points on the CAD model [11] are then used as displacement BCs to deform the CAD model towards the scanned model through FEA. In [11] pre-selected sample points are in fact calculated as barycenters of sample points that are manually selected in specific areas on the model, which is an obstacle to fully automating the inspection process. Defects are then identified by generating a Euclidean distance between deformed CAD and scanned models. Due to significant scanning errors while capturing boundary edges, applying corresponding sample points located on bounding edges and assembly features may bring about inaccurate inspection results. Our team developed an automatic fixtureless inspection approach [12] that uses GNIF to generate a prior set of corresponding sample points. Then, sample points that are close to defects are filtered out, based on curvature and von Mises criteria, which leads to an accurate and automatic inspection results for non-rigid parts.

All these fixtureless CAI methods for non-rigid parts are based on using scanned data, which is acquired from scanning devices. It is commonly known that these data acquisition devices introduce measuring errors that are either due to their technical limits or to effects such as light fraction, reflectivity of the scanned surfaces or inaccessible features. Noisy scan data used in fixtureless CAI methods is likely to affect performance of these methods. Therefore, robustness of fixtureless CAI methods for non-rigid parts with respect to noisy scanned data should be assessed. One alternative in doing that is

using *Verification and Validation* (V&V) recommendations. Indeed, applying V&V recommendations to computational simulation models allows assessing accuracy and reliability of these models [14]. Verification relates to assessing the accuracy of a solution while validation relates to assessing the consistency of computational simulation results, if compared with the actual results. Due to various sources of uncertainty in computer codes and simulations, all computational models should be thoroughly verified and validated.

This paper is organized as follows. Section 5.3 presents our approach to automatic fixtureless CAI for non-rigid parts. It is followed, in section 5.4, by an introduction of ASME verification and validation (V&V) recommendations along with a presentation about how these methods are applied for assessing the robustness of our fixtureless CAI approach for non-rigid parts. Results obtained using our CAI method, along with an assessment of its performance and robustness based on V&V recommendations, are then presented in section 5.5. For this, two typical non-rigid parts used in the aerospace industry are considered along with various distributions of noise in scan data. The paper ends with a conclusion and ideas for future work in section 5.8.

5.3 Background on the approach to fixtureless CAI for non-rigid parts

As mentioned in Section 5.2, we have proposed, in a previous paper [12], a new automatic fixtureless CAI method for non-rigid manufactured parts using scan data in a free-state condition without any conformation or constrain operations. This method is based on FEA non-rigid registration and on two filters applied on corresponding sample points between scanned and CAD models. Basically, these filters allow making a difference between flexible deformation in a free-state and defects. The method is illustrated on a typical non-rigid aluminum panel, which is used in the aerospace industry. The CAD model of this panel is shown in Figure 5-2, and the associated simulated scanned model for inspection in a free-state is depicted in Figure 5-6-a. This scanned model includes

three bump defects, for which the nominal size and shape are known in order to assess the accuracy and robustness of inspection results.

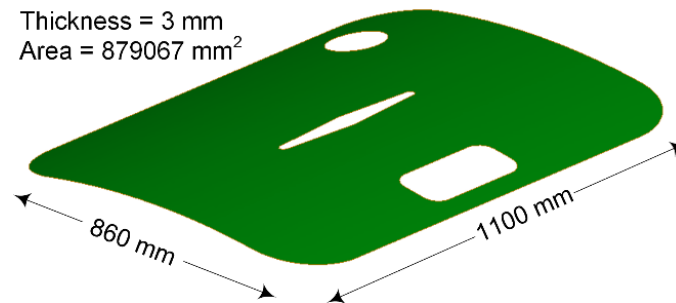


Figure 5-2: 3D view of the CAD model of a non-rigid aluminum panel.

A pre-registration, based on the ICP algorithm [15], best fits CAD and scanned models through a preliminary rigid registration. Then, the *Generalized Numerical Inspection Fixture* (GNIF) [10] method is applied to generate an initial set of evenly distributed corresponding sample points between nominal CAD and scan data in a free-state. Indeed as shown in Figure 5-3, based on an isometric deformation assumption, on *Generalized Multi-Dimensional Scaling* (GMDS) [16] and on computing geodesic distances with the *fast marching method* [17], GNIF generates a list of corresponding sample points on each model (CAD and scanned). Since mesh quality of the CAD model is generally better than that of the scanned model, *Finite Element Analysis Non-rigid Registration* (FENR) is applied on the CAD mesh. For this, corresponding sample points are inserted as nodes in the CAD mesh using a classical Delaunay point insertion method [18]. Displacement boundary conditions are then applied on these nodes, which deforms the CAD model to the scanned model via FENR. Since these corresponding sample points are evenly distributed over both CAD and scanned models, some of these points can be located, close to, or even on defects. If this occurs, it eventually results in an inaccurate estimation of the size of these defects since FENR tends to bring these nodes to the shape of defects. Thus, sample points that are close to defects must be filtered out. As explained in detail in [12], these sample points are successively filtered out based on two criteria: principal curvatures and von Mises stress. The process starts with applying a first FENR based on using all GNIF sample points. By doing that, the CAD model is deformed to take on the

shape of the scanned model, including in locations on and around defects. Then, analyzing the difference in principal curvatures between the initial CAD model and the deformed CAD model (after the first FENR) allows a first rough estimate of the location of defects. A first set of corresponding sample points that are close enough to these estimated defects is removed on both models and a second FENR is applied. The second filtration of sample points is applied, based on analyzing von Mises results obtained from this second FENR, which allows a better estimation of defects since some more sample points are filtered out. A third and last FENR is performed from sample points remaining. Initial GNIF corresponding sample points on the CAD model, as shown in Figure 5-4, are illustrated as red spots (●) while filtered sample points are illustrated as blue spots (●).

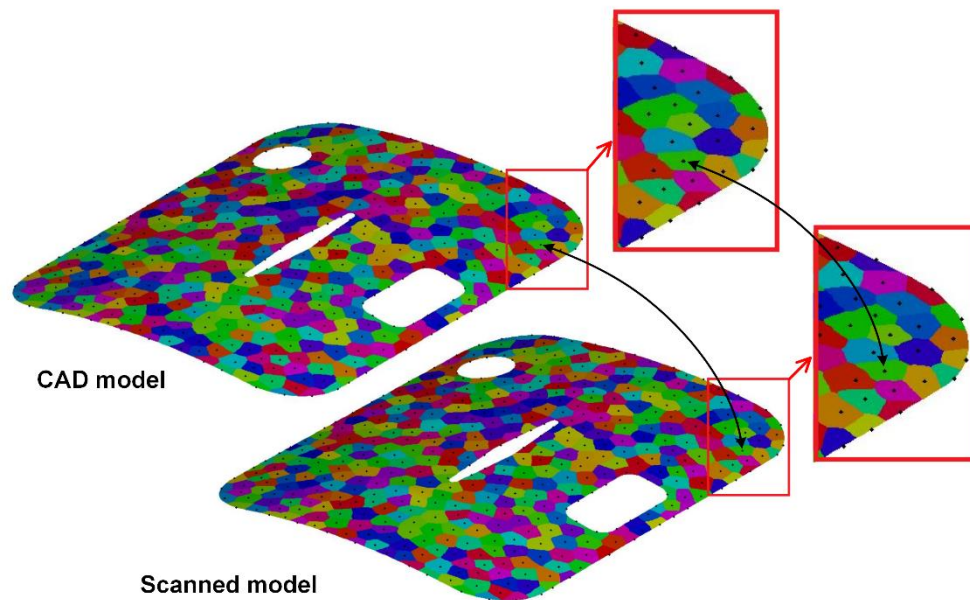


Figure 5-3: GNIF corresponding sample points (in black) are located in the center of colorful zones on the CAD and scanned models.

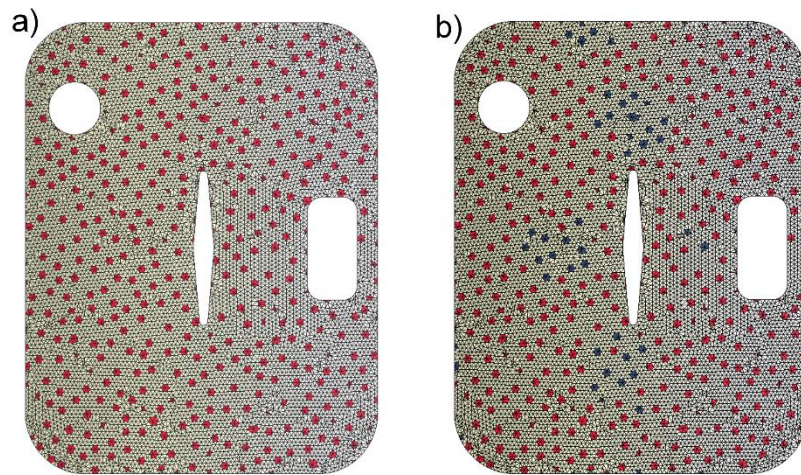


Figure 5-4: a) all GNIF sample points inserted into the CAD mesh based on classical Delaunay method (red spots) b) automatic sample point filtration based on curvature and von Mises stress criteria and criteria (blue spots).

Once this last FENR applied (in red in Figure 5-4-b) the CAD model is deformed to the scanned model in a free-state condition and color map of Euclidean distance distribution between the two models can be plotted. This graphical representation (shown in Figure 5-6-a) allows assessing the magnitude of defects with respect to a priori specified tolerance. According to ASME Y14.5 and ISO-GPS profile tolerance definition, defects are defined as zones for which the actual manufactured part deviates from the specified geometry, with respect to a tolerance value as specified on detailed engineering drawings. For all validation cases presented in this paper, ± 0.4 mm is considered as specified profile tolerance. 0.8 mm is indeed a representative geometric profile tolerance value for the type of thin-walled aerospace parts used in this paper. For a given part, N_{defect} refers to the number of defects identified on the scanned model. As shown in Figure 5-5, at the location of a given defect, the maximum deviation between nominal (after FENR) and specified geometry occurs at tip or valley of the defect i (wherein $i = 1, \dots, N_{defect}$). This deviation is referred to as the maximum amplitude of the defect i (D_i^{max}). At the location of a given defect we also assess the area of each defect. As illustrated in Figure 5-5, this area (A_i) is defined as the region of the actual geometry (after FENR) that is at a distance,

from the specified geometry, that exceeds the tolerance value. In Section 5.4.2, the analysis of defects will be pushed one more step forward by assessing the distance distribution of defects.

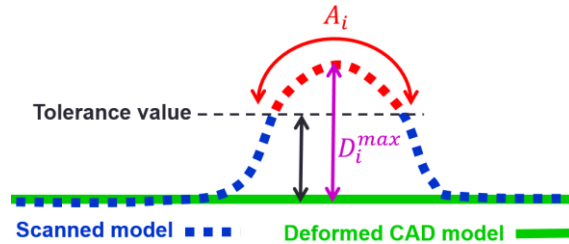


Figure 5-5: Definition of maximum amplitude D_i^{max} and area of a defect A_i .

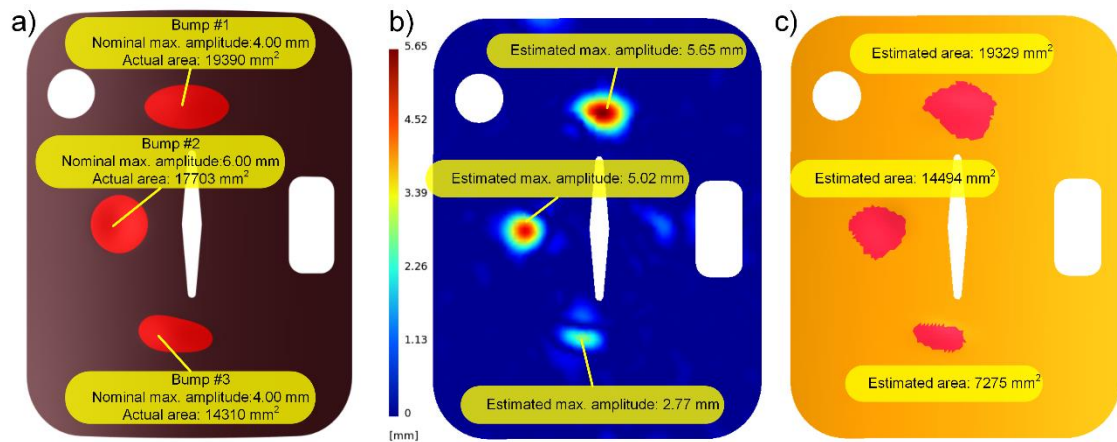


Figure 5-6: a) the scanned part with the nominal dimensions of defects b) estimated and nominal maximum amplitude (D_i^{max}) of defects [mm] c) estimated and nominal area (A_i shown as red zones) of defects [mm²].

The flowchart of our automatic fixtureless CAI method for non-rigid parts is illustrated in Figure 5-7. It shows that our CAI inspection method uses scan data, the CAD model, and a specified profile tolerance as input. Then using the GNIF method, sets of corresponding sample points are generated on CAD and scanned models. Sample points that are located around or on defects are filtered out and the CAD model is deformed towards the scanned model, to compensate for free-state deformation of the scanned. The output of this inspection process consists of a global distance distribution, as a color map,

the number of identified defects (N_{defect}) along with maximum amplitude (D_i^{max}) and its area (A_i) of each defect i .

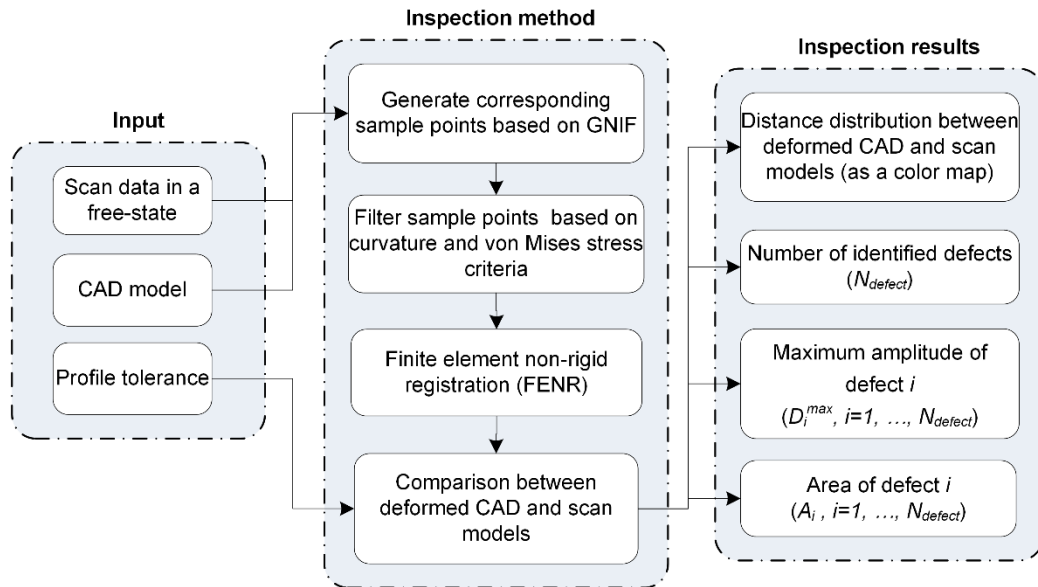


Figure 5-7: Flowchart of our automatic fixtureless CAI method.

Results obtained in estimating D_i^{max} (Figure 5-6-b) and A_i (Figure 5-6-c) of the three defects, in the part introduced in Figure 5-6-a, show that estimated inspection results are promising. Indeed, both maximum amplitude and area of defects are quite well estimated with respect to their nominal values for the three defects in the part. However, a further investigation of these inspection results can be made to assess similarity between distance distributions of estimated versus nominal defects.

5.4 Assessing the robustness of our CAI method based on ASME V&V recommendations

5.4.1 ASME recommendations for verification and validation

As introduced, all computational methods, among which CAI, include uncertainties and numerical errors that justify applying verification and validation (V&V) recommendations. A broad investigation of the application and theory of verification and

validation in computational engineering is presented in [19-21]. Traditional validation activities qualitatively measure the discrepancy through visual inspection of graphic plots between prediction and observation datasets [22], wherein uncertainties in the models are not taken into account. However, several disciplines, such as fluid and solid mechanics, have developed and applied systematic, rigorous and disciplined approaches for verifying and validating computational models in order to assess their prediction accuracy. For example, guides for V&V of computational solid mechanics [22], fluid dynamics [23], heat transfer [24] and material engineering [25] have already been published. Verification is defined as a process of determining how accurately a computational model represents the underlying mathematical model and its solution, while validation is defined as the process of determining the degree to which a model is an accurate representation of the real world. It is also stated that, in a V&V implementation, code verification must always precede its validation. This ASME standard concludes that system response features, validation testing and accuracy requirements are key elements of a V&V method in which the acceptable agreement for the predictive capability of the computational model is demonstrated by comparing its features of interest (validation metrics) with respect to the real model in its intended use.

In [26, 27] an overview of model validation metrics is presented as a quantitative measure of agreement between a predictive model and physical observation (measurements). In these references, a set of desired features that model validation metrics should process are highlighted and the validation metrics are categorized as hypothesis testing-based and distance-based. In [28], validation metrics are described by comparing the probability distributions of random variables representing the prediction and relevant observations. This comparison can be limited to assessing the difference between mean values of distributions or can be pushed further on comparing statistical shapes (behavior) of distributions for achieving a more detailed validation of the model. In order to perform this detailed comparison between statistic distributions, a test of significance from the hypothesis testing theory is applied. This test can be made through a comparison between cumulative distribution functions (CDFs) of estimated and actual results at a specific

significance level. Two hypotheses are considered for such a hypothesis test: a null hypothesis (H_0) against an alternative hypothesis (H_A). If CDFs of estimated and actual results are sufficiently close at a specific significance level, the test results in “we cannot reject H_0 ”. This means that the result only suggests that there is not sufficient evidence against H_0 , at the significance level, in favor of H_A . This does not necessarily mean that the null hypothesis is true. In contrast, the hypothesis test results in “reject of H_0 ” when the CDFs of estimated and actual results are not sufficiently close at the significance level. The significance level in hypothesis testing, referred to as α , is defined as the probability of rejecting H_0 when it is actually true, which is also known as “Type I” error (error α) in these tests. Moreover, a confidence level in hypothesis testing, defined as $(1 - \alpha)$, is the probability of accepting a null hypothesis while it is actually false. The confidence level defines a critical region, namely a confidence interval, in which a test can face a “Type II” error (error β). Specifying a lower significance level in a test reduces the chance of rejecting a valid null hypothesis, which reduces consequently the error “Type I”. In other words, a lower significance level increases the probability of accepting an invalid null hypothesis, which increases consequently the error “Type II” [22, 26, 29, 30]. Several research work, in various engineering fields such as structural dynamics [31], steady and transient heat conduction and shocks [32], thermal decomposition of polyurethane foam [33, 34] and sheet metal forming processes [35] have already considered validation metrics applied to numerical calculations, based on this type of statistical hypothesis testing for ASME V&V recommendations.

The hypothesis testing is extended to measure differences between empirical and prediction CDFs by applying fit tests such as the *Anderson–Darling* (A-D) test, the *Kolmogorov–Smirnov* (K-S) test, the *Cramer–von Mises* (C-vM) test, etc. [22, 36-38]. The K-S test [39, 40] used in this paper, is based on the maximum difference between empirical and hypothetical CDFs. It is a nonparametric test, which means that sampling distributions introduced in the test do not depend on any distribution parameters (imposed type of distribution, mean value, standard deviation, etc.).

The robustness of a computational model is related to its ability to provide satisfying results, which is also assessed by ASME V&V recommendations in this work, despite the presence of slight errors in the input data. In CAI, these errors principally originate from measurement noise that is inherent to optical and laser data acquisition tools. This means that the robustness of CAI methods should be studied with respect to scanning device noise [41, 42]. A 3D scanner analyses extracts, from a real-world object, scan data about the shape of this object. This data is translated into triangulated 3D models and consequently, a noisy data acquisition takes the form of noisy triangulations. Errors found in scanning device triangulations can originate from a systematic bias, due to an improper calibration of the device, and/or from random errors (noise) due to ambient light and characteristics of surfaces on which scan data is obtained, such as light refraction, reflectiveness, and transparency. As illustrated in [43], during 3D data acquisition, the length of measurement ray is elongated along the direction of the ray, due to beam reflection and propagation in diverse directions, which results in higher noise along the light beam than in along transverse directions. Although the noise distribution of a real scanner is not strictly Gaussian [41], experimental measurement of noise is often assumed to be Gaussian in many disciplines [43, 44]. Since a Gaussian noise gives low weight to outliers, the effect of noise amplitude is analyzed by changing the standard deviation of noise distribution. In this work, synthetic Gaussian noise with increasing amplitude is added to the scanned model to assess the effect of noise amplitude on the estimation of defects.

In the next section, K-S test is applied to develop a validation metric to assess the ability of our method in defect identification. This ability is investigated for different amplitudes of noise, which allows validating robustness of our automated inspection method.

5.4.2 Verification and validation methodology for CAI

Based on metrology standards, during an inspection, interest is put on estimating the magnitude of defects in a part. As mentioned, the magnitude of a defect i is basically represented by maximum amplitude (D_i^{max}) and its area (A_i). So, a first validation can be

done directly on these metrics [12]. However, a deeper investigation of inspection results can be made. It consists in assessing how accurately the CAI process is generally able to evaluate the distance distribution of defects. The distance distribution of a defect in a CAI is defined as the Euclidean distance value assigned to a set of nodes located on the identified defect of scanned mesh wherein the Euclidean distance between the scan model and deformed CAD model (after FENR) exceeds the tolerance value. Since the nominal distance distribution of defects is known, we can compare the estimated distance distribution of defects with the nominal ones to investigate the estimated inspection results. As introduced in the previous paragraphs, this comparison can be made based on verification and validation (V&V) recommendations and tools. We propose in this paper a validation metric that is intended to compare estimated defects versus nominal defects. As introduced in Section 5.3 (see Figure 5-5), maximum amplitude D_i^{max} and area A_i of defects, on a given manufactured part, are identified with respect to engineering tolerances. These characteristics of defects are obtained from Euclidean distance distributions between scan and CAD models. These distributions are computed as discrete Euclidean distances at each node of the scanned mesh and then a continuous distribution is calculated by interpolating these discrete distance across triangles of the scanned mesh. A defect is basically defined as a zone for which the actual manufactured part, once FENR applied, deviates from the specified geometry (outside the tolerance zone).

In this study, scanned models are simulated by adding defect (e.g. bumps) in CAD models, which is followed by applying an elastic deformation due to gravity and residual stress effects in free-state. By doing that (considering simulated defects) the distance distribution of defects, as estimated with our method, can be easily compared with the nominal distance distribution of defects, since it is known. The example introduced in section 5.3 (see Figure 5-6-a) features 3 bumps. Figure 5-8 presents, for these 3 bumps, a visual comparison between nominal and estimated identified defects.

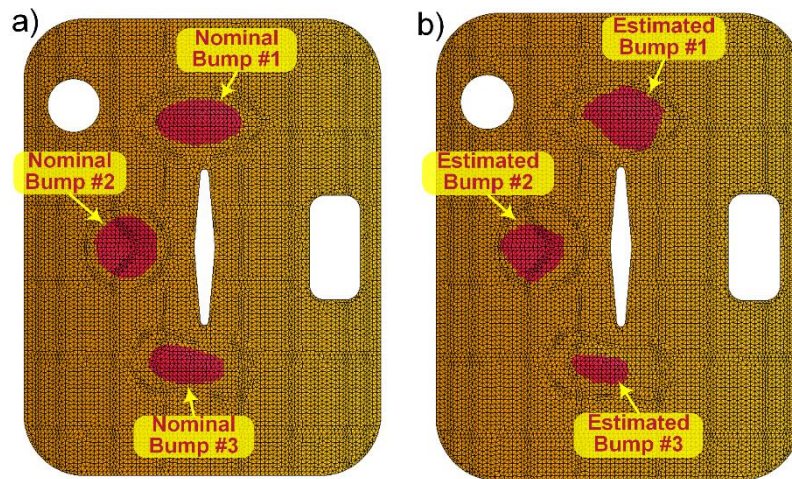


Figure 5-8: defects are identified as red zones based on the tolerance value (0.4 mm) a) for nominal defects b) for estimated defects.

The comparison between nominal and estimated defects is performed using a statistical validation method as presented in Section 5.4.1. It is based on ASME V&V recommendations and on the K-S test. The result of a K-S test at a given significance level is provided as a p-value that is calculated between two data sets (the two data sets and their sizes are referred to as n and n'). This p-value is related to K-S statistic, which is the maximum distance ($S_{n,n'}$) between CDFs of the two data sets, and to sizes of the 2 data sets. The p-value can be interpreted as a measure of plausibility of the null hypothesis (H_0). This means that if the K-S test results in a p-value that is higher than the significance level considered, “we cannot reject H_0 ”. In our case, the 2 data sets that are compared with a K-S test are the distance distributions (between CAD and scanned models) associated with nominal defects and respective estimated defects. Note that this comparison is performed defect by defect and not globally. Therefore, the null hypothesis for a K-S test is that the distance distributions associated with nominal and estimated defects are sufficiently similar. In general, supposing the size of sample data stays approximately unchanged, the probability of rejecting the null hypothesis increases when the maximum distance between CDFs of the two data increases. As a consequence, a K-S test will result in a lower p-value when $S_{n,n'}$ increases. This can be observed in

Figure 5-9 where a comparison is presented between the CDFs of nominal and estimated defects for Bump #1 and Bump #2 as defined in the example introduced above (Figure 5-6-a). It can be visually observed in Figure 5-8 that distance distributions of nominal and estimated defects for Bump #2 are likely to be more similar to each other than for Bump #1. This is reflected in the result of K-S test at 5% of significance level as presented in Figure 5-9. Indeed, for Bump #1 p-value is 0.000 (*with* $n = 180, n' = 192, S_{n,n'} = 0.211$) while for Bump #2 p-value is 0.356 (*with* $n = 195, n' = 157, S_{n,n'} = 0.098$). In this case, the result of the K-S test is that H_0 can be rejected for Bump #1 and that H_0 cannot be rejected for Bump #2.

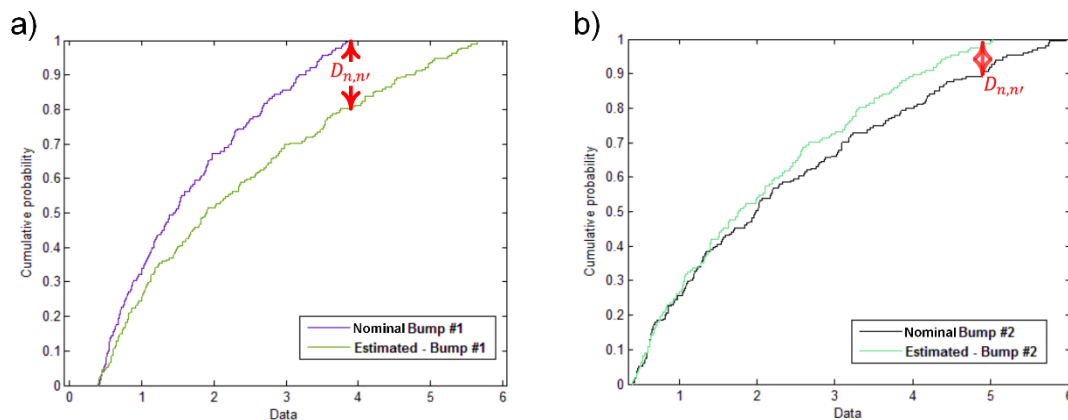


Figure 5-9: CDF for nominal and estimated defects for Bump #1 and Bump #2.

As introduced previously, validation tests on distance distributions (between CAD and scanned data) associated with each defect are performed as a comparison between the distance distribution of the nominal defect (Dd_a) and the distance distribution of the estimated defect as identified (Dd_e). Dd_a is calculated on the set of nodes associated with the nominal defect on the scanned mesh before adding the flexible deformation (shown as purple dots in Figure 5-10-a). Dd_e is calculated on the set of nodes associated with the estimated defect as identified, on the scanned mesh in a free-state (shown as red dots in Figure 5-10-b, c, and d). Subsequent comparisons are made, based on applying a K-S test on these two distance distributions. The distance distribution of a defect is well estimated or validated when this K-S test shows satisfying results (example shown in Figure 5-10-

b). When it is the case, enough sample points have been removed but not too many. Indeed, if too many sample points are removed, deformation in free-state is likely to be badly captured in FENR. In Figure 5-10-c, the deformed CAD model (after FENR) does not follow accurately enough the flexible deformation of the scanned model in free-state because too many sample points have been removed. This results in overestimating the defect. In this case, K-S test (Figure 5-10-b) will tend to “reject H_0 ”. In Figure 5-10-d, due to in-plane GNIF errors and to not removing enough sample points, CAD sample points are pushed to the defect shape. This leads to badly estimating the defect, but the result of K-S test associated with Figure 5-10-d depends on the location of falsely remaining sample points after filtering. If falsely remaining sample points are close to the tip of defect, the K-S test is likely to tend to “reject H_0 ”. On the contrary, if these falsely remaining sample points are far from the tip of defect, the distance distribution of estimated defect can still be statistically similar to the nominal one, wherein the K-S test is likely to tend to “cannot reject H_0 ”.

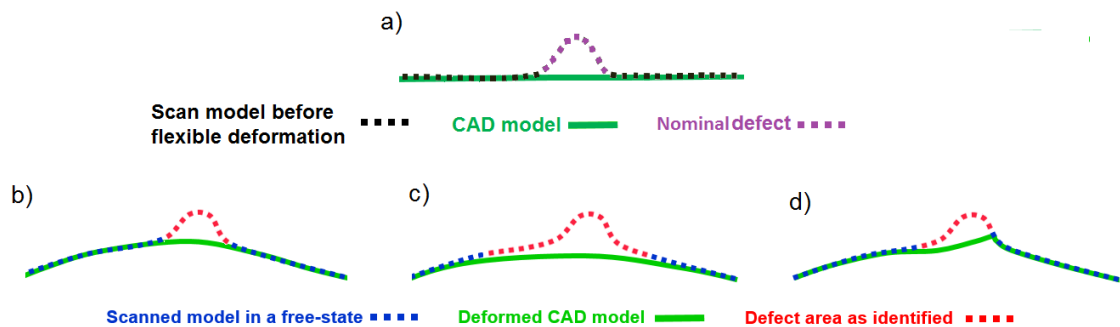


Figure 5-10: Estimation of the distance distribution of a defect a) nominal defect, b) for an accurate inspection c) for an overestimated defect d) for a badly estimated defect.

5.4.3 Robustness of our CAI method

As mentioned above, synthetic noise is added to the simulated scan data. This is aimed at replicating the actual noise that cannot be avoided in real scan data during the scanning (digitization) process. Since this noise is synthetic, various amplitudes and distributions of noise can be considered, which allows assessing the robustness of our automatic

fixtureless inspection method for non-rigid parts. Synthetic noise applied is Gaussian and since the magnitude of noise for optic and laser scanners is much higher along the beam direction, this synthetic noise is added as random numbers to node coordinates of the scanned mesh in the normal direction (perpendicular to the surface). These random numbers are generated as Gaussian distributions with null mean values ($\mu=0$) and with three different standard deviations (σ): 0.01, 0.02 and 0.03 mm. In order to keep the magnitude of noise in a reasonable range with respect to tolerances, these random numbers are taken in the $[-2\times\sigma, 2\times\sigma]$ interval for a given standard deviation (σ). For the part introduced in Figure 5-6-a, 4 scan models are presented and compared in Figure 5-11 with various amplitudes of noise.

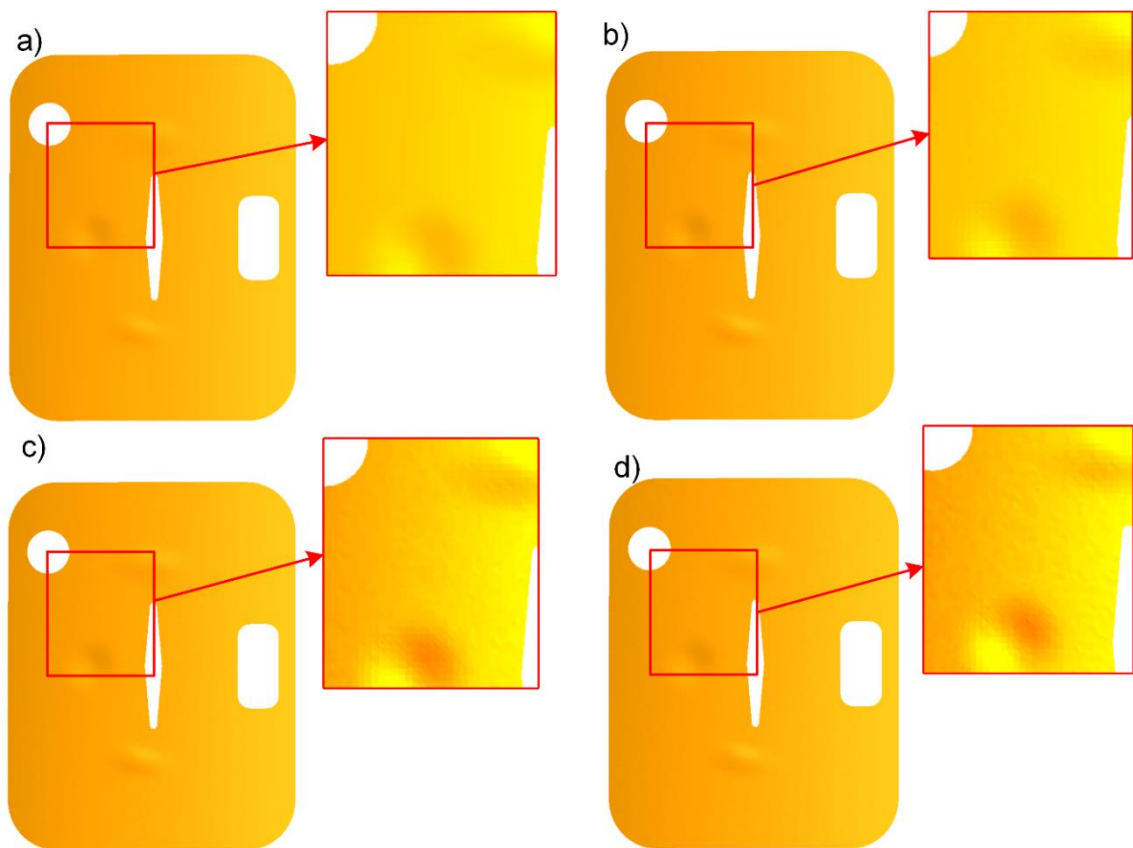


Figure 5-11: a) a noise-free scan mesh b), c), d) scan meshes with synthetic noise with Gaussian distribution with zero mean value and standard deviation equal to b) 0.01mm c) 0.02mm d) 0.03mm.

The model shown in Figure 5-11-a is noise-free while the models shown in Figure 5-11-b, Figure 5-11-c, and Figure 5-11-d were respectively generated using standard deviations equal to 0.01, 0.02 and 0.03 mm.

In the next section, our automatic and fixtureless CAI method for non-rigid parts is applied and validated in several cases. These cases consider 2 different parts with, for each part, different types and distributions of defects, different deformations associated with the free-state and different amplitudes of noise.

5.5 Validation results for cases with small free-state deformation

5.5.1 Validation cases considered

In this section, the robustness of our automatic and fixtureless CAI method is validated on two aluminum parts (referred to as part A and part B). Part A is the part introduced in Figure 5-2, and part B is a second non-rigid part, which is also typical of non-rigid parts used in the aerospace industry (see Figure 5-16). It is worthy to mention that scan models used as validation cases in this article are simulated by deforming CAD models via FEA and by adding geometrical deviations (defects). To this end, one single free-state deformation (referred to as bending) is applied on part A while two free-state deformations are considered for part B (referred to as bending and torsion). For both parts, as illustrated in Figure 5-12, small (local) and big (global) defects are considered. For each validation case, the robustness of our inspection method is studied by applying synthetic noise, as introduced above. Since defects are a priori known for all case studies considered, comparisons can be made between size, area and distance distributions of estimated defects in comparison with nominal defects.

For maximum amplitude and area of defects, absolute (in mm) and relative (in percentage) error between estimated and nominal sizes of defects are calculated for each case, using:

$$\text{Absolute error (mm)} = (\text{estimated size}) - (\text{nominal size}) \tag{5-1}$$

$$\text{Relative error (\%)} = \frac{(\text{estimated size}) - (\text{actual size})}{(\text{actual size})} \times 100 \tag{5-2}$$

Therefore, in results presented below, for both maximum amplitude and area of defects, negative error values represent an underestimation of defects and positive error values an overestimation of defects.

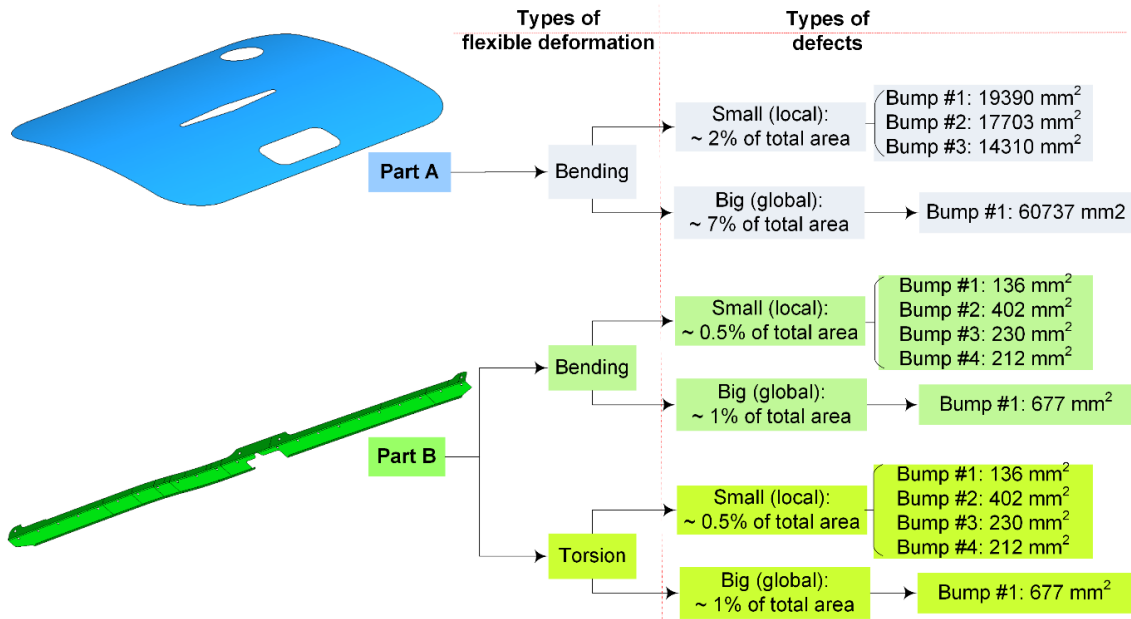


Figure 5-12: Synthesis of validation cases with small free-state deformation.

We have successfully implemented our automated and fixtureless CAI method and its validation using several tools. GNIF calculations are carried out using a MATLAB™ code to generate sets of corresponding sample points. The generation of around 500 corresponding sample points, with this code, takes approximately 8 minutes on a computer equipped with an Intel^(R) Core™ i7 at 3.60 GHz with 32 GB RAM. Mesh generation, mesh transformation, discrete curvature calculations, FEA non-rigid registration and Euclidean distance calculations between deformed CAD and scan data

are performed using the research platform developed by our research team [45]. This platform is based on C⁺⁺ code, on Open CASCADE[™] libraries for geometry and on Code_Aster[™] as FEA solver. We also use Gmsh[™] [46] for visualizing 3D models and distance distributions. Sample points filtering takes around 2 minutes for a CAD mesh featuring 10545 nodes on a computer with specifications as mentioned above. Finally, the K-S tests are performed in a negligible CPU time by applying MATLAB[™] (using *kstest2*) to validate the distance distribution of estimated defects.

5.5.2 Results for part A

The first model, referred to as part A, is shown in Figure 5-2 and Figure 5-13. This part is approximately 1100 mm long, 860 mm wide and 3 mm thick with 879067 mm² area. The scanned model associated with this model in free-state is simulated using a bending deformation for which maximum displacement is approximately 10 mm. Thus, if compared to the part dimensions (1100 mm length) this state of deformation is consistent with a small displacement assumption.

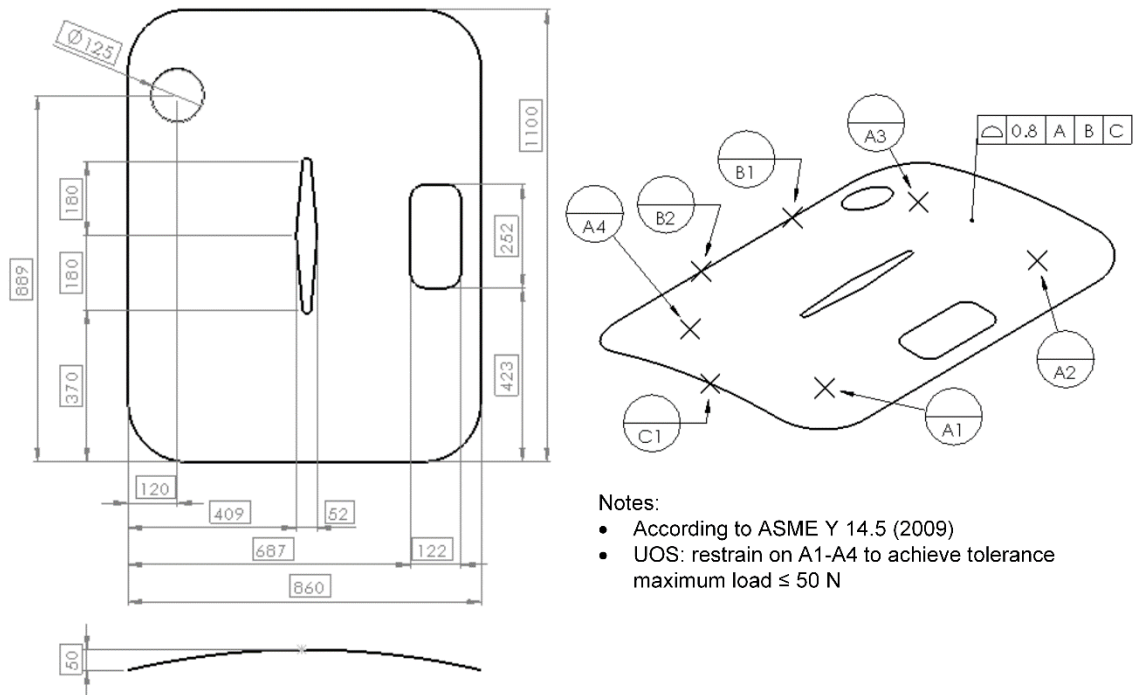


Figure 5-13: CAD model along with GD&T specification for part A (dimensions are in mm).

Depending on the case considered, the scanned model of part A features two types of defects, small (local) defects (see Figure 5-6-a) or big (global) defects (see Figure 5-15-a). The distance distribution related to the nominal size of defects for part A, with small (local) defects, is presented in Figure 5-14-a. Estimated inspection results, as distance distributions, are illustrated with noise-free and different noisy scanned meshes in Figure 5-14-b, c, d and e wherein the noise amplitude are increasing (as mentioned previously for a noisy scanned model with a standard deviation of 0.01, 0.02 and 0.03 mm respectively).

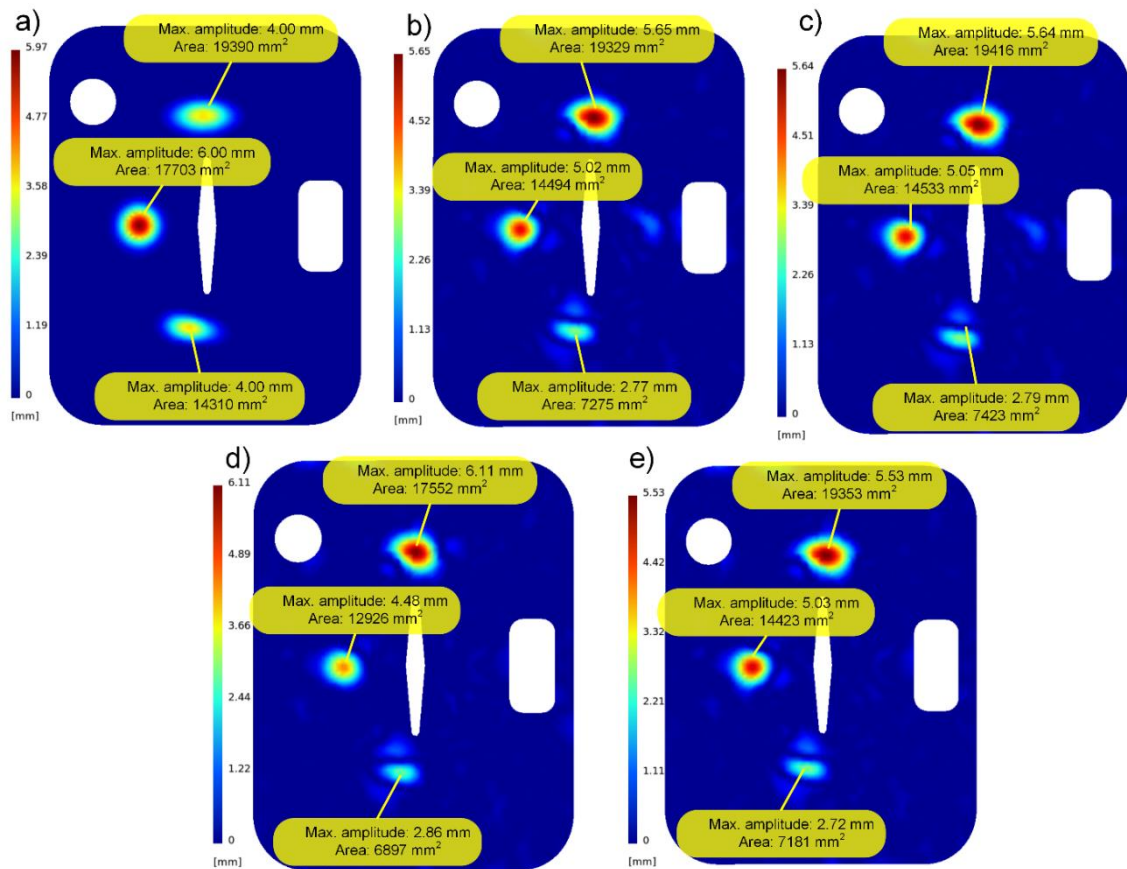


Figure 5-14: a) nominal defect distance distribution for part A with small (local) defects, comparison between the CAD and scanned model of part A with small (local) defects and bending deformation as a distance distribution for b) noise-free scan mesh c) noisy scan mesh with $\sigma=0.01$ mm d) noisy scan mesh with $\sigma=0.02$ mm e) noisy scan mesh with $\sigma=0.03$ mm.

It is worth noting that the flexible deformation and the nominal size of defects are the same for all noise-free and noisy scanned meshes. Results obtained with our automatic fixtureless CAI method (maximum amplitude and area of defects) are summarized in Table 5-1. These results show that the estimation of maximum amplitude is better for Bump #2 than for Bump #3 and especially for Bump #1. Regarding the estimation of defects area, these results show that area is well estimated for Bump #1 and is reasonably estimated for Bump #2. These results also show that the presence of noise as well as



increasing the amplitude of noise has not a very significant effect on the estimation of maximum amplitude and area of defects. As introduced in section 3.2, the robustness of our method is validated by applying K-S test for distance distribution of defects as identified (Table 5-2) using the K-S test on these inspection results. The K-S test results presented in this paper are illustrated with colors (green for “ H_0 cannot be rejected”, red for “ H_0 is rejected” and brown for “ H_0 is borderline”). Results presented in Table 5-2 globally show that, according to the V&V process presented in this paper, distance distributions for Bump #2 and Bump #3 are considered as sufficiently similar to the nominal distance distributions, at a 5% significance level, which is not the case for Bump #1. As explained in section 5.4.2, for Bump #1, too many sample points are filtered out close to the defect (see Figure 5-4-b), which implies that the deformed CAD model cannot accurately fit free-state deformation of the scanned model. This leads to overestimating the maximum amplitude of this defect.

Table 5-1: Estimated size of defects and errors for part A with small (local) defects and bending deformation.

		Maximum amplitude of defects (D_i^{max})				Area of defects (A_i)			
		Nominal [mm]	Estimated [mm]	Absolute error [mm]	Error [%]	Nominal [mm ²]	Estimated [mm ²]	Absolute error [mm]	Error [%]
BUMP #1	Noise-free	4.00	5.65	1.65	41.16	19390	19329	-61	-0.31
	$\sim N(0, \sigma = 0.01)$	4.00	5.64	1.64	41.08	19390	19416	26	0.13
	$\sim N(0, \sigma = 0.02)$	4.00	6.11	2.11	52.71	19390	17552	-1838	-9.48
	$\sim N(0, \sigma = 0.03)$	4.00	5.53	1.53	38.24	19390	19353	-37	-0.19
BUMP #2	Noise-free	6.00	5.02	-0.98	-16.33	17703	14494	-3209	-18.13
	$\sim N(0, \sigma = 0.01)$	6.00	5.05	-0.95	-15.78	17703	14533	-3170	-17.91
	$\sim N(0, \sigma = 0.02)$	6.00	4.48	-1.52	-25.33	17703	12926	-4777	-26.98
	$\sim N(0, \sigma = 0.03)$	6.00	5.03	-0.97	-16.10	17703	14423	-3281	-18.53
BUMP #3	Noise-free	4.00	2.77	-1.23	-30.75	14310	7275	-7035	-49.16
	$\sim N(0, \sigma = 0.01)$	4.00	2.79	-1.21	-30.34	14310	7423	-6887	-48.12
	$\sim N(0, \sigma = 0.02)$	4.00	2.86	-1.14	-28.50	14310	6897	-7413	-51.81
	$\sim N(0, \sigma = 0.03)$	4.00	2.72	-1.28	-32.00	14310	7181	-7129	-49.82

Table 5-2: Validation results with K-S tests (H_0 : the distance distribution of nominal and estimated defects are sufficiently similar) at 5% significance level for part A with small (local) defects and bending deformation.

		p-value
BUMP #1	Noise-free	0.000
	$\sim N(0, \sigma = 0.01)$	0.000
	$\sim N(0, \sigma = 0.02)$	0.000
	$\sim N(0, \sigma = 0.03)$	0.001
BUMP #2	Noise-free	0.356
	$\sim N(0, \sigma = 0.01)$	0.376
	$\sim N(0, \sigma = 0.02)$	0.039
	$\sim N(0, \sigma = 0.03)$	0.293
BUMP #3	Noise-free	0.144
	$\sim N(0, \sigma = 0.01)$	0.141
	$\sim N(0, \sigma = 0.02)$	0.235
	$\sim N(0, \sigma = 0.03)$	0.090

■ H_0 is rejected
 ■ H_0 cannot be rejected
 ■ H_0 is borderline

In the following paragraph, as presented in Figure 5-12, another validation case is applied on part A. The difference with previous cases is about defects. For this new case, scan data includes a big (global) defect instead of three small (local) defects. The nominal size of this defect is illustrated, as a distance distribution, in Figure 5-15-a. It is compared with results provided by our automatic fixtureless CAI method with bending deformation in Figure 5-15-b for noise-free scan data. Inspection results for noisy scanned meshes (with $\sigma = 0.01, 0.02$ and 0.03 mm) are also shown respectively in Figure 5-15-c, d, and e. Maximum amplitude and area of estimated defects along with the relative error with respect to the nominal size of defect are summarized in Table 5-3. Like in the previous case for this part, these results show that the defect size is reasonably well estimated, and that noise does not seem to have a clear effect and a potential worsening of estimation results.

As for small (local) defects, the validation of these results based on K-S test at a 5% significance level, for distance distribution of defects as identified is presented in Table 5-4. In this case, V&V results show that the distance distribution of the estimated defect is sufficiently similar to the nominal defect at a 5% significance level.

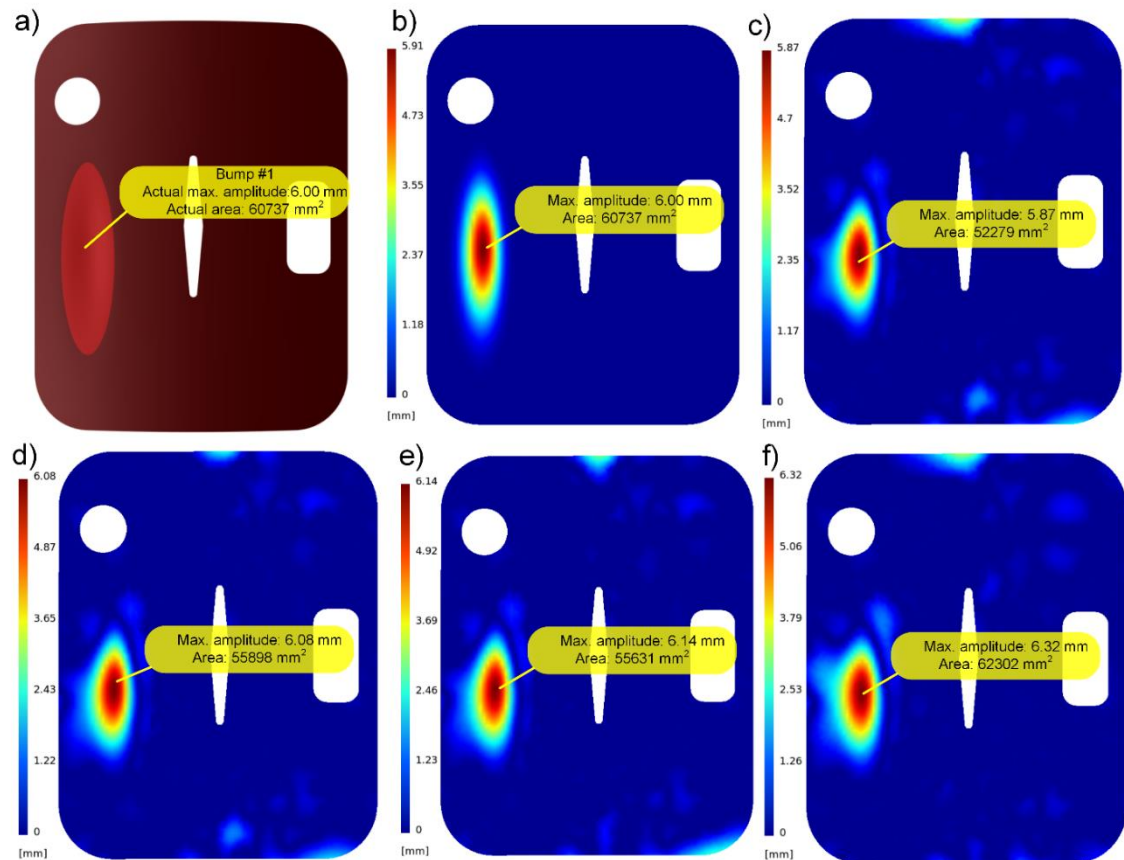


Figure 5-15: a) the scanned part with the nominal dimensions of big (global) defect b) nominal defect distance distribution for part A with a big (global) defect, comparison between the CAD and scanned model of part A with a big (global) defect and bending deformation as a distance distribution for c) noise-free scan mesh d) noisy scan mesh with $\sigma=0.01$ mm e) noisy scan mesh with $\sigma=0.02$ mm f) noisy scan mesh with $\sigma=0.03$ mm.

Table 5-3: Estimated size of defects and errors for part A with a big (global) defect and bending deformation.

		Maximum amplitude of defects (D_i^{max})				Area of defects (A_i)			
		Nominal [mm]	Estimated [mm]	Absolute error [mm]	Error [%]	Nominal [mm ²]	Estimated [mm ²]	Absolute error [mm]	Error [%]
BUMP #1	Noise-free	6.00	5.87	-0.13	-2.16	60737	52279	-8458	-13.93
	$\sim N(0, \sigma = 0.01)$	6.00	6.08	0.08	1.41	60737	55898	-4839	-7.97
	$\sim N(0, \sigma = 0.02)$	6.00	6.14	0.14	2.40	60737	55631	-5106	-8.41
	$\sim N(0, \sigma = 0.03)$	6.00	6.32	0.32	5.37	60737	62302	1565	2.58

Table 5-4: Validation results with K-S tests (H_0 : the distance distribution of nominal and estimated defects are sufficiently similar) at 5% significance level for part A with a big (global) defect and bending deformation.

		p-value
BUMP #1	Noise-free	0.755
	$\sim N(0, \sigma = 0.01)$	0.865
	$\sim N(0, \sigma = 0.02)$	0.930
	$\sim N(0, \sigma = 0.03)$	0.414

■ H_0 is rejected
 ■ H_0 cannot be rejected
 ■ H_0 is borderline

5.5.3 Results for part B

Next validation cases are intended to validate the robustness of our automatic fixtureless inspection method for non-rigid parts on a more featured type part (referred to as part B in Figure 5-12). This part, shown in Figure 5-16, is a long part which is also inspired from parts used in the aerospace industry. It features more details and smaller features as well as higher curvature in some locations. This part, made of aluminum, is approximately 1150 mm long and dimensions of the U channel are approximately $20 \times 40 \times 7$ mm with 1 mm thickness. As synthesized in Figure 5-12, two types of defects (small (local) and big (global)) are applied on this part as well as two types flexible deformation in a free-state. One is referred to as bending deformation (Figure 5-17-a) and the other one as torsion deformation (Figure 5-17-b). In both cases, these free-state deformations are consistent with a small displacement assumption.

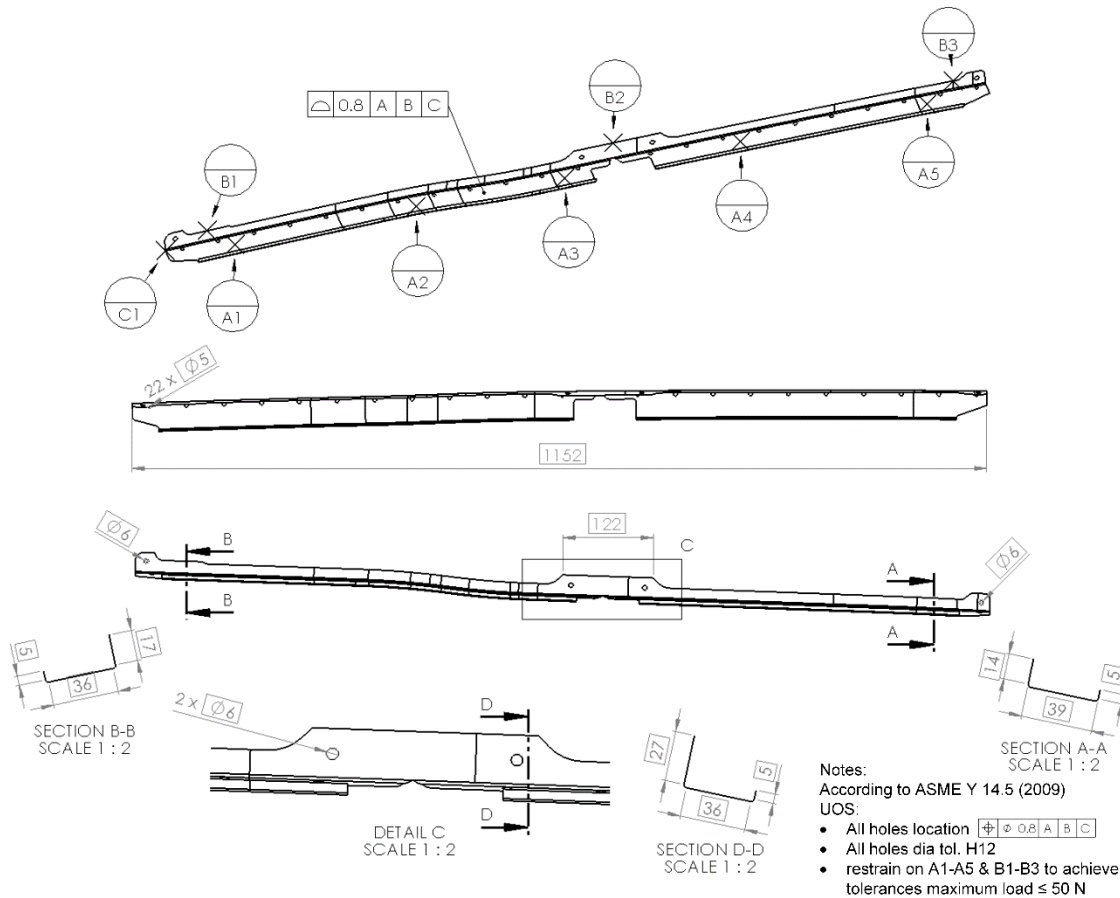


Figure 5-16: CAD model along with GD&T specification for part B (dimensions are in mm).

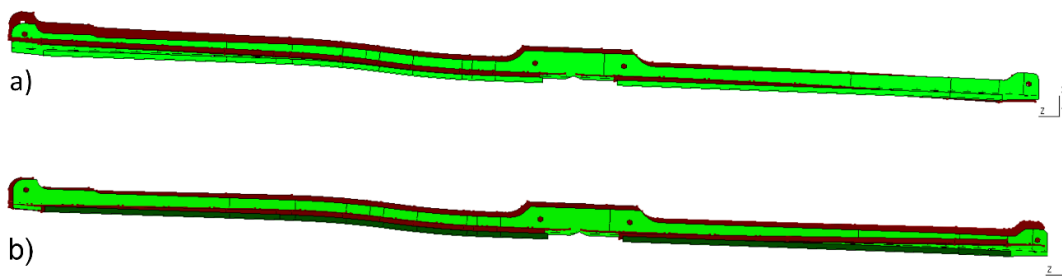


Figure 5-17: Side views of the CAD model for part B (in green) compared with scan data in a free-state (in brown) with a) bending deformation b) torsion deformation.

In the first validation case for part B, the flexible deformation of the scanned model in a free-state is simulated by bending, and four small (local) bump defects are applied. The

nominal size of defects (amplitude and area) for this case are presented in Figure 5-18-a. The nominal size of defects is compared with results provided by our automatic fixtureless CAI method with bending deformation in Figure 5-18-b for noise-free scan data. Inspection results for noisy scanned meshes (with $\sigma = 0.01, 0.02$ and 0.03 mm) are also shown respectively in Figure 5-18-c, d, and e.

Maximum amplitude and area of estimated defects along with the relative error with respect to the nominal size of defects are summarized in Table 5-5. In this case, amplitude and area of defects are estimated with reasonably good accuracy in all cases and for all defects. These results also show that noise does not have a negative effect on the estimation of defects. In some cases, noise can surprisingly even improve defect identification instead of worsening it. Validation of these results, based on K-S test at a 5% significance level, is presented in Table 5-7. V&V results for this case show that the distance distribution of defects is quite well estimated at a 5% significance level.

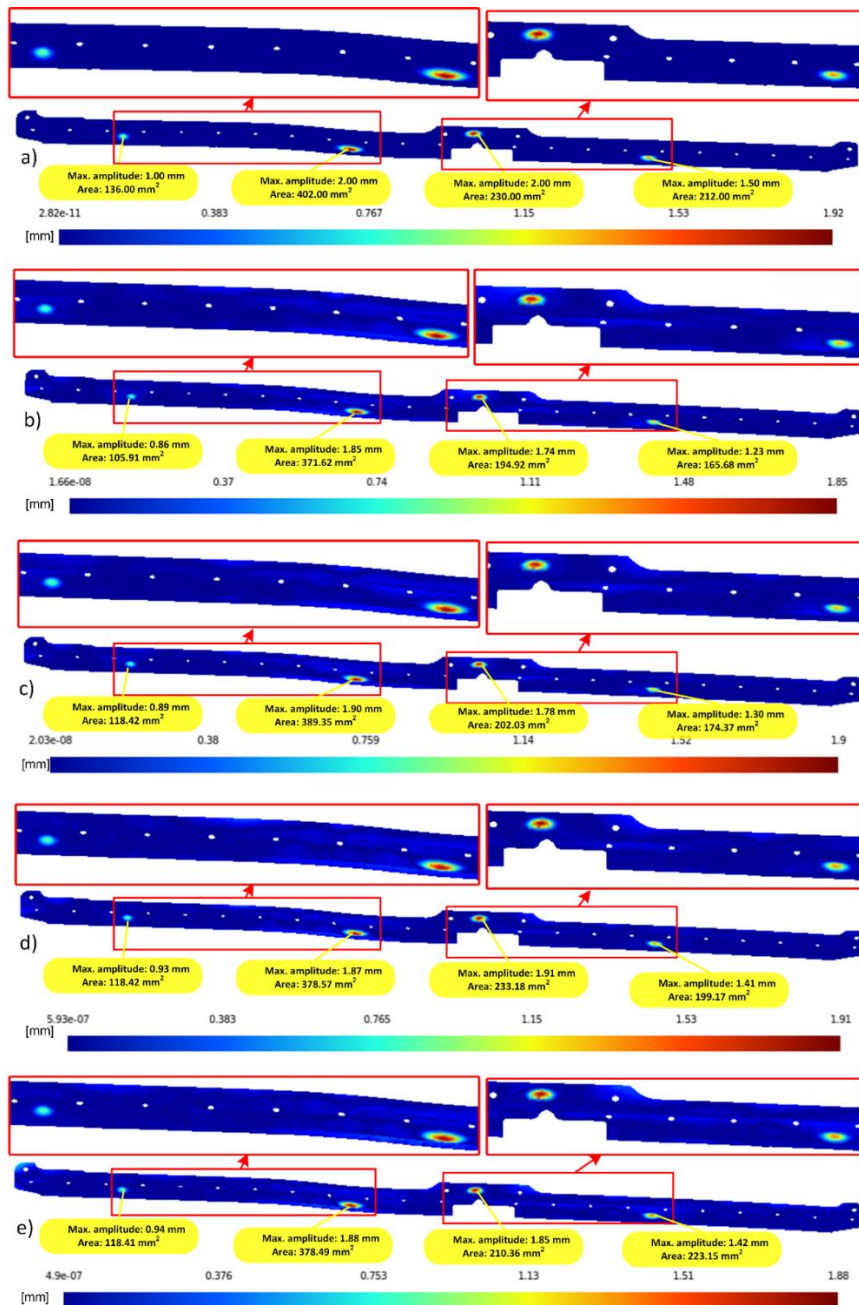


Figure 5-18: a) nominal defect distance distribution for part B with small (local) defects, comparison between the CAD and scanned model with small (local) defects and bending deformation as a distance distribution for b) noise-free scan mesh c) noisy scan mesh with $\sigma=0.01$ mm d) noisy scan mesh with $\sigma=0.02$ mm e) noisy scan mesh with $\sigma=0.03$ mm.

Table 5-5: Estimated size of defects and errors for part B with small (local) defects and bending deformation.

		Maximum amplitude of defects (D_i^{max})				Area of defects (A_i)			
		Nominal [mm]	Estimated [mm]	Absolute error [mm]	Error [%]	Nominal [mm ²]	Estimated [mm ²]	Absolute error [mm]	Error [%]
BUMP #1	Noise-free	1.00	0.86	-0.14	-14.00	136	106	-30	-22.13
	$\sim N(0, \sigma = 0.01)$	1.00	0.89	-0.11	-11.00	136	118	-18	-12.93
	$\sim N(0, \sigma = 0.02)$	1.00	0.93	-0.07	-7.00	136	118	-18	-12.91
	$\sim N(0, \sigma = 0.03)$	1.00	0.94	-0.06	-6.00	136	118	-18	-12.93
BUMP #2	Noise-free	2.00	1.85	-0.15	-7.50	402	372	-30	-7.56
	$\sim N(0, \sigma = 0.01)$	2.00	1.90	-0.10	-5.00	402	389	-13	-3.15
	$\sim N(0, \sigma = 0.02)$	2.00	1.87	-0.13	-6.50	402	379	-23	-5.83
	$\sim N(0, \sigma = 0.03)$	2.00	1.88	-0.12	-6.00	402	378	-24	-5.85
BUMP #3	Noise-free	2.00	1.74	-0.26	-13.00	230	195	-35	-15.25
	$\sim N(0, \sigma = 0.01)$	2.00	1.78	-0.22	-11.00	230	202	-28	-12.16
	$\sim N(0, \sigma = 0.02)$	2.00	1.91	-0.09	-4.50	230	233	3	1.38
	$\sim N(0, \sigma = 0.03)$	2.00	1.85	-0.15	-7.50	230	210	-20	-8.54
BUMP #4	Noise-free	1.50	1.23	-0.27	-18.00	212	166	-46	-21.85
	$\sim N(0, \sigma = 0.01)$	1.50	1.30	-0.20	-13.33	212	174	-38	-17.75
	$\sim N(0, \sigma = 0.02)$	1.50	1.41	-0.09	-6.00	212	199	-13	-6.05
	$\sim N(0, \sigma = 0.03)$	1.50	1.42	-0.08	-5.33	212	223	11	5.26

The nominal size of defects for part B with small (local) defects (Figure 5-19-a) is then compared with results provided by our automatic fixtureless CAI method, with torsion deformation, in Figure 5-19-b for noise-free scan data. Inspection results for noisy scanned meshes (with $\sigma = 0.01, 0.02$ and 0.03 mm) are also shown respectively in Figure 5-19-c, d, and e. Maximum amplitude and area of estimated defects along with the relative error with respect to the nominal size of defects are summarized in Table 5-6. Like in the first case for part B, these results also show that noise does not have a negative effect on the estimation of defects and that the estimation is even improved with noise for some cases. Amplitude and area of defects are estimated with reasonably good accuracy in general with higher errors for Bump #1 and Bump #2. As for bending deformation, validation of these results, based on K-S test at a 5% significance level, are presented in Table 5-7. V&V results show that the distance distribution of defects zones is well estimated in all cases.

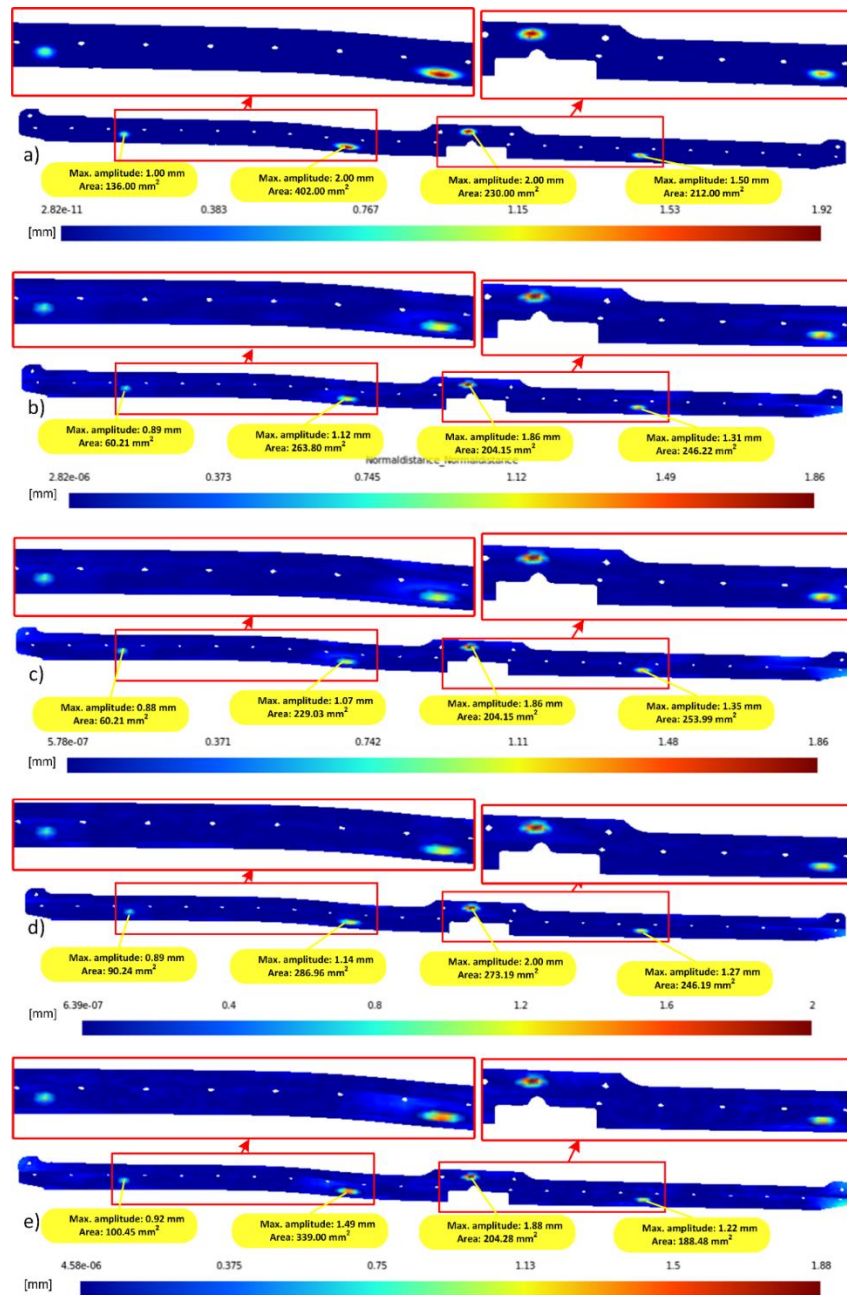





Figure 5-19: a) nominal defect distance distribution for part B with small (local) defects, comparison between the CAD and scanned model with small (local) defects and torsion deformation as a distance distribution for b) noise-free scan mesh c) noisy scan mesh with $\sigma=0.01$ mm d) noisy scan mesh with $\sigma=0.02$ mm e) noisy scan mesh with $\sigma=0.03$ mm.

Table 5-6: Estimated size of defects and errors for part B with small (local) defects and torsion deformation.

		Maximum amplitude of defects (D_i^{max})				Area of defects (A_i)			
		Nominal [mm]	Estimated [mm]	Absolute error [mm]	Error [%]	Nominal [mm ²]	Estimated [mm ²]	Absolute error [mm]	Error [%]
BUMP #1	Noise-free	1.00	0.89	-0.11	-11.00	136	90	-46	-33.67
	$\sim N(0, \sigma = 0.01)$	1.00	0.88	-0.12	-12.00	136	90	-46	-33.67
	$\sim N(0, \sigma = 0.02)$	1.00	0.89	-0.11	-11.00	136	90	-46	-33.65
	$\sim N(0, \sigma = 0.03)$	1.00	0.92	-0.08	-8.00	136	100	-36	-26.14
BUMP #2	Noise-free	2.00	1.12	-0.88	-44.00	402	264	-138	-34.38
	$\sim N(0, \sigma = 0.01)$	2.00	1.07	-0.93	-46.50	402	229	-173	-43.03
	$\sim N(0, \sigma = 0.02)$	2.00	1.14	-0.86	-43.00	402	287	-115	-28.62
	$\sim N(0, \sigma = 0.03)$	2.00	1.49	-0.51	-25.50	402	339	-63	-15.67
BUMP #3	Noise-free	2.00	1.86	-0.14	-7.00	230	204	-26	-11.24
	$\sim N(0, \sigma = 0.01)$	2.00	1.86	-0.14	-7.00	230	204	-26	-11.24
	$\sim N(0, \sigma = 0.02)$	2.00	2.00	0.00	0.00	230	273	43	18.78
	$\sim N(0, \sigma = 0.03)$	2.00	1.88	-0.12	-6.00	230	204	-26	-11.18
BUMP #4	Noise-free	1.50	1.31	-0.19	-12.67	212	246	34	16.14
	$\sim N(0, \sigma = 0.01)$	1.50	1.35	-0.15	-10.00	212	254	42	19.81
	$\sim N(0, \sigma = 0.02)$	1.50	1.27	-0.23	-15.33	212	246	34	16.13
	$\sim N(0, \sigma = 0.03)$	1.50	1.22	-0.28	-18.67	212	188	-24	-11.09

Table 5-7: Validation results with K-S tests (H_0 : the distance distribution of nominal and estimated defects are sufficiently similar) at 5% significance level for part B with small (local) defects under bending and torsion deformation.

		Bending deformation p-value	Torsion deformation p-value
BUMP #1	Noise-free	0.534	0.318
	$\sim N(0, \sigma = 0.01)$	0.820	0.318
	$\sim N(0, \sigma = 0.02)$	0.891	0.550
	$\sim N(0, \sigma = 0.03)$	0.625	0.318
BUMP #2	Noise-free	0.890	0.433
	$\sim N(0, \sigma = 0.01)$	0.990	0.254
	$\sim N(0, \sigma = 0.02)$	0.998	0.471
	$\sim N(0, \sigma = 0.03)$	0.995	0.791
BUMP #3	Noise-free	0.740	0.997
	$\sim N(0, \sigma = 0.01)$	0.896	0.997
	$\sim N(0, \sigma = 0.02)$	0.999	0.768
	$\sim N(0, \sigma = 0.03)$	0.988	0.997
BUMP #4	Noise-free	0.864	0.957
	$\sim N(0, \sigma = 0.01)$	0.955	0.957
	$\sim N(0, \sigma = 0.02)$	0.931	1.000
	$\sim N(0, \sigma = 0.03)$	0.996	0.982

 H_0 is rejected
  H_0 cannot be rejected
  H_0 is borderline

Two other validation cases are also applied on part B with a big (global). The nominal size of this defect is illustrated, as a distance distribution, in Figure 5-20-a. It is compared with results provided by our automatic fixtureless CAI method with bending deformation in Figure 5-20-b for noise-free scan data. Inspection results for noisy scanned meshes (with $\sigma = 0.01, 0.02$ and 0.03 mm) are also shown respectively in Figure 5-20-c, d, and e. Maximum amplitude and area of estimated defects along with the relative error with respect to the nominal size of defects are summarized in Table 5-8. Like in the two first cases for part B, these results also show that noise does not generally have a negative

effect on the estimation of area and the maximum amplitude of the defect, except for $\sigma = 0.01$ mm. Also, except for $\sigma = 0.01$ mm in this case, amplitude and area of the defect are estimated with good accuracy. As for bending deformation, validation of these results, based on K-S test at a 5% significance level, is presented in Table 5-10. These V&V results confirm that the big (global) defect under bending free-state deformation is well estimated, except for $\sigma = 0.01$ mm. This last result (for $\sigma = 0.01$ mm) is due to the presence of high magnitude noise around the defect, which makes that the inspection method filters out too many sample points around the defect, which leads to overestimating the defect.

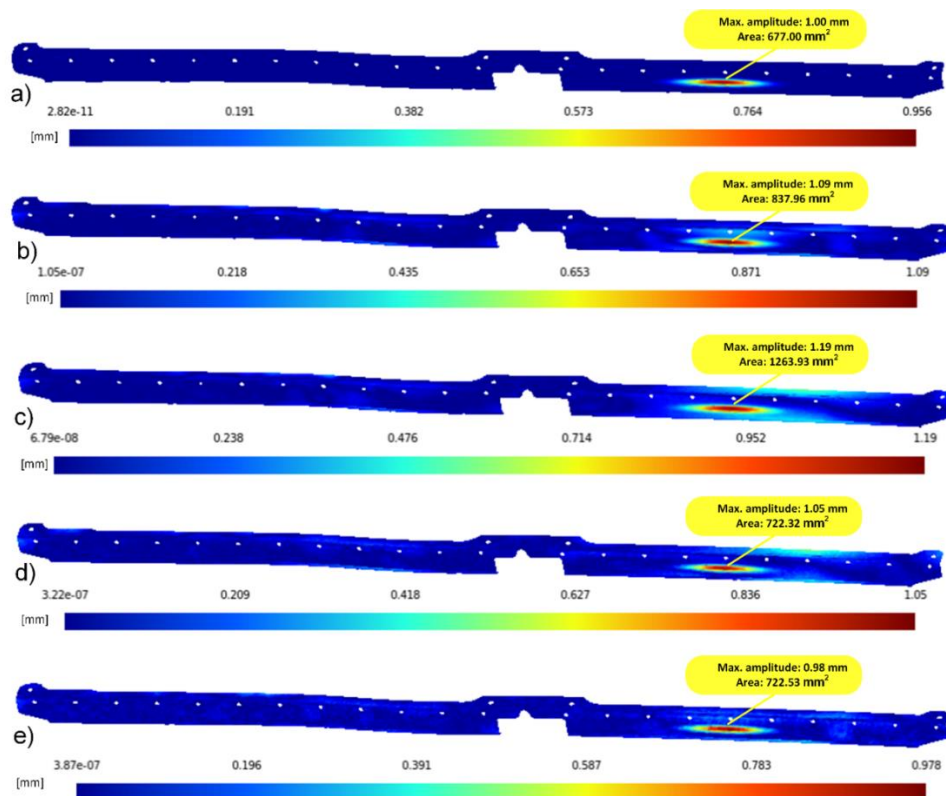


Figure 5-20: a) nominal defect distance distribution for part B with a big (global) defect, comparison between the CAD and scanned model with a big (global) defect and bending deformation as a distance distribution for b) noise-free scan mesh c) noisy scan mesh with $\sigma=0.01$ mm d) noisy scan mesh with $\sigma=0.02$ mm e) noisy scan mesh with $\sigma=0.03$ mm.

Table 5-8: Estimated size of defects and errors for part B with a big (global) defect and bending deformation.

		Maximum amplitude of defects (D_i^{max})				Area of defects (A_i)			
		Nominal [mm]	Estimate d [mm]	Absolute error [mm]	Error [%]	Nominal [mm ²]	Estimated [mm ²]	Absolute error [mm]	Error [%]
BUMP #1	Noise-free	1.00	1.09	0.09	9.00	677	838	161	23.78
	$\sim N(0, \sigma = 0.01)$	1.00	1.19	0.19	19.00	677	1264	587	86.70
	$\sim N(0, \sigma = 0.02)$	1.00	1.05	0.05	5.00	677	722	45	6.69
	$\sim N(0, \sigma = 0.03)$	1.00	0.98	-0.02	-2.00	677	723	46	6.73

Like in the previous case of part B, the nominal result as distance distribution is compared with estimated results obtained for noise-free along with noisy cases of torsion deformation (see Figure 5-21). A summary of the inspection results for maximum amplitude and area of estimated defects are presented in Table 5-9. Here again, these results show that noise does not have a negative effect on the estimation of area and the maximum amplitude of the defect and that amplitude and area of the defect are estimated with good accuracy. Validation of the estimated results based on K-S test at 5% significance level is also presented in Table 5-10. In this case, V&V results are satisfying.

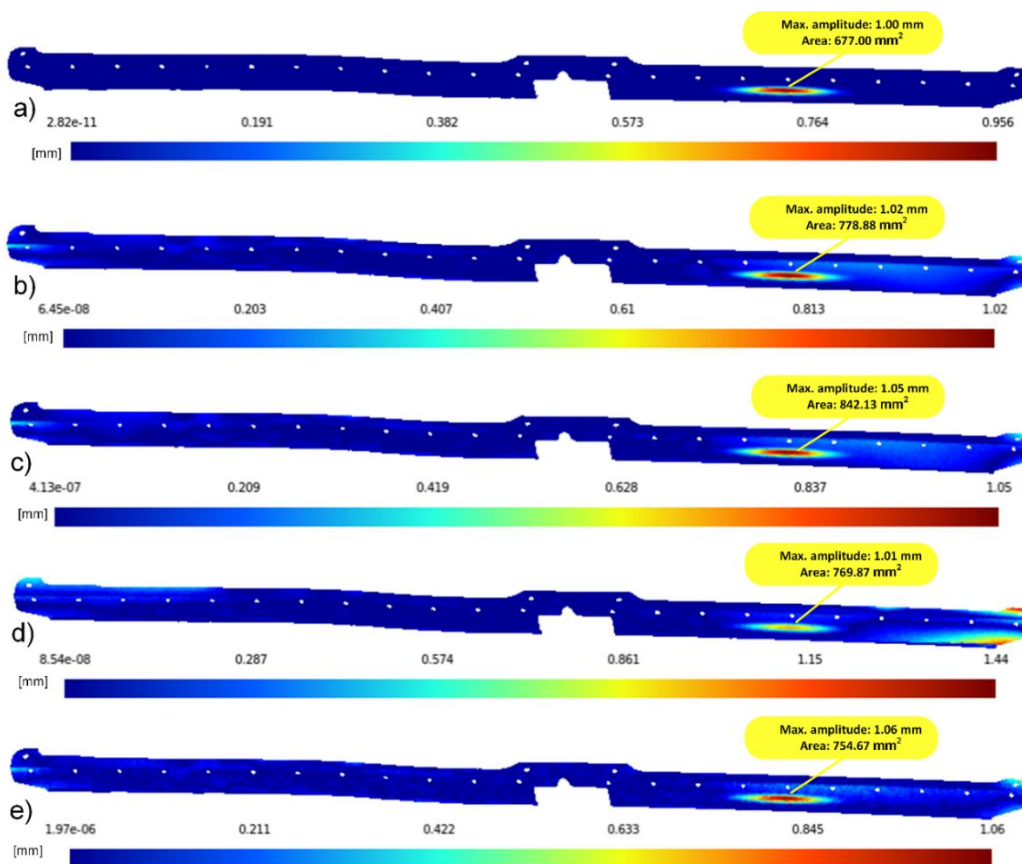


Figure 5-21: a) nominal defect distance distribution for part B with a big (global) defect, comparison between the CAD and scanned model with a big (global) defect and torsion deformation as a distance distribution for b) noise-free scan mesh c) noisy scan mesh with $\sigma=0.01$ mm d) noisy scan mesh with $\sigma=0.02$ mm e) noisy scan mesh with $\sigma=0.03$ mm.

Table 5-9: Estimated size of defects and errors for part B with a big (global) defect and torsion deformation.

		Maximum amplitude of defects (D_i^{max})				Area of defects (A_i)			
		Nominal [mm]	Estimated [mm]	Absolute error [mm]	Error [%]	Nominal [mm ²]	Estimated [mm ²]	Absolute error [mm]	Error [%]
BUMP #1	Noise-free	1.00	1.02	0.02	2.00	677	779	102	15.05
	$\sim N(0, \sigma = 0.01)$	1.00	1.05	0.05	5.00	677	842	165	24.39
	$\sim N(0, \sigma = 0.02)$	1.00	1.01	0.01	1.00	677	770	93	13.72
	$\sim N(0, \sigma = 0.03)$	1.00	1.06	0.06	6.00	677	755	78	11.47

Table 5-10: Validation results with K-S tests (H_0 : the distance distribution of nominal and estimated defects are sufficiently similar) at 5% significance level for part B with a big (global) defect and under bending and torsion deformation.

		Bending deformation p-value	Torsion deformation p-value
BUMP #1	Noise-free	0.115	0.687
	$\sim N(0, \sigma = 0.01)$	0.015	0.475
	$\sim N(0, \sigma = 0.02)$	0.853	0.525
	$\sim N(0, \sigma = 0.03)$	0.937	0.549

■ H_0 is rejected
 ■ H_0 cannot be rejected
 ■ H_0 is borderline

5.5.4 Conclusions about validation cases for part B

Figure 5-22 summarizes, for part B, the variation of error, on the maximum amplitude and on the area of estimated defects, with respect to noise amplitude. It shows intervals in which errors are distributed for each level of noise from noise-free cases to the noisiest cases ($\sigma = 0.01, 0.02$ and 0.03 mm). This figure illustrates that, in this case, error intervals do not extend when noise amplitude increases for both amplitude and area of defects. Meanwhile, a slight decrease in the mean absolute error is observed for maximum amplitude and area when noise amplitude increases. This confirms that for part B, the accuracy of results provided by our automatic fixtureless CAI method for non-rigid parts is not affected by the presence of noisy scan data since estimation errors for noisy cases remain in the same order of magnitude as for noise-free cases. No clear trend of results worsening with noise can be observed and it also appears that, in some cases, results are surprisingly improved with the introduction of noise in scanned data.

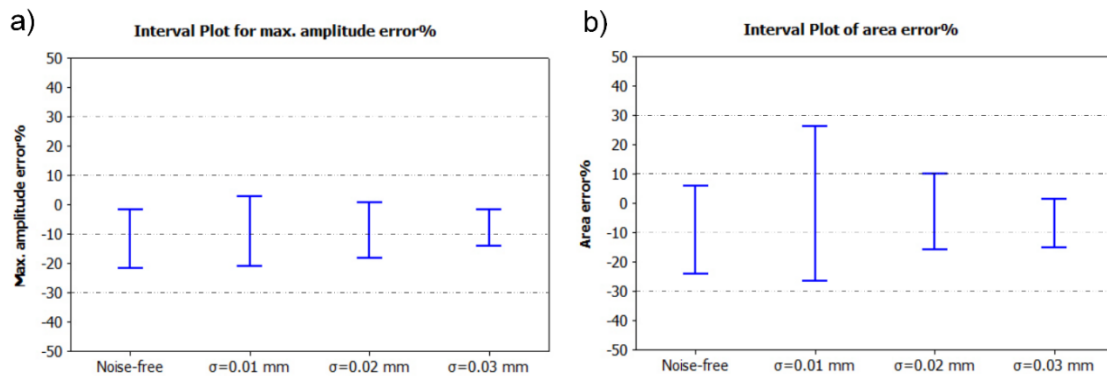


Figure 5-22: Error intervals for part B with respect to the increase of noise amplitude.

In the results obtained for part B, it seems that maximum amplitude is generally better estimated for big (global) defects than for small (local) defects, but area of defects for this part is slightly better identified for small (local) defects than for big (global) defects. Also, the nature of flexible deformation (bending or torsion) doesn't seem to have an effect on this estimation. As mentioned just above, noise generally does not have a significant effect on the accuracy of results obtained. In some cases, noise improves the accuracy of the estimation. It also shows that some of the identification results are better with torsion deformation than in the case of bending deformation but a clear trend cannot be stated. These results also show that, in the case of small (local) defects, the location of defects has an influence on estimation results, which is not surprising. Indeed, defects are not equally affected by deformation of the part in free-state. This also suggests that, in general, results for a given defect are likely to be affected by the type of free-state deformation.

5.6 Effect of large free-state deformation

5.6.1 Cases considered and results obtained

In this section, we assess the effect of the amplitude of free-state deformation on results obtained. Indeed, in the previous sections, for both part A and part B, free-state deformation (bending and torsion for part B) was consistent with a small displacement

assumption. Indeed for both parts and all deformation states maximum displacements were around 10 mm for approximately 1000 mm long parts. In the two cases presented below part A is used and bending free-state deformation is still applied, but in contrast to Figure 5-23-a, free-state deformation (shown in Figure 5-23-b) is not any more consistent with a small displacement assumption. Indeed, maximum bending displacement is now around 75 mm if compared to 10 mm in Figure 5-23-a. Like in section 5.5.2, two scanned models are considered here: one with 3 small (local) defects and another one with one big (global) defect. It is very important to point out that like in previous sections, these scanned models with large flexible deformation are still simulated using a linear FEA formulation, which means using a small displacement FEA formulation.

The scanned model for the first validation case of part A with large bending deformation includes three small (local) defects. The nominal size of defects (Figure 5-24-a) is compared with results provided by our automatic fixtureless CAI method in Figure 5-24-b for noise-free scan data. Inspection results for noisy scanned meshes (with $\sigma = 0.01$, 0.02 and 0.03 mm) are also shown respectively in Figure 5-24-c, d, and e.

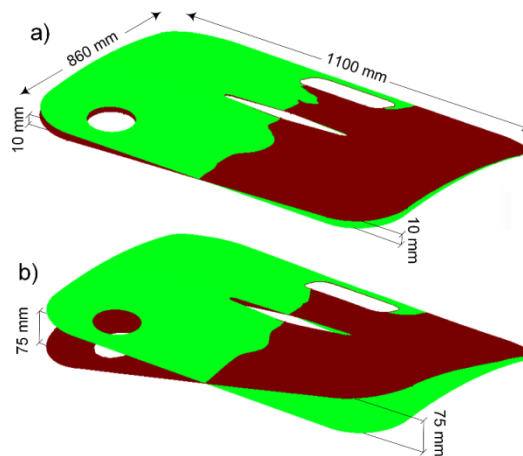


Figure 5-23: 3D views of CAD model (in green) compared with scan data in a free-state (in brown) for part A with a) small bending deformation b) large bending deformation.

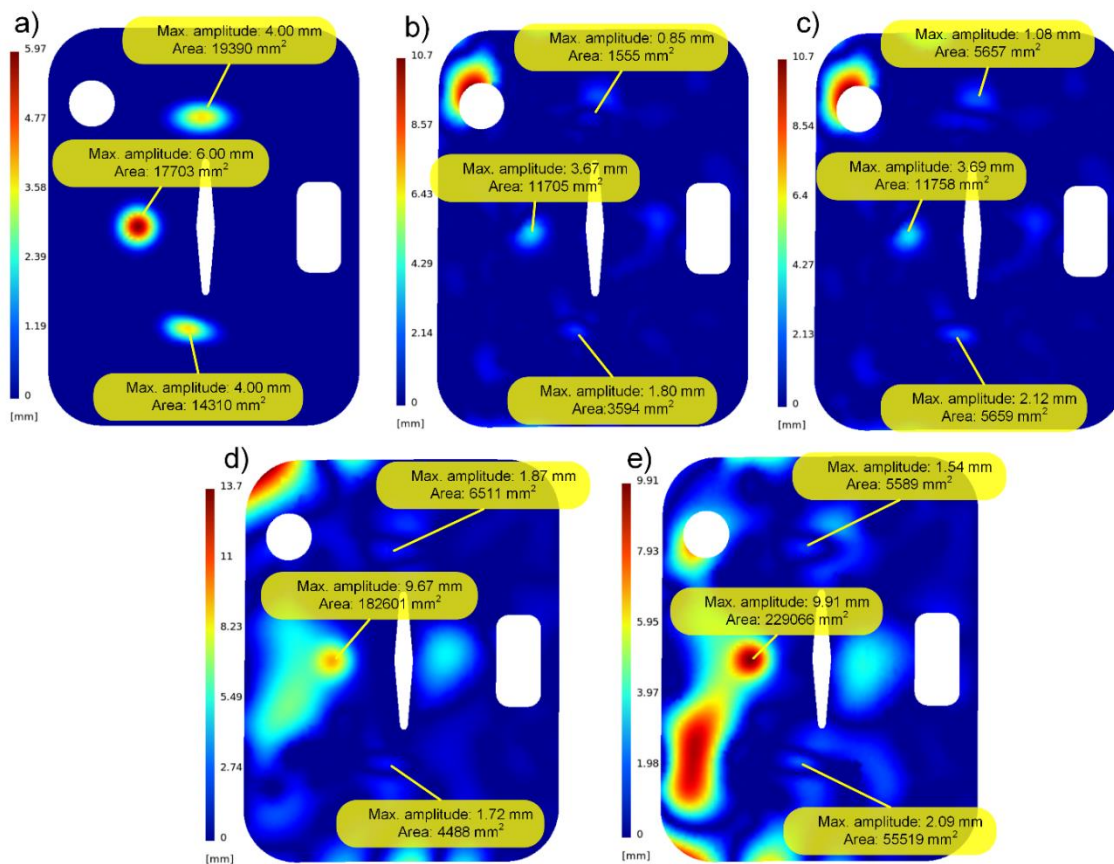


Figure 5-24: a) nominal defect distance distribution for part A with small (local) defects, comparison between the CAD and scanned model of part A with small (local) defects and large bending deformation as a distance distribution for b) noise-free scan mesh c) noisy scan mesh with $\sigma=0.01$ mm d) noisy scan mesh with $\sigma=0.02$ mm e) noisy scan mesh with $\sigma=0.03$ mm.




Maximum amplitude and area of estimated defects are compared with the nominal size of defects in Table 5-11. Results in Table 5-11 show that defects are poorly estimated in general, both for maximum amplitude and area. Like for small free-state deformation in section 5.5.2, V&V results, based on K-S test at a 5% significance level are presented in Table 5-12. These results show that distance distributions associated with estimated defects are not similar to the corresponding distance distributions for nominal defects. Indeed, H_0 hypothesis can be rejected in all cases.

Table 5-11: Estimated size of defects and errors for part A with small (local) defects and large bending deformation.

		Maximum amplitude of defects (D_i^{max})				Area of defects (A_i)			
		Nominal [mm]	Estimated [mm]	Absolute error [mm]	Error [%]	Nominal [mm ²]	Estimated [mm ²]	Absolute error [mm]	Error [%]
BUMP #1	Noise-free	4.00	0.85	-3.15	-78.74	19390	1555	-17835	-91.98
	$\sim N(0, \sigma = 0.01)$	4.00	1.08	-2.92	-72.91	19390	5657	-13733	-70.82
	$\sim N(0, \sigma = 0.02)$	4.00	1.87	-2.13	-53.25	19390	6511	-12879	-66.42
	$\sim N(0, \sigma = 0.03)$	4.00	1.54	-2.46	-61.51	19390	5589	-13801	-71.17
BUMP #2	Noise-free	6.00	3.67	-2.33	-38.80	17703	11705	-5998	-33.88
	$\sim N(0, \sigma = 0.01)$	6.00	3.69	-2.31	-38.52	17703	11758	-5945	-33.58
	$\sim N(0, \sigma = 0.02)$	6.00	9.67	3.67	61.20	17703	182601	164898	931.4 6
	$\sim N(0, \sigma = 0.03)$	6.00	9.91	3.91	65.24	17703	229066	211363	1193. 93
BUMP #3	Noise-free	4.00	1.80	-2.20	-54.90	14310	3594	-10717	-74.89
	$\sim N(0, \sigma = 0.01)$	4.00	2.12	-1.88	-47.02	14310	5659	-8652	-60.46
	$\sim N(0, \sigma = 0.02)$	4.00	1.72	-2.28	-57.06	14310	4488	-9822	-68.64
	$\sim N(0, \sigma = 0.03)$	4.00	2.09	-1.91	-47.72	14310	55519	41209	287.9

Table 5-12: Validation results with K-S tests (H_0 : the distance distribution of nominal and estimated defects are sufficiently similar) at 5% significance level for part A with small (local) defects and large bending deformation.

		p-value
BUMP #1	Noise-free	0.000
	$\sim N(0, \sigma = 0.01)$	0.000
	$\sim N(0, \sigma = 0.02)$	0.000
	$\sim N(0, \sigma = 0.03)$	0.000
BUMP #2	Noise-free	0.000
	$\sim N(0, \sigma = 0.01)$	0.000
	$\sim N(0, \sigma = 0.02)$	0.004
	$\sim N(0, \sigma = 0.03)$	0.000
BUMP #3	Noise-free	0.000
	$\sim N(0, \sigma = 0.01)$	0.002
	$\sim N(0, \sigma = 0.02)$	0.000
	$\sim N(0, \sigma = 0.03)$	0.000

 H_0 is rejected  H_0 cannot be rejected  H_0 is borderline

In the next case, a big (global) defect is considered on part A with a large bending deformation. Nominal and estimated sizes of defects are compared (see Figure 5-25) and V&V results are provided. Like in the previous case, results presented in Table 5-13 show that defects are poorly estimated both for maximum amplitude and area. Using K-S test at 5% significance level for validating the inspection results for this case, with noise-free and noisy scanned meshes (with $\sigma = 0.01, 0.02$ and 0.03 mm) results in “ H_0 is rejected” in all cases.

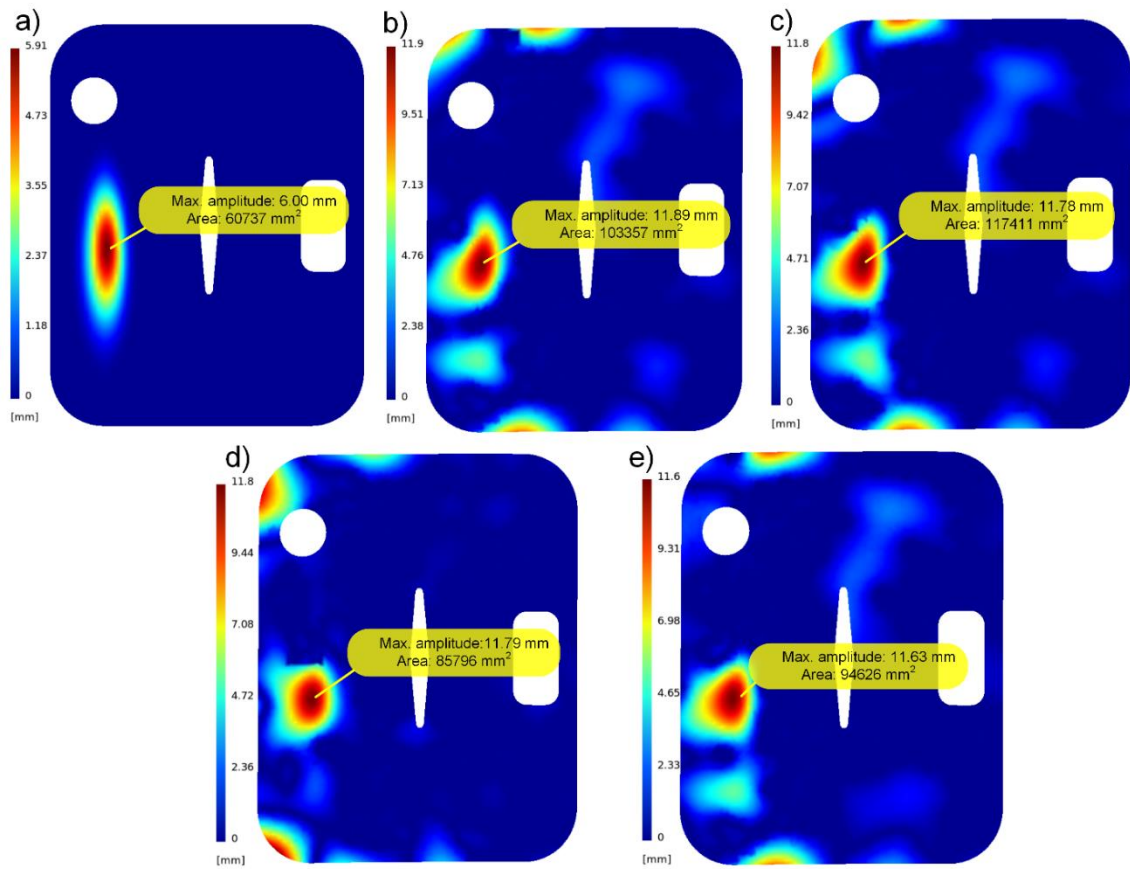


Figure 5-25: a) nominal defect distance distribution for part A with a big (global) defect, comparison between the CAD and scanned model of part A with a big (global) defect and large bending deformation as a distance distribution for b) noise-free scan mesh c) noisy scan mesh with $\sigma=0.01$ mm d) noisy scan mesh with $\sigma=0.02$ mm e) noisy scan mesh with $\sigma=0.03$ mm.

Table 5-13: Estimated size of defects and errors for part A with a big (global) defect and large bending deformation.

		Maximum amplitude of defects (D_i^{max})				Area of defects (A_i)			
		Nominal [mm]	Estimated [mm]	Absolute error [mm]	Error [%]	Nominal [mm ²]	Estimated [mm ²]	Absolute error [mm]	Error [%]
BUMP #1	Noise-free	6.00	11.89	5.89	98.15	60737	103357	42620	70.17
	$\sim N(0, \sigma = 0.01)$	6.00	11.78	5.78	96.28	60737	117411	56674	93.31
	$\sim N(0, \sigma = 0.02)$	6.00	11.79	5.79	96.57	60737	85796	25059	41.26
	$\sim N(0, \sigma = 0.03)$	6.00	11.63	5.63	93.87	60737	94626	33889	55.80

5.6.2 Conclusions about the effect of large free-state deformation

Results presented in the previous section clearly show that the amplitude of free-state deformation has a major effect on inspection results. Indeed, for the two cases featuring a large free-state deformation, inspection results are a lot worse than inspection results obtained for corresponding cases featuring small deformation, as presented in section 5.5.2. The same trend is observed for both the assessment of maximum amplitude and area of defects and V&V results, which is not surprising. Indeed, if the maximum amplitude and area of defects are badly estimated, distance distributions associated with nominal and estimated defects are not expected to be very similar.

Figure 5-26 presents a comparison between results obtained for small and large free-state deformation on part A. Figure 5-26-a summarizes cases with three small (local) defects (as presented in Table 5-1 and Maximum amplitude and area of estimated defects are compared with the nominal size of defects in Table 5-11. Results in Table 5-11 show that defects are poorly estimated in general, both for maximum amplitude and area. Like for small free-state deformation in section 5.5.2, V&V results, based on K-S test at a 5% significance level are presented in Table 5-12. These results show that distance distributions associated with estimated defects are not similar to the corresponding distance distributions for nominal defects. Indeed, H_0 hypothesis can be rejected in all cases.

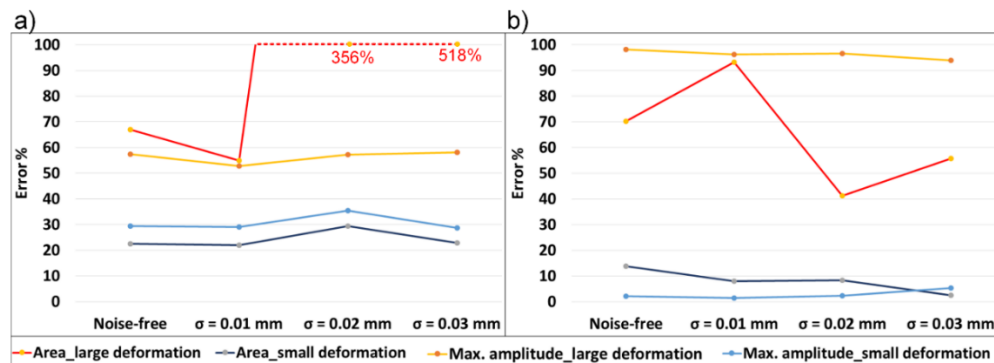


Figure 5-26: Absolute error (in %) in the estimation of defects for part A for small versus large deformation.

Figure 5-26 clearly show the degradation of results brought about by large free-state deformation for the two cases considered and for both estimations of maximum amplitude and area of defects. This degradation is not surprising since, in all cases, a linear FEA formulation has been used for both simulating scanned data and *Finite Element Non-rigid Registration* (FENR). Indeed linear FEA formulations are based on a small displacement assumption and as much as free-state deformation increases, this assumption is less and less verified, which explains the trend shown about the degradation of inspection results. Going further in the comparison between inspection results obtained with small and large free-state deformation, it appears in Table 5-1 and Maximum amplitude and area of estimated defects are compared with the nominal size of defects in Table 5-11. Results in Table 5-11 show that defects are poorly estimated in general, both for maximum amplitude and area.

Like for small free-state deformation in section 5.5.2, V&V results, based on K-S test at a 5% significance level are presented in Table 5-12. These results show that distance distributions associated with estimated defects are not similar to the corresponding distance distributions for nominal defects. Indeed, H_0 hypothesis can be rejected in all cases.

Table 5-11 shows that the degradation of results for Bump #2 is globally more severe than for Bump #1 and Bump #3. Looking at Figure 5-6-a and Figure 5-23, it appears that Bump #2 is located in a zone that is likely to be more affected than others by the free-state deformation. This may explain why the degradation is more severe for Bump #2 than for Bump #1 and Bump #3. This is confirmed when comparing results shown in Table 5-3 and Table 5-13 for the case with a big (global) defect only. In this case, the degradation of inspection results with large free-state deformation is even more severe as globally illustrated in Figure 5-26-b. Indeed this big (global) defect is located in the same zone than Bump #2 in the case with three small (local) defects.

As introduced above, this degradation of inspection results with large free-state deformation can be explained considering that both the simulation of free-state

deformation and FENR are performed using a linear FEA formulation, thus based on a small displacement hypothesis. Applying a linear FEA formulation to problems featuring large displacement results in unwanted and non-realistic stretching that is likely to affect the shape of defects and by the way inspection results. Of course, this non-realistic stretching increases with free-state deformation which increases the degradation of inspection results. It is worth noting that this non-realistic stretching adds to the effect of GNIF accuracy, which also causes non-realistic stretching and also directly and negatively affects inspection results. Moreover, it tends to decrease GNIF accuracy itself since GNIF is based on the assumption that the deformation of a non-rigid part in free-state is isometric (preserves geodesic distances). Indeed, in the context of large displacement in free-state, this isometry assumption requires using a large displacement FEA formulation to be fulfilled. As mentioned in the conclusion, this is part of our plans for future work on the subject.

5.7 Discussion about results

As illustrated in Figure 5-10-d, a source of error that affects the distance distribution of estimated defects is indeed a significant bias in the generation of sample points with the GNIF method. This bias in GNIF comes from significant inaccuracies in the calculation of geodesic distances with the fast marching algorithm [17]. Inaccurate geodesic distances indeed result in inaccuracy in the in-plane location of sample points generated by GNIF. Error in the in-plane location of these sample points causes non-realistic stretching in FENR, which is a source of inaccuracy in inspection results.

It has been found in several cases that noise surprisingly tends to improve estimation results. This can be explained considering the fact that the introduction of randomly distributed noise applied to the scanned mesh does not necessarily tend to filter more sample points. It appears that, in some cases, noise tends to decrease the final number of sample points used but it also appears that, in other cases, it tends to increase the final number of sample points used. This explains why the introduction of noise can either improve or worsen the estimation of defects. Indeed, for a given case, there is globally an

optimal density of sample points for obtaining the most accurate estimation results. Using too many sample points makes that sample points that are too close to defects are used, which worsens estimation results. Not using enough sample points makes that the free-state deformation is not captured accurately enough, which also worsens estimation results. Therefore, the presence of noise close to a defect will sometimes result in an improvement of inspection results since it will remove more sample points and makes it closer to the optimal density but it will also result, in other cases, in worsening results since the density of sample points will become too low for capturing free-state deformation itself.

In some cases, the shape of defects is affected by flexible deformation during FENR. This effect depends on the nature and magnitude of flexible deformation and on the type and dimensions of defects. Indeed, if flexible deformation in the vicinity of a given defect is high and if the defect itself is quite flexible, this may affect the shape of the defect.

5.8 Conclusion

This paper proposes a metric aimed at validating an automatic fixtureless *Computer-Aided Inspection* (CAI) method for non-rigid parts. This CAI method is based on establishing a correspondence between scanned and CAD data through sets of sample points, on filtering sample points that may be close to defects and on *Finite Element Non-rigid Registration* (FENR). This metric allows assessing the similarity of distance distribution for the estimated defects, which are identified with our inspection method, in comparison with that of nominal defects on a manufactured part. The metric applies statistical hypothesis testing, namely the *Kolmogorov–Smirnov* (K-S) test, to make comparisons between cumulative distribution functions (CDFs) associated with estimated and nominal defects. Robustness of the CAI method is validated by adding noise to the scan data. Applying this validation process to CAI results obtained on two aerospace parts shows that the assessment of maximum amplitude and area of estimated defects is not significantly affected by noise since error distributions remain in the same magnitude of magnitude. Results obtained from K-S tests with respect to the ability of the CAI method

in assessing distance distributions of estimated defects also infer that, in general, the method provides sufficiently accurate results and that distance distributions of estimated defects can be reasonably well identified. These results show that the accuracy of a CAI depends on the magnitude of flexible deformation applied on the scanned model, especially in the vicinity of defects, but the nature of flexible deformation (bending or torsion) as well as the nature of defects (small (local) or big (global) defects) does not have a significant effect on the inspection accuracy.

It is important to underline that the validation metric proposed in this paper is not restricted to assessing the performance of our CAI method. Applying it to our method is an example of what can be done in many other contexts. For metrology purposes, this metric can indeed be successfully applied to any CAI method, since the only input data required is sets of distance distributions between CAD geometry and scanned geometry. Thus, a natural extension of this work would be applying this validation metric to other CAI approaches.

Even if these validation results are promising, they reveal that several improvements can be foreseen towards improving this CAI method with respect to its different sources of uncertainty. Improving accuracy of the non-rigid registration method used (GNIF) would be a first interesting step forward. We found out that the main source of inaccuracy in applying GNIF is related to sources of inaccuracy in fast marching calculations underlying GNIF. We are presently investigating numerical strategies that should improve the accuracy of fast marching results. Also, since the inspection method is based on discretized curvature calculation and FEA, the mesh size and its quality especially on features with high curvatures can be a source of error on the estimation of defects in the final inspecting results. Meanwhile, all free-state flexible deformations in scanned models are considered as linear, which means in the small displacement hypothesis range and that FENR is performed using linear FEA calculations. As shown in section 5.6, this hypothesis is not verified in many practical cases. Consequently, a natural extension of this work is setting up an extension of this CAI method based on a large displacement FEA formulation. Results obtained using a large displacement FEA formulation could be

compared with results obtained using the *Coherent Point Drift* (CPD) algorithm [47]. This algorithm is indeed a promising non-FEA-based inspection method that shows, in some cases, good efficiency for large flexible deformation.

5.9 Acknowledgment

The authors would like to thank the National Sciences and Engineering Research Council of Canada (NSERC), industrial partners, Consortium for Aerospace Research and Innovation in Québec (CRIAQ) and UQTR foundation for their support and financial contribution. In this paper, we use GmshTM [46] for visualizing meshes, stress, curvature and error distributions.

5.10 References

- [1] G. N. Abenhaim, A. Desrochers, and A. Tahan, "Nonrigid parts' specification and inspection methods: notions, challenges, and recent advancements," *International Journal of Advanced Manufacturing Technology*, vol. 63, pp. 741-752, Nov 2012.
- [2] G. N. Abenhaim, S. A. Tahan, A. Desrochers, and J.-F. Lalonde, "Aerospace Panels Fixtureless Inspection Methods with Restraining Force Requirements; A Technology Review," *SAE Technical Paper* 2013.
- [3] A. Weckenmann and J. Weickmann, "Optical Inspection of Formed Sheet Metal Parts Applying Fringe Projection Systems and Virtual Fixation," *Metrology and Measurement Systems*, vol. 13, pp. 321-330, 2006.
- [4] I. Gentilini and K. Shimada, "Predicting and evaluating the post-assembly shape of thin-walled components via 3D laser digitization and FEA simulation of the assembly process," *Computer-aided design*, vol. 43, pp. 316-328, 2011.
- [5] G. N. Abenhaim, A. Desrochers, A. S. Tahan, and J. Bigeon, "A virtual fixture using a FE-based transformation model embedded into a constrained optimization for the dimensional inspection of nonrigid parts," *CAD Computer Aided Design*, vol. 62, pp. 248-258, 2015.

- [6] A. Weckenmann, J. Weickmann, and N. Petrovic, "Shortening of inspection processes by virtual reverse deformation," in 4th international conference and exhibition on design and production of machines and dies/molds, Cesme, Turkey, 2007.
- [7] A. Jaramillo, F. Prieto, and P. Boulanger, "Fixtureless inspection of deformable parts using partial captures," *International Journal of Precision Engineering and Manufacturing*, vol. 14, pp. 77-83, 2013.
- [8] G. N. Abenhaim, A. S. Tahan, A. Desrochers, and R. Maranzana, "A Novel Approach for the Inspection of Flexible Parts Without the Use of Special Fixtures," *Journal of Manufacturing Science and Engineering-Transactions of the Asme*, vol. 133, Feb 2011.
- [9] A. Aidibe, A. S. Tahan, and G. N. Abenhaim, "Distinguishing profile deviations from a part's deformation using the maximum normed residual test," *WSEAS Transactions on Applied & Theoretical Mechanics*, vol. 7, 2012.
- [10] H. Radvar-Esfahlan and S.-A. Tahan, "Nonrigid geometric metrology using generalized numerical inspection fixtures," *Precision Engineering*, vol. 36, pp. 1-9, 2012.
- [11] V. Sabri, S. A. Tahan, X. T. Pham, D. Moreau, and S. Galibois, "Fixtureless profile inspection of non-rigid parts using the numerical inspection fixture with improved definition of displacement boundary conditions," *International Journal of Advanced Manufacturing Technology*, vol. 82, pp. 1343-1352, 2016.
- [12] S. Sattarpanah Karganroudi, J.-C. Cuillière, V. Francois, and S.-A. Tahan, "Automatic fixtureless inspection of non-rigid parts based on filtering registration points," *The International Journal of Advanced Manufacturing Technology*, pp. 1-26, 2016.
- [13] A. Weckenmann, P. Gall, and J. Hoffmann, "Inspection of holes in sheet metal using optical measuring systems," in *Proceedings of VIth International Science Conference Coordinate Measuring Technique (April 21-24, 2004, Bielsko-Biala, Poland)*, 2004, pp. 339-346.

- [14] L. Schwer, H. Mair, and R. Crane, "Guide for verification and validation in computational solid mechanics," American Society of Mechanical Engineers, ASME V&V, vol. 10.1, 2012.
- [15] P. J. Besl and N. D. McKay, "A Method for Registration of 3-D Shapes," *Ieee Transactions on Pattern Analysis and Machine Intelligence*, vol. 14, pp. 239-256, Feb 1992.
- [16] A. M. Bronstein, M. M. Bronstein, and R. Kimmel, "Generalized multidimensional scaling: A framework for isometry-invariant partial matching," *Proceedings of the National Academy of Sciences of the United States of America*, vol. 103, pp. 1168-1172, 2006.
- [17] R. Kimmel and J. A. Sethian, "Computing geodesic paths on manifolds," *Proceedings of the National Academy of Sciences*, vol. 95, pp. 8431-8435, 1998.
- [18] H. Borouchaki, P. L. George, and S. H. Lo, "Optimal delaunay point insertion," *International Journal for Numerical Methods in Engineering*, vol. 39, pp. 3407-3437, 1996.
- [19] W. L. Oberkampf, T. G. Trucano, and C. Hirsch, "Verification, validation, and predictive capability in computational engineering and physics," *Applied Mechanics Reviews*, vol. 57, pp. 345-384, 2004.
- [20] D. Sornette, A. Davis, K. Ide, K. Vixie, V. Pisarenko, and J. Kamm, "Algorithm for model validation: Theory and applications," *Proceedings of the National Academy of Sciences*, vol. 104, pp. 6562-6567, 2007.
- [21] W. L. Oberkampf and M. F. Barone, "Measures of agreement between computation and experiment: Validation metrics," *Journal of Computational Physics*, vol. 217, pp. 5-36, 2006.
- [22] R. G. Hills and T. G. Trucano, "Statistical validation of engineering and scientific models: Background," Sandia National Laboratories, Albuquerque, NM, Report No. SAND99-1256, 1999.

- [23] A. S. Committee, "AIAA Guide for the Verification and Validation of Computational Fluid Dynamics Simuations (G-077-1998)," ed: AIAA, 1998.
- [24] V. Committee, "Standard for verification and validation in computational fluid dynamics and heat transfer," American Society of Mechanical Engineers, New York, 2009.
- [25] B. Cowles, D. Backman, and R. Dutton, "Verification and validation of ICME methods and models for aerospace applications," *Integrating Materials and Manufacturing Innovation*, vol. 1, pp. 1-16, 2012.
- [26] Y. Liu, W. Chen, P. Arendt, and H. Z. Huang, "Toward a better understanding of model validation metrics," *Journal of Mechanical Design, Transactions of the ASME*, vol. 133, 2011.
- [27] W. L. Oberkampf and T. G. Trucano, "Verification and validation benchmarks," *Nuclear engineering and Design*, vol. 238, pp. 716-743, 2008.
- [28] S. Ferson and W. L. Oberkampf, "Validation of imprecise probability models," *International Journal of Reliability and Safety*, vol. 3, pp. 3-22, 2009.
- [29] J. P. Kleijnen, "Statistical validation of simulation models," *European Journal of Operational Research*, vol. 87, pp. 21-34, 1995.
- [30] T. Buranathiti, J. Cao, W. Chen, L. Baghdasaryan, and Z. C. Xia, "Approaches for model validation: methodology and illustration on a sheet metal flanging process," *Journal of Manufacturing Science and Engineering*, vol. 128, pp. 588-597, 2006.
- [31] T. L. Paez and A. Urbina, "Validation of mathematical models of complex structural dynamic systems," in *Proceedings of the ninth international congress on sound and vibration*, Orlando, FL, 2002.
- [32] R. G. Hills and I. H. Leslie, "Statistical validation of engineering and scientific models: validation experiments to application," Sandia National Labs., Albuquerque, NM (US); Sandia National Labs., Livermore, CA (US)2003.

- [33] K. J. Dowding, I. H. Leslie, M. L. Hobbs, B. M. Rutherford, R. G. Hills, and M. M. Pilch, "Case study for model validation: assessing a model for thermal decomposition of polyurethane foam," Sandia National Laboratories 2004.
- [34] B. Rutherford and K. Dowding, "An approach to model validation and model-based prediction—polyurethane foam case study," SAND2003-2336, Sandia National Laboratories, Albuquerque, 2003.
- [35] W. Chen, L. Baghdasaryan, T. Buranathiti, and J. Cao, "Model validation via uncertainty propagation and data transformations," *AIAA journal*, vol. 42, pp. 1406-1415, 2004.
- [36] R. Rebba and S. Mahadevan, "Computational methods for model reliability assessment," *Reliability Engineering & System Safety*, vol. 93, pp. 1197-1207, 2008.
- [37] R. B. D'Agostino, *Goodness-of-fit-techniques* vol. 68: CRC press, 1986.
- [38] R. G. Ghanem, A. Doostan, and J. Red-Horse, "A probabilistic construction of model validation," *Computer Methods in Applied Mechanics and Engineering*, vol. 197, pp. 2585-2595, 2008.
- [39] F. J. Massey Jr, "The Kolmogorov-Smirnov test for goodness of fit," *Journal of the American statistical Association*, vol. 46, pp. 68-78, 1951.
- [40] S. Mahadevan and A. Haldar, *Probability, reliability and statistical method in engineering design*: John Wiley & Sons, 2000.
- [41] X. Sun, P. L. Rosin, R. R. Martin, and F. C. Langbein, "Noise in 3D laser range scanner data," in *Shape Modeling and Applications*, 2008. SMI 2008. IEEE International Conference on, 2008, pp. 37-45.
- [42] C. Boehnen and P. Flynn, "Accuracy of 3D scanning technologies in a face scanning scenario," in *3-D Digital Imaging and Modeling*, 2005. 3DIM 2005. Fifth International Conference on, 2005, pp. 310-317.

- [43] J. R. Diebel, S. Thrun, and M. Brünig, "A Bayesian method for probable surface reconstruction and decimation," *ACM Transactions on Graphics (TOG)*, vol. 25, pp. 39-59, 2006.
- [44] M. Alexa, "Wiener filtering of meshes," in *Shape Modeling International*, 2002. *Proceedings*, 2002, pp. 51-57.
- [45] J. C. Cuillière and V. Francois, "Integration of CAD, FEA and Topology Optimization through a Unified Topological Model," *Computer-Aided Design and Applications*, vol. 11, pp. 1-15, // 2014.
- [46] C. Geuzaine and J.-F. Remacle, "Gmsh: a three-dimensional finite element mesh generator with built-in pre- and post-processing facilities," *International Journal for Numerical Methods in Engineering*, vol. 79, pp. 1309-1331, 2009.
- [47] A. Aidibe and A. Tahan, "Adapting the coherent point drift algorithm to the fixtureless dimensional inspection of compliant parts," *International Journal of Advanced Manufacturing Technology*, vol. 79, pp. 831-841, 2015.

CHAPTER 6 FIXTURELESS INSPECTION OF NON-RIGID PARTS BASED ON VIRTUAL MOUNTING IN AN ASSEMBLY- STATE USING PERMISSIBLE LOADS

Sasan Sattarpanah Karganroudi¹, Jean-Christophe Cuillière¹, Vincent Francois¹,
Souheil-Antoine Tahan²

¹Équipe de Recherche en Intégration Cao-CALcul (ÉRICCA), Université du Québec à Trois-
Rivières, Trois-Rivières, Québec, Canada

²Laboratoire d'ingénierie des produits, procédés et systèmes (LIPPS), École de Technologie
Supérieure, Montréal, Québec, Canada

6.1 Abstract

Recent developments in the fixtureless inspection of non-rigid parts based on *Computer-Aided Inspection* (CAI) methods significantly contribute to diminishing the time and cost of geometrical dimensioning and inspection. Generally, CAI methods aim to compare scan meshes which are acquired using scanners as point clouds from non-rigid manufactured parts in a free-state, with associated nominal *Computer-Aided Design* (CAD) models. Due to the compliance of non-rigid parts, costly and complex physical inspection fixtures are required to retrieve their functional shape in the assembly-state. Fixtureless inspection methods eliminate the need for physical fixtures and virtually compensate for the flexible deformation of non-rigid parts in a free-state. Inspired by industrial inspection techniques wherein weights (e.g. sandbags) are applied as restraining loads on non-rigid parts, a fixtureless inspection method is presented that predicts the functional shape in assembly-state for the scan mesh of a non-rigid part. The proposed *Virtual Mounting Assembly-State Inspection* (VMASI) method is capable of virtually mounting the scan mesh of a deviated non-rigid part (including defects), acquired in a free-state, into the designed assembly-state using permissible restraining forces. The functional shape is predicted via a linear FE-based transformation where the value and position of required restraining loads, which are introduced as pressures on the surface of the part, are assessed by our developed *Restraining Pressures Optimization* (RPO) approach. In fact, the functional shape minimizes the orientation difference and distance between the assembly mounting holes on the predicted shape of the non-rigid part with

respect to the nominal ones. The inspection is then accomplished by examining the mounting holes offset on the predicted shape of the scan model concerning the nominal CAD model. This ensures that the mounting holes on the predicted shape of a scan model in assembly-state remain in the dedicated tolerance range. This method is evaluated on two non-rigid parts to predict the required restraining pressures limited to the permissible forces during the inspection process and to predict the eventual functional shape of the scan model. The inspection results for each part, including different types of defects in the scan mesh, are evaluated to determine whether the manufactured part proceeds to the assembly stage.

Keywords: Fixtureless inspection, non-rigid parts, virtual mounting in assembly-state, computational metrology, optimization, FEA.

6.2 Introduction

Geometric Dimensioning and Tolerancing (GD&T) is an essential need for the functionality and quality control of manufactured parts. The geometrical precision of manufactured parts directly affects the functional efficiency of assembled products. Despite recent progress in manufacturing methods towards reducing the lead time of production, quality control is still time-consuming and requires significant manual intervention. Dimensional inspection in the quality control process is especially challenging for thin-walled sheet metals that are used in various industrial sectors among which aerospace and automotive industries. These parts feature a very small thickness compared to the other dimensions that makes them non-rigid (flexible). This is referred to as compliance (compliant behavior of non-rigid parts in a free-state) in tolerancing contexts. The main issue of GD&T is that these non-rigid parts may easily deform during a free-state inspection process. This requires applying over constrained fixtures and restraining the part under permissible loads during the dimensional inspection process to retrieve the functional part shape. Therefore, even though the shape variation of non-rigid parts due to flexible deformation in a free-state exceeds the allocated dimensioning tolerances of the model, these manufactured parts can still be assembled when the

functional shape of the model is retrieved under permissible loads on the inspection fixtures.

Metrology standards such as ASME Y14.5 and ISO-GPS state that the inspection of parts is performed in a free-state, except for non-rigid parts, as mentioned in ISO-10579 and ASME Y14.5 (2009). Free-state refers to a situation in which a manufactured part is not submitted to any other load than its weight. A non-rigid aerospace panel in a free-state, as shown in Figure 6-1-a, deforms due to compliance under its weight and/or residual stress remaining from manufacturing processes. Conventional dimensioning and inspection methods for non-rigid parts require sophisticated, expensive and time-consuming inspection fixtures to compensate for the flexible deformation of these parts. These fixtures reacquire the functional shape of the manufactured part with respect to its designed CAD model ensuring measurement repeatability and reproducibility. The measurement setup (fixture) represents the nominal assembly-state wherein the manufactured part is aligned with the reference frame during the measuring process. Figure 6-1-b illustrates an example of such an inspection fixture for the part shown in a free-state in Figure 6-1-a.

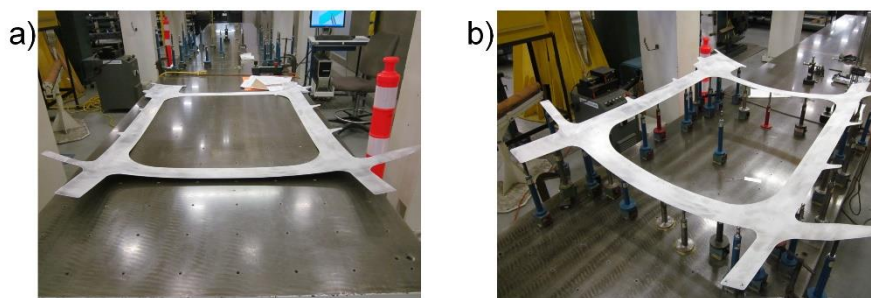


Figure 6-1: An ordinary aerospace panel a) in free-state, b) constrained on supports of the inspection fixture [1].

The dimensional inspection of non-rigid parts is generally accomplished in restrained conditions, such as applying limited forces to impose the functional shape of the part on the fixture [2]. As shown in Figure 6-2, a practical inspection technique applies weights (sandbags) on the surface of a deviated non-rigid part to retrieve its functional shape

constrained on the physical fixture. These sandbags are permissible weights that present pressure loads in the gravity direction on surfaces of a part. The permissible loads are commonly presented as a note in design drawings authorizing their application during the inspection process. An example of such a note that specifies the permissible load and the associated fixture is “A load of X N/m can be used to achieve tolerance,” which is indicated next to the associated geometrical requirements. The restraints which apply permissible loads on non-rigid parts are usually used for large parts such as aerospace panels for which the functional requirements are retrieved by imposing certain constraints during assembly.



Figure 6-2: An aerospace panel under permissible restrained loads (the weight of black sandbags applied on the surface of part) achieves the functional shape on physical fixture [1].

In order to accomplish geometric dimensioning, the first step is to assign proper tolerances with respect to property, functionality and part manufacturing process. Tolerance allocation and analysis for non-rigid parts take into account parts' shape variation (such as warping or changing in the nominal curvature of the model) in their final assembly-state. These geometrical variations are due to manufacturing defects (such as springback effect and residual stress), handling and transporting defects (such as residual plastic deformation) or assembling defects (such as welding deformation caused by locally overheating the part). Once proper tolerances are specified, GD&T specifications are assessed through inspection of the parts based on *Computer-Aided*

Inspection (CAI) methods. The improvements in 3D non-contact data acquisition devices such as 3D laser and optic scanners [3], along with computational calculations, allow progress in CAI methods. The CAI methods apply optic and laser scanners to obtain a 3D point cloud from the surface of part in a free-state. A triangular mesh is then generated from this point cloud, which represents the shape of a manufactured part as a scan mesh. The inspection is accomplished by virtually comparing this scan mesh with the associated nominal CAD model to evaluate geometric deviation of the manufactured part with respect to assigned tolerances. Conventional inspection methods apply a hard inspection fixture [4] to keep non-rigid parts in its functional state, but ongoing studies on fixtureless inspection methods intend to eliminate the need of these complex and expensive fixtures. Fixtureless non-rigid inspection methods [1, 5-13] are developed as CAI methods in which different approaches are applied to compensate for the flexible deformation of measured manufactured part in a free-state. These methods take into consideration the permissible displacements, due to the compliance behavior, during the assembly of non-rigid parts. The primary step for fixtureless inspection of non-rigid parts is performing a rigid registration. During this process, a transformation matrix is applied (regardless of the flexible deformation of the parts) to displace the CAD and scan models close to each other in a common coordinate system. Then, the fixtureless inspection methods try to distinguish between flexible deformation of the scan model in free-state and geometrical deviations associated with defects. Therefore, virtually compensating for the flexible deformation of the scan model in a free-state allows the estimation of defects on the parts with respect to the nominal CAD model. In general, these fixtureless non-rigid registration methods search for correspondence between the CAD and scan models to deform the CAD or scan model towards the other one, by using FEA or using iterative displacements. However, the permissible assembly loads are not considered in these fixtureless inspection methods. The assembly loads are practically applied in inspection techniques (for instance by applying weights) to place a geometrically deviated non-rigid part into assembly-state. Therefore, even a deviated manufactured part including defects that exceed the geometrical tolerances can be accepted for final assembly within the

assembly tolerance ranges. These defects (geometrical deviations) such as warpage, shrinkage, springback or any type of plastic deformation can occur during manufacturing or handling before inspection. These defects result in misalignments during the assembly process, but excessive geometrical variations with respect to the assembly tolerances can be absorbed by the compliance non-rigid parts.

Inspired by inspection techniques using weights, a fixtureless inspection method for non-rigid parts is presented in this paper that aims to verify the feasibility of assembling deviated parts in the nominal assembly-state with respect to assembly tolerances. This *Virtual Mounting Assembly-State Inspection* (VMASI) method considers the presence of profile [k, d] and localization [j] defects, as defined by ASME Y14.5, on inspected non-rigid parts. This method develops a virtual fixture using the GD&T specification of the CAD model to retrieve the functional shape of a deviated non-rigid part in assembly-state. The VMASI estimates the required restraining loads which are limited to the permissible assembly loads. The estimated loads in this method are in fact estimated pressures on specific zones distributed on the surface of deviated part. These estimated pressures are oriented in the gravity direction, to replicate the weight of sandbags on the surface of manufactured part. To this end, the scan mesh of the deviated manufactured part is partitioned into zones where the estimated pressures are introduced. The required pressures are estimated using our developed *Restraining Pressures Optimization* (RPO) approach to minimize the distance and orientation differences between assembly mounting holes on the scan mesh and nominal mounting holes on the CAD model. The predicted shape of scan mesh in an assembly-state is obtained applying the estimated pressures in a FE-based transformation. The inspection is performed by verifying each mounting hole on the predicted shape of scan mesh with respect to assembly tolerance values as specified. Based on the proposed inspection method, a deviated non-rigid part is likely to be assembled if all mounting holes on the predicted shape of scan mesh remain within the tolerance range.

This paper is organized as follows. Section 6.3 presents a literature review of tolerancing and fixtureless inspection of non-rigid parts. It is followed by an introduction of the

proposed *Virtual Mounting Assembly-State Inspection* (VMASI) method in section 6.4. This section describes the steps to estimate the required restraining loads on scan mesh of deviated manufactured non-parts using the developed *Restraining Pressures Optimization* (RPO) approach. Results obtained using our VMASI method on non-rigid parts are then presented in section 6.5. For this, two typical non-rigid parts used in the aerospace industry are considered, wherein various types of defects are presented. The paper ends with a conclusion and perspectives for future work in section 6.6.

6.3 Literature review

In order to assess the required quality of manufactured parts, *Geometric Dimensioning and Tolerancing* (GD&T) based on ASME Y14.5 and ISO-GPS standards are handy references. Unlike traditional GD&T methods, non-rigid tolerancing methods must take into consideration permissible displacements of non-rigid parts during the assembly process due to flexible deformations. A review of studies on *Computer-Aided Tolerancing* (CAT), tolerance analysis and allocation strategy for compliant (non-rigid) parts is presented in [14-16]. Like tolerance allocation, relevant inspection methods for non-rigid parts must take into consideration the flexible deformation of non-rigid parts for evaluating the geometrical deviation of manufactured parts with respect to assigned tolerances. A classification of specifications for GD&T of non-rigid parts is presented in [2] wherein GD&T requirements have to be respected in a restrained condition such as restraining shape fixtures, datum reference frame, movable datum targets and restraining forces. Therefore, the CAI methods that apply rigid registration only, such as *Iterative Closest Point* (ICP) algorithm [17], do not fit the inspection of non-rigid parts in a free-state. To this end, classical inspection methods are used by restraining non-rigid parts in physical fixtures [4] during the inspection process. However, significant drawbacks of these complex fixtures, where the setup and repeatability of the fixtures are costly, lead to developing inspection methods by eliminating the need of fixtures. The core idea of fixtureless inspection methods is to compensate for flexible deformation of non-rigid parts in a free-state and enable comparison between the scan mesh of part and its CAD

model. To this end, a few fixtureless inspection methods are developed based on virtually deforming the scan model towards the CAD model [1, 5, 6], while other methods are developed based on virtually deforming the CAD model toward the scan model [7-13].

The first group of fixtureless methods apply a set of displacement boundary conditions (BCs) in a *Finite Element Analysis* (FEA) to displace the scan mesh towards the corresponding CAD model. BCs used in the *virtual fixation concept* [5] are imposed on the assembly fixation features (e.g. holes) of the scan mesh, which can be automatically identified using feature extraction techniques [18]. However, imposing BCs on all fixation features to displace them towards their design location for complex non-rigid parts is not always possible and may cause geometrical deviations in the part during assembly. An alternative approach is proposed in [6], which estimates the optimized BCs to virtually deform the scan mesh via FEA towards the CAD model. Considering a pre-defined BCs applied on scan mesh, this method estimates new BCs to minimize the location and orientation of fixation features between the predicted shape of the scan model (after virtual deformation) and the CAD model. The predicted displacement BCs applied on the scan mesh via FEA, satisfy the requirements of assembly constraints. Eventually, a *virtual inspection* is performed by comparing the deformed scan mesh in its assembly-state and the CAD model. However, the movable datum targets and restraining forces are not considered in the mentioned CAI methods. These restraining forces are commonly used in aerospace industry to constrain non-rigid parts during inspection. To this end, a virtual fixture method based on *Boundary Displacement Constrained* (BDC) optimization is developed in [1]. The BDC optimization virtually constrains the scan mesh of a part, which is acquired in a free-state, by a combination of restraining forces that are located only on datum targets. This method aims at a non-rigid registration by estimating required restraining forces to displace the scan mesh towards the datum targets. Meantime, these restraining forces minimize the Euclidian distance between the deformed scan mesh and CAD model. The final inspection is performed by evaluating the distance between the positions of datums on the deformed scan mesh in assembly-state and the nominal ones on the CAD model.

The second group of fixtureless inspection methods is developed to especially eliminate the time-consuming drawbacks of treating the scan point cloud to generate a FE mesh and of locating appropriate BCs for each scan model. The high-quality mesh of CAD model is always used in these methods to be deformed towards scan mesh. Therefore, in contrast to the *virtual fixation concept* [5], displacement BCs applied in *virtual reverse deformation* [7] are imposed on each fixation feature of the CAD model. These BCs are used to displace these features towards their corresponding features on the scan model. During the scanning process, some zones on the surface of parts can be missed in the scan point clouds. The loss of scan data is more crucial for fixation features of the scan mesh because the BCs associated with these fixation features cannot be calculated and applied. A fixtureless inspection method based on approximating the location of missing fixation features by an interpolating technique is presented in [8]. In this method, an iterative transformation to the CAD model has been applied, wherein the error between the deformed CAD and partially scanned mesh is minimized. The application of iterative transformation without using a FEA to the CAD model is presented in the *Iterative Displacement Inspection (IDI)* approach [9, 10], whose aim is to displace the CAD model iteratively towards the scan mesh except for defects. IDI applies identification methods that distinguish between defects and flexible deformation and identify possible defect areas on the scan mesh. Afterwards, a smooth and iterative displacement of the CAD model towards the scan mesh is performed by applying proper displacement vectors, while identified defects are excluded from the calculation of these displacement vectors. However, an IDI identification algorithm is limited to localized defects which make it inefficient for manufactured parts with big (global) defects. The *Generalized Numerical Inspection Fixture (GNIF)* approach [11], see Appendix A, also features a fixtureless inspection method that claims to inspect both small (local) and big (global) defects. GNIF assumes that the deformation of a non-rigid part in free-state is isometric (preserves geodesic distances). In other words, the assumption is that there is no stretch in the free-state deformation of inspected non-rigid parts. GNIF generates sets of corresponding sample points between CAD and scan meshes by considering them as geodesic distance

metric spaces and finding sample points distributions that minimize distortion between metrics using *Generalized Multi-Dimensional Scaling* (GMDS) [19]. Discrete geodesic distances for CAD and scan meshes are calculated using *fast marching* [20]. These corresponding sample points are then used as BCs in a FE calculation referred to as *Finite Element Non-rigid Registration* (FENR) to deform the CAD mesh towards the scan mesh. However, some of the sample points generated by GNIF can be located on and/or around defects. Therefore, in [11] sample points are only located on bounding edges, assembly features, which are used as BCs in FENR. This assumes that there are no defects on these features and they are perfectly scanned, which is not necessarily the case. In [12], specific pre-selected sample points calculated as barycenters of manually selected groups of sample points in specific areas on the CAD model are used, as displacement BCs, to deform the CAD mesh towards the scan mesh through FEA. In order to fully automate the inspection process, an automatic fixtureless inspection approach based on filtering sample points is presented in [13]. In this last method, corresponding sample points that are on or close to defects are automatically filtered out, based on curvature and von Mises stress criteria, which automatically leads to a more accurate inspection of non-rigid parts. However, none of those above-mentioned inspection methods can automatically assess whether or not a given manufactured non-rigid part with defects can still be assembled by using perishable restraining loads. As already stated regarding the virtual fixture developed in [1], the required restrained forces are only estimated and introduced on random datum targets. Therefore, the method is not capable of assessing the feasibility of retrieving the functional shape of a geometrically deviated part (scan mesh) because the location of restraining forces is limited to specific zones. In other words, the functional shape of a geometrically deviated scan mesh may be retrieved by applying required restraining loads on zones rather than only datum targets. This is practically confirmed in aerospace industry inspection techniques wherein random restraining loads on the surface of deviated non-rigid parts in a physical fixture retrieve the functional shape of the part. In fact, manufactured parts including different types of defects may still be accepted and assembled under restraining loads introduced at specific locations on the surfaces of the

deviated part. The fixtureless inspection method presented along with the following section is inspired by industrial inspection techniques using weights (such as sandbags) at specific locations on the surface of manufactured parts to retrieve their functional shape. The proposed method can automatically predict the functional shape of a scan mesh acquired from a deviated non-rigid manufactured part and make the decision to accept or reject the part by verifying the predicted shape with respect to GD&T requirements.

6.4 Virtual Mounting Assembly-State Inspection method (VMASI)

The virtual inspection method presented in this paper seeks two purposes for non-rigid parts: 1) eliminating the need for expensive and time-consuming inspection fixtures, 2) finding the possibility of assembling a deviated manufactured part that includes defects. This method applies a non-rigid registration to retrieve the shape of a non-rigid part that may have some level of geometrical deviation, by virtually mounting the part into its assembly-state. The geometrical deviations caused by springback effect, residual stress or any plastic deformation can be presented in manufactured parts. The proposed method assesses the required loads and introduces them on specific zones on the surface of part to find a possibility of placing the deviated manufactured part into assembly-state. This is done by adjusting and aligning assembly mounting features (e.g. holes) which are essential for assembling the part. These mounting features hold the non-rigid part in its functional shape in the assembly position. Considering that the scan mesh of the part is acquired in a known arbitrary free-state condition, this method restricts this scan mesh using permissible loads via FEA and predicts the shape of the scan mesh in assembly-state condition. This is followed by inspecting each mounting hole on the predicted shape of the scan mesh in assembly-state with respect to the dedicated tolerances.

The scan mesh of a part is generated from the scan point cloud obtained by data acquisition devices such as 3D optic scanners. This scan mesh represents the outer surface

(skin) of the manufactured part in a free-state. Due to their compliant behavior, non-rigid parts usually do not match with their final assembly configuration, and their shape in a free-state varies significantly from the nominal CAD geometry [21]. Therefore, the proposed virtual inspection method determines an optimal mapping of scan mesh toward the CAD model under restricting loads on virtual inspection fixtures. Typically, these loads are limited by thresholds that are specified in the engineering technical drawing depending on part material, dimensions and thicknesses. As mentioned, the method is inspired by inspection techniques used in the aerospace industry. These techniques use weights or vacuum as restraining loads on a physical inspection fixture (see Figure 6-2). The proposed method virtually applies equivalent permissible pressures over pre-partitioned zones on the surface of scan model with the objective of retrieving the functional shape in the assembly-state. These partitioned zones replicate areas of contact between weights and the part surface. The *Virtual Mounting Assembly-State Inspection* (VMASI) method intend to virtually deform the scan mesh in an optimal way to adjust and align its mounting holes, as accurately as possible, with corresponding holes in the CAD model. Then the VMASI method assesses if the non-rigid part is acceptable for assembly or if it has to be rejected. This decision depends on how accurately the mounting holes of the part can be oriented and aligned in the virtual assembly-state. The part is rejected when it cannot be put in its assembly-state by using permissible loads as specified in the drawing.

As already mentioned, a triangulated mesh (STL format) is generated from the point cloud. This mesh is smoothed and simplified (decimated) to decrease the effect of scanning noise and to reduce the mesh size [22]. The geometrical deviations associated with the scan model of manufactured parts are generated by adding different synthetic defects to the CAD model of the parts. This is done to control and quantify the type and size of synthetic defects and to assess the effect of defect type, shape and amplitude on results obtained.

A detailed explanation of the proposed VMASI method is provided in the following subsections. The VMASI method features four modules as shown in Figure 6-3. After the

scanning process, these modules are sequentially applied. These modules are pre-registration (section 6.4.1), partitioning of the scan mesh (section 6.4.1), non-rigid registration (section 6.4.2), and inspection evaluation (section 6.4.3). After presenting these modules, the whole sequence is summarized in section 6.4.4.

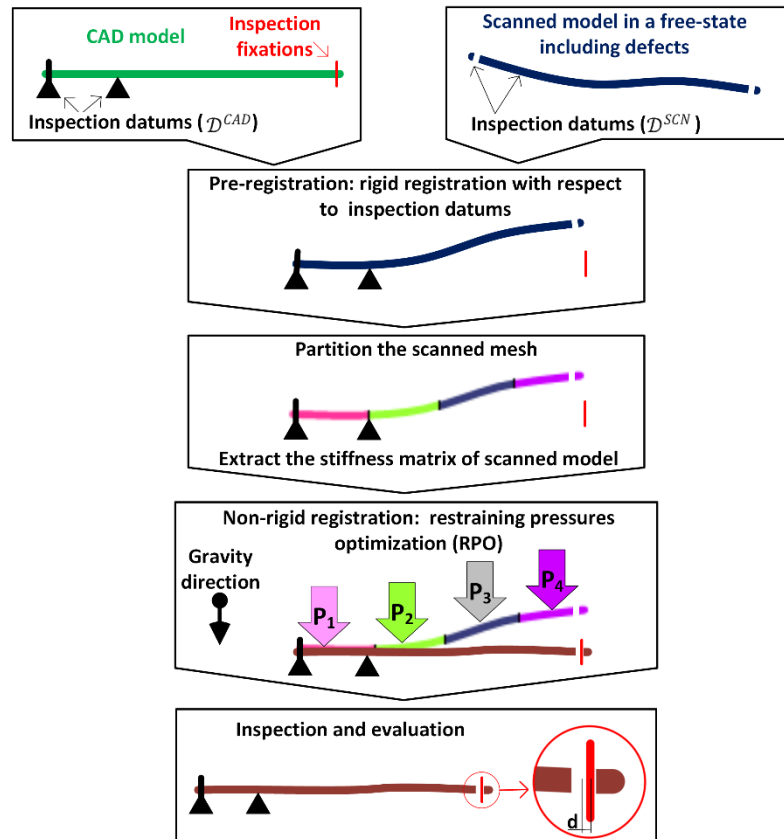


Figure 6-3: Schematic flowchart of the proposed assembly assessing method.

6.4.1 Pre-registration and partition of the scan mesh

As shown in Figure 6-3, the nominal CAD model along with GD&T specifications such as inspection datum information is part of the inputs of the proposed VMASI method. A 3D scan mesh of the part in a free-state is the other input of the method. The pre-registration module seeks to find a proper ICP-based rigid registration to bring the scan mesh and the CAD model close together in a common coordinate system. The assumption of VMASI is that the datum features of the scan model can be perfectly positioned and

aligned with respect to the position and orientation of corresponding datums on the CAD model.

The processed scan mesh with FE-mesh quality in the measurement coordinate system can be presented by a set of N_S^{SCN} nodes in scan mesh with $\mathcal{S}^{SCN} = \{s_1^{SCN}, \dots, s_{N_S^{SCN}}^{SCN} | s_i^{SCN} \in \mathbb{R}^3\}$. On the other side, the CAD mesh in design coordinate system also can be presented by a set of N_S^{CAD} nodes in CAD mesh with $\mathcal{S}^{CAD} = \{s_1^{CAD}, \dots, s_{N_S^{CAD}}^{CAD} | s_i^{CAD} \in \mathbb{R}^3\}$. GD&T specifications of the part determine the datums where the part should be constrained during inspection process. Therefore, a subset of scan mesh presented as $\mathcal{D}^{SCN} = \{d_1^{SCN}, \dots, d_{N_D^{SCN}}^{SCN} | d_i^{SCN} \in \mathbb{R}^3, d_i^{SCN} \in \mathcal{S}^{SCN}\}$ are N_D^{SCN} nodes on inspection datums of scan mesh. Meanwhile, a subset of CAD mesh presented as $\mathcal{D}^{CAD} = \{d_1^{CAD}, \dots, d_{N_D^{CAD}}^{CAD} | d_i^{CAD} \in \mathbb{R}^3, d_i \in \mathcal{S}^{CAD}\}$ are the N_D^{CAD} nodes on inspection datums of CAD mesh. During the pre-registration process, a rigid registration displaces the scan mesh (as a single part) to place it on designed datums and align it with CAD mesh based on datums. Therefore, datum features such as flat surfaces along with fixation holes that considered as datums are aligned between the scan mesh with those of the CAD mesh. The rigidly aligned scan mesh based on designed datums is presented as $\mathcal{S} = \{s_1, \dots, s_{N_S} | s_i \in \mathbb{R}^3\}$ with a set of N_S nodes on the rigidly aligned scan mesh. Consequently, the nodes on the datums identified on the rigidly aligned scan mesh is $\mathcal{D} = \{d_1, \dots, d_{N_D} | d_i \in \mathbb{R}^3, d_i \in \mathcal{S}\}$ where N_D nodes are located on inspection datums of scan mesh after rigid registration.

The inspection result is based on evaluating the distance of assembly fixation features such as mounting holes on the scan mesh with their corresponding mounting hole on the CAD mesh. Therefore, N_J nodes presented by $\mathcal{J} = \{l_1, \dots, l_{N_J} | l_i \in \mathbb{R}^3, l_i \in \mathcal{S}\}$ are also a subset of scan mesh after rigid registration located on inspecting mounting holes. A list of $\mathcal{L} = [\{\mathcal{L}_1\} \dots \{\mathcal{L}_{N_L}\}]$ represents N_L mounting holes that are used for inspection of the scan mesh. For each inspection mounting hole i , $\{\mathcal{L}_i\}$ contains of nodes located on the

edge of the mounting hole associated with scan mesh after rigid registration. For the CAD mesh, $\mathcal{J}^{CAD} = \{l_1^{CAD}, \dots, l_{N_j^{CAD}}^{CAD} \mid l_1^{CAD} \in \mathbb{R}^3\}$ represents N_j^{CAD} nodes on the inspecting mounting holes, and a list $\mathcal{L}^{CAD} = [\{\mathcal{L}_1^{CAD}\} \dots \{\mathcal{L}_{N_{\mathcal{L}}^{CAD}}^{CAD}\}]$ presents nodes located on the edge of each $N_{\mathcal{L}}^{CAD}$ mounting hole on the CAD mesh where $N_{\mathcal{L}}^{CAD} = N_{\mathcal{L}}$.

The step after pre-registration is to partition the scan mesh to meet the requirements for applying the VMASI method. As already mentioned, VMASI method is inspired by the inspection technique using loads as restraining method. Therefore, the scan mesh is properly partitioned into zones where each zone represents the contact surface between each load and the part surface. The partitioning operation can be done automatically by applying *Voronoi tessellation* [23], or it can be performed manually by separating and partitioning connected triangles on scan mesh for each zone. The partitioned into N_p zones is presented as $\mathcal{T} = [\{\mathcal{T}_{(1)}\} \dots \{\mathcal{T}_{(N_p)}\}]$, where $\mathcal{T}_{(i)}$ represents a list of connected triangles allocated to each partitioned zone. A non-rigid registration based on our proposed VMASI method, applies restraining loads in the gravity direction introduced on the partitioned zones to deform the scan mesh towards the nominal assembly-state. This method applies an optimization method to determine restraining loads as presented in section 6.4.2 aiming to minimize the distance and orientation differences between the mounting holes on the scan mesh and their corresponding mounting holes on the CAD mesh.

6.4.2 Non-rigid registration using restraining pressures optimization (RPO)

In this step, the rigidly aligned and partitioned scan mesh of a manufactured part is virtually deformed towards the CAD mesh to place the scan mesh in assembly-state. To virtually deform this aligned and partitioned scan mesh towards the designed assembly mounting holes, the permissible forces are applied on the scan mesh using FEA. In this article, the linear FE-based transformation is applied and presented as:

$$\{f\} = [K]\{u\} \quad 6-1$$

Where $\{f\}$ is the force vector, $[K]$ is the global stiffness matrix and $\{u\}$ is the displacement vector. It should be underlined that the global stiffness matrix for FEA is calculated using Code_AsterTM software. To fulfill the proposed VMASI method, the applied weights (sandbags) used in the practical inspection technique is simulated as pressures introduced in the gravity direction on the scan mesh. Therefore, the force vector applied in the FE calculation based on Equation 6-1 should be modified to take into consideration the applied pressures on each zone of partitioned scan mesh. Therefore, an extrapolation of applied pressure to nodal forces is calculated for each triangle of scan mesh.

After establishing the FE-based transformation model of scan mesh, a non-rigid registration is performed using our developed Restraining Pressures Optimization (RPO) approach. The RPO approach aims at minimizing the distance and orientation differences of mounting holes on the scan mesh with respect to the nominal mounting holes on the CAD mesh. For each mounting hole, a center along with a normal vector of the hole are calculated based on the nodes located on the edge of the hole. The center of a hole is the center of mass associated with the nodes located on the edge of the hole. The normal vector of the hole, which presents the orientation of mounting hole, is the normal vector of a plane passing approximately through all the nodes on the edge of the mounting hole. The RPO approach intends to minimize the distance and orientation differences of mounting holes on the scan mesh with respect to those on the CAD mesh by estimating the required pressures on partitioned zones of the scan mesh. The RPO approach estimates these restraining pressures by setting up an optimization problem to minimize both Euclidean distances for the center of mass and orientation differences between the holes on scan and CAD meshes. The center of mass $\mathbf{C}_{\mathcal{L}}$ is calculated for each list of $\{\mathcal{L}_i\}$ presenting the nodes located on the edge of a mounting hole in the scan mesh. On the other side, the center of mass $\mathbf{C}_{\mathcal{L}^{CAD}}$ is also calculated for each list of $\{\mathcal{L}_i^{CAD}\}$, which is representing the nodes on the edge of mounting hole in the CAD mesh. As shown in

Equation 6-2, an arithmetic average of differences (Δ) between centers of mass associated with mounting holes on the scan and CAD mesh for $N_{\mathcal{L}}$ number of mounting holes are calculated. Meanwhile, for each mounting hole the best planar fit to the coordinate of nodes located on the edge of a hole is calculated via a least squares regression, and then a unite vector normal to this plane presents the orientation of the hole. The normal to the plane passing through the nodes on the edge of a mounting hole (for each list of $\{\mathcal{L}_i\}$) in scan mesh is presented by $\mathbf{n}_{\mathcal{L}}$, whereas the normal vector for CAD mesh (for each list of $\{\mathcal{L}_i^{CAD}\}$) is presented by $\mathbf{n}_{\mathcal{L}^{CAD}}$.

$$\Delta = \frac{1}{N_{\mathcal{L}}} \sum_{i=1}^{N_{\mathcal{L}}} \|\mathbf{C}_i - \mathbf{C}_i^{CAD}\| \quad 6-2$$

To compare the mounting hole orientation on the scan mesh with respect to the CAD mesh, the angle between the normal of holes on the CAD and scan meshes is represented by $\theta_{\mathbf{n}, \mathbf{n}^{CAD}}$. A root mean square deviation (O), as shown in Equation 6-3, is calculated for $N_{\mathcal{L}}$ number of mounting holes.

$$O = \sqrt{\frac{1}{N_{\mathcal{L}}} \sum_{i=1}^{N_{\mathcal{L}}} (\theta_{\mathbf{n}, \mathbf{n}^{CAD}(i)})^2} \quad 6-3$$

In order to establish a proper objective function based on both *distance* and *orientation* values, a weighting factor (w) is applied to balance the magnitude between the values of *distance* (Δ) and *orientation* (O). Therefore, the objective function (OF) is generated as Equation 6-4.

$$OF(p) = \Delta + w \times O \quad 6-4$$

Wherein w can be formulated based on the proportion of initial values for *distance* and *orientation* as presented in Equation 6-5.

$$w \approx \frac{\Delta_{initial}}{O_{initial}} \quad 6-5$$

As mentioned in section 6.4.1, the scan mesh is partitioned into N_p zones presented as triangulations lists of the scan mesh $\mathcal{T} = [\{\mathcal{T}_{(1)}\} \dots \{\mathcal{T}_{(N_p)}\}]$ wherein $\{\mathcal{T}_{(i)}\}$ is a list of connected triangles associated with each partitioned zone on the scan mesh. The RPO

approach is followed by solving the constrained nonlinear optimization problem, presented in Equation 6-6, to minimize both distance and orientation differences between the scan and CAD meshes by estimating the permissible required pressures (\mathcal{P}) applied on $N_{\mathcal{P}}$ partitioned zones of scan mesh in the gravity direction.

$$\arg \min_{\mathcal{P}} OF(\mathcal{P}) \quad 6-6$$

$$\text{subject to } P_i \leq P_i^{Max}, i = 1, \dots, N_{\mathcal{P}}$$

The argument of the objective function \mathcal{P} represent the magnitude of pressures in the gravity direction introduced to each partitioned zone on the scan mesh. This optimization problem is solved using the constrained nonlinear optimization function *fmincon* with the *active-set* algorithm implemented in MATLAB™. The output of Equation 6-6 is an estimation of required pressures on the scan mesh that predicts the functional shape of scan mesh through the FE-bases transformation in the assembly-state whereas the minimum distance and orientation differences between the mounting holes on the predicted shape of scan mesh and nominal CAD model are achieved. The argument is generated as a $N_{\mathcal{P}} \times 1$ vector $\mathcal{P} = \langle P_1, \dots, P_{N_{\mathcal{P}}} \rangle$, where $P_i \in \mathbb{R}^+$ and the magnitude of the pressure P_i is limited, with an inequality constraint in the optimization problem, to the magnitude of maximum permitted pressure on each partitioned zone (P_i^{Max}). The permitted pressure P_i^{Max} is calculated by multiplying the magnitude of maximum permitted restraining force as presented in the GD&T specifications multiplied by the area of each partitioned zone $A_{\mathcal{P}_i}$. The direction of restraining pressures is always that of the gravity since it is simulating the realistic weight of sandbags applied in each partitioned zone. Applying the optimized pressure values \mathcal{P} in the FEA-based transformation, the scan mesh (\mathcal{S}) is deformed towards the nominal assembly mounting holes generating the predicted functional shape of scan mesh in assembly-state (\mathcal{S}_{opt}).

6.4.3 Inspection and evaluation

As mentioned in section 6.4.2, the optimization problem of Equation 6-6 estimates the required restraining pressures on the partitioned zones of the scan mesh. Using the

optimized pressures in the FEA-based transformation presented in Equation 6-1, the scan mesh (\mathcal{S}) is deformed to generate the predicted functional shape of a scan mesh in assembly-state (\mathcal{S}_{opt}). The nodes associated with the N_L mounting holes on the predicted shape of scan mesh are accordingly presented with \mathcal{J}_{opt} , and a list of $\mathcal{L}_{opt} = [\{\mathcal{L}_{opt1}\} \dots \{\mathcal{L}_{optN_L}\}]$ specify nodes located on the edge of each mounting hole on the predicted shape of scan mesh. To evaluate the acceptance of the deviated manufactured part in assembly-state, each mounting hole on the predicted shape of scan mesh is examined with reference to the nominal mounting holes and the dedicated tolerances. Based on GD&T standards, the assembly tolerance of a part consists of the position and profile tolerances. For ordinary non-rigid parts used in aerospace industry, the position and profile tolerances are commonly determined as ± 0.4 mm. Referring to section 7.5 (paragraph 7.5.5) in ASME Y14.5 (2009), the position and profile offset of a part, as shown in Figure 6-4, depends directly to the position of center of mass associated with a mounting hole. The Euclidian distance between the center of mass for the hole on scan and CAD mesh (between \mathbf{C}_i and \mathbf{C}_i^{CAD}) is presented with blue dotted-lined in Figure 6-4. According to ASME Y14.5 (2009), the projection of this line on the normal direction of the CAD surface presents the profile offset, whereas the projection of the Euclidian distance on the tangent direction of the CAD surface presents the position offset. Therefore, a deviated manufactured part can be accepted for the assembly-state if the position and profile offsets for each mounting hole on the predicted shape of the scan mesh under estimated pressures remains in the dedicated tolerance range ($\emptyset 0.8$ mm).

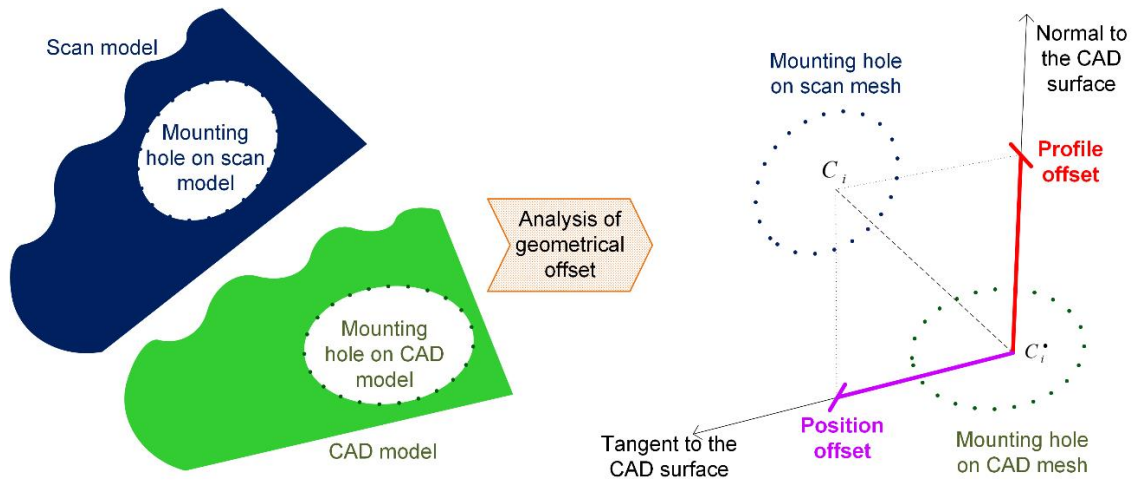


Figure 6-4: Analysis of geometrical offset based on GD&T specification.

The orientation of mounting holes on the predicted shape of a scan mesh is an additional criterion for accepting or rejecting a deviated manufactured part. As depicted in Figure 6-5, the orientation offset (δ) of a mounting hole depends to the thickness of non-rigid part. The acceptance criterion of a non-rigid part in an assembly-state based on GD&T specification mandates that the orientation offset (δ) of a mounting hole must remain in the tolerance range. The orientation difference, which is the representative angle between the normal vectors associated to the mounting hole on the CAD and scan models, is related to the orientation offset with Equation 6-7.

$$t \times \tan \theta_{n,n_{CAD}} = \delta \quad 6-7$$

Regarding the determined tolerance for typical aerospace parts (± 0.4 mm) and considering the thickness of a non-rigid part, the maximum tolerable orientation difference ($\theta_{n,n_{CAD}}$) is obtained from Equation 6-7.

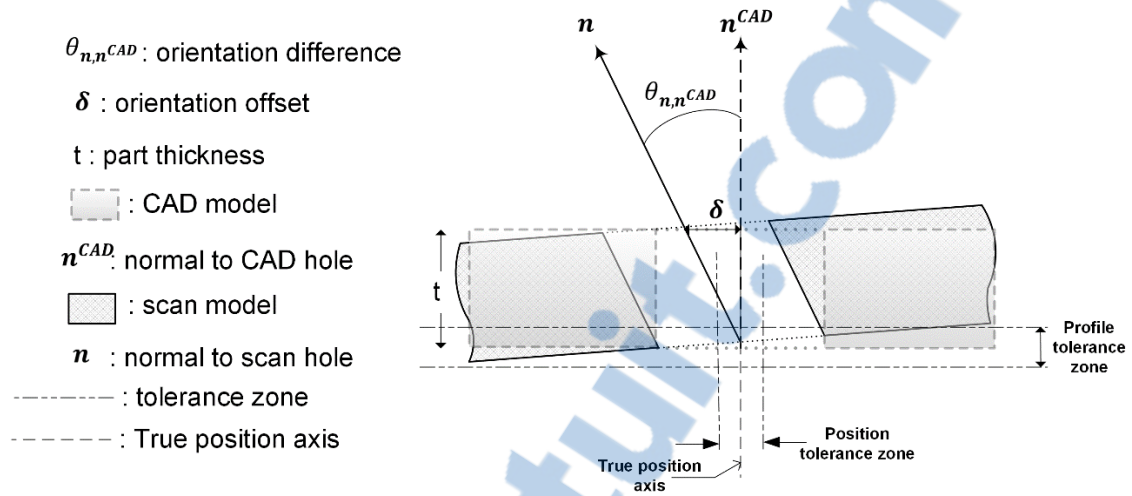


Figure 6-5: Schematic misalignment of assembly mounting hole on predicted shape of scan model with respect to the CAD model.

6.4.4 The proposed VMASI algorithm

The VMAI method outlined in the above four modules is summarized and illustrated in the flowchart shown in Figure 6-6. The scan mesh of a manufactured part in a free-state and its nominal CAD model along with GD&T specification is considered as the inputs of our proposed method. In other words, inspection datums information, mounting holes position, CAD mesh (\mathcal{S}^{CAD}) and scan mesh (\mathcal{S}^{SCN}) with acceptable mesh quality for FEA are the inputs required for the proposed method. From these inputs, the method proceeds through the following main steps:

1. ICP-based pre-registration between \mathcal{S}^{SCN} and \mathcal{S}^{CAD} aligns the datums on scan mesh with respect to datums on the CAD mesh for which the scan mesh after rigid registration is presented as \mathcal{S} .
2. Partitioning the scan mesh into N_p zones for which the partitioned scan mesh is presented by lists of connected triangles in each partition as $\mathcal{T} = \{ \{ \mathcal{T}_{(1)} \} \dots \{ \mathcal{T}_{(N_p)} \} \}$.

- Establishing the FE-based transformation as $\{f\} = [K]\{u\}$, and extracting the relevant stiffness matrix for the scan mesh of manufactured part.

Applying a non-rigid registration using the RPO approach to estimate the required restraining pressures as $\mathcal{P} = \langle P_1, \dots, P_{N_p} \rangle$ for minimizing the distance and orientation differences between the scan and CAD mounting holes.

Introducing the required restraining pressures to the scan mesh via the FE-based transformation and predicting the shape of scan mesh in assembly-state as \mathcal{S}_{opt} .

Inspecting each mounting hole on the predicted shape of scan mesh with respect to tolerances to accept or reject the manufactured part for pursuing the assembly stage.

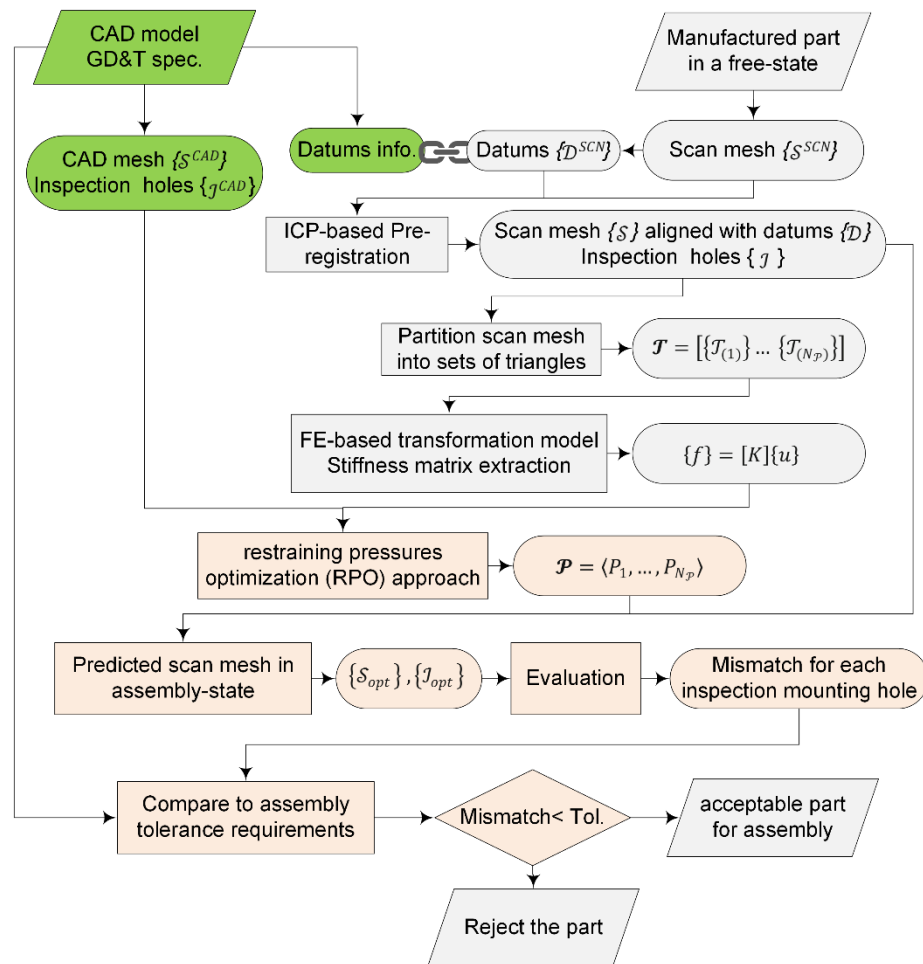


Figure 6-6: Flowchart algorithm of proposed VMASI method.

6.5 Application of proposed VMASI method on real parts

6.5.1 Introduction: validation cases

In this section, our proposed fixtureless inspection method (VMASI) is applied on two aluminum parts referred as part A and part B to validate the performance of the proposed method including different types of defects in free-state. Part A is a non-rigid support V-shaped part formed with a specific forming angle, and part B is a relatively large non-rigid panel typical used in aerospace industry. Scan models of the parts studied in this paper are generated by adding synthetic defects into the CAD model of parts wherein the magnitude and location of defects are known which permit analyzing the results of VMASI method with respect to the known defects. The generated scan meshes, representing different types of deviated non-rigid manufactured parts (as depicted in Figure 6-7), are then virtually inspected by VMASI method to ensure the feasibility of assembling these deviated parts in its functional assembly-state. The VMASI assesses the required restraining loads as a set of pressure on the scan mesh in the direction of gravity, which replicates the inspection technique using weights (sandbags). These required pressures are calculated using our developed restraining pressures optimization (RPO) approach. As introduced in section 6.4, along this optimization process, a maximum threshold is applied on restraining pressures depending on part material, dimensions and thicknesses. Applying these required pressures on a scan mesh of a deviated part predict the functional shape of scan mesh wherein the position and orientation of mounting holes are well-aligned with those of nominal CAD model. Inspecting each mounting hole on the predicted shape of scan mesh in assembly-state with respect to the determined assembly tolerances ensures the possibility of successful assemblage for the geometrically deviated part. As mentioned in Equation 6-6, the proper weighting factor (w) is required to be calculated for these non-rigid parts to balance the magnitude of *distance* and *orientation* (respectively Equation 6-2 and 6-3 in the RPO approach). Based on different attempts for each case studied in this paper, the weighting factor (w) that properly satisfy the magnitude balance between the elements of Equation 6-6 is calculated

by Equation 6-8. The coefficient of proportionality in this equation is empirically determined as 0.5 because this value well-moderate the proportion that is used as trials for the cases studied in this paper.

$$w = 0.5 \left(\frac{\Delta_{initial}}{O_{initial}} \right) \tag{6-8}$$

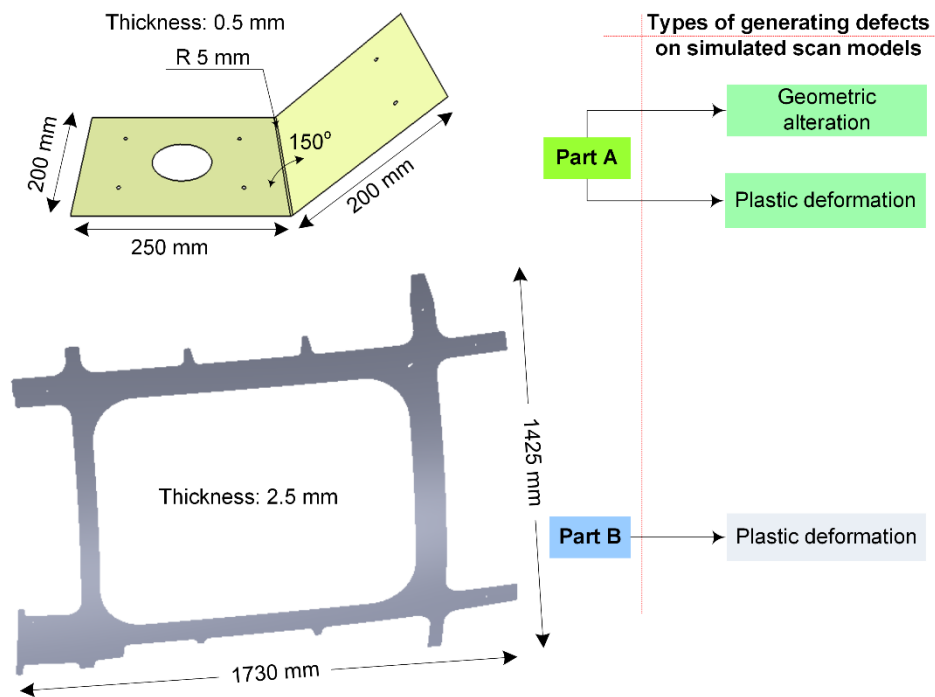


Figure 6-7: Synthesis of validation cases with different types of defects.

We have implemented our fixtureless method on validation parts using several tools. Mesh generation, FEA simulation and extracting the stiffness matrix of scan mesh are performed using the research platform developed by our research team [24]. This platform is based on C++ code, on Open CASCADE™ libraries for geometry and on Code_Aster™ as FEA solver. We also use Gmsh™ [25] for visualizing 3D models. Finally, the automatic mesh partition process, as well as optimization problem, is solved using the constrained nonlinear optimization function in MATLAB™ (using *fmincon* with the *active-set* algorithm) to validate the distance distribution of estimated defects. This

process takes approximately 8 minutes on a computer equipped with an Intel^(R) Core™ i7 at 3.60 GHz with 32 GB RAM.

6.5.2 Results for part A

The different scan meshes for cases studied based on part A are attained by adding two different types of synthetic defects such as geometric alterations for some selected features and plastic deformation(s) (see Figure 6-7). Part A is an aluminum plate with 0.5 mm thickness which is formed in a V-shape with an angle 150 deg. (250×200 mm for the horizontal side, and 200×200 mm for the other side). The horizontal side of the part should be constrained as shown in Figure 6-8. Therefore, the horizontal side of the part is located on the plane as datum A. Referring to the GD&T specification, the pattern of 4 holes also should be constrained as datum B. These holes during the inspection are fixed in the design datum position. It should be emphasized that we assume datum features on the scan models are perfect, which means the flatness of the horizontal side and the position of four datum holes are perfectly respected. The inspection is also accomplished on the two mounting holes located on the right side where the assembly tolerance is $\varnothing 0.8$ mm.

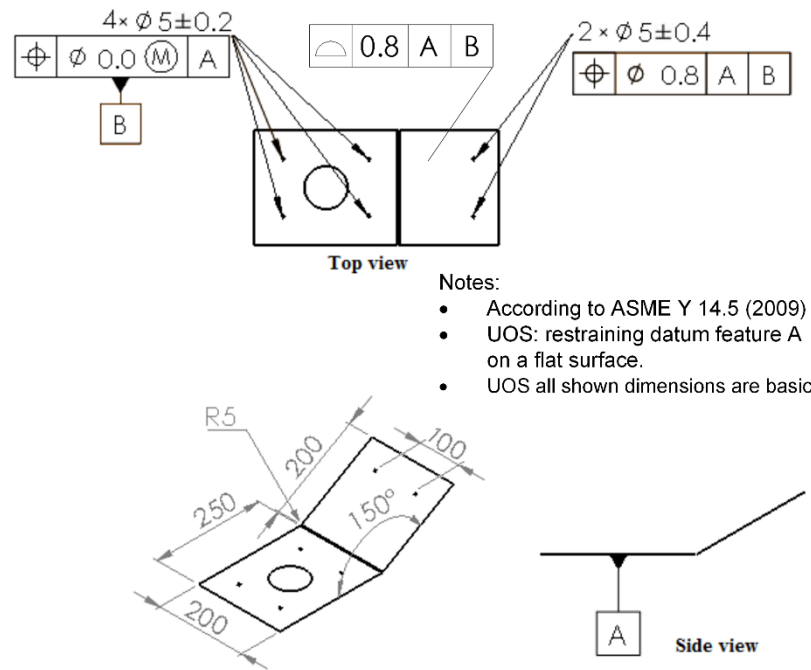


Figure 6-8: GD&T specification for part A (dimensions are in mm).

To evaluate the performance of our proposed method, different types of defects are generated and simulated based on the CAD model. Therefore, geometric alterations (described in section 6.5.2.1) representative for springback effect in sheet metal forming process are used to generate a defect by decreasing the forming angle. Another type of defect that is simulated on part A is a plastic deformation that can be occurred during any manufacturing or handling process before inspection process. As described in section 6.5.2.2, a non-linear FE simulation is performed wherein a plastic deformation is added into the CAD model of part A. To accomplish this, a proper load is first introduced on the CAD model to deform the model into the plastic zone. The plastic deformation remaining on the model after releasing the load represents the added defect to the CAD model of the part. In Table 6-1, a synthesis of validation cases for part A, describing each validation case along with an assigned label, is shown. It should be underlined that the maximum permissible restraining pressure for part A is 10 lbf/ft² (approximately 480 Pa). Meanwhile, the maximum tolerable orientation difference for mounting holes on the CAD

and scan models is calculated as 38 deg. with respect to the dedicated tolerance ($\emptyset 0.8$ mm) and the constant thickness of part A (0.5 mm).

Table 6-1: Synthesis of validation cases defects for part A.

Description for defects of part A	Assigned label for each validation case
Generated by decreasing 1 deg. of forming angle	A-1
Generated by decreasing 3 deg. of forming angle	A-2
Generated by decreasing 5 deg. of forming angle	A-3
Simulated as a small plastic defect	A-4
Simulated as a large plastic defect	A-5

6.5.2.1 Scan models of part A with defects generated by geometric alteration

As previously mentioned, scan models in this study are generated by adding defects to the CAD model. In this section, defects are generated by decreasing the forming angle of the V-shaped model using geometric transformation. Therefore, three magnitudes of defects are performed by decreasing 1, 3 and 5 deg. of forming angle with respect to the nominal forming angle (150 deg.). These defects respectively result in a maximum displacement of 3.5, 10.5 and 17.5 mm in the corresponding scan models. To implement the proposed VMASI method on the scan models of part A, a FE mesh of the scan model is generated to present the scan mesh.

The first scan model of part A, as labeled in Table 6-1 with A-1, includes a defect where the V-shaped forming angle is decreased to 149 deg. with respect to the nominal angle, which is 150 deg. The displacement distribution of scan model with respect to the CAD model of part A is depicted in Figure 6-9-a. This shows the maximum displacement between the models reaches to 3.5 mm. The scan mesh of this model is generated with a FE mesh quality and then is partitioned into 10 zones as shown in Figure 6-9-b. Then the

stiffness matrix of the scan mesh is extracted based on the mechanical property and thickness of the part. Applying the *Restraining Pressures Optimization* (RPO) approach, the required pressures in the gravity direction on each partitioned zone of the scan mesh is found in which the scan mesh under these pressures is deformed to predict the functional shape of scan mesh in assembly-state. To this end, the optimization approach aims to minimize the distance and orientation difference between the mounting holes on the predicted shape of scan mesh with respect to the CAD mesh. Based on GD&T specification, the horizontal side of the part consisting of zones 7, 8, 9 and 10 should be constrained on datum A. Therefore, applying restraining pressures on these zones is meaningless since these partitions of the part are already constrained on a flat surface in the gravity direction. For this reason, the RPO approach is applied to estimate the restraining pressures only on the right side of the part restraining the zones 1, 2, 3, 4, 5 and 6. As depicted in Figure 6-9-b and summarized in Table 6-2, these pressures should be applied on partitioned zones of 3, 4, 5 and 6 respectively with 60, 62, 19 and 30 Pa. The inspection for the predicted shape of scan mesh under the required pressures is performed for the mounting holes placed on the right side of the part A shown as FEATURE 1 and FEATURE 2 in Figure 6-9-b. As depicted in Table 6-3, position and profile offsets for both mounting holes are less than the dedicated tolerances while the orientation of holes is also acceptably aligned with the CAD model. This means that the geometrically deviated scan mesh (presenting defect) can be assembled in the functional position with respect to the tolerance. Therefore, the deviated manufactured part is accepted to pass forward to the assembly stage.

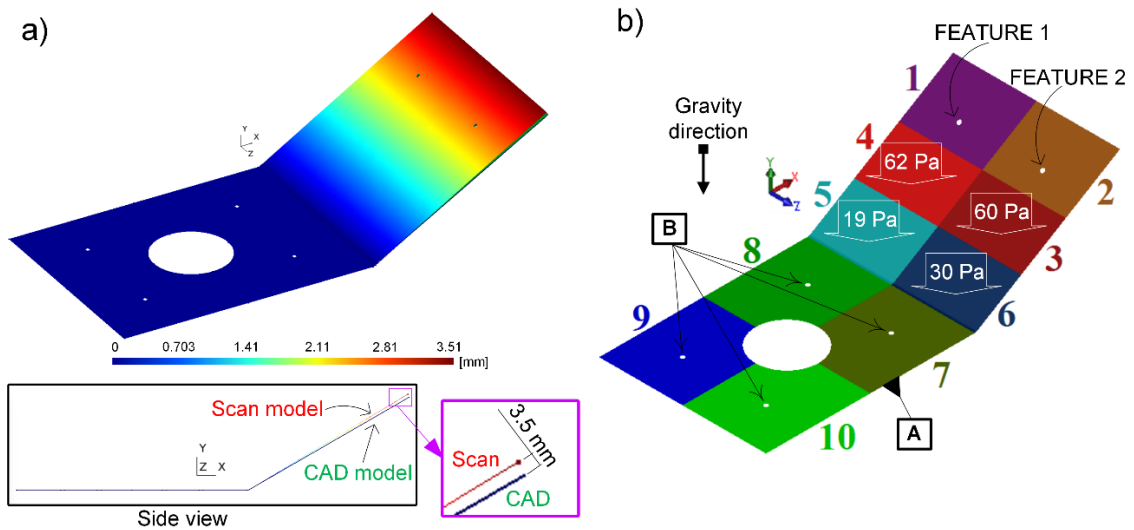


Figure 6-9: a) Displacement distribution [mm] of deviated scan model generated by decreasing 1 deg. of forming angle; b) The partitioned scan model and predicted assembly pressure.

Table 6-2: Assembly pressure and force results for the validation case A-1.

Zones	Area [mm ²]	Permissible restraining pressures [Pa]	Pressure [Pa]	Force [N]
1	7563	480	0	0.00
2	7563	480	0	0.00
3	6208	480	60	0.37
4	6208	480	62	0.38
5	6490	480	19	0.12
6	6490	480	30	0.20

Table 6-3: Position, profile and orientation results for the validation case A-1.

Mounting holes	Position offset [mm]	Profile offset [mm]	Orientation difference [deg.]
Feature 1	0.03 (accepted)	0.03 (accepted)	0.25 (accepted)
Feature 2	0.03 (accepted)	0.02 (accepted)	0.25 (accepted)

The second scan model, as shown in Table 6-1 with A-2, is generated in the same way with a forming angle decreased by 3 deg., which consequently result in 10.5 mm of maximum displacement comparing as shown in Figure 6-10-a. The FE mesh of this deviated model is generated and partitioned into 10 zones. Considering the constraints of datum A, the RPO approach is applied to zones 1, 2, 3, 4, 5 and 6. The required pressures in the gravity direction on the corresponding partitioned zones minimize the distance and orientation differences between the mounting holes of the scan and CAD meshes. These required pressures and the corresponding zones are summarized in Table 6-4 and depicted in Figure 6-10-b. Recovering the predicted shape of a scan mesh in assembly-state under the required pressures via FEA, the inspection is accomplished by comparing each mounting hole on the predicted scan mesh and CAD model with respect to the tolerance. As presented in

Table 6-5, the position and profile offset of mounting holes on the predicted scan mesh in assembly-state are still in the tolerance zone, and the orientation differences are negligible.

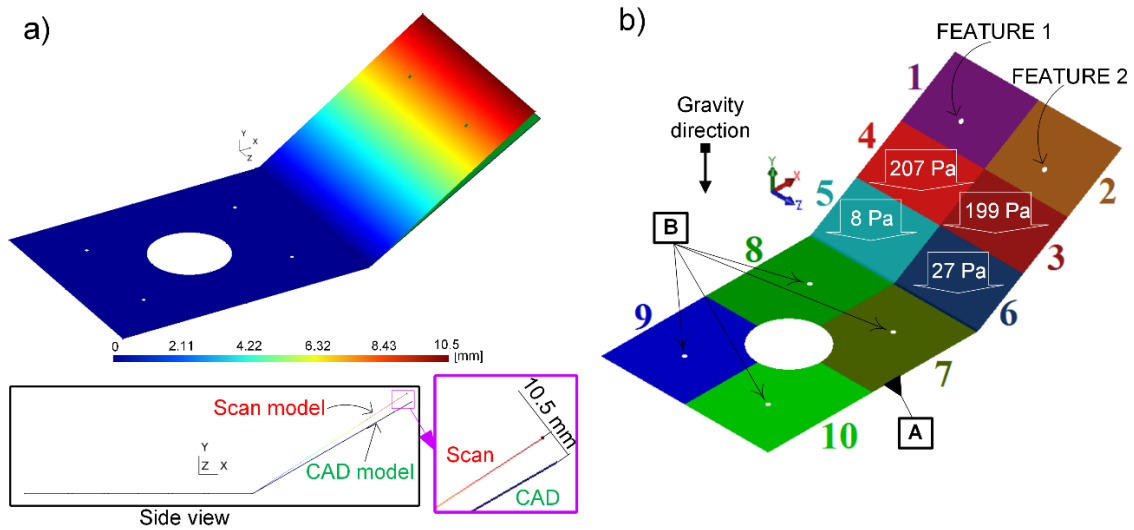


Figure 6-10: a) Displacement distribution [mm] of deviated scan model generated by decreasing 3 deg. of forming angle; b) The partitioned scan model and predicted assembly pressure.

Table 6-4: Assembly pressure and force results for the validation case A-2.

Zones	Area [mm ²]	Permissible restraining pressures [Pa]	Pressure [Pa]	Force [N]
1	7731	480	0	0.00
2	7731	480	0	0.00
3	6125	480	199	1.22
4	6125	480	207	1.27
5	6407	480	8	0.05
6	6407	480	27	0.17

Table 6-5: Position, profile and orientation results for the validation case A-2.

Mounting holes	Position offset [mm]	Profile offset [mm]	Orientation difference [deg.]
Feature 1	0.22 (accepted)	0.18 (accepted)	0.71 (accepted)
Feature 2	0.21 (accepted)	0.21 (accepted)	0.71 (accepted)

Decreasing the forming angle by 5 deg. (from 150 deg. to 145 deg.) in the third case of part A, as labeled in Table 6-1 with A-3, the maximum displacement between the scan and CAD models reaches 17.5 mm as shown in Figure 6-11-a. The scan mesh with FE mesh-quality is generated from the deviated scan model, and then it is partitioned into the zones. Applying RPO, the required pressures on the right side of the part (zones 1, 2, 3, 4, 5 and 6) to minimize the distance and orientation difference between the predicted shape of scan mesh and CAD is calculated as presented in Figure 6-11-b and Table 6-6. Using these pressures on the scan mesh and recovering the predicted shape of scan mesh

in the assembly-state, the inspection is accomplished by comparing between the mounting holes of the scan mesh with the CAD mesh. As summarized in

Table 6-7 in red, both position and profile offsets are exceeding the assembly tolerance for typical non-rigid parts, and the orientation offset surpasses 1 deg. of orientation difference. In fact, this deviated scan model cannot be assembled in the functional state with respect to the assembly tolerances.

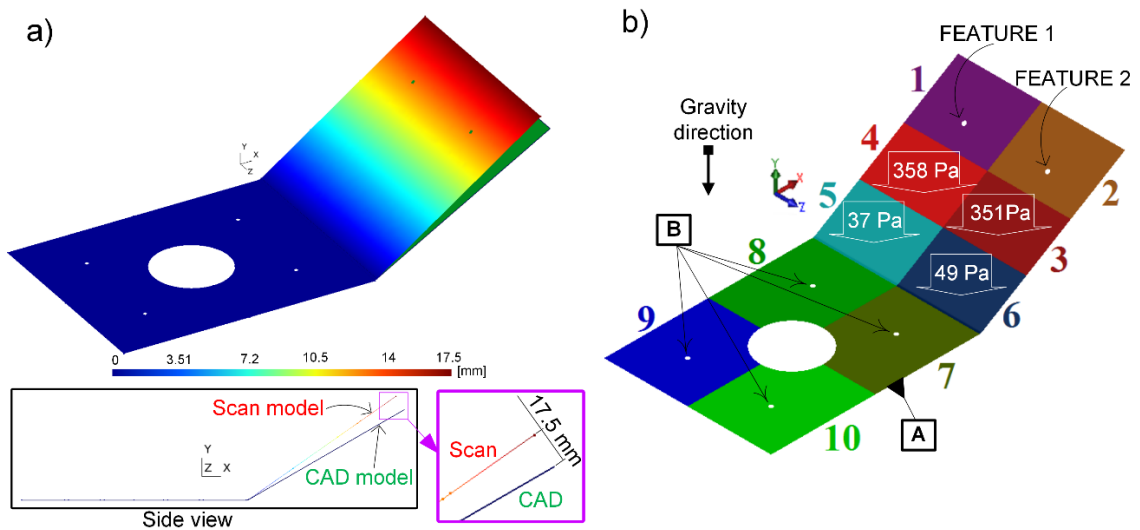


Figure 6-11: a) Displacement distribution [mm] of deviated scan model generated by decreasing 5 deg. of forming angle; b) The partitioned scan model and predicted assembly pressure.

Table 6-6: Assembly pressure and force results for the validation case A-3.

Zones	Area [mm ²]	Permissible restraining pressures [Pa]	Pressure [Pa]	Force [N]
1	7915	480	0	0.00
2	7915	480	0	0.00
3	6032	480	351	2.11
4	6032	480	358	2.16
5	6315	480	37	0.24
6	6315	480	49	0.31

Table 6-7: Position, profile and orientation results for the validation case A-3.

Mounting holes	Position offset [mm]	Profile offset [mm]	Orientation difference [deg.]
Feature 1	0.56 (rejected)	0.52 (rejected)	1.05 (accepted)
Feature 2	0.56 (rejected)	0.54 (rejected)	1.05 (accepted)

6.5.2.2 Scan models of part A with defects simulated by plastic deformation

The deviated scan model can also represent plastic deformations. This type of defect is simulated using non-linear FEA and simulating a plastic deformation of a model after releasing the applied loads. The fourth case of part A, as labeled in Table 6-1 with A-4 and shown in Figure 6-12-a, represents a scan model in which the maximum displacement with reference to the CAD model reaches to 9.2 mm. This scan mesh of the model is generated and partitioned into 10 zones. Applying the RPO approach on the right side (on zones 1, 2, 3, 4, 5 and 6), the required pressures are presented in Table 6-8. These pressures on the scan mesh are calculated to minimize the distance and orientation difference of the mounting holes on the predicted shape of scan mesh with respect to the CAD mesh. Inspecting the predicted shape of scan mesh, as summarized in Table 6-9, the

position and profile offsets for both mounting holes are in tolerance range, and the orientation difference is negligible. Therefore, this deviated scan model is acceptable for being assembled in the assembly-state.

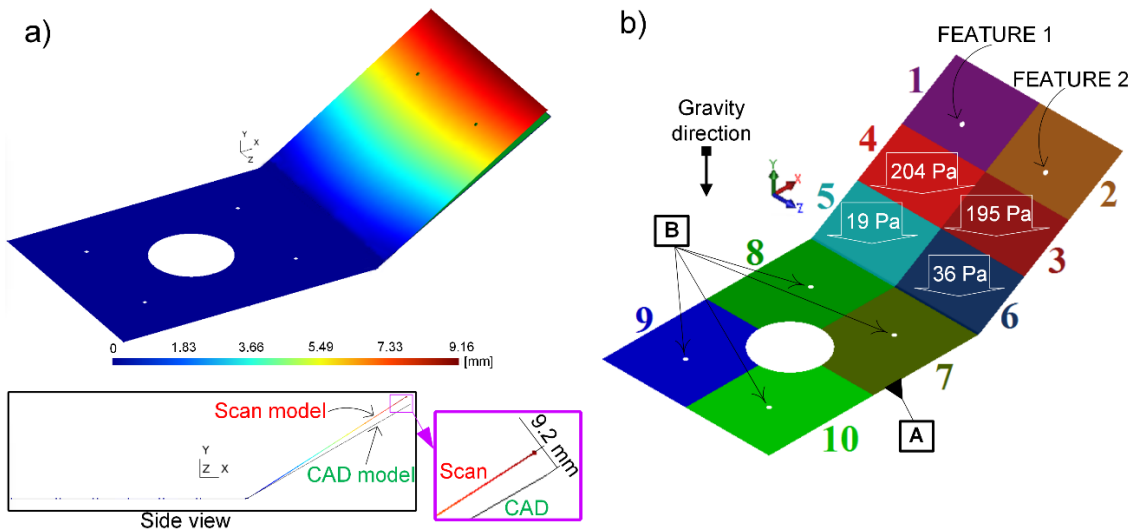


Figure 6-12: a) Displacement distribution [mm] of slightly deviated scan mesh simulating a plastic defect; b) The partitioned scan model and predicted assembly pressure.

Table 6-8: Assembly pressure and force results for the validation case A-4.

Zones	Area [mm ²]	Permissible restraining pressures [Pa]	Pressure [Pa]	Force [N]
1	7486	480	0	0.00
2	7486	480	0	0.00
3	6247	480	195	1.22
4	6247	480	204	1.28
5	6529	480	19	0.12
6	6529	480	36	0.24

Table 6-9: Position, profile and orientation results for the validation case A-4.

Mounting holes	Position offset [mm]	Profile offset [mm]	Orientation difference [deg.]
Feature 1	0.30 (accepted)	0.15 (accepted)	0.32 (accepted)
Feature 2	0.30 (accepted)	0.15 (accepted)	0.32 (accepted)

The last case of part A, as labeled in Table 6-1 with A-5, is simulating a greater plastic defect. In this case, the maximum displacement of scan model reaches 12.5 mm (see Figure 6-13-a). Applying the RPO approach on the deviated scan mesh (on zones 1, 2, 3, 4, 5 and 6), the required pressures are calculated as presented in Figure 6-13-b and Table 6-10. Applying these pressures on the deviated scan mesh via FEA and recovering the predicted shape of scan mesh in the assembly-state. As presented in Table 6-11, position offsets for both mounting holes exceed the tolerance value which means that we cannot accept this deviated part for precise assembly.

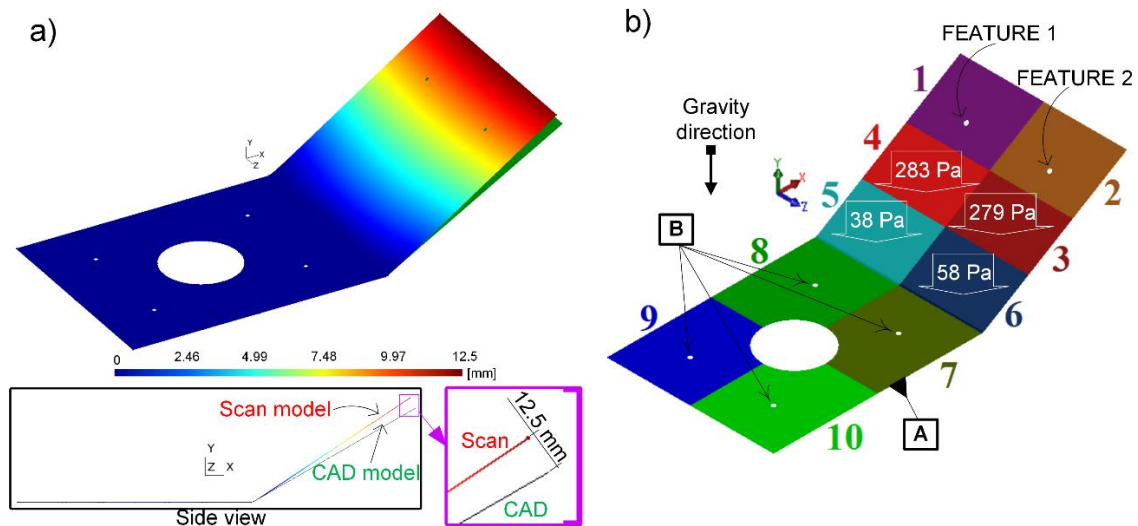


Figure 6-13: a) displacement distribution [mm] of deviated scan mesh simulating a plastic defect; b) the partitioned scan model and predicted assembly pressure.

Table 6-10: Assembly pressure and force results for the validation case A-5.

Zones	Area [mm ²]	Permissible restraining pressures [Pa]	Pressure [Pa]	Force [N]
1	7486	480	0	0.00
2	7486	480	0	0.00
3	6247	480	279	1.75
4	6247	480	283	1.77
5	6529	480	38	0.25
6	6529	480	58	0.38

Table 6-11: Position, profile and orientation results for the validation case A-5.

Mounting holes	Position offset [mm]	Profile offset [mm]	Orientation difference [deg.]
Feature 1	0.56 (rejected)	0.28 (accepted)	0.34 (accepted)
Feature 2	0.56 (rejected)	0.22 (accepted)	0.39 (accepted)

6.5.3 Results for part B

Part B (Figure 6-7) is representative of an aerospace aluminum panel with 2.5 mm thickness, and dimensions of approximately 1730 × 1425 mm (area of 0.59 m²). To make an inspection on this part, as depicted in Figure 6-14, the part is first mounted on datum targets (datum A). Then, the tooling (fixing) hole of datum B is adjusted in its designed position by using an adjusting pin. In order to perform the inspection in reality, applying physical datums, the part is imposed to be statically stable by inserting another adjusting pin into a slotted tooling hole (datum C). The tooling hole of datum C located on the diagonally opposite side with respect to the tooling hole associated with datum B. In fact, the slotted tooling hole is aligned along the diagonal line (dotted line in Figure 6-14-b)

passing through the center of the tooling hole for datum B. The datum C constrained the part against free rotation around datum B but still let freedom for adjustment and alignment of the part in its assembly-state along the diagonal line. The restraining loads such as weights (sandbags) on different zones on the surface of the panel can be applied to place the deviated manufactured panel in its assembly position. As shown in Figure 6-14-a, conventional inspection methods apply a huge number of fixtures to retrieve the fictional shape of the deviated manufactured part on these physical complex inspection fixture. However, the simulation through our VMASI method aims at virtually mounting deviated manufactured parts in assembly-state, wherein datums are imposed as boundary conditions in a FEA. In this study, the least possible number of fixtures (only 9 fixtures) are used for simulating datum targets (datum A). It is supposed that the tooling (fixing) hole of datum B is perfectly positioned in the design location. Therefore, imposed displacement on the edges of tooling hole is introduced as constraints in FEA. Imposing displacement constraints on the edges of a tooling hole provides a statically stable model for our VMASI method. Therefore, the VMASI method for the cases studied on part B considers only datum A and B as imposed BCs applied in FEA regardless of imposing any boundary condition on datum C. The position and value of required pressures, representing weights, are calculated using our RPO approach where the scan model in the assembly-state is predicted by minimizing the distance and orientation difference of mounting holes. Then, the inspection is accomplished on these mounting holes shown as FIXTURE 1, 2, 3 and 4 in Figure 6-15-b, to ensure they are placed in the assembly-state with respect to the tolerance range ($\varnothing 0.8$ mm). Dimensions of part B make that the maximum permissible restraining force is 20 lbf/ft² (approximately 960 Pa). Meanwhile, the maximum tolerable orientation difference for mounting holes on the CAD and scan models is calculated as 9 deg. based on the constant thickness of part B (2.5 mm).

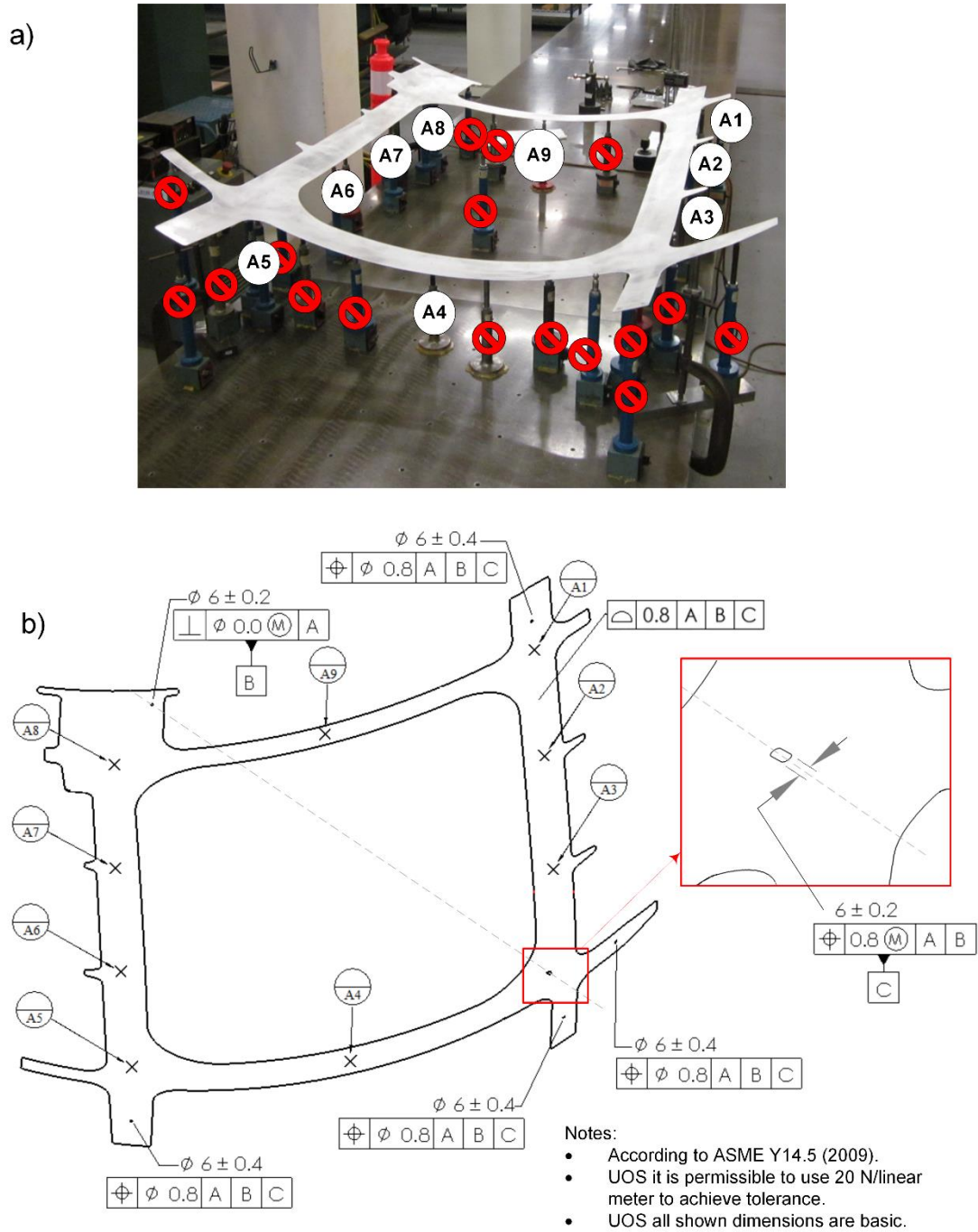


Figure 6-14: a) The manufactured part mounted on inspection fixtures where a real point cloud of scan mesh can be acquired, in our proposed method only 9 fixation features are kept as datums; b) GD&T specification for part B (dimensions are in mm).

The first case of part B presents a deviated scan model as shown in Figure 6-15-a, which simulates a plastic deformation remaining in the manufactured part. This defect results in a maximum displacement of 15 mm in the scan mesh of the part in a free-state. This defect on the scan mesh is simulated using a non-linear FE where the CAD mesh is loaded to deform into the plastic zone, and then the residual displacement simulates the defects after removing the load. Partitioning the deviated scan mesh and applying RPO approach on all partitioned zones, the required pressures on each partitioned zone is calculated to predict the functional shape of scan mesh in assembly-state as presented in Figure 6-15-b and Table 6-12. Inspecting the predicted shape of a scan mesh on each mounting hole concerning the CAD mesh, as presented in Table 6-13, demonstrates that the mounting holes on the predicted scan mesh in assembly-state are in the tolerance range. This means that the deviated scan model can be assembled in its assembly-state with respect to the tolerance.

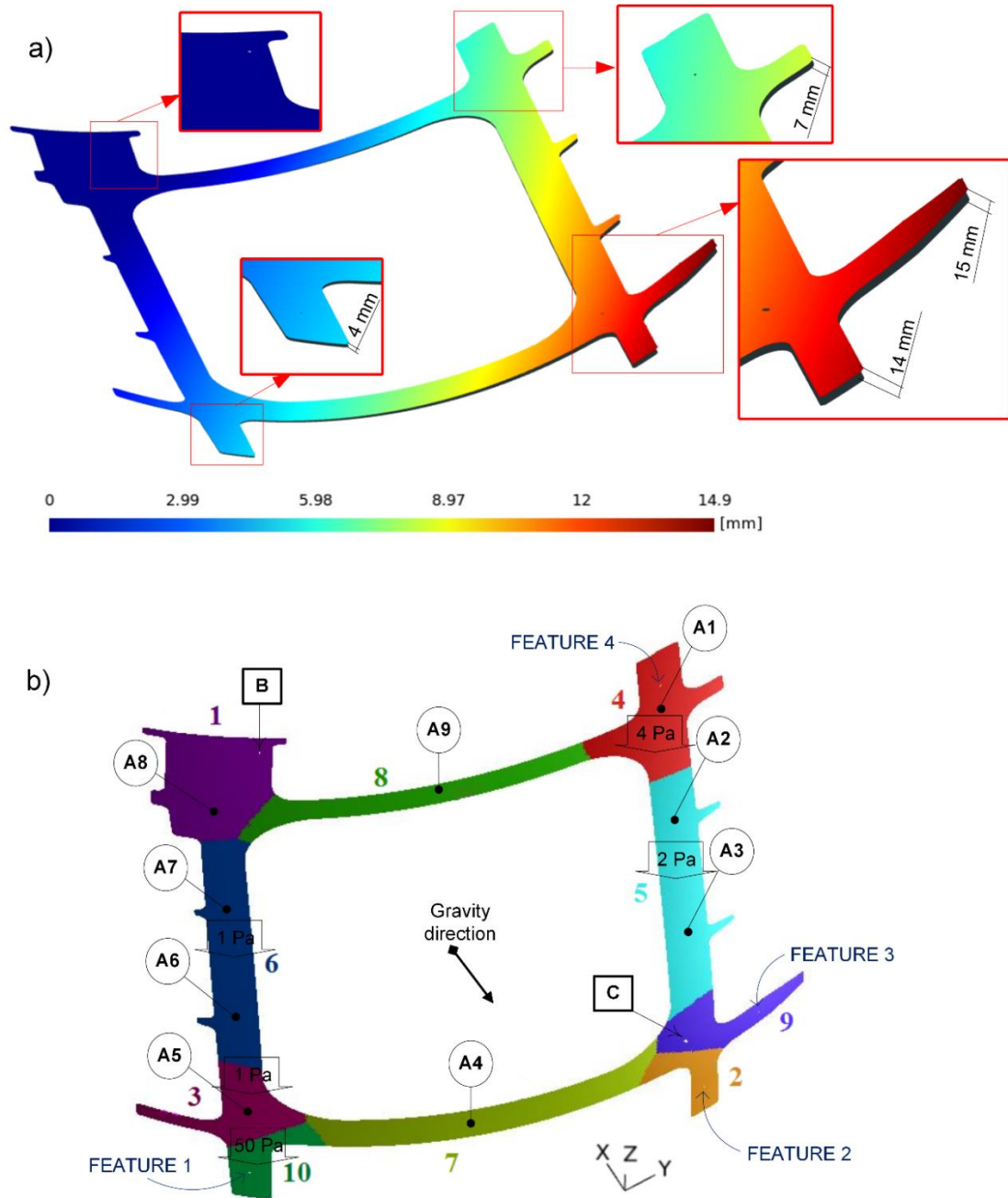


Figure 6-15: a) Displacement distribution [mm] of deviated scan mesh simulating a small plastic defect; b) The partitioned scan model and predicted assembly pressure.

Table 6-12: Assembly pressure and force results for the validation case of part B simulated as a small plastic defect.

Zones	Area [mm ²]	Permissible restraining pressures [Pa]	Pressure [Pa]	Force [N]
1	79536	960	0	0.00
2	27415	960	0	0.00
3	47603	960	1	0.05
4	64293	960	4	0.23
5	87762	960	2	0.16
6	79926	960	1	0.10
7	80801	960	0	0.00
8	52094	960	0	0.00
9	42547	960	0	0.00
10	30067	960	50	1.50

Table 6-13: Position, profile and orientation results for the validation case of part B simulated as a small plastic defect.

Mounting holes	Position offset [mm]	Profile offset [mm]	Orientation difference [deg.]
Feature 1	0.01 (accepted)	0.00 (accepted)	0.07 (accepted)
Feature 2	0.03 (accepted)	0.17 (accepted)	0.02 (accepted)
Feature 3	0.03 (accepted)	0.13 (accepted)	0.02 (accepted)
Feature 4	0.00 (accepted)	0.01 (accepted)	0.08 (accepted)

The second case of part B simulates an intermediate plastic defect for deviated scan mesh in a free-state. The maximum displacement of this intermediate plastic defect concerning

the CAD model reaches to 21 mm (see Figure 6-16), which is between small plastic defect (15 mm as shown in Figure 6-15) and large plastic defect (28 mm as shown in Figure 6-17). After partitioning this scan model, the required assembly loads are estimated by RPO approach and presented in Table 6-14. Applying these estimated pressures on the partitioned zones via a FE-based transformation, the functional shape of scan model in assembly-state is predicted. The mounting holes on this predicted shape are aligned and approached with respect to the nominal features on the CAD model. The inspection is implemented on the mounting holes and presented in Table 6-15, which results that the profile offsets associated with mounting holes (Feature 1 and 2) are out of the tolerance range. This concludes that the deviated scan model cannot be appropriately assembled.

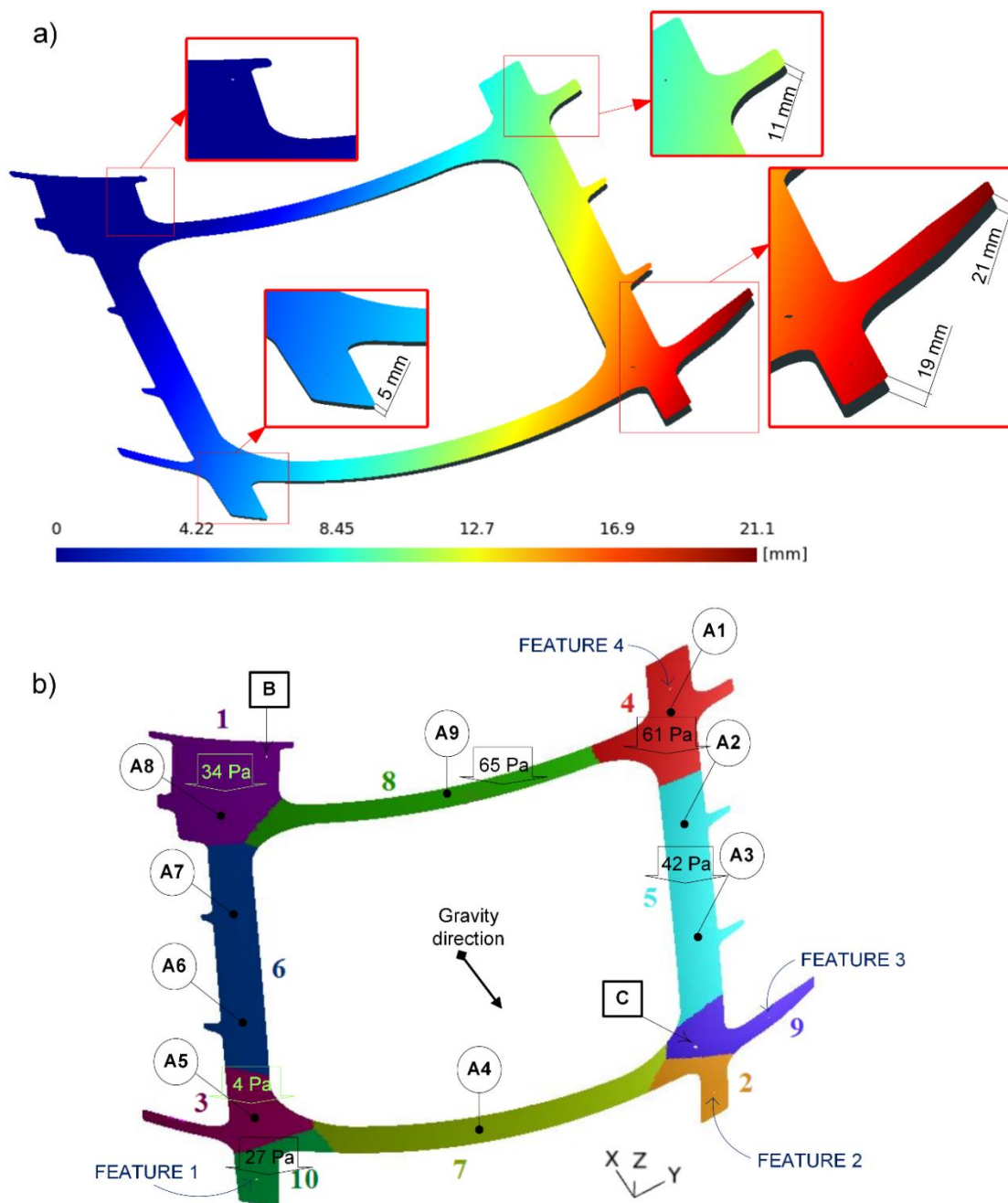


Figure 6-16: a) Displacement distribution [mm] of deviated scan mesh simulating an intermediate plastic defect; b) the partitioned scan model and predicted assembly pressure.

Table 6-14: Assembly pressure and force results for the validation case of part B simulated as an intermediate plastic defect.

Zones	Area [mm ²]	Permissible restraining pressures [Pa]	Pressure [Pa]	Force [N]
1	79536	960	34	2.71
2	27417	960	0	0.00
3	47631	960	4	0.19
4	64296	960	61	3.91
5	87768	960	42	3.69
6	79928	960	0	0.00
7	80779	960	0	0.03
8	52096	960	65	3.38
9	42550	960	0	0.00
10	30069	960	27	0.81

Table 6-15: Position, profile and orientation results for the validation case of part B simulated as an intermediate plastic defect.

Mounting holes	Position offset [mm]	Profile offset [mm]	Orientation difference [deg.]
Feature 1	0.01 (accepted)	0.28 (accepted)	0.13 (accepted)
Feature 2	0.10 (accepted)	0.43 (rejected)	0.06 (accepted)
Feature 3	0.05 (accepted)	0.47 (rejected)	0.06 (accepted)
Feature 4	0.01 (accepted)	0.06 (accepted)	0.17 (accepted)

The large plastic deformation simulated in the last case of part B induces a maximum displacement of 28 mm (see Figure 6-17) concerning the CAD model. The RPO approach is applied on the partitioned zones of scan mesh as presented in Table 6-16. The required

restraining pressures on the pertained zones are estimated to minimize the distance and orientation difference between the mounting holes on the scan mesh (where the inspection takes place) and the corresponding hole on the CAD mesh. After applying the estimated restraining pressures on the deviated scan mesh the predicted shape of scan mesh is recovered. Performing an inspection on the mounting holes of the part, as presented in Table 6-17 in red, the profile offsets for mounting holes (Feature 1 and 2) are out of the tolerance range which means this deviated scan mesh cannot be assembled.

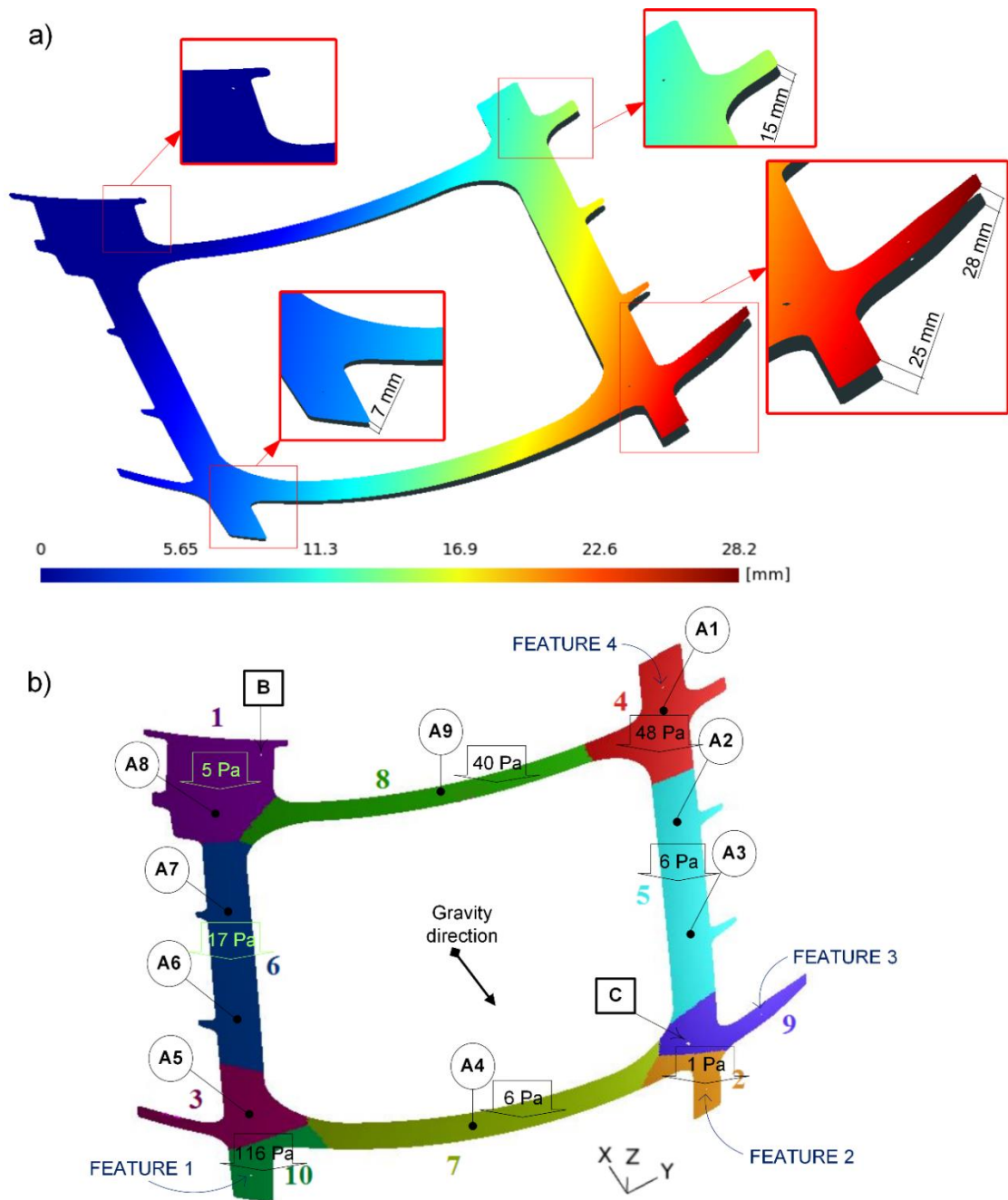


Figure 6-17: a) Displacement distribution [mm] of deviated scan mesh simulating a large plastic defect; b) the partitioned scan model and predicted assembly pressure.

Table 6-16: Assembly pressure and force results for the validation case of part B simulated as a large plastic defect.

Zones	Area [mm ²]	Permissible restraining pressures [Pa]	Pressure [Pa]	Force [N]
1	79536	960	5	0.41
2	27420	960	1	0.02
3	47635	960	0	0.00
4	64302	960	48	3.07
5	87804	960	6	0.55
6	79931	960	17	1.33
7	80786	960	6	0.47
8	52099	960	40	2.10
9	42527	960	0	0.00
10	30071	960	116	3.50

Table 6-17: Position, profile and orientation results for the validation case of part B simulated as a large plastic defect.

Mounting holes	Position offset [mm]	Profile offset [mm]	Orientation difference [deg.]
Feature 1	0.02 (accepted)	0.06 (accepted)	0.25 (accepted)
Feature 2	0.15 (accepted)	0.75 (rejected)	0.09 (accepted)
Feature 3	0.11 (accepted)	0.61 (rejected)	0.09 (accepted)
Feature 4	0.01 (accepted)	0.03 (accepted)	0.28 (accepted)

6.5.4 Discussion

Based on the inspection results from part A and part B, we conclude that the magnitude of defects seriously affects the possibility of recovering the shape of a deviated manufactured part in assembly-state. In this study, the scan models are generated by geometric transformation or plastic deformation. Our proposed VMASI method predicts the shape of scan mesh placed in assembly-state by estimating and introducing permissible restraining pressures on the scan mesh. The efficiency of our proposed inspection method regarding the types of generating case studies as deviated scan meshes, especially for highly deviated scan models, needs to be analyzed. It should be asserted that the *Restraining Pressures Optimization* (RPO) approach is established as a linear FE-base transformation. Therefore, any type of nonlinearity concerning the FEA calculation can affect the precision of the VMASI method. The geometrical aspects that can affect the method are large displacement and stretch of the deviated scan model. Large displacement nonlinearity in FEA calculation can occur in deviated scan models with larger defects. The highly deviated parts, especially under plastic deformation, can also stretch these thin-walled parts. The stretch in deviated scan models cannot be compensated with the compliant behavior of non-rigid parts during the inspection process. Meanwhile, the material nonlinearity, such as plastic analysis, also can be another source of uncertainty in VMASI method. In other words, the RPO approach calculates required pressures for predicting the shape of scan mesh only in the elastic deformation zone although scan meshes under required pressures can enter the plastic deformation zone. Ultimately, it should be mentioned that the optimization method used in RPO is not an absolute minimization solution for the established optimization problem in Equation 6-6. We have applied the global search minimization method that aims at finding the global minimum of the optimization problem. This is based on minimizing the objective function using a scatter-search mechanism for generating start points for the optimization problem. Therefore, uncertainties concerning the discrete optimization method can directly affect the result of our VMASI method.

6.6 Conclusion

This paper introduces a new *Computer-Aided Inspection* (CAI) method, which is a fixtureless inspection for non-rigid parts in a free-state. This method is developed to virtually replicate a practical inspection technique that is used in aerospace industry. This technique applies weights to place a geometrically deviated non-rigid manufactured part into its functional position (assembly-state) while datums of the part are constrained into physical fixtures. These datums are extracted from GD&T specification of the part. Our proposed *Virtual Mounting Assembly-State Inspection* (VMASI) method applies a linear FE-based transformation inside a *Restraining Pressure Optimization* (RPO) approach which seeks required restraining pressures on specific zones of the non-rigid part to predict the optimized shape of scan mesh in its assembly-state. This optimized predicted shape of scan mesh approaches positions and orientations of mounting holes of the scan mesh with respect to those of the nominal CAD model. Inspecting each mounting hole on the predicted shape of scan mesh in assembly-state with respect to dedicated assembly tolerances leads to accepting or rejecting the non-rigid manufactured part. Applying the VMASI method on two non-rigid aerospace parts shows that acceptance of deviated manufactured parts is related to the magnitude of defects. Indeed, some of the most highly deviated parts could not be recovered in their assembly-state and thus rejected.

Short-term future work on this method should introduce nonlinear FEA formulations in the RPO module, which would increase the accuracy of our VMASI method for deviated scan models featuring large displacement defects. Evaluating robustness and uncertainties of the proposed inspection method would also be an interesting investigation. Indeed, applying VMASI to a large spectrum of geometries would allow a deeper analysis and validation of performance and robustness of the method. As justified in section 6.4, the method is validated by scan models that are generated by adding the synthetic defects into CAD model to control and quantify the shape and size of defects and assess their effect on results obtained. Therefore, working on real scan data, acquired from scanning a real

part in a free-state, and retrieving the functional form on physical fixtures would assess performance and accuracy of the proposed inspection method in the real world.

6.7 Acknowledgments

The authors would like to thank the National Sciences and Engineering Research Council of Canada (NSERC), industrial partners, Consortium for Aerospace Research and Innovation in Québec (CRIAQ) and UQTR foundation for their support and financial contribution. In this paper, we use GmshTM [25] for visualizing the distance distributions of models.

6.8 References

- [1] G. N. Abenhaim, A. Desrochers, A. S. Tahan, and J. Bigeon, "A virtual fixture using a FE-based transformation model embedded into a constrained optimization for the dimensional inspection of nonrigid parts," *CAD Computer Aided Design*, vol. 62, pp. 248-258, 2015.
- [2] G. N. Abenhaim, A. Desrochers, and A. Tahan, "Nonrigid parts' specification and inspection methods: notions, challenges, and recent advancements," *International Journal of Advanced Manufacturing Technology*, vol. 63, pp. 741-752, Nov 2012.
- [3] Z. Bi and L. Wang, "Advances in 3D data acquisition and processing for industrial applications," *Robotics and Computer-Integrated Manufacturing*, vol. 26, pp. 403-413, 2010.
- [4] R. Ascione and W. Polini, "Measurement of nonrigid freeform surfaces by coordinate measuring machine," *The International Journal of Advanced Manufacturing Technology*, vol. 51, pp. 1055-1067, 2010.
- [5] A. Weckenmann and J. Weickmann, "Optical Inspection of Formed Sheet Metal Parts Applying Fringe Projection Systems and Virtual Fixation," *Metrology and Measurement Systems*, vol. 13, pp. 321-330, 2006.

- [6] I. Gentilini and K. Shimada, "Predicting and evaluating the post-assembly shape of thin-walled components via 3D laser digitization and FEA simulation of the assembly process," *Computer-aided design*, vol. 43, pp. 316-328, 2011.
- [7] A. Weckenmann, J. Weickmann, and N. Petrovic, "Shortening of inspection processes by virtual reverse deformation," in 4th international conference and exhibition on design and production of machines and dies/molds, Cesme, Turkey, 2007.
- [8] A. Jaramillo, F. Prieto, and P. Boulanger, "Fixtureless inspection of deformable parts using partial captures," *International Journal of Precision Engineering and Manufacturing*, vol. 14, pp. 77-83, 2013.
- [9] G. N. Abenhaim, A. S. Tahan, A. Desrochers, and R. Maranzana, "A Novel Approach for the Inspection of Flexible Parts Without the Use of Special Fixtures," *Journal of Manufacturing Science and Engineering-Transactions of the Asme*, vol. 133, Feb 2011.
- [10] A. Aidibe, A. S. Tahan, and G. N. Abenhaim, "Distinguishing profile deviations from a part's deformation using the maximum normed residual test," *WSEAS Transactions on Applied & Theoretical Mechanics*, vol. 7, 2012.
- [11] H. Radvar-Esfahlan and S.-A. Tahan, "Nonrigid geometric metrology using generalized numerical inspection fixtures," *Precision Engineering*, vol. 36, pp. 1-9, 2012.
- [12] V. Sabri, S. A. Tahan, X. T. Pham, D. Moreau, and S. Galibois, "Fixtureless profile inspection of non-rigid parts using the numerical inspection fixture with improved definition of displacement boundary conditions," *International Journal of Advanced Manufacturing Technology*, vol. 82, pp. 1343-1352, 2016.
- [13] S. Sattarpanah Karganroudi, J.-C. Cuillière, V. Francois, and S.-A. Tahan, "Automatic fixtureless inspection of non-rigid parts based on filtering registration points," *The International Journal of Advanced Manufacturing Technology*, pp. 1-26, 2016.
- [14] K. G. Merkle, "Tolerance analysis of compliant assemblies," Citeseer, 1998.

- [15] M. Mounaud, F. Thiebaut, P. Bourdet, H. Falgarone, and N. Chevassus, "Assembly sequence influence on geometric deviations propagation of compliant parts," *International Journal of Production Research*, vol. 49, pp. 1021-1043, 2011.
- [16] H. Chen, S. Jin, Z. Li, and X. Lai, "A comprehensive study of three dimensional tolerance analysis methods," *Computer-Aided Design*, vol. 53, pp. 1-13, 2014.
- [17] S. Ravishankar, H. Dutt, and B. Gurumoorthy, "Automated inspection of aircraft parts using a modified ICP algorithm," *The International Journal of Advanced Manufacturing Technology*, vol. 46, pp. 227-236, 2010.
- [18] A. Weckenmann, P. Gall, and J. Hoffmann, "Inspection of holes in sheet metal using optical measuring systems," in *Proceedings of VIth International Science Conference Coordinate Measuring Technique (April 21-24, 2004, Bielsko-Biala, Poland)*, 2004, pp. 339-346.
- [19] A. M. Bronstein, M. M. Bronstein, and R. Kimmel, "Generalized multidimensional scaling: A framework for isometry-invariant partial matching," *Proceedings of the National Academy of Sciences of the United States of America*, vol. 103, pp. 1168-1172, 2006.
- [20] R. Kimmel and J. A. Sethian, "Computing geodesic paths on manifolds," *Proceedings of the National Academy of Sciences*, vol. 95, pp. 8431-8435, 1998.
- [21] A. D. Spence, H.-L. Chan, J. P. Mitchell, and D. W. Capson, "Automotive sheet metal and grid digitizing solutions," *Computer-Aided Design and Applications*, vol. 2, pp. 135-144, 2005.
- [22] M. Botsch, M. Pauly, L. Kobbelt, P. Alliez, B. Lévy, S. Bischoff, et al., "Geometric modeling based on polygonal meshes," 2007.
- [23] P. J. Frey and P.-L. George, *Mesh generation : Application to finite elements*, 2008.

- [24] J. C. Cuillère and V. Francois, "Integration of CAD, FEA and Topology Optimization through a Unified Topological Model," *Computer-Aided Design and Applications*, vol. 11, pp. 1-15, // 2014.
- [25] C. Geuzaine and J.-F. Remacle, "Gmsh: a three-dimensional finite element mesh generator with built-in pre- and post-processing facilities," *International Journal for Numerical Methods in Engineering*, vol. 79, pp. 1309-1331, 2009.

CHAPTER 7 GENERAL DISCUSSION

The main objective of this thesis is to develop automatic fixtureless inspection methods for non-rigid parts that are measured in a free-state. This leads to identify and quantify defects on measured parts. Advancements in optical measuring devices (scanners) along with computational calculations are integrated into *Computer-Aided Inspection* (CAI) methods, which allow eliminating fixtures in an automatic inspection. Like all computational methods, the reliability and accuracy of fixtureless CAI methods are required to be verified and validated. The results of CAI methods are then validated with the presence of input noise to assess the robustness of methods. Proved by an industrial technique, the functional shape of deviated non-rigid parts in some cases can be retrieved on fixtures by using permissible loads in assembly-state. Therefore, the objective of this study is extended to develop a fixtureless CAI method that virtually assesses the possibility of assembling such a geometrically deviated part in assembly-state.

7.1 Discussion on the sample points filtering method

In the first step, an improved fixtureless approach based on the *Generalized Numerical Inspection Fixture* (GNIF) method, see Appendix A, is developed in Chapter 4. The GNIF method, compared to the other fixtureless CAI methods that are demonstrated in section 2.4.2, can identify both small (local) and big (global) defects. GNIF is also efficient for large non-rigid panels with complex shapes that are used commonly in aerospace and automobile industries. Meanwhile, GNIF has the potential of being automated and integrated as a fixtureless CAI method. The abovementioned advantages and potentials of GNIF makes it outstanding among the other CAI methods, and worthy to be improved and automated in this study. GNIF generates corresponding sample points that are evenly distributed on the CAD and scan models. Applying all sample points, including those located in defect areas, to determine displacement BCs in FENR result in an inaccurate inspection. Therefore, GNIF is improved in this study by filtering out sample points that are located in defect areas using curvature and von Mises stress criteria. Once filtered out, the remained sample points are used in a new FENR to deform the CAD

model towards the scan mesh. Finally, a geometrical comparison between deformed CAD and scan models results in an accurate and automatic inspection that is capable of detecting defects even on the boundaries of parts. Inserting sample point into CAD mesh, using Delaunay point insertion approach (Borouchaki, George et al. 1996), without degrading the quality of the mesh is a powerful contribution to this study. Applying BCs automatically in the FENR, which is integrated with mesh modification tools, makes an automatic and uninterrupted process. In fact, the original contribution in this part of the study refers to the automatic sample point filtration tool, which is integrated with mesh modification and FENR to allow an automatic and precise inspection for non-rigid parts. The efficiency of this method is validated on two typical parts in Aerospatiale for which the results are presented in section 4.5. It should be underlined that the mentioned size for part A in Chapter 4 should be corrected to 110 mm length and 86 mm width. Therefore, the part A in Chapter 4 is not representative of a thin-walled sheet metal and consequently a non-rigid part, since the thickness of the part (1 mm) is not very small compared to the other dimensions. However, the method of filtering sample points theoretically is not affected by the mistake in this part and sample points are correctly filtered out in defect areas. It is worth to remind that the bump-shaped defects on scan model are generated by geometrical transformation and the flexible deformations are simulated via linear FEA on the CAD model. Meanwhile, to eliminate any doubt about the accuracy of results for part A in Chapter 4, the same form of part (skin panel) with the modified dimensions (1100×860 mm) is validated by the filtration method in Chapter 5. The results presented in section 5.5.2 proves the same conclusions as obtained in Chapter 4.

In Chapter 4, the results associated with von Mises stress show a very high stress in the models. The physical interpretation of this high stress for deformation through FENR is related to the inherent errors of the GNIF method that generates corresponding sample points with in-plane displacement error. Using these faulty corresponding sample points in FENR results in very high values of stress in deformed CAD models. However, these faulty sample points are also filtered out during sample point filtering process based on von Mises criterion. The final FENR, which uses the remained sample points after

filtering based on curvature and stress criteria, avoid involving sample points on defect areas as well as faulty sample points due to GNIF error.

The improved method in Chapter 4 encounter also some limitations concerning the presence of stretching in non-rigid parts. Since GNIF hypothesizes an isometric deformation for non-rigid parts, it does not support the stretch on the part. As a consequence, the stretch on the part results in generating inaccurate corresponding sample points and eventually an inaccurate inspection. Moreover, the inherent GNIF errors associated with generating corresponding sample points add a level of uncertainty to the inspection results that can be assessed by a *Verification and Validation* (V&V) method.

7.2 Discussion on nonlinear FEA

As already mentioned in Chapter 4 and Chapter 5, we generate scan models by adding defects (as geometrical transformation) into the relevant CAD model. Then, the flexible deformation of scan model in a free-state is simulated by introducing boundary conditions (BCs) via linear FE formulation (small displacement hypothesis and elastic deformation). Meanwhile, we applied linear FEA for the process of deforming CAD model towards scan mesh via FENR in Chapter 4 and Chapter 5. In the course of this research, we have adapted nonlinear FEA using large displacement formulation into our calculations. This allows simulating a large flexible deformation of scan models in a free-state. For example, such a large flexible deformation of a scan model is depicted in Figure 7-1 for which the maximum displacement of the scan model with respect to the CAD model reaches to 10 mm. This is considered as large displacement concerning that the length of the part is 110 mm. In this section, we perform preliminary studies concerning the effect of using large displacement formulation on the inspection results based on our developed sample points filtering method.

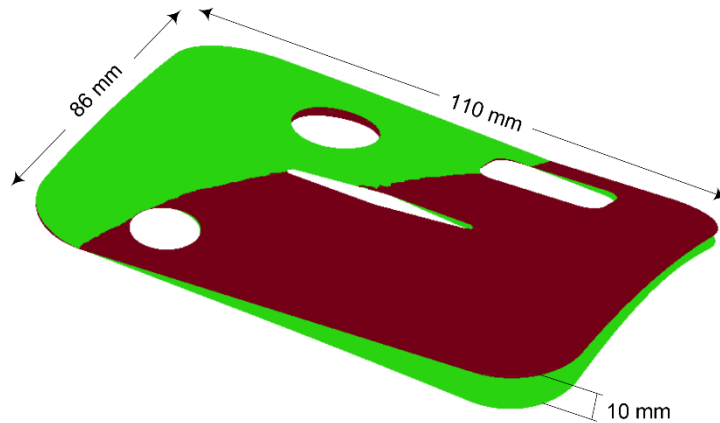


Figure 7-1: 3D views of CAD model (in green) compared with scan model in a free-state (in brown) simulated based on large displacement formulation.

Since the scan model features a large flexible deformation, the non-rigid registration process that deforms the CAD model towards the scan mesh through FENR can be affected. In other words, using linear or nonlinear FENR can influence the accuracy of our non-rigid inspection. To verify this influence, we perform separately both linear and nonlinear FENR for the scan model presented in Figure 7-1. Our sample point filtering method applies successively the curvature and von Mises stress criteria to filter out sample point close to defect areas (see Figure 4-8). In fact, a FENR is applied before performing each filtering step. Once filtered out, the final FENR deforms the CAD model towards the scan mesh except for defect areas. The remained corresponding sample points that contribute in final FENR are shown in Figure 7-2 as red spots (●). The effect of nonlinear and linear FENR on filtering sample points is depicted between Figure 7-2-a and b for noise-free scan mesh and in Figure 7-2-c and d for noisy scan mesh with $\sigma=0.01$ mm. It appears that more sample points are filtered out for registration process based on linear FENR compared to those based on nonlinear FENR. This can generally be justified by taking in consideration that linear FENR causes stretch for a large deformation simulation. The distribution of von Mises stress after applying non-linear and linear FENR for noise-free scan meshes are illustrated in Figure 7-3-a and b. This distribution of stress after applying non-linear and linear FENR for noisy scan meshes with $\sigma=0.01$ mm are also shown in Figure 7-3-c and d. Referring to Figure 7-3, we can observe that

the stretch in linear analyses for large deformation lead to a higher level of stress in linear FENR compared to non-linear FENR. This stretch result in high von Mises stress distributed over the part, which consequently leads to filtering out more sample points in these high-stress areas.

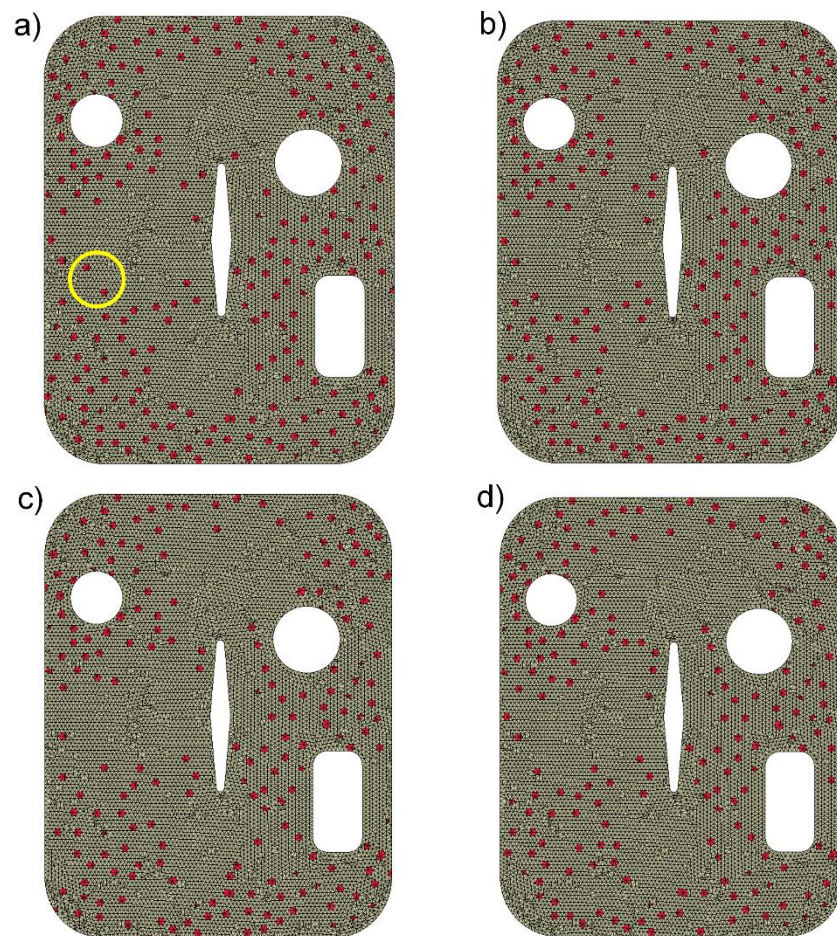


Figure 7-2: Remained sample points (as red spots) after applying filtering registration points method using a) nonlinear FENR for noise-free scan mesh b) linear FENR for noise-free scan mesh c) nonlinear FENR for noisy scan mesh with $\sigma=0.01$ mm d) linear FENR for noisy scan mesh with $\sigma=0.01$ mm.

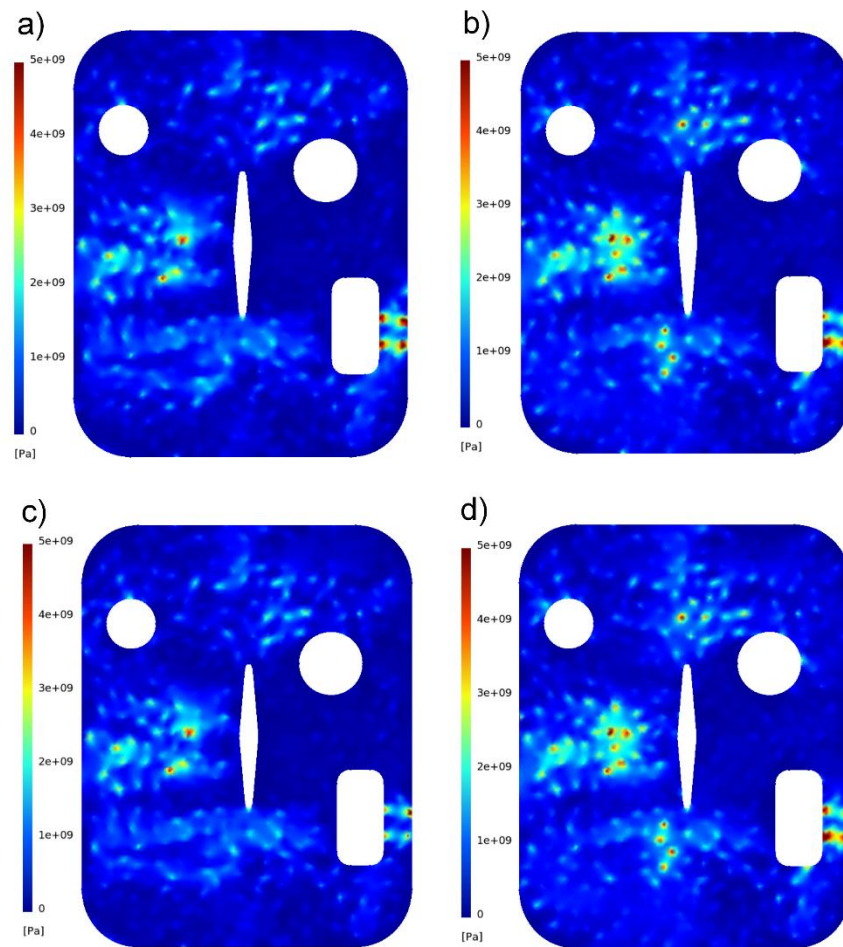


Figure 7-3: Distribution of von Mises stress [Pa] when using GNIF sample points after
 a) nonlinear FENR for noise-free scan mesh b) linear FENR for noise-free scan mesh c)
 nonlinear FENR for noisy scan mesh with $\sigma=0.01$ mm d) linear FENR for noisy scan
 mesh with $\sigma=0.01$ mm.

To verify the inspection results, we compare the results using nonlinear FENR (large displacement) with those using linear FENR as depicted in Figure 7-4. To this end, the nominal defects size (Figure 7-4-a) are used as references to verify the comparison between the deformed CAD and scan models using nonlinear and linear FENR for noise-free scan meshes (Figure 7-4-b and c) as well as the noisy scan meshes with $\sigma=0.01$ mm (Figure 7-4-d and e). It is worthy to underline that the non-rigid registration in Figure 7-4-b and d apply nonlinear FEA whereas it uses linear FEA in Figure 7-4-c and e. These

inspection results are summarized in Table 7-1, which appears that in this case we generally obtain better results (for both maximum amplitude and area of defects) concerning registration processes that apply nonlinear FENR. Like for noise-free scan mesh, we observe better inspection results for registration processes that apply nonlinear FENR. However, the only exception appears in Bump #2 for noise-free scan mesh wherein the inspection result of registration processes applying nonlinear FENR (inspection error for maximum amplitude is 20.43% and for area is 51.40%) is worse than registration processes applying linear FENR (inspection error for maximum amplitude is 14.60% and for area is 35.41%). This can be explained by considering the fact that sample points around defect areas using linear FENR are more filtered out compared to the one using nonlinear FENR, as depicted by yellow circle in Figure 7-2-a. Eventually, using fewer sample points in defect areas for the final FENR results in a better defect estimation for our non-rigid CAI. However, to make an accurate conclusion further investigations are required as mentioned in the perspectives of the thesis in section 8.2.

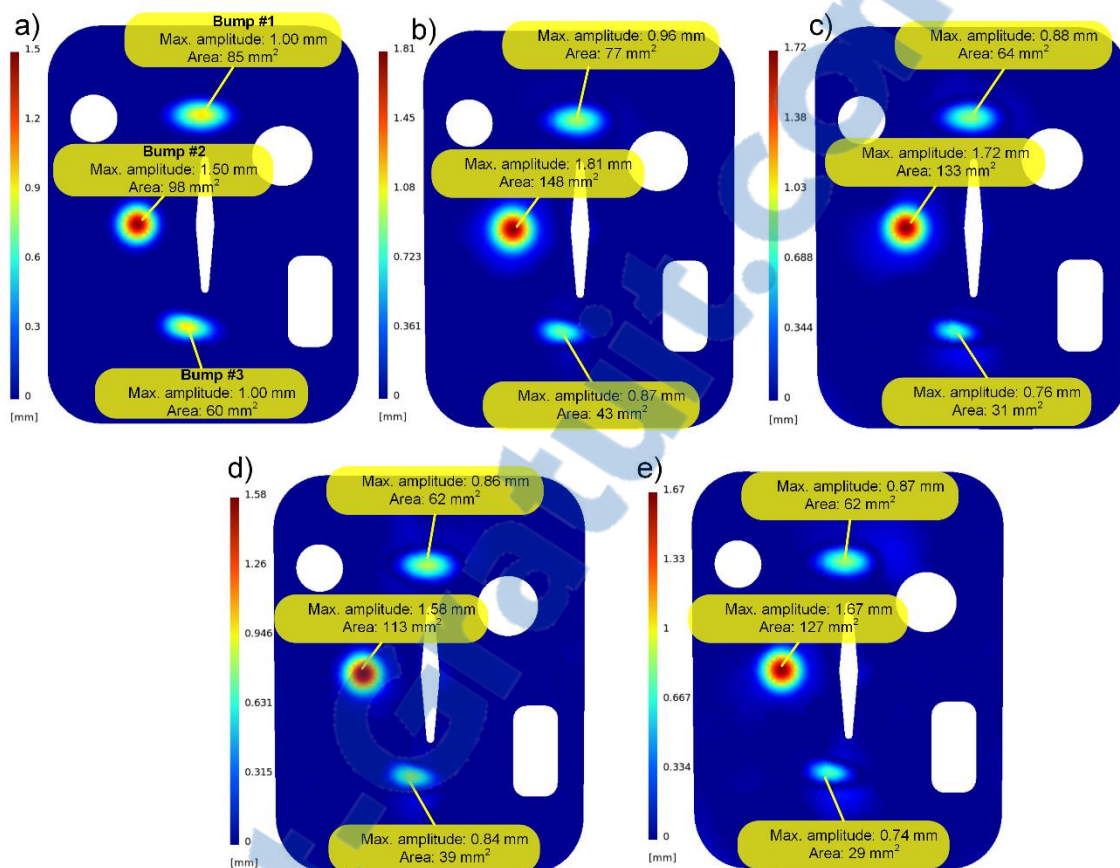


Figure 7-4: a) nominal defect distance distribution, comparison between the deformed CAD and scan models as a distance distribution using b) nonlinear FENR for noise-free scan mesh c) linear FENR for noise-free scan mesh d) nonlinear FENR for noisy scan mesh with $\sigma=0.01$ mm e) linear FENR for noisy scan mesh with $\sigma=0.01$ mm.

Table 7-1: Estimated size of defects and errors implementing nonlinear and linear FENR.

			Maximum amplitude of defects (D_i^{max})				Area of defects (A_i)			
			Nominal [mm]	Estimated [mm]	Absolute error [mm]	Error [%]	Nominal [mm ²]	Estimated [mm ²]	Absolute error [mm]	Error [%]
Nonlinear FENR uses large displacement formulation	BUMP #1	Noise-free	1.00	0.96	-0.04	-4.14	85	77	-8.25	-9.71
		$\sim N(0, \sigma = 0.01)$	1.00	0.86	-0.14	-13.74	85	62	-23.02	-27.08
	BUMP #2	Noise-free	1.50	1.81	0.31	20.43	98	148	50.38	51.40
		$\sim N(0, \sigma = 0.01)$	1.50	1.58	0.08	5.17	98	113	14.60	14.90
	BUMP #3	Noise-free	1.00	0.87	-0.13	-13.02	60	43	-17.31	-28.86
		$\sim N(0, \sigma = 0.01)$	1.00	0.84	-0.16	-16.24	60	39	-21.32	-35.53
Linear FENR uses small displacement formulation	BUMP #1	Noise-free	1.00	0.88	-0.12	-11.81	85	64	-20.58	-24.21
		$\sim N(0, \sigma = 0.01)$	1.00	0.87	-0.13	-13.38	85	62	-23.03	-27.10
	BUMP #2	Noise-free	1.50	1.72	0.22	14.60	98	133	34.70	35.41
		$\sim N(0, \sigma = 0.01)$	1.50	1.67	0.17	11.17	98	127	28.85	29.44
	BUMP #3	Noise-free	1.00	0.76	-0.24	-24.13	60	31	-29.26	-48.76
		$\sim N(0, \sigma = 0.01)$	1.00	0.74	-0.26	-25.91	60	29	-30.73	-51.22

7.3 Discussion on our developed V&V method

The reliability and robustness of our improved CAI method based on filtering registration points are validated concerning the ASME recommendations. Therefore, a new validation metric for V&V of CAI methods is developed in Chapter 5. This metric validates the distance distributions of the estimated defects with the nominal ones. To this end, a nonparametric statistical test, namely *Kolmogorov–Smirnov* (K-S) test, is applied at a specific significance level. The developed validation metric along with the maximum amplitude and area of defects are then used for evaluating the robustness of the improved CAI method in the presence of scanning noise. The parts from aerospace industry with different magnitude of noise are used to evaluate the robustness of the method. The results, presented in section 5.5, shows in general that scanning noise does not have a significant effect on the results of the CAI method. However, large deformation of scan models affects dramatically the result of inspection. This can be justified by considering that GNIF supports only isometric deformation, and the FENR applies a linear FEA based on small displacement hypothesis. Therefore, large deformation of scan models can violate the hypotheses considered in GNIF and FENR. It is also noticed that flexible deformations, especially in the vicinity of defect areas, can affect the shape of the original (nominal) defect. Therefore, the estimated defect on the deformed scan model in a free-state can slightly be different from the nominal defect on the scan model in assembly-state. This phenomenon is especially observed in the differences of the distance distributions between the nominal defects and the estimated defects affected by flexible deformation.

7.4 Discussion on our developed virtual mounting method

It is proved by an industrial inspection technique that some deviated non-rigid parts, including defects that exceed the tolerances, can be put in assembly-state under permissible loads. The functional shape of these deviated parts in some cases can be retrieved on an inspection fixture that represents the nominal assembly-state. Inspired by

this inspection technique, a fixtureless CAI is developed in Chapter 6 to assess the feasibility of assembling deviated non-rigid parts in assembly-state. The *Virtual Mounting Assembly-State Inspection* (VMASI) method, proposed in section 6.4, applies a non-rigid registration that seeks for required permissible assembly loads via a linear FE-based transformation. The method applies the developed *Restraining Pressures Optimization* (RPO) approach, in section 6.4.2, that determines the value and position of required assembly loads on the scan models. The method is validated on different industrial parts with different types of defects in section 6.5. These results demonstrate that highly deviated parts are less likely to be assembled because the assembly features cannot be matched in their nominal position and orientation. In fact, since the method is based on linear FEA and small displacement hypothesis, large deformation, and material non-linearity can affect the accuracy of optimization result.

It is worthy to mention that scan models used as validation cases in the framework of this these are simulated via FEA or generated by geometrical transformation from the respective CAD models. The reason of using simulated scan models instead of real measured data (point clouds) is that measuring actual defects on real scan data includes uncertainty and unknown scanning noise. These uncertainties result in a faulty evaluation of actual defects and consequently an inaccurate efficiency evaluation of the methods. We applied simulated scan models wherein added defects to the CAD model is known and can perfectly be quantified. However, applying real data is foreseen as perspectives of this study in section 8.2.

CHAPTER 8 CONTRIBUTIONS, PERSPECTIVES, AND CONCLUSIONS

8.1 Major contributions

The significant contributions presented within the framework of this thesis are as follows:

- Developing a comprehensive method to identify defect areas and distinguish between flexible deformation and defects on scan models based on curvature and von Mises stress criteria.
- Filtering out automatically corresponding sample points, which are generated by GNIF method and distributed evenly on the CAD and scan models, associated with defect areas.
- Improving the determination and calculation of BCs used in GNIF method via FENR to achieve an automatic and accurate CAI approach. To this end, our developed defect identification method is integrated with the sample point filtering technique to automatically define the accurate displacement BCs. Once filtered out, the displacement BCs are calculated between the remained sample points on CAD model and their corresponding sample points on the scan model. This allows a non-rigid registration that compensates for flexible deformation of non-rigid parts in a free-state.
- Developing an automatic integration of the following steps in our improved CAI:
 - Calculating displacement BCs allocated to sample points,
 - Automatic insertion of sample points into CAD mesh while conserving the mesh quality,
 - Automatic determination of displacement BCs in FENR,
 - Geometrical comparison between the scan model and the deformed CAD model (after FENR).

- Developing an automatic and accurate CAI method to detect and quantify defects on scan models. The defect evaluation is presented based on maximum amplitude, area and distance distribution of defects between the deformed CAD model (after FENR) and the scan model.
- Developing a validation metric, based on hypothesis testing for distance distribution of defects.
- Assessing the effect of noise in scan meshes with various magnitudes of noise.
- Evaluating the robustness of our improved CAI method (based on filtering registration points) using our developed validation metrics.
- Developing a non-rigid registration to retrieve the functional shape of a deviated part under permissible loads in assembly-state.
- Developing an optimization method using FE-based transformation to estimate the required assembly loads for placing a deviated part in assembly-state.
- Evaluating the feasibility of placing a geometrically deviated non-rigid part under permissible loads in assembly-state.
- Applying the developed methods and approaches on real parts from aerospace industries.
- Our research platform (Cuillière and Francois 2014), which is based on C++ code, on Open CASCADE™ libraries and on Code_Aster™ as FEA solver, was developed only for CAD and FEA applications. At the end of my study, this platform is enriched and adapted to perform metrology applications by developing the proper tools inside the platform.

A synthesis of contributions along with the presented articles is also demonstrated in Figure 8-1.

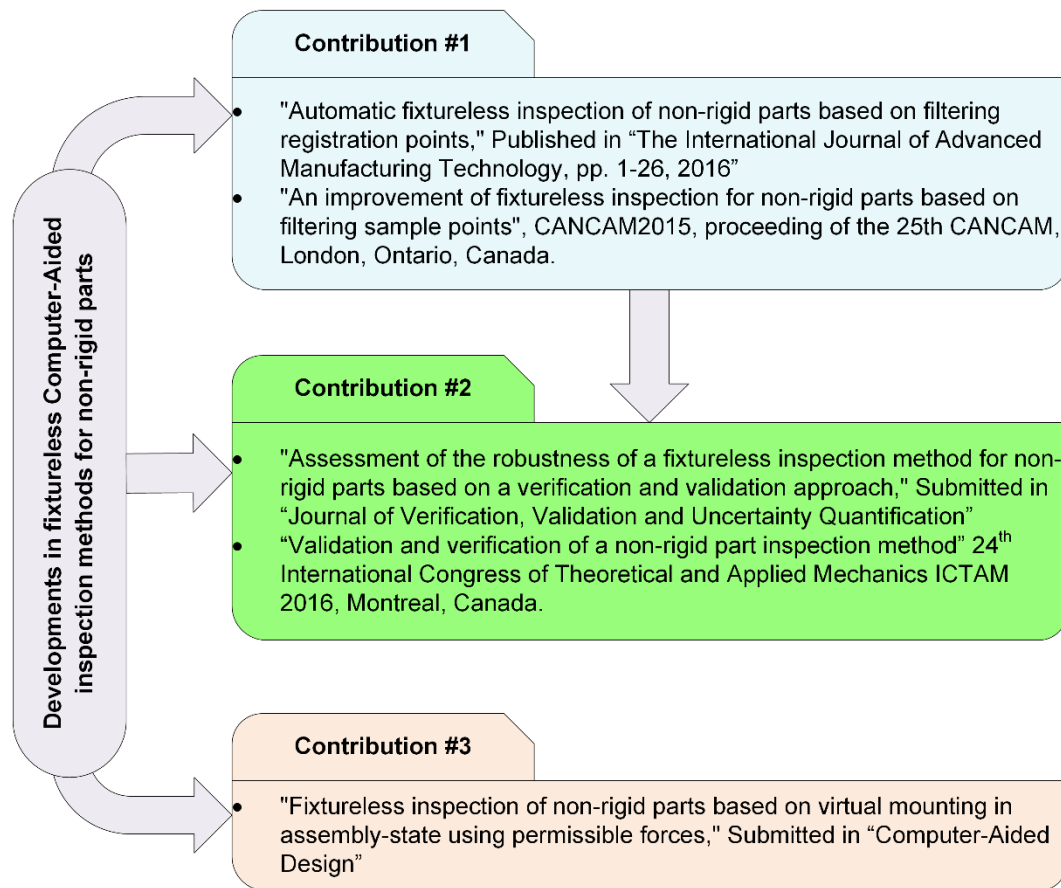


Figure 8-1: A synthesis of contributions in the thesis.

8.2 Perspectives

In this section, several perspectives are presented that are foreseen to continue this research in future. Although the results obtained from the presented approaches in Chapter 4, Chapter 5 and Chapter 6 are promising, several topics associated with the uncertainty and generality of these approaches can be investigated. These recommendations indicate the orientation of future studies in this field and cover broadly the perspectives of this thesis. The general perspectives foreseen for this thesis are as follows:

- As already mentioned, the scan models used in this study are generated by adding defects and synthetic noise to the CAD models. A perspective of the

research can be dedicated to experimental validation of the methods based on applying point clouds obtained by scanning real manufactured parts in a free-state. This validation can be performed by setting up conventional inspections in which the parts are scanned on physical fixtures. The results of these conventional inspections would be then compared with estimated results obtained from our developed methods. Practically, measuring actual defects on fixtures include significant measuring errors. These errors can be due to uncertainties of measuring tools, calibration and fixtures adjustments. In fact, the magnitude of these uncertainties are bigger than the error magnitude of our developed CAI methods. Therefore, the actual defects of real data cannot be known accurately with the conventional metrology methods. Meanwhile, one of the important obstacles to using real scan data is tackling with very dense raw scan point clouds. For example, GNIF method can encounter calculation limits for models with a large amount of data. Therefore, those massive scan point clouds presented as a very fine triangular mesh should be processed prior to being used in our developed methods. To this end, mesh decimation algorithm and eventually, adaptive mesh refinement methods should be applied.

- The actual point clouds acquired from real parts can be used as measured data (real scan data) for the further analysis of the presented methods. However, all measuring data include uncertainty. Therefore, quantifying the level of uncertainty in the real measured parts can be foreseen for future studies. There are various sources of uncertainties for measured data consisting uncalibrated devices, light dispersion errors, processing errors, etc.
- All FE-based transformations and FE calculations associated with our developed CAI methods are based on linear FE formulation (based on small displacement hypothesis). Considering the geometry and compliance of non-rigid parts, these parts in a free-state can experience large flexible deformation. Simulating these large deformations using small displacement hypothesis results in a wrong simulation. Meanwhile, the process of retrieving the functional shape of

geometrically deviated non-rigid parts may cause plastic deformation on these parts. Therefore, an extension of this study can be implemented by adapting large displacement hypothesis and material nonlinearity (e.g. plastic deformation) in our FE simulations. However, nonlinear FEA calculations are iterative and sensitive to calculation parameters such as time steps. In order to integrate nonlinear calculation in our developed methods, these parameters should be carefully determined. Meanwhile, the CPU time dedicated to the integrated nonlinear FE calculations inside our *restraining pressures optimization* (RPO) approach would significantly be increased. In fact, a long iterative FE calculation should be performed for each iteration of optimization calculation. Moreover, the FE-based transformation applied in our RPO approach is based on linear FEA that uses the extracted stiffness matrix to find the optimized restraining pressures on the surface of scan model. This stiffness matrix for a linear FEA can be extracted once from a FEA software, and it can be used for all the iterations of our optimization method. However, adapting nonlinear FEA in RPO requires extracting an updated stiffness matrix for each optimization iteration.

- Efficiency analysis of the presented methods on different types of parts with different types of defects can be foreseen. Parts with different complex geometries, varying thickness and also including stiffeners can be the types of parts to be considered for future studies.
- The non-rigid parts used in this study were all made of aluminum. However, the application of composite materials in transportation industries is increasing due to the lightness and durability of these materials. Therefore, another recommendation is to generalize the developed approaches by taking into account more complex non-rigid parts with non-isotropic materials such as composites. However, FE calculations for non-isotropic materials are very delicate due to varying material properties in these parts. The distribution of material properties also needs to be determined for these parts. In fact, a study

concerning the metrology of non-rigid composite materials is ongoing in the framework of another CRIAQ project.

Further detailed recommendations associated with our developed CAI method presented in Chapter 4 and Chapter 5 are also described as follows:

- The discrete curvature calculation and FE analysis are essential elements that are used in curvature and von Mises criteria to identify defect areas on scan models. The accuracy of curvature calculation and FEA directly depends on the mesh size of CAD and scan models. The application of adaptive mesh on these meshes can increase the accuracy of the calculations and eventually the performance of the developed CAI method.
- There are different sources of uncertainties associated with our improved CAI method. These uncertainties are regarding the method of generating sample points (GNIF method) and FEA calculations. For example, the estimation of geodesic distances for GNIF includes unavoidable calculation errors due to the *Fast Marching Algorithm* (Kimmel and Sethian 1998). Moreover, the *Multi-Dimensional Scaling* method (Bronstein, Bronstein et al. 2006) also adds uncertainties in GNIF concerning the determination of correspondence between sample points on the CAD and scan models. In addition, uncertainties regarding FEA formulations applied in FENR affect the inspection accuracy. Therefore, performing an uncertainty validation can evaluate the source of these errors and their impact weights on the inspection result.
- The errors in generating corresponding sample points have a straight effect on the inspection result. During the efforts on validation cases and studying GNIF method, we observed that the geodesic calculation using *Fast Marching Algorithm* is a major source of errors and uncertainties in the method. The accuracy of *Fast Marching Algorithm* depends on the quality of triangulated mesh for which this mesh quality criterion is not the same as FE mesh quality criterion. Therefore, using a triangulated mesh of the CAD and scan models

which meet the mesh quality required for *Fast Marching Algorithm* can be foreseen. In fact, the mesh for geodesic distance estimation can be independent of the FE mesh. Meanwhile, developing a more accurate geodesic distance calculation in triangulated meshes is an interesting perspective for this study.

There are also detailed recommendations specifically related to Chapter 6 that presents a fixtureless CAI for geometrically deviated non-rigid parts. These recommendations are presented as follows:

- Validating the robustness of the presented VMASI method with respect to different magnitudes of scanning noise can be an interesting extension to this research work. This can be implemented by adding different magnitudes of synthetic noise to scan meshes and verifying the inspection results with reference to the assembly tolerances.
- Different types of optimization methods can be employed in our *restraining pressures optimization* (RPO) approach to better approximate the minimum of our objective function in a shorter time. Besides, the objective function of our RPO approach minimizes both distance and orientation difference between mounting holes on the CAD and scan models. Therefore, applying multi-objective optimization methods can specifically be foreseen in RPO approach. These can lead to finding more efficient optimization techniques for our study.
- The inspection evaluation in Chapter 6 was only based on assessing offsets for the position and orientation of assembly features (mounting holes) regarding the nominal features. Therefore, an extension to this study could calculate the profile geometry on the surface of parts to assess profile defects on the scan model in assembly-state. To this end, the profile inspection of parts can be recommended by geometrically comparing the predicted shape of scan models in assembly-state with the CAD models.

8.3 Conclusions

This thesis investigates on metrology of non-rigid parts in a free-state. Industrial sectors such as transportation industries encounter challenges regarding the inspection of non-rigid parts. These industries apply conventional inspection fixtures that are costly and time-consuming. This study facilitates the *Geometric Dimensioning and Inspection* (GD&I) of flexible parts by exploiting the advancements in scanning devices and computational calculations through an automatic *computer-aided inspection* (CAI) method. It also develops a *verification and validation* (V&V) method to evaluate the robustness of CAI methods. Concerning the compliance of non-rigid parts, this thesis also develops a CAI method to virtually assess the feasibility of assembling a geometrically deviated non-rigid part under permissible loads.

The CAI methods tend to distinguish between defects and flexible deformation of non-rigid parts. Compensating for flexible deformation, the inspection is accomplished by geometrical comparison between the *computer-aided design* (CAD) and scan models. In Chapter 4, a substantial improvement concerning identifying defect areas on a scan model based on curvature and von Mises stress criteria is presented. Using *generalized numerical inspection fixture* (GNIF) method, corresponding sample points between the CAD and scan models are generated. Applying the developed criteria, sample points on defect areas are filtered out. Then, using the remained sample points as displacement boundary conditions via *Finite Element Non-rigid Registration* (FENR), the CAD model is deformed towards the scan mesh to compensate for the flexible deformation of the part. This improvement in CAI methods results in an automatic and accurate inspection of defects in non-rigid parts. This part of the research is published in a scientific journal and also presented at a conference.

Like all numerical methods, CAI methods are required to be verified and validated. In addition to the validation of maximum amplitude and area for estimated defects, a quantitative validation metric is innovated in Chapter 5. This validation metric provides a deeper investigation on the distance distribution of estimated defects with respect to the

nominal ones. The developed validation metric applies statistical hypothesis testing, *Kolmogorov–Smirnov* (K-S) test, based on ASME V&V recommendations. Applying these validation metrics, the robustness of our developed CAI method is evaluated by introducing different magnitudes of synthetic noise to scan models. The inspection results of aerospace parts conclude that the presence of noise, in general, do not have a significant effect on the developed CAI method. This part of the research is submitted to a scientific journal and presented at a conference.

In the framework of this thesis, a fixtureless CAI method is innovated which assesses the possibility of assembling geometrically deviated non-rigid parts. Inspired by an industrial inspection technique, the developed *Virtual Mounting Assembly-State Inspection* (VMASI) method estimates required permissible loads by which deviated parts are virtually imposed into assembly-state. In fact, the geometrical deviation is absorbed by compliance of non-rigid parts restrained under assembly loads. In Chapter 6, the VMASI method applies a non-rigid registration using *restraining pressures optimization* (RPO) approach to estimate the required assembly loads. These permissible assembly loads minimize the distance and orientation of assembly features on the scan model with reference to nominal features. Eventually, a deviated part can be assembled if the offset of these assembly features remains in the tolerance range. This part of the research is submitted to a scientific journal.

As the conclusion of this work, an inspection method is improved to an automatic and precise CAI approach, a validation metric is developed for evaluating the robustness of CAI methods and a CAI method is developed to assess the feasibility of putting deviated non-rigid parts in assembly-state.

BIBLIOGRAPHY

- Abenheim, G. N., A. Desrochers and A. Tahan (2012). "Nonrigid parts' specification and inspection methods: notions, challenges, and recent advancements." International Journal of Advanced Manufacturing Technology **63**(5-8): 741-752.
- Abenheim, G. N., A. Desrochers, A. S. Tahan and J. Bignon (2015). "A virtual fixture using a FE-based transformation model embedded into a constrained optimization for the dimensional inspection of nonrigid parts." CAD Computer Aided Design **62**: 248-258.
- Abenheim, G. N., A. S. Tahan, A. Desrochers and R. Maranzana (2011). "A Novel Approach for the Inspection of Flexible Parts Without the Use of Special Fixtures." Journal of Manufacturing Science and Engineering-Transactions of the Asme **133**(1).
- Aidibe, A. and A. Tahan (2015). "Adapting the coherent point drift algorithm to the fixtureless dimensional inspection of compliant parts." International Journal of Advanced Manufacturing Technology **79**(5-8): 831-841.
- Aidibe, A., A. S. Tahan and G. N. Abenheim (2012). "Distinguishing profile deviations from a part's deformation using the maximum normed residual test." WSEAS Transactions on Applied & Theoretical Mechanics **7**(1).
- Allen, B., B. Curless and Z. Popović (2003). The space of human body shapes: reconstruction and parameterization from range scans. ACM Transactions on Graphics (TOG), ACM.
- Ascione, R. and W. Polini (2010). "Measurement of nonrigid freeform surfaces by coordinate measuring machine." The International Journal of Advanced Manufacturing Technology **51**(9-12): 1055-1067.
- Bentley, J. L. (1975). "Multidimensional Binary Search Trees Used for Associative Searching." Communications of the Acm **18**(9): 509-517.
- Besl, P. J. and N. D. McKay (1992). "A Method for Registration of 3-D Shapes." Ieee Transactions on Pattern Analysis and Machine Intelligence **14**(2): 239-256.
- Bi, Z. and L. Wang (2010). "Advances in 3D data acquisition and processing for industrial applications." Robotics and Computer-Integrated Manufacturing **26**(5): 403-413.
- Blaedel, K., D. Swift, A. Claudet, E. Kasper and S. Patterson (2002). Metrology of non-rigid objects, Lawrence Livermore National Lab., CA (US).
- Boehnen, C. and P. Flynn (2005). Accuracy of 3D scanning technologies in a face scanning scenario. 3-D Digital Imaging and Modeling, 2005. 3DIM 2005. Fifth International Conference on, IEEE.
- Borouchaki, H., P. L. George and S. H. Lo (1996). "Optimal delaunay point insertion." International Journal for Numerical Methods in Engineering **39**(20): 3407-3437.
- Bronstein, A. M., M. M. Bronstein and R. Kimmel (2006). "Generalized multidimensional scaling: A framework for isometry-invariant partial matching."

Proceedings of the National Academy of Sciences of the United States of America **103**(5): 1168-1172.

Bronstein, A. M., M. M. Bronstein and R. Kimmel (2009). "Topology-invariant similarity of nonrigid shapes." International journal of computer vision **81**(3): 281-301.

Camelio, J. A., S. J. Hu and D. J. Ceglarek (2002). Impact of fixture design sheet metal assembly variation. ASME 2002 International Design Engineering Technical Conferences and Computers and Information in Engineering Conference, American Society of Mechanical Engineers.

Chen, H., S. Jin, Z. Li and X. Lai (2014). "A comprehensive study of three dimensional tolerance analysis methods." Computer-Aided Design **53**: 1-13.

Chen, W., L. Baghdasaryan, T. Buranathiti and J. Cao (2004). "Model validation via uncertainty propagation and data transformations." AIAA journal **42**(7): 1406-1415.

Committee, A. S. (1998). AIAA Guide for the Verification and Validation of Computational Fluid Dynamics Simuations (G-077-1998), AIAA.

Committee, V. (2009). "Standard for verification and validation in computational fluid dynamics and heat transfer." American Society of Mechanical Engineers, New York.

Cowles, B., D. Backman and R. Dutton (2012). "Verification and validation of ICME methods and models for aerospace applications." Integrating Materials and Manufacturing Innovation **1**(1): 1-16.

Cuillière, J. C. and V. Francois (2014). "Integration of CAD, FEA and topology optimization through a unified topological model." Computer-Aided Design and Applications **11**(5): 1-15.

Dijkstra, E. W. (1959). "A note on two problems in connexion with graphs." Numerische mathematik **1**(1): 269-271.

Dowding, K. J., I. H. Leslie, M. L. Hobbs, B. M. Rutherford, R. G. Hills and M. M. Pilch (2004). Case study for model validation: assessing a model for thermal decomposition of polyurethane foam, Sandia National Laboratories.

Dyer, R., H. Zhang and T. Möller (2008). Surface sampling and the intrinsic Voronoi diagram. Computer Graphics Forum, Wiley Online Library.

Gao, J., N. Gindy and X. Chen (2006). "An automated GD&T inspection system based on non-contact 3D digitization." International Journal of Production Research **44**(1): 117-134.

Gentilini, I. and K. Shimada (2011). "Predicting and evaluating the post-assembly shape of thin-walled components via 3D laser digitization and FEA simulation of the assembly process." Computer-aided design **43**(3): 316-328.

Greenspan, M. and G. Godin (2001). "A nearest neighbor method for efficient ICP." Third International Conference on 3-D Digital Imaging and Modeling, Proceedings: 161-168.

- Henrikson, J. (1999). "Completeness and total boundedness of the Hausdorff metric." MIT Undergraduate Journal of Mathematics **1**: 69-80.
- Hills, R. G. and I. H. Leslie (2003). Statistical validation of engineering and scientific models: validation experiments to application, Sandia National Labs., Albuquerque, NM (US); Sandia National Labs., Livermore, CA (US).
- Hills, R. G. and T. G. Trucano (1999). "Statistical validation of engineering and scientific models: Background." Sandia National Laboratories, Albuquerque, NM, Report No. SAND99-1256.
- Jaramillo, A., F. Prieto and P. Boulanger (2013). "Fast dimensional inspection of deformable parts from partial views." Computers in Industry **64**(9): 1076-1081.
- Karbacher, S. and G. Haeusler (1998). A new approach for modeling and smoothing of scattered 3D data [3313-21]. PROCEEDINGS-SPIE THE INTERNATIONAL SOCIETY FOR OPTICAL ENGINEERING, SPIE INTERNATIONAL SOCIETY FOR OPTICAL.
- Karbacher, S. and G. Hausler (1998). "A new approach for modeling and smoothing of scattered 3D data." Three-Dimensional Image Capture and Applications **3313**: 168-177.
- Kimmel, R. and J. A. Sethian (1998). "Computing geodesic paths on manifolds." Proceedings of the National Academy of Sciences **95**(15): 8431-8435.
- Leake, J. M. and J. L. Borgerson (2013). Engineering design graphics: sketching, modeling, and visualization, John Wiley & Sons.
- Li, Y. D. and P. H. Gu (2004). "Free-form surface inspection techniques state of the art review." Computer-Aided Design **36**(13): 1395-1417.
- Li, Y. D. and P. H. Gu (2005). "Inspection of free-form shaped parts." Robotics and Computer-Integrated Manufacturing **21**(4-5): 421-430.
- Liu, S., S. Hu and T. Woo (1996). "Tolerance analysis for sheet metal assemblies." Journal of Mechanical Design **118**(1): 62-67.
- Liu, S. C. and S. J. Hu (1997). "Variation simulation for deformable sheet metal assemblies using finite element methods." Journal of manufacturing science and engineering **119**(3): 368-374.
- Liu, Y., W. Chen, P. Arendt and H. Z. Huang (2011). "Toward a better understanding of model validation metrics." Journal of Mechanical Design, Transactions of the ASME **133**(7).
- Martínez, S., E. Cuesta, J. Barreiro and B. Álvarez (2010). "Analysis of laser scanning and strategies for dimensional and geometrical control." The International Journal of Advanced Manufacturing Technology **46**(5-8): 621-629.
- Masuda, T. and N. Yokoya (1995). "A Robust Method for Registration and Segmentation of Multiple Range Images." Computer Vision and Image Understanding **61**(3): 295-307.

- Merkley, K. G. (1998). Tolerance analysis of compliant assemblies, Citeseer.
- Mounaud, M., F. Thiebaut, P. Bourdet, H. Falgarone and N. Chevassus (2011). "Assembly sequence influence on geometric deviations propagation of compliant parts." International Journal of Production Research **49**(4): 1021-1043.
- Oberkampf, W. L. and M. F. Barone (2006). "Measures of agreement between computation and experiment: Validation metrics." Journal of Computational Physics **217**(1): 5-36.
- Oberkampf, W. L. and T. G. Trucano (2008). "Verification and validation benchmarks." Nuclear engineering and Design **238**(3): 716-743.
- Oberkampf, W. L., T. G. Trucano and C. Hirsch (2004). "Verification, validation, and predictive capability in computational engineering and physics." Applied Mechanics Reviews **57**(1-6): 345-384.
- Paez, T. L. and A. Urbina (2002). Validation of mathematical models of complex structural dynamic systems. Proceedings of the ninth international congress on sound and vibration, Orlando, FL.
- Radvar-Esfahlan, H. (2010). Geometrical inspection of flexible parts using intrinsic geometry. Master's thesis, École de technologie supérieure, Montreal.
- Radvar-Esfahlan, H. and S.-A. Tahan (2012). "Nonrigid geometric metrology using generalized numerical inspection fixtures." Precision Engineering **36**(1): 1-9.
- Radvar-Esfahlan, H. and S.-A. Tahan (2014). "Robust generalized numerical inspection fixture for the metrology of compliant mechanical parts." The International Journal of Advanced Manufacturing Technology **70**(5-8): 1101-1112.
- Ravishankar, S., H. Dutt and B. Gurumoorthy (2010). "Automated inspection of aircraft parts using a modified ICP algorithm." The International Journal of Advanced Manufacturing Technology **46**(1-4): 227-236.
- Rusinkiewicz, S. and M. Levoy (2001). "Efficient variants of the ICP algorithm." Third International Conference on 3-D Digital Imaging and Modeling, Proceedings: 145-152.
- Rutherford, B. and K. Dowding (2003). "An approach to model validation and model-based prediction—polyurethane foam case study." SAND2003-2336, Sandia National Laboratories, Albuquerque.
- Sabri, V., S. A. Tahan, X. T. Pham, D. Moreau and S. Galibois (2016). "Fixtureless profile inspection of non-rigid parts using the numerical inspection fixture with improved definition of displacement boundary conditions." International Journal of Advanced Manufacturing Technology **82**(5-8): 1343-1352.
- Savio, E., L. De Chiffre and R. Schmitt (2007). "Metrology of freeform shaped parts." Cirp Annals-Manufacturing Technology **56**(2): 810-830.

Schwer, L., H. Mair and R. Crane (2012). "Guide for verification and validation in computational solid mechanics." American Society of Mechanical Engineers, ASME V&V **10.1**.

Sornette, D., A. Davis, K. Ide, K. Vixie, V. Pisarenko and J. Kamm (2007). "Algorithm for model validation: Theory and applications." Proceedings of the National Academy of Sciences **104**(16): 6562-6567.

Sun, X., P. L. Rosin, R. R. Martin and F. C. Langbein (2008). Noise in 3D laser range scanner data. Shape Modeling and Applications, 2008. SMI 2008. IEEE International Conference on, IEEE.

Weckenmann, A. and A. Gabbia (2006). "Testing formed sheet metal parts using fringe projection and evaluation by virtual distortion compensation." Fringe 2005: 539-546.

Weckenmann, A., P. Gall and J. Hoffmann (2004). Inspection of holes in sheet metal using optical measuring systems. Proceedings of Vith International Science Conference Coordinate Measuring Technique (April 21-24, 2004, Bielsko-Biala, Poland).

Weckenmann, A. and J. Weickmann (2006). "Optical Inspection of Formed Sheet Metal Parts Applying Fringe Projection Systems and Virtual Fixation." Metrology and Measurement Systems **13**(4): 321-330.

Weckenmann, A., J. Weickmann and N. Petrovic (2007). Shortening of inspection processes by virtual reverse deformation. 4th international conference and exhibition on design and production of machines and dies/molds, Cesme, Turkey.

Zhu, L., J. Barhak, V. Srivatsan and R. Katz (2007). "Efficient registration for precision inspection of free-form surfaces." International Journal of Advanced Manufacturing Technology **32**(5-6): 505-515.

APPENDIX A: GENERALIZED NUMERICAL INSPECTION FIXTURE (GNIF)

The *Generalized Numerical Inspection Fixture* (GNIF) method is developed to inspect non-rigid parts in a free-state. GNIF is developed by Radvar-Esfahlan in École de Technologie Supérieure and presented for the first time in his master thesis titled as *geometrical inspection of flexible parts using intrinsic geometry*. This method aims at making a comparison between the CAD and scan models of a part to identify and evaluate defects on scan models. However, non-rigid parts in a free-state may deform due to the compliance of these parts. Therefore, the scan model of non-rigid parts needs to be aligned and registered with respect to its CAD model in a common coordinate system. In fact, GNIF performs a non-rigid registration for which corresponding sample points on the CAD and scan models are generated. These corresponding sample points are generated based on the assumption that the CAD and scan models are intrinsically similar, which means the corresponding inter-point geodesic distances on the surfaces of these models remain similar. This assumption is valid for deformed scan models in a free-state on which their surfaces are not stretched. It should be noted that the similarity between non-rigid parts can be divided into intrinsic and extrinsic similarity. Intrinsic similarity refers to the metric structure on the surface of parts whereas extrinsic similarity refers to how these parts are laid out in the Euclidean space (Bronstein, Bronstein et al. 2009). As illustrated in Figure A-1, the three geometries (shape (a), (b) and (c)) are intrinsically similar. Referring to this figure, shape (b) and (c) are also extrinsically similar but shape (a) is extrinsically dissimilar compared to shape (b) and (c). In other words, shape (b) and (c) belong to the same metric space (X, d_X) , where X is a set (coordinates of nodes on the surface of shapes) and d_X is a geodesic metric on X with a metric function defined as $d: X \times X \rightarrow \mathbb{R}$. However, shape (a) belongs to a different metric space (Y, d_Y) even though this shape is intrinsically similar to shapes (b) and (c).

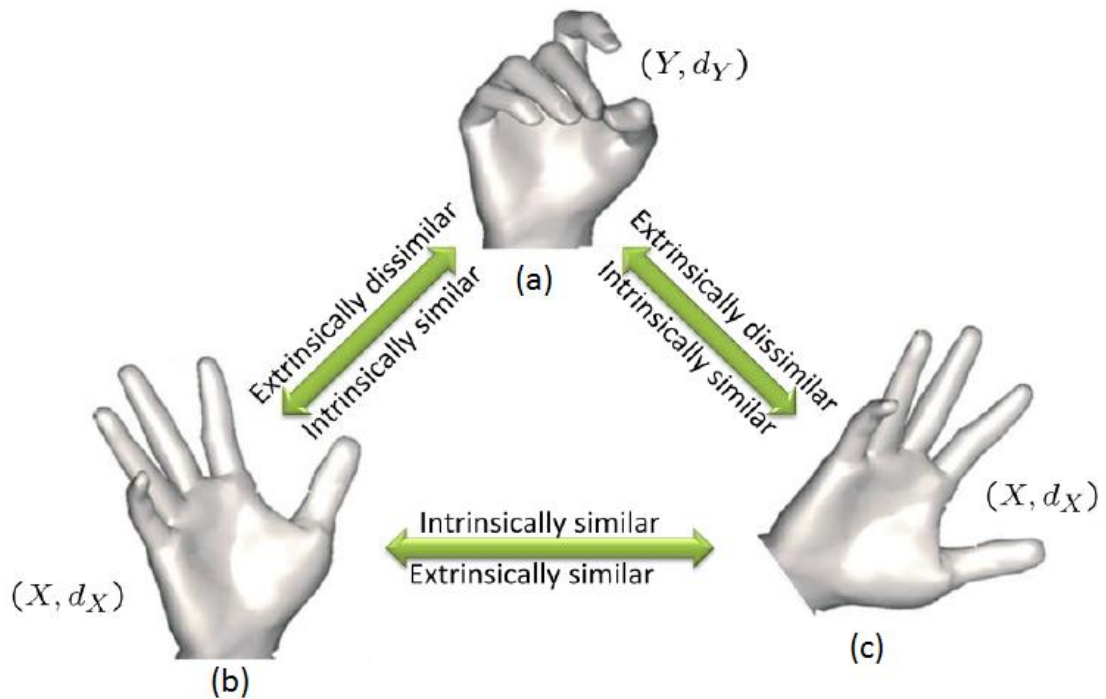


Figure A-1: Illustration of intrinsic and extrinsic similarity between the models (Radvar-Esfahlan 2010).

In order to generate corresponding sample points, GNIF initially generates sets of sample points which are randomly distributed on CAD and scan models. These sample points are evenly distributed on surfaces of a model for which each sample point is located the farthest possible with respect to the others. This random distribution is performed by using *Voronoi tessellation* method (Dyer, Zhang et al. 2008). However, this initial distribution of sample points on CAD model does not correspond with those on scan model. In other words, this initial distribution of sample points cannot be used for a non-rigid registration. Therefore, GNIF determines the corresponding pair of sample points on the CAD and scan models by finding the minimum difference between estimated geodesic distances of sample points on the CAD model with respect to those on the scan model. To this end, the pairwise geodesic distances on the discretized form of models (CAD mesh and scan point clouds) are estimated by using *Fast Marching Algorithm* (FMA) (Kimmel and Sethian 1998). It is worthy to mention that other methods such as *Dijkstra's shortest path algorithm* (Dijkstra 1959) can also estimate geodesic distances on dense meshes.

However, as shown in Figure A-2, the geodesic distance on a triangulated mesh (with an optimized number of nodes) results in a more accurate estimation by using FMA (illustrated in red color) compared to *Dijkstra's shortest path algorithm* (illustrated in green color).

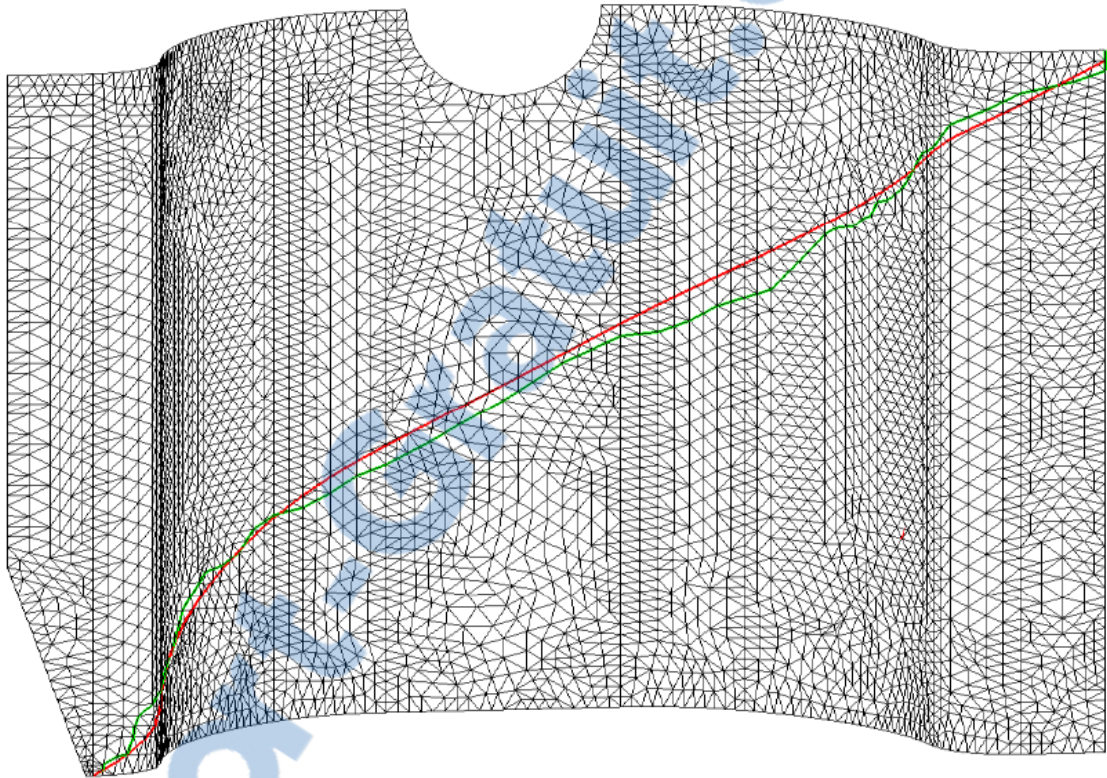


Figure A-2: Geodesic distance between two points on a triangulated mesh is better estimated with *Fast Marching Algorithm* (the red path) compared to *Dijkstra's shortest path algorithm* (the green path) (Radvar-Esfahlan 2010).

As mentioned above, GNIF aims at generating corresponding sample points on the CAD and scan models by finding the minimum difference between geodesic distances of sample points on the CAD and scan models. This minimum geodesic difference is determined by using *Generalized Multi-Dimensional Scaling* (GMDS) (Bronstein, Bronstein et al. 2006). In Figure A-3, the CAD and scan models of a non-rigid part are sampled with two different metric spaces of (X, d_x) and (Y, d_y) . The GNIF generates these initial sets of n sample points on the surfaces of these models. The pairwise geodesic distances between these sample

points on the CAD and scan models are then calculated by *fast marching algorithm*. These geodesic distances are presented by $n \times n$ symmetric matrices (D_x and D_Y as illustrated in Equations A-1 and A-2) wherein the geodesic distance from a point to itself is zero ($d_{ii} = 0$ and $\delta_{ii} = 0$).

$$D_X = \begin{bmatrix} 0 & d_{12} & d_{13} & \dots \\ & 0 & d_{23} & \dots \\ & & 0 & \dots \\ & & & \dots \end{bmatrix}, \quad d_{ii} = 0, (i = 1, \dots, n) \quad \text{A-1}$$

$$D_Y = \begin{bmatrix} 0 & \delta_{12} & \delta_{13} & \dots \\ & 0 & \delta_{23} & \dots \\ & & 0 & \dots \\ & & & \dots \end{bmatrix}, \quad \delta_{ii} = 0, (i = 1, \dots, n) \quad \text{A-2}$$

Then, the corresponding sample points on these models are determined using GMDS which minimizes the differences between pairwise distances of generated sample points on the CAD model with respect to those on the scanned model. In fact, GMDS solves Equation A-3, which is a minimization (nonlinear least-square) problem, to determine the corresponding sample points on the scan model (Y').

$$Y' = \arg \min_{Y \in R^3} \sigma_2(Y) \quad \text{A-3}$$

Wherein $\sigma_2(Y)$, which measures the distortion of scan model with respect to CAD model, is called distortion criterion. As defined in Equation A-4, $\sigma_2(Y)$ is based on the differences of inter-point distances between the generated sample points on the CAD and scan models.

$$\sigma_2(Y) = \sum_{i>j} |d_Y(y_i, y_j) - d_X(x_i, x_j)|^2 \quad \text{A-4}$$

In Equation A-4, x_1, \dots, x_n are n initial sample points evenly distributed on the CAD model (X) and y_1, \dots, y_n are n initial sample points evenly distributed on the scan model (Y). As illustrated in Figure A-3, the corresponding sample points on the scan

model (Y'), which is the solution of Equation A-3, is presented with n points y'_1, \dots, y'_n on the scan model. These sample points correspond the scan model with respect to the CAD model to fulfill the non-rigid registration process.

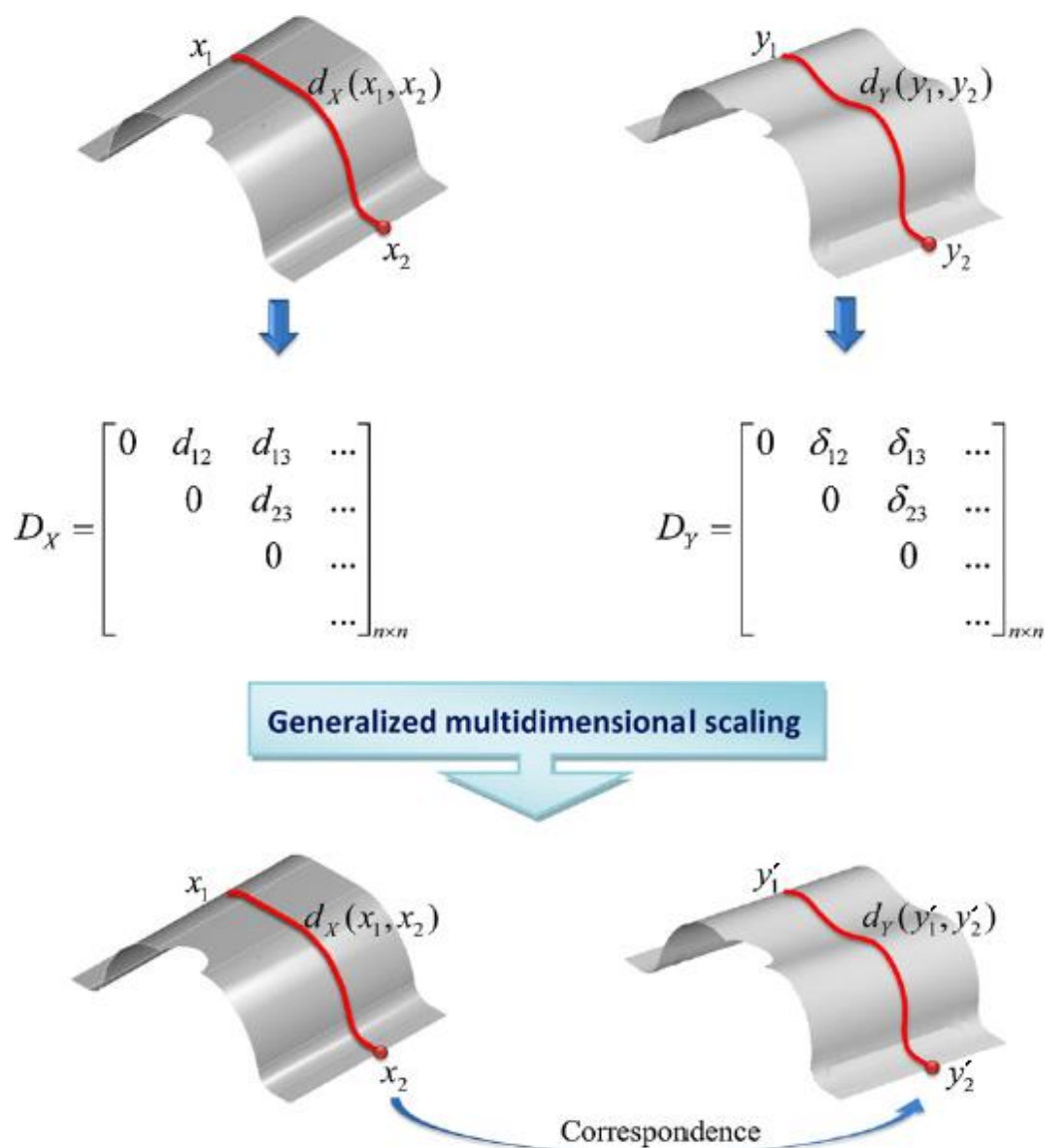


Figure A-3: Determining the correspondence between sample points (*number of sample points = n*) on the CAD and scan models (D_x and D_y represent symmetric matrices of pairwise geodesic distances, calculated by *fast marching algorithm*) (Radvar-Esfahlan 2010).

Corresponding sample points on the surfaces of CAD and scan models of a non-rigid part is illustrated in Figure A-4. Once the corresponding sample points are determined, displacement vectors are calculated based on the coordinate of sample points on the CAD model and their corresponding sample points on the scan model. These displacement vectors are then used as displacement boundary conditions via *Finite Element Non-rigid Registration* (FENR) to deform the CAD model towards scan model. FENR aims at compensating for the flexible deformation of scan model in a free-state. Finally, a geometrical comparison between the scan model and the CAD model after FENR allows an inspection to evaluate defects on the scanned part.

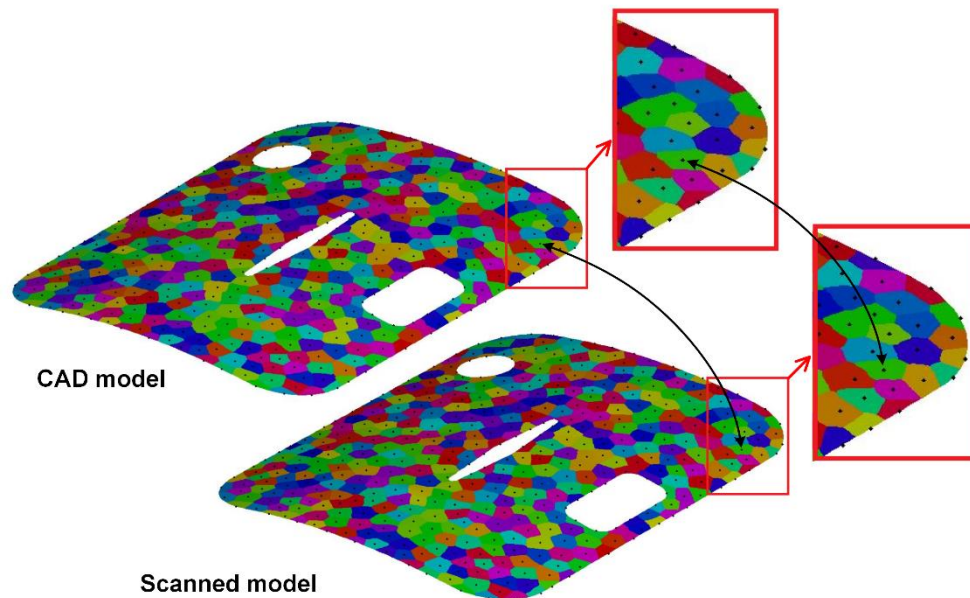


Figure A-4: *Finite element non-rigid registration* using corresponding sample points generated by GNIF method on the CAD and scan models.